Karlsruhe Institute of Technology

Computational modeling of syntaxial overgrowth cementation and fracture propagation in sedimentary rocks

Zur Erlangung des akademischen Grades

Doktor der Ingenieurwissenschaften

von der KIT-Fakultät für Maschinenbau

des Karlsruher Instituts für Technologie (KIT)

genehmigte **Dissertation**

von

M.Sc. Nishant Prajapati

Tag der mündlichen Prüfung:	29.07.2020
Erstgutachter:	Prof. Dr. rer. nat. Britta Nestler
Zweitgutachter:	Prof. Dr. rer. nat. habil. Christoph Hilgers

Abstract

Present dissertation deals with the computational modeling of the phenomenon of a) syntaxial overgrowth cementation and b) brittle anisotropic fracture propagation in sedimentary rocks, with the aid of phase-field approach.

In the first part of this research, a multiphase-field (MPF) model of cementation was adapted to investigate the role of crack opening rates and cement growth rates on the development of different calcite vein morphologies, as a result of bitaxial growth in syntaxial veins in two dimensions (2-D). A geometric shift algorithm was developed to simulate the incremental fracture opening under different boundary conditions. The numerical results elucidate the transition of vein textures from fibrous to elongate-blocky forms, and finally to open-space euhedrally-terminated crystal morphologies, for increasing crack opening rates. For the first time, the formation mechanisms of uniform and non-uniform fibrous veins depending upon the initial crack aperture is unravelled. A stark resemblance of the numerically sealed vein microstructures with the natural vein samples demonstrates the capabilities of the adapted MPF model in comprehending the growth dynamics of calcite veins.

Next, the MPF model was adapted to study the syntaxial quartz cementation in sandstones in 3-D. The impact of initial grain size of unicrystalline quartz aggregates on the evolution of key petrophysical rock properties, i.e. porosity, permeability and pore size distributions, during progressive quartz cementation was investigated. The dynamic correlations between these properties were further established, and critically analysed in comparison with the existing literature. During the course of this research, the MPF model was extended to more rigorously account for the faceting-dependent growth tendencies of quartz cements. Further, a systematic procedure was developed to generate several digital grain packs comprising of different proportions of unicrystalline and polycrystalline aggregates, analogous to natural sandstones in terms of grain shapes, sizes and depositional porosity. Utilizing these digital packs, the effect of polycrystallinity of grains on the cement volumes, porosity and permeability of sandstones during progressive quartz cementation was investigated. The simulated growth velocities along different facets under undisturbed growth conditions show sound agreement with the analytical solution

as well as previous studies. The numerically cemented microstructures of unicrystalline and polycrystalline packs exhibit clear similarities with the corresponding natural samples in terms of crystal morphologies and remaining pore space. The numerically derived relationships between the petrophysical properties and their variation in different sandstones during progressive cementation, while consistent with the previous experimental findings and empirical laws, provide valuable insights on the dynamics of quartz growth in sandstones.

In the last part, a separate MPF model of fracture was adapted to address the phenomenon of brittle microfracturing in quartz sandstones. Two novel aspects of this model are the formulations of I) anisotropic- and II) reduced interfacial crack resistance. While the former accounts for preferred cleavage planes inside each quartz grain, the latter provides a reducible crack resistance along the grain boundaries in a continuous and smooth manner, thereby enabling the model to simulate intergranular fracture growth. With these ingredients, the model is able to simulate the competition between trans- and intergranular modes of crack propagation, while exhibiting preferred fracturing directions within each grain. The model can serve as a powerful tool to investigate complicated fracturing processes in heterogeneous polycrystalline rocks comprising of grains of distinct elastic properties, cleavage planes and grain boundary attributes. The performance and capabilities of the model are demonstrated through the representative numerical examples.

Results of the present dissertation successfully demonstrate the feasibility and applicability of the phase-field method in capturing the essential physics of these processes in an efficient and elegant manner.

Kurzfassung

Die vorliegende Dissertation befasst sich mit der rechnerischen Modellierung des Phänomens a) syntaktischer Überwuchszementierung und b) spröder anisotroper Bruchausbreitung in Sedimentgesteinen, mithilfe des Phasenfeldansatzes.

Im ersten Teil wurde ein Multiphasenfeldmodell (MPF-Modell) für die Zementierung angepasst, um die Rolle von Rissöffnungsraten und Zementwachstumsraten bei der Entwicklung verschiedener Calcitvenenmorphologien als Ergebnis des bitaxialen Wachstums in syntaxialen Venen in zwei Dimensionen (2-D) zu untersuchen. Ein geometrischer Verschiebungsalgorithmus wurde entwickelt, um die inkrementelle Öffnungsweite unter verschiedenen Randbedingungen zu simulieren. Die numerischen Ergebnisse erläutern den bergang von Venentexturen von faserigen zu länglichen blockartigen Formen und schließlich zu euhedrisch terminierten Kristallmorphologien im offenen Raum, zur Erhöhung der Rissöffnungsraten. Zum ersten Mal wurden die Bildungsmechanismen gleichmäßiger und ungleichmäßiger Faservenen in Abhängigkeit von der anfänglichen Rissöffnung verstanden. Die starke Ähnlichkeit der numerisch versiegelten Venenmikrostrukturen mit den natürlichen Venenproben zeigt die Fähigkeit des angepassten MPF-Modells, die Wachstumsdynamik von Calcitvenen zu erfassen.

Als nächstes wurde das MPF-Modell angepasst, um die syntaktische Quarzzementierung in Sandsteinen in 3-D zu untersuchen. Während der fortschreitenden Quarzzementierung wurde der Einfluss der anfänglichen Korngröße von unikristallinen Quarzaggregaten auf die Entwicklung der wichtigsten petrophysikalischen Gesteinseigenschaften, d. h. Porosität, Permeabilität und Porengrößenverteilung, untersucht. Die dynamischen Zusammenhänge zwischen diesen Eigenschaften wurden weiter ermittelt und im Vergleich zur vorhandenen Literatur kritisch analysiert. Im weiteren Forschungsverlauf wurde das MPF-Modell erweitert, um die facettierungsabhängigen Wachstumstendenzen von Quarzzementen genauer zu berücksichtigen. Darüber hinaus wurde ein systematisches Verfahren entwickelt, um mehrere digitale Kornpackungen zu erzeugen, die, analog zu natürlichen Sandsteinen und mit Hinblick auf die Kornformen, Größen und Ablagerungsporositäten, aus unterschiedlichen Anteilen unikristalliner und polykristalliner Aggregate bestehen. Unter Verwendung dieser digitalen Packungen wurde während der

fortschreitenden Quarzzementierung der Einfluss der Polykristallinität von Körnern auf das Zementvolumen, die Porosität und die Permeabilität von Sandsteinen untersucht. Die simulierten Wachstumsgeschwindigkeiten entlang verschiedener Facetten, unter ungestörten Wachstumsbedingungen, zeigen eine gute Übereinstimmung mit der analytischen Lösung sowie früheren Studien. Die numerisch zementierten Mikrostrukturen von unikristallinen und polykristallinen Packungen zeigen hinsichtlich der Kristallmorphologien und des verbleibenden Porenraums deutliche Ähnlichkeiten mit den entsprechenden natürlichen Proben. Die numerisch abgeleiteten Beziehungen zwischen den petrophysikalischen Eigenschaften und ihren Variationen in verschiedenen Sandsteinen, die auf der Grundlage der anfänglichen Korngröße und des Anteils der polykristallinen Quarzaggregate während der fortschreitenden Zementierung variieren, liefern im Einklang mit den vorherigen experimentellen Befunden und empirischen Gesetzen wertvolle Einblicke in die Dynamik des Quarzwachstums in Sandsteinen.

Im letzten Teil wurde ein separates MPF-Bruchmodell angepasst, um das Phänomen der spröden Mikrofrakturierung in Quarzsandsteinen anzugehen. Zwei neue Aspekte dieses Modells sind die Formulierungen von I) anisotroper und II) reduzierter Grenzflächenrissbeständigkeit. Während im ersteren Fall die bevorzugten Spaltungsebenen in jedem Quarzkorn berücksichtigt werden, bietet der letztere Fall kontinuierlich und gleichmäßig eine reduzierbare Rissbeständigkeit entlang der Korngrenzen, wodurch das Modell das intergranulare Bruchwachstum simulieren kann. Mit diesen Bestandteilen kann die Konkurrenz zwischen trans- und intergranularen Rissausbreitungsmodi durch das Modell simuliert und dabei bevorzugte Bruchrichtungen innerhalb jedes Korns aufgezeigt werden. Das Modell kann als leistungsstarkes Werkzeug zur Untersuchung der komplizierten Bruchprozesse in heterogenen polykristallinen Gesteinen dienen, die aus Körnern mit unterschiedlichen elastischen Eigenschaften, Spaltungsebenen und Korngrenzattributen bestehen. Die Leistung und Fähigkeiten des Modells werden anhand der repräsentativen numerischen Beispiele verdeutlicht.

Die Ergebnisse der vorliegenden Dissertation zeigen erfolgreich, dass die Phasenfeldmethode angewendet werden kann, um die wesentliche Physik dieser Prozesse effizient und elegant erfassen zu können.

Dedicated to my late Dada ji,
a man of extraordinary integrity,
a literary scholar and a teacher by profession,
who taught us the importance of education.

Acknowledgments

It fills me with immense joy to express my gratitude to everyone who has contributed to this work. Foremost, I thank Majisa who has been a divine source of my inner strength and a driving force of all my endeavors.

I acknowledge my deepest and sincerest gratitude to Prof. Britta Nestler for trusting my abilities and providing me an opportunity to pursue my doctoral research at the Institute for Applied Materials (IAM-CMS), Karlsruhe Institute of Technology (KIT). Her encouragement, liberty in pushing forward various projects and decisive inputs in the same have not only benefited my research work, but also enriched my academic experience as a PhD student. Thank you Ma'am for your unflinching support and motivation during the last four years.

I thank the Helmholtz association for financial support through the program "Renewable Energies (RE)", efficient use of geothermal energy 35.14.01.

I would like to thank my former and present group leaders, Prof. Kumar Ankit, Dr. Michael Selzer and Dr. Daniel Schneider for their guidance and valuable inputs in different projects. This research work would not have been complete without the cooperation of Prof. Christoph Hilgers and Dr. Benjamin Busch. Thank you Prof. Hilgers and Benjamin for providing experimental support, thin-section analysis and feedback on the modeling results. I am grateful to my collaborators: Christoph Herrmann, Andres Abad Gonzalez and Michael Späth, for their technical support in different projects. Special thanks to Dr. Arnab Mukherjee, Sumanth Nani and Dr. Amol Subhedar for the countless stimulating technical discussions from which I have gained immensely. Exposure to the research work of other colleagues during monthly doctoral seminars have also enhanced the quality of my work. Therefore, I extend my gratitude to all the fellow mates of IAM-CMS and IDM.

I am also thankful to the secretariat at IAM-CMS, KIT, particularly Ms. Inken Heise for helping me with all the paper work during business trips and conferences.

The last four years in Karlsruhe would not have been delightful without lunch-break discussions on a wide range of topics, and weekend activities (such as Friday evening

cricket, poker nights, Sunday afternoon movies and occasional volleyball) with Arnab, Nani, Jay, Walter, Amol, Paul, Fei, Pavan and Nikhil. Thank you guys for making this journey a joyful ride.

I would like to thank Mummy-Daddy, Bai, Nana ji-Nani ji and Simpi for their unconditional love and emotional support. Last but not the least, I express my love and gratitude to my wife Purvi. These years would not have been stress-free without your constant support in all the possible ways. I owe you everything.

List of symbols

Fluid dynamics

$\bar{v}_\mathrm{i}$	Mean velocity in the direction i
$\Delta\bar{p}$	Applied pressure drop
κ	Permeability
κ_i	Permeability in direction i, i being 1, 2 or 3
$\mathcal{S}_\mathrm{k}$	Plane surface with the applied constant pressure $\bar{p}_\mathrm{k}$
μ_f	Dynamic viscosity of the fluid
$\boldsymbol{f_b}$	Body force
$\boldsymbol{v}$	Fluid velocity
l_i	length of computational domain in the direction of the applied pressure drop
p	Pressure
v_τ	Tangential component of the fluid velocity
v_n	Normal component of the fluid velocity

Mechanics

R_c	Crack resistance ratio
$\epsilon_1^\alpha, \epsilon_2^\alpha, \epsilon_3^\alpha$	Phase-specific principal strains for phase α
λ^α	Phase-specific Lame$'$ parameter 1 for phase α
μ^α	Phase-specific Lame$'$ parameter 2 for phase α
$\mathbb{C}^\alpha$	Phase-specific isotropic stiffness tensor for phase α

$\bar{\boldsymbol{\sigma}}$ Effective stresses

$\boldsymbol{\sigma}^{\alpha}$ Phase-specific stresses of phase α

$\phi_{\mathrm{c}}^{\mathrm{crit}}$ Critical crack phase-field

$\boldsymbol{\varepsilon}$ Strain tensor field

$\boldsymbol{u}$ Displacement field

ζ Interfacial crack resistance reduction factor

f_{el} Elastic strain energy density

w_{c} Potential energy density function for crack

Physics

$\mathcal{S}$ Fluid supersaturation index

φ Porosity

φ_{d} Dihedral angle

A_s/M Surface area to mass ratio

d Grain size

G Gibb's free energy

k_{-} Reaction rate constant

R Gas constant

$V_{\mathrm{m}}^{\mathrm{H_2O}}$ Molar volume of water

$V_{\mathrm{m}}^{\mathrm{H_4SiO_4(aq)}}$ Molar volume of aqueous orthosilicic acid solution

$V_{\mathrm{m}}^{\mathrm{Qtz}}$ Molar volume of quartz

T Temperature

Phase-field modeling

h_{s}^{α} Interpolation function of solid phase α

$\boldsymbol{\phi}$ Phase-field vector

$\boldsymbol{\phi}_{\mathrm{s}}$ Set of phase-fields of all the solid phases

Δf_{sl}	Driving force of crystallization
Δt	Numerical time step width
Δx	Numerical grid size
δ	Kinetic anisotropy strength parameter
ε	Length scale parameter
ε_{c}	Length scale parameter for crack surface
$\gamma_{\alpha\beta}$	Surface energy density of the α-β interface
$\Gamma_{\alpha\beta}$	Interface between α and β phases
$\gamma_{\mathcal{I}c}$	Surface energy of the crack-solid interface $\mathcal{I}$
$\gamma_{\mathcal{I}}$	Surface energy of the interface $\mathcal{I}$
γ_{sl}	Surface energy density of the solid-liquid interface
$\hat{\mathbf{n}}_{\mathrm{sl}}$	Unit vector normal to the solid-liquid interface
κ_{c}	Curvature
λ	Lagrange multiplier
$\mathcal{F}$	Helmholtz free energy
$\mathcal{T}$	Interface thickness
$\mathfrak{f}^{\mathrm{Qtz}}$	Anisotropic strength factor for quartz
$\mathfrak{f}_d^{\alpha}$	Phase-specific anisotropic strength factor in the direction d
$\mathfrak{n}_{\mathrm{c,i}}^{\alpha}$	i^{th} component of rotated unit vector for the crack-α interface
μ	Effective kinetic mobility
μ_{sl}^0	Kinetic mobility of solid-liquid interface
μ_{ss}^0	Kinetic mobility of solid-solid interface
μ_{c}	Relaxation parameter
ϕ	Phase-field variable
ϕ_α	Phase-field variable of phase α

ϕ_c	Crack phase-field
$\boldsymbol{\eta}_k^\mathrm{cap}$	Set of vertex vectors of the capillary anisotropy shape
$\boldsymbol{\eta}_k^\mathrm{kin}$	Set of vertex vectors of the kinetic anisotropy shape
$\mathfrak{n}_{\alpha\beta}$	Unit vector normal to the α-β interface
$\mathfrak{n}_\mathrm{c}^\alpha$	Rotated unit vector for the crack-α interface
$\mathfrak{q}_{\alpha\beta}$	Generalized phase-field gradient vector normal to the α-β interface
$\mathfrak{q}_\mathrm{sl}$	Generalized phase-field gradient vector normal to the solid-liquid interface
$\boldsymbol{Q}^\alpha$	Phase-specific rotation matrix
τ	Kinetic coefficient or reciprocal of effective mobility
τ_sl	Inverse kinetic mobility of solid-liquid interface
τ_ss	Inverse kinetic mobility of solid-solid interface
$\mathbf{M}$	Effective diffusion coefficient
a	Gradient energy density function
$a_{\alpha\beta}^\mathrm{cap}$	Capillary anisotropy function for the α-β interface
$a_{\alpha\beta}^\mathrm{kin}$	Kinetic anisotropy function for the α-β interface
f	Bulk free energy density function
f_α	Bulk free energy density of phase α
f_l	Bulk free energy density of liquid phase
f_s	Bulk free energy density of solid phase
$G_{\mathrm{c},0}^\alpha$	Crack resistance of phase α
G_c	Crack resistance
h	Interpolation function for the bulk free energy density
k	Scalar constant for the regularized crack surface energy density
k_w	Scalar constant for the one-sided well type potential energy density function for crack

n_{cap}	Number of vertices of the capillary anisotropy shape
n_{kin}	Number of vertices of the kinetic anisotropy shape
$R_{\text{c/a}}$	c- to a- axis ratio
v_{sl}	Velocity of the solid-liquid interface
w	Potential energy density function
$\mathcal{Q}$	General objective quantity
$\mathfrak{c}_\alpha^{\text{eq}}$	Equilibrium concentration of phase α
$\mathfrak{c}_\alpha$	Molar concentration of phase α
$\boldsymbol{\mathfrak{c}}$	Composition vector
$\boldsymbol{\mathfrak{s}}$	Set of state variables
$\boldsymbol{\mu}$	Chemical potential vector
σ	Surface density
q	Volumetric density
V_α	Volume of phase α

List of abbreviations

1-D One dimension. xix, 30, 31, 39, 40

2-D Two dimensions. i, iii, xvi, xviii–xx, xxiii, xxiv, xxvii, 6, 9, 17–20, 45–47, 57–60, 62–64, 68, 71, 77, 79, 80, 90–92, 104, 105, 115–117, 125, 131, 134, 135

3-D Three dimensions. i, iii, xv, xvi, xviii–xxiv, xxvii, 6, 8, 9, 18–20, 46, 57–60, 62, 63, 68, 69, 71, 79, 80, 83, 84, 90–92, 94, 95, 97, 105, 116, 117, 131, 134, 135

c/a Crystallographic c- to a-axis ratio. xxi, 58, 63, 65–68, 79

CFD Computational fluid dynamics. 32, 33

CFM Computational fracture mechanics. 19

COD C-axes orientation difference. 100–102

CZM Cohesive zone modeling. 21

DEM Discrete element method. 19

MAT Medial axis transform. 76

MPF Multiphase-field model. i–iv, 6, 18, 21, 29, 38, 43, 44, 58, 59, 63, 72, 79, 82, 84, 86, 111, 114, 119, 129, 132–136

ODE Ordinary differential equation. 30, 31, 40

PDE Partial differential equation. 28, 29

RSG Rotated staggered grid. 38

TDGL Time-dependent Ginzburg-Landau. 133, 135

Contents

List of Figures

List of Tables

Part I
Introduction and literature review

Chapter 1

Introduction: Motivation and synopsis

1.1 Motivation

Sandstones and limestones are two important sedimentary rocks, that account for more than 50% of the world hydrocarbon reservoirs. The microstructure and petrophysical characteristics (e.g. porosity, flow behavior) of reservoir rocks evolve with time due to different processes such as cementation, fluid-flow, fracturing, among several others. Understanding these processes through experimental observation is an arduous task, as it requires a three-dimensional representation of rock microstructure and an in situ observation of temporal evolution. Consequently, phenomenological computational models based on the governing physics, that are able to simulate these processes and predict their impact on rock microstructure and physical properties are adopted. In the hydrocarbon and geothermal energy industry, computational approach offers fascinating tools for different purposes. These include reservoir characterization, process controllability enhancement and decision making on various engineering issues that arise during different stages of evaluation, development and expansion of projects related to oil or gas recovery as well as geothermal energy. The present dissertation focusses on addressing two important processes, namely *cementation* and *fracturing*, in the context of reservoir rocks, by utilizing a computational approach known as the *phase-field method*.

Process 1. Cementation: Cementation is broadly described as precipitation of new minerals in the intergranular pore spaces, resulting in reduction of porosity and permeability of rocks. The hydrothermal solutions or formation fluids, circulating in the pore spaces of rocks, serve as the source of cement forming minerals. When the aggregates/grains of

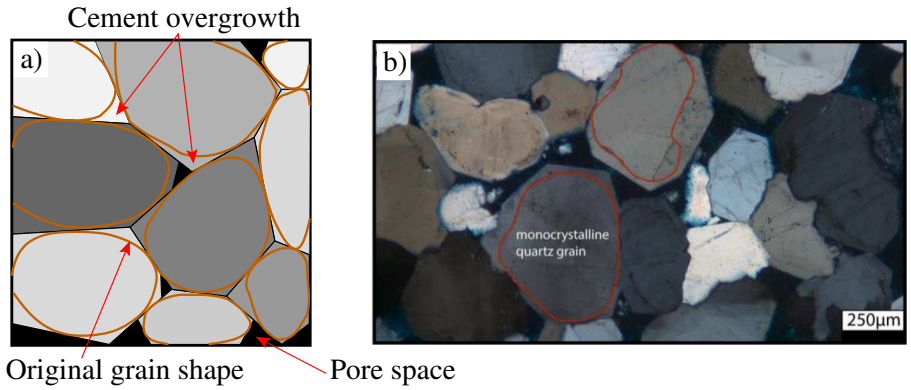

Figure 1.1: a) Schematics of the syntaxial quartz cementation process: Quartz cements deposit in optical continuity with the grains and the grains grow anisotropically such that they develop flat facets and sharp corners according to their growth habit. The original grain shapes are shown in brown lines. b) Thin-section microphotograph of a Rotliegendes sandstone sample from North England visualized under the cross polarized light. The sample illustrates differently oriented quartz grains (shown in different colors), optically continuous quartz cements (depicted in same color as the grains), original grain boundaries (thin greyish lines and highlighted in red for two grains) and the remaining pore space (black color). Thin-section image is adapted from Prajapati et al. *[1] in accordance with the permission policy of the original publisher, American Geophysical Union.*

a rock and the precipitating cement are the same mineral, cement deposition on the grain surface occurs epitaxially. As a result, the grains grow anisotropically according to the growth habit of the mineral, and this growth phenomenon in rocks is known as *syntaxial overgrowth cementation*. During this particular process, cement growth occurs in optical continuity with the original grains. The deposited cements manifest in the form of overgrowths on grains. For the quartz mineral exhibiting the prismatic growth habit (figure 2.1 of chapter 2), the quartz grains grow such that the overgrowths develop flat facets and sharp corners, as schematically illustrated for quartz cement growth in sandstones in figure 1.1a. Figure 1.1b depicts the thin-section image of a Rotliegendes sandstone sample from North England. The sample illustrates quartz grains, optically continuous quartz cement overgrowths, original grain boundaries and pore space. When cementation occurs in the open fractures of rocks, crack-seal morphologies, popularly known as *geological veins*, are formed. For instance, two visibly distinct calcite vein morphologies, formed due to syntaxial calcite cementation in open fractures of limestone under different boundary conditions, are depicted in figure 1.2. The vein-textures carry enormous amount of information about the crack-opening, cement growth and fluid-flow histories, and therefore, have always been a topic of intensive research for the petrographers and geophysicists. Thus, the work presented in the first part of this dissertation was carried out with a motivation to investigate the phenomenon of syntaxial overgrowth cementa-

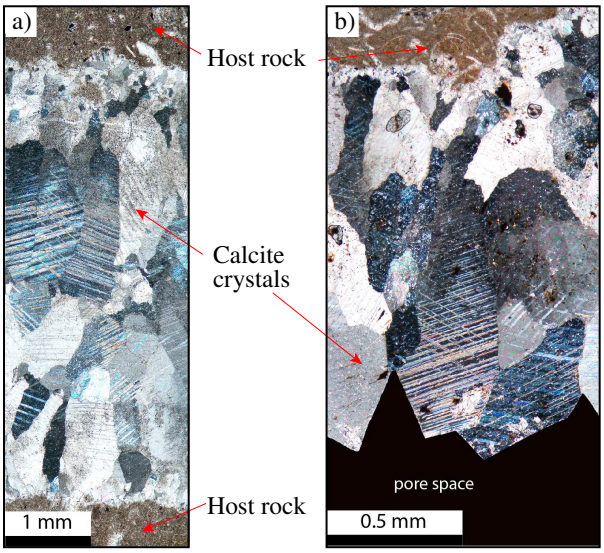

Figure 1.2: Thin-section microphotographs of two different calcite vein morphologies a) elongate-blocky and b) euhedral, observed in the natural samples of Jurassic limestone from southern England. The image is adapted from Prajapati et al. *[2], in accordance with permission policy of the original publisher, Springer.*

tion, its implications on the resulting morphologies and different rock properties in calcite limestone and quartz sandstone.

Process 2. Fracturing: In reservoir rocks, fractures may be classified as microfractures and macrofractures, based on the length scale [3]. Macrofracturing finds extensive applications in a wide range of rock engineering problems (e.g. rock cutting, underground excavations, etc.) particularly for the analysis of damage and crack-induced failure. On the other hand, microfractures, that require microscopy for detection, are useful in providing key evidences about the stress states, processes of rock failure and anisotropies at the grain scale. Microfractures serve as nucleation sites for macrofractures and control the physical properties such as strength, elastic wave velocities, and permeability of rocks. Due to the above-mentioned reasons, a deep understanding of the process of microfracturing is imperative. At microscale, sandstones and limestones are heterogeneous multiphasic materials, as they are composed of a large population of differently oriented crystalline grains which are cemented together. In such heterogeneous multigrain systems, the grains may exhibit preferred cleavage planes arising due to crystallographic direction-dependent material properties. Moreover, the tendency of a crack to propagate along the grain boundaries may be higher or lower than through the grains, depending upon e.g. the presence of second-phase particles, impurity or atom segregation at the grain boundaries. Such heterogeneities and anisotropies at grain-scale render microfracturing a highly complex phenomenon. In the context of polycrystalline reservoir rocks considered at the microscale, a microfracture can be classified into the following categories

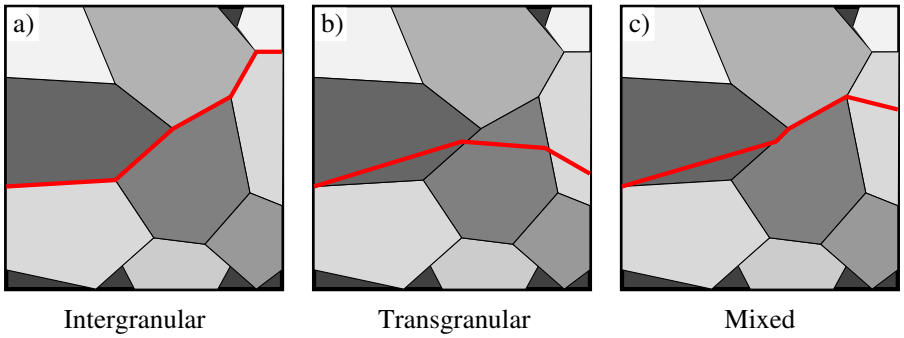

Figure 1.3: Schematics illustrating different types of microfracturing in polycrystalline materials: a) Intergranular, b) Transgranular and c) Mixed, with the fracture path shown in red color.

[4, 5] (see also figure 1.3a-c):

1. *Intergranular*: Fracture propagating along the grain boundaries.
2. *Transgranular*: Fracture propagating through the grains.
3. *Mixed*: Combination of intergranular and transgranular fracture.

In a strict sense, most of the natural samples undergo the mixed type of fracturing. The work presented in the second part of this dissertation was carried out with a motivation to formulate, adapt and extend a phase-field model that can describe the phenomenon of brittle anisotropic microfracturing in polycrystalline rocks.

An increasing availability of computational resources has facilitated the numerical investigations in delineating the intricacies of complex phenomena in the three dimensions. Phase-field method is one such numerical approach, which is utilized in the present dissertation for studying the two above-discussed processes in reservoir rocks. The phase-field method has two characteristic features that distinguish it from other computational approaches. One, in addition to the standard thermodynamic variables present in other models, the phase-field method introduces a scalar variable, called *phase-field*, in order to describe different phases of a system, differing in atleast one physical property (e.g. strength, chemical composition, etc.). Two, the binary interfaces (e.g. grain boundaries, fracture surface, solid-liquid interface), which are present in different systems, are described as diffuse regions. These two features obviate the need for explicit tracking of the interfaces, which is a strenuous aspect of the conventional sharp-interface computational approaches (e.g. front tracking methods for crystal growth [6, 7], extended finite element method for crack propagation [8], etc.). This unique quality renders the phase-field method, a standout approach in modeling different processes like microstructure evolu-

tion during phase-transitions [9–12], crack propagation [13, 14] and mineral growth in geological systems [15–18].

1.2 Synopsis

The present dissertation is organized as follows. In chapter 2, a theoretical background and literature review of the processes of cementation and fracturing in reservoir rocks are presented. In the same chapter, a review of the computational methods for modeling these processes leading up to the phase-field method is done. Subsequently, the generalized multiphase-field (MPF) formulations utilized for investigating the specific processes of syntaxial overgrowth cementation and brittle anisotropic microfracturing are elaborated in chapters 3 and 4, respectively. In chapter 3, the model utilized for the computational fluid dynamic analysis, to compute the flow behavior of the rock structures, is also outlined. In the subsequent chapters 5, 6, 7 and 8, the results of the numerical investigations carried out within the scope of this research work, along with their analysis and discussions are presented in detail. The two-dimensional (2-D) numerical results of syntaxial calcite cementation in bitaxial veins occurring in limestone are discussed in chapter 5. The investigations in this chapter were performed using the MPF model introduced in chapter 3. Next, in chapter 6, the MPF model of cementation is adapted for the simulation of syntaxial quartz cementation occurring in the intergranular pore space of sandstones in 3-D. In particular, the role of initial grain size on the morphological evolution and the dynamic relationships between porosity, permeability and pore size distributions during quartz cementation in sandstones is studied. In chapter 7, the previous MPF model for quartz cementation is extended to capture the quartz growth tendencies and intricacies of the process in a more rigorous manner. Moreover, complete parameter set of the MPF model is determined for the temperature and pressure matching common reservoir conditions. Finally, the extended model is utilized to investigate the influence of polycrystallinity of quartz aggregates on the relationships between cement volumes, porosity and permeability, in comparison with experimental results as well as empirical equations. Chapter 8 presents the numerical results addressing the phenomenon of brittle anisotropic fracturing in sandstones based on the MPF model for crack propagation introduced in the chapter 4. This investigation includes the procedure to adapt the MPF crack model in accordance with the material properties of polycrystalline sandstones at micro-scale, followed by a set of representative numerical examples for the demonstration of the model predictions and performance. Finally, in chapter 9, the dissertation is concluded with a brief summary of the findings, highlights and achievements of this research work, followed by an outlook and possible directions for the future.

Chapter 2

Background and literature review

Sedimentary rocks are formed as a result of complex physical, chemical and biological changes that may occur at different time scales. The entire phenomenon of transformation of freshly deposited sediments during the early periods to the present-day sedimentary rocks is known as *lithification*. Lithification involves *cementation* and *mechanical compaction* as the two main processes, that result in loss of rock porosity, and thereby, the flow-through behaviour. During cementation, authigenic cement phases (e.g. quartz, calcite, etc.) precipitate from the circulating formation fluids and occlude the intergranular pore space or fractures, ultimately altering the flow pathways in sedimentary rocks [19]. Mechanical compaction, driven by self-weight or other forms of loading, additionally reduces the pore volume [20]. As opposed to these two phenomena, *fracturing* is a process that increases rock porosity due to the formation of new flow pathways. In reservoir rocks (e.g. sandstones, limestones), the quality of a reservoir is evaluated based on petrophysical characteristics such as *porosity* and *permeability* [21, 22]. Therefore, cementation, mechanical compaction and fracturing are some of the main factors governing the quality of sandstone and carbonate reservoirs [19, 20, 23–32]. In addition to the purpose of reservoir quality prediction, a deep understanding of these processes and their controls is imperative for several other applications such as design of engineered geothermal systems, laboratory synthesis of crystals and geological veins, rock mechanical analysis, among others.

Present dissertation focusses on computational modeling and investigation of the following two specific physical processes in sedimentary rocks: I) *syntaxial overgrowth cementation* and II) *brittle anisotropic microfracturing*. A comprehensive review of the relevant aspects of these processes is presented in sections 2.1 and 2.2. Subsequently, a detailed review of the theoretical and computational advancements leading up to the methodology adopted for this work is presented in section 2.3.

2.1 Syntaxial overgrowth cementation in sedimentary rocks

Cementation is the precipitation of new minerals in the open spaces (i.e. intergranular pore space and open cracks) of rocks from the circulating formation fluids. These fluids supply the cementing minerals (e.g. quartz, calcite, dolomite, etc.) and are generally supersaturated with respect to the cement-forming solute [33, 34]. When the detrital grains of a rock and the cements are the same mineral, the cements deposit in crystallographic continuity with the grain, resulting in syntaxial (also referred as 'epitaxial') growth of grains [33]. This particular process is known as *syntaxial overgrowth cementation*. The deposited cements manifest in the form of *overgrowths* on detrital grains, and recreate the growth habit of mineral when sufficient space is present. Syntaxial overgrowth cementation results in the evolution of microstructure as well as physical properties of rocks. This phenomenon is also responsible for the formation of distinct crack-seal microstructures known as *geological veins*. A wide variety of vein textures (e.g. fibrous, elongate-blocky, euhedral) are formed when cracks are filled with cements under different boundary conditions [35].

In the upcoming parts of this section, the following two syntaxial growth processes are discussed in more detail: I) quartz cementation in sandstones, and II) calcite cementation in fractured limestones resulting in different vein morphologies.

2.1.1 Syntaxial quartz cementation in sandstones

When sandstones are exposed to supersaturated siliceous formation fluids at elevated temperatures (i.e. above 75^{o}C), quartz cements may precipitate epitaxially on detrital quartz grains [26, 27, 36], subsequently reproducing the growth habit of quartz crystals when enough space is present. Depending upon the source area, quartz crystals exhibit a wide variety of growth habits (e.g. Cumberland, Dauphiné, Muzo, Needle, prismatic, Tessin, among several others), see The Quartz Page [37], for example. *Prismatic* habit is one of the most common growth morphology observed in nature [38, 39]. Figure 2.1 depicts the three dimensional (3-D) geometry of the euhedral form of quartz according to prismatic growth habit. This growth form possesses one c-axis, three a-axes and families of z $\{1\bar{1}01\}$, r $\{01\bar{1}1\}$ and m $\{10\bar{1}0\}$ facets (six in each family). Collectively, r- and z-facets are also known as *pyramidal* facets, while m- facets are known as *prismatic* facets. Epitaxially deposited quartz cements manifest in the form of *overgrowths*, with straight edges and sharp corners, on detrital grains. For instance, figure 2.2a,b depicts the thin-section microphotographs of a less compacted Rotliegend sandstone sample from northern

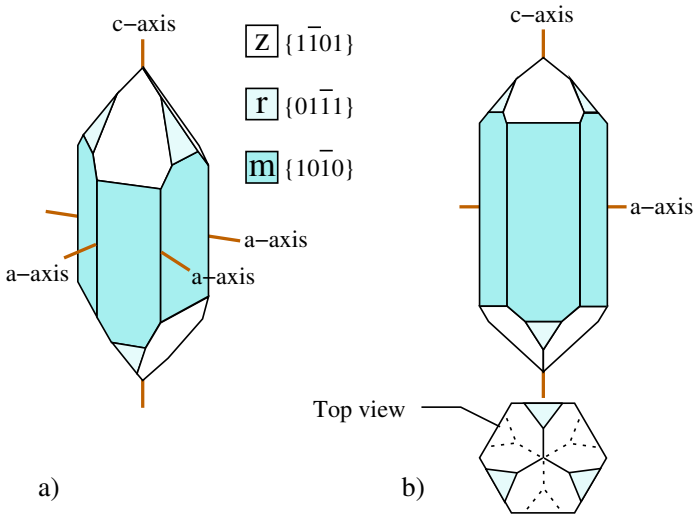

Figure 2.1: a) 3-D geometry of the euhedral form of quartz with one c-axis, three a-axes and m-, r- and z-facets (total eighteen, six of each type), according to prismatic growth habit. b) A symmetric 2-D projection of the 3-D geometry along with top view. Image was adapted from Prajapati et al. *[1], in accordance with the permission policy of the original publisher, American Geophysical Union.*

England, illustrating quartz grains, cement overgrowths and remaining pore space. The pigmented hematite dust rims, shown by brownish grain outlines in figure 2.2a, distinguish the detrital grains from optically continuous quartz cement overgrowths. These dust rims provide information about the original shape of detrital grains in thin-sections. The crystallographic orientations of overgrowths are same as those of the substrate grains, as indicated by the same interference colors in figure 2.2b. A typical cross section of a quartz crystal (i.e. hexagonal shape with prismatic faces when cut perpendicular to the crystallographic c-axis) can also be observed in the epitaxial overgrowths, as highlighted in figure 2.2a. Depending upon the time spent at elevated temperatures, also known as *thermal exposure*, different sandstones may exhibit different cement volumes and porosity. Figure 2.2c,d showcases thin-section microphotographs of a natural sample derived from the Rotliegend sandstones of northern Germany [40]. In contrast to the sandstones from north England with lesser amount of quartz cements and more retained porosity, the pore space of sandstones from northern Germany is completely occluded by quartz cements, due to a relatively higher thermal exposure in the latter case. The aforementioned samples showcase the sandstones comprising of unicrystalline grains (i.e. aggregates that are single crystals). However, many quartzarenites also contain polycrystalline detrital quartz grains, depending upon the source area. A polycrystalline grain comprises of several subdomains of quartz crystals, known as *subgrains*. Each subgrain possesses a distinct crystallographic orientation differing from other subgrains within the same grain. Thus, polycrystalline overgrowths form in optical continuity with individual subgrains that may

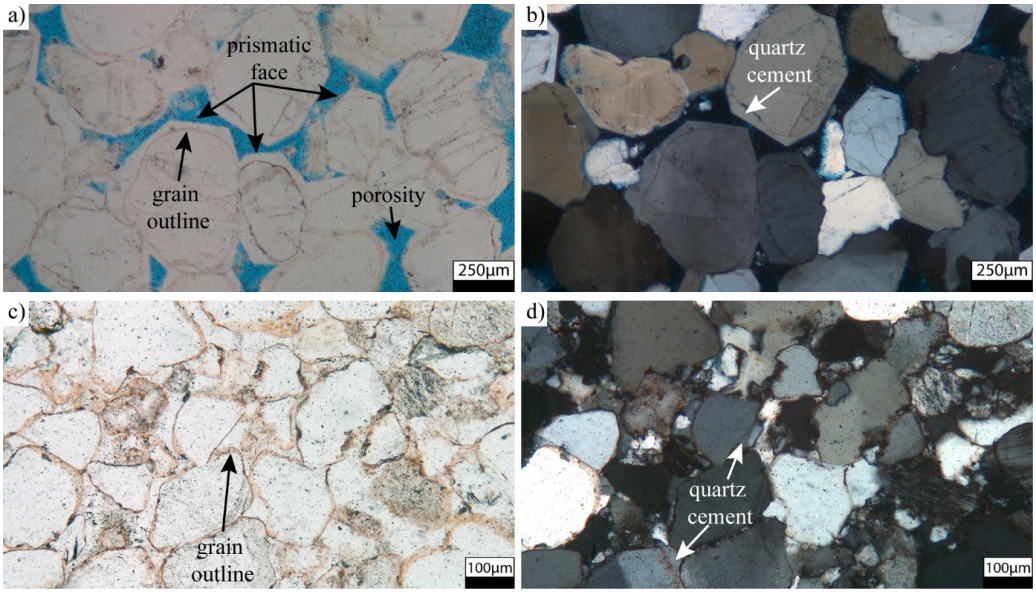

Figure 2.2: a) Microphotograph of a Rotliegendes sandstone sample from North England. Quartz cements developed crystal facets while still retaining porosity (stained with blue epoxy). The original grain outlines are visualized by the reddish-brown pigmented hematite (iron-oxide) rims. b) Microphotograph of the same sample in cross polarized light indicating the cements grew in optical continuity of the substrate grain based on the same interference color of cement and grain. c) Microphotograph of a Rotliegend sandstone sample from north Germany where no visible porosity is retained (no blue epoxy is visible). The original grain outlines are marked by reddish-brown pigmented hematite (iron-oxide) rims. d) Microphotograph of the same sample in cross polarized light indicating that the complete pore space is occluded by quartz cements, grown in optical continuity on substrate grains. Microphotographs are reused from Prajapati et al. *[1], in accordance with the permission policy of the original publisher, American Geophysical Union.*

attain the euhedral form depending upon the available space [25, 36, 41]. For instance, figure 2.3a,b depicts the thin-section microphotographs of an aeolian sandstone [BQ_1 from Busch et al. 42]. The sample, when seen under cross polarizers, reveals that the detrital quartz grains are composed of unicrystalline as well as polycrystalline grains, see figure 2.3b. In the same figure, it can also be deduced that the amount of quartz cements deposited on unicrystalline grains is different from those on polycrystalline grains with the same surface area.

Under identical thermal exposure, cement volume and growth rates are dependent on the geometrical characteristics of quartz aggregates such as grain size and polycrystallinity, among others. Heald and Renton [44], in their hydrothermal experiments, reported that fine-grained sandstones are cemented faster as compared to the coarser ones, under an identical influx of the cementing fluids. The undisturbed quartz cement

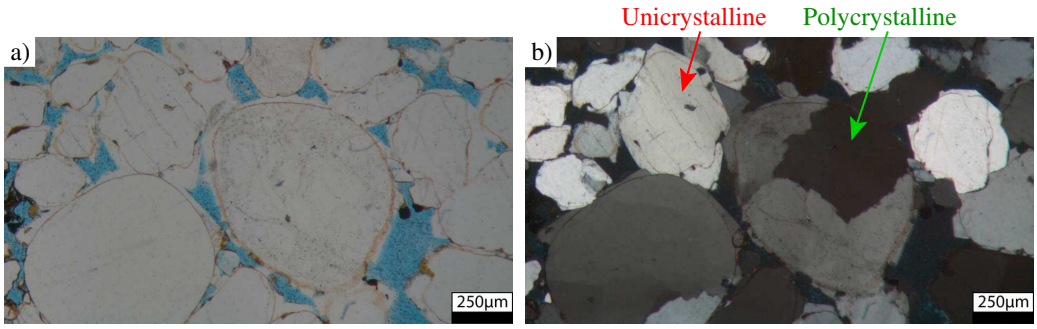

Figure 2.3: a) Microphotograph of an aeolian sandstone sample from Bowscar Quarry (BQ_1) illustrating quartz grains and cement (in white) along with pore space (in blue). The brownish dust rims reveal the original grain shapes before cement deposition. b) Microphotograph of the same sample under cross polarized light highlighting the unicrystalline and polycrystalline grains with the optically continuous cement overgrowths. Microphotographs are reused from Prajapati et al. *[43], in accordance with the permission policy of the original publisher, American Geophysical Union.*

growth experiments of Lander et al. [36] further revealed that smaller grains attain their euhedral form earlier as compared to the coarser ones, as they require lower overgrowth volume to reach their faceted shape. Heald and Renton [44] also found that polycrystalline grains are cemented at a slower rate than unicrystalline ones and the rate reduces with decreasing size of subgrains in the former case. This experimental observation is coherent with the petrographic analysis of natural samples of Nugget Sandstones by James et al. [45], which reported that polycrystalline aggregates are less likely to possess well-developed overgrowths in comparison with the unicrystalline counterparts. Worden and Morad [30] explicated that the competitive growth of overgrowths on differently oriented subgrains within each polycrystalline aggregate is responsible for the common observation that overgrowths are more extensively developed on unicrystalline grains than on polycrystalline aggregates. This essentially implies that for same-sized polycrystalline aggregates with an identical crystal structure, the cement volume differs for different crystallographic orientations of subgrains, and decreases as the mutual hindrance amongst the overgrowths on adjacent subgrains increases. Hence, sandstones made up of larger populations of polycrystalline and chert grains are expected to have lesser quartz cements.

In comprehending the intricacies associated with the phenomenon of quartz cementation, hydrothermal experiments have played a useful role [36, 44, 46–52]. Many experimental investigations have confirmed that quartz cement growth occurs most rapidly along the c-axis in comparison with the a-axis [36, 50, 51]. Consequently, under the undisturbed growth conditions when enough space is present, elongated quartz crystals are formed. In the work of Ballmann and Laudise [52], the following order of growth

rates (high to low) of the common quartz facets was determined: basal plane $\{0001\}$ > pyramidal r $\{01\bar{1}1\}$ > pyramidal z $\{1\bar{1}01\}$ > prismatic m $\{10\bar{1}0\}$. The slower growth of z-facets than the r-facets has also been reconfirmed in the micro-infrared spectroscopic analysis of quartz crystals [53] as well as in the laboratory synthesis [36]. Furthermore, experiments of LANDER ET AL. [36] found that the growth rate of quartz cements is faster during the pre-euhedral phase (i.e. before complete faceting occurs) than the post-euhedral stage, and reported that the growth rate reduces by a factor of about 20 as soon as the facet formation is finished. Their results indicated that this growth behavior of quartz cements is responsible for the overgrowths to grow more slowly on smaller grains as compared to larger ones.

Sandstone is the most significant reservoir rock accounting for more than 50 % of the petroleum reserves of the world [54]. Thus, the process of quartz cementation and its implications on the microstructure and petrophysical properties of sandstones, have been an important research area since several decades. This topic will be revisited in section 2.3.1, where a detailed review of the empirical, theoretical and computational advancements in the investigation of this process leading up to the method adopted for the present work is discussed.

2.1.2 Syntaxial calcite cementation in fractured limestones: Formation of different vein morphologies

Geological veins are prevalent morphological entities in the earth's crust, that carry a wealth of information about the histories of fluid-flow, cementation and fracturing of rocks [55–57]. In the open cracks exposed to formation fluids, when the geophysical conditions (e.g. pCO2, pH, solution ionic composition, saturation state, reacting surface area, presence of inhibiting substances, and solution hydrodynamics [58–61]) favor precipitation of cements, syntaxial fracture cementation takes place, consequently sealing the cracks. In nature, diverse crack-seal vein microstructures are formed depending upon the type of mineral (e.g. quartz, calcite, dolomite), directions of growth (e.g. syntaxial, antitaxial), number of fracturing and sealing events, and the crack-opening trajectories (e.g. elongate-blocky, fibrous, euhedral) as reported in literature [62–68].

An in-depth understanding of the intricacies associated with the vein growth process and the morphological controls are highly pertinent for the analysis of naturally fractured geothermal systems [69, 70] and hydrocarbon exploration and production [71–74]. In geothermal and hydrocarbon reservoirs, the presence of opens fractures enhances the flow capacity and thereby the reservoir quality. Natural fractures can be formed due to hydrofracturing (i.e. repeated fluid pressurization events), which result in an intermit-

tant, non-continuous and episodic opening of cracks that might grow rapidly over human time scales. However, recent petrographical studies related to fractured sandstone in the Cretaceous Travis Peak formation [75] indicated the occurrence of a prolonged crack growth driven by gas generation, at an estimated fracture-opening rate ranging between 16-23 $\mu m/m.y.$ over a period of 48 $m.y.$ (time unit $m.y.$ denoting million year).

Due to a large number of possible boundary conditions for vein growth that may be found in different geological settings, a specific vein morphology can result from different mechanisms. For example, Taber [76], in his early work, proposed that *fibrous* veins are developed when the mineral is deposited at the interface of wall rock and vein, without any fracturing. Durney and Ramsay [62] coined this mechanism of vein growth as *antitaxial*, that was subsequently reproduced in laboratory [77] as well as in numerical simulations [78, 79]. Alternatively, Mügge [80] proposed that fibrous textures are formed when the rate of cement growth is much faster than that of crack opening, when the fractures are in their growth phase. Cementation contemporaneous with the crack opening is called synkinematic cementation after Laubach [65]. Thus, regardless of the presence of a crack-seal texture, any cement precipitated during the fracture opening stage is a synkinematic deposit. The size of incremental crack opening can range from few micrometers to millimeters in nature [66]. In this range, accounts of precise incremental opening sizes (or so-called *gaps*) have been further reported for quartz in Laubach et al. [81] and for carbonate rocks in Hooker et al. [82]. During synkinematic cementation, a complex interplay of the crack opening and syntaxial cement growth occurs, that govern the textural patterns of the resulting veins based on the relative growth rates, and was shown to influence the calcite-bearing veins [79], quartz veins [65, 83] and carbonate veins in dolostones [84]. Carbonate vein morphologies can also be subject to an interplay of synkinematic and postkinematic cement growth [85]. The analysis of different generations of cements can be done by utilizing equipments such as a cathodoluminescence detector mounted on a scanning electron microscope (SEM-CL) [85].

Figure 2.4a-d depicts the microphotographs of natural samples extracted from the Jurassic limestones of southern England, exhibiting four distinct calcite vein textures. Different calcite crystals in the vein samples possess distinct crystallographic orientations as highlighted by different interference colors. Figure 2.4a showcases a *fibrous* vein morphology, characterized by parallel grain boundaries due to the presence of thin fiber-like calcite crystals of varying lengths and high length-to-thickness ratios. The *elongate-blocky* vein texture depicted in figure 2.4b exhibits crystals with increasing width towards the vein centre. The presence of larger number of smaller crystals near the vein-host rock interface as compared to those reaching the vein centre indicates the occurrence of growth competition during the initial stages of the vein formation. Elongate-blocky textures often occur as *partially-open* veins, with a possibility of euhedral crystals (with straight

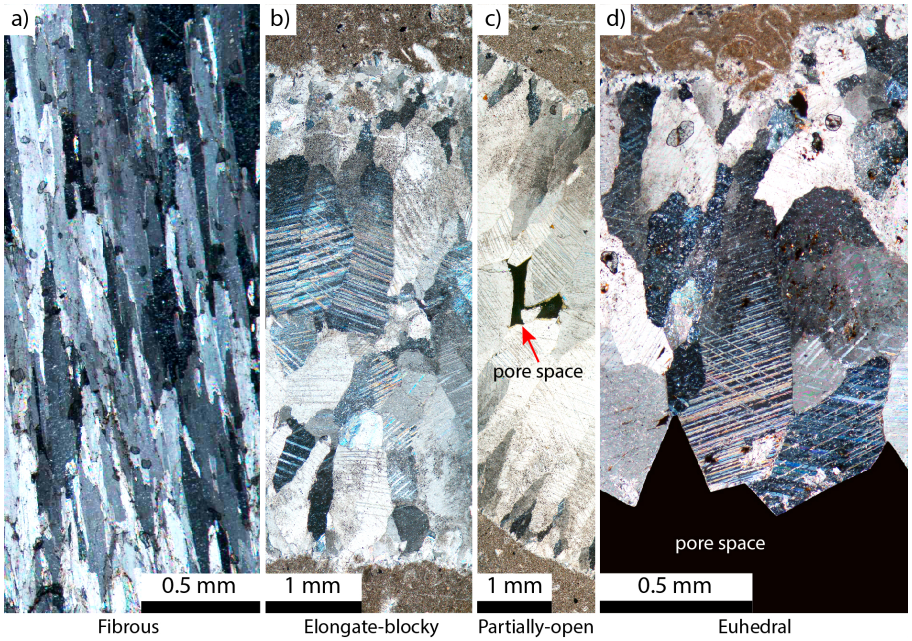

Figure 2.4: Microphotographs of natural calcite vein samples taken from the Jurassic limestones of southern England obtained using transmitted microscopy and crossed polarizers. These samples exhibit the following four distinct vein morphologies: a) fibrous, b) elongate-blocky, c) partially-open and d) euhedral. The host rock in the fibrous vein sample is located towards the base of the microphotograph. Distinct crystals exhibit different crystallographic orientation visible in different interference colors. The microphotographs are reused from Prajapati et al. *[2], in accordance with permission policy of the original publisher, Springer.*

edges and sharp corners) as highlighted in figure 2.4c. Lander and Laubach [83] referred to one such texture as rind morphologies. There also exist the *euhedral* vein textures comprising of faceted crystals in the open pore space (black color) of a crack, shown in figure 2.4d.

Carbonate reservoirs account for over 40% of gas and 60% of oil reserves of the world. Petrographical analysis of different veins textures occurring in these reservoir rocks, aided with a sound understanding of the mechanisms of vein formation, can potentially provide highly relevant information for hydrocarbon and geothermal explorations. Due to these reasons, geological veins have always attracted the attention of petrographers, geologists and reservoir engineers, and has been a topic of intensive research for almost a century. With respect to the computational advancements in the modeling of vein formation leading up to the model adopted in the present work, this topic will be revisited in section 2.3.1.

2.2 Brittle anisotropic microfracturing in sedimentary rocks

Cracks are ubiquitously present in reservoir rocks [86] and originate when the stresses exceed the rock strength. The stresses may arise due to a wide range of mechanical boundary conditions, resulting in an isotropic or anisotropic fracture propagation depending upon the material properties of the rock. At microscale, sandstones are multiphase systems comprising of large populations of crystalline quartz grains of different shapes and sizes. These grains are cemented together due to the precipitation of cements (e.g. quartz, calcite) resulting in a heterogeneous solid rock mass [30, 87, 88]. Each quartz grain possesses a distinct crystallographic orientation which is different from its neighboring grains, thereby resulting in the presence of grain boundaries. The grain material properties vary depending upon the crystallographic directions. For the quartz grains of prismatic growth habit (figure 2.1), the fracture toughness, and therefore the crack resistance, has been experimentally found to vary along different crystallographic directions [89–93]. Consequently, there exist preferred cleavage planes for crack growth within each grain. Petrographic studies reveal that the intragranular cracks are frequently observed to follow cleavage planes, resulting in the arrays of parallel fractures [chapter 4 in Guéguen and Boutéca 4]. Moreover, the interaction of cracks with the grain boundaries depends upon the fracture toughness at the grain-grain contact. When the grain boundaries offer lesser crack resistance than the bulk region, due to e.g. corrosion by the chemically active fluids at the grain-grain interface [94], intergranular fracture propagation may take place [4, 5]. For instance, figure 2.5a,b depict the microphotographs of two sandstone samples, namely ST sandstone type IIIB and SFGI sandstone type IVA, exhibiting different types

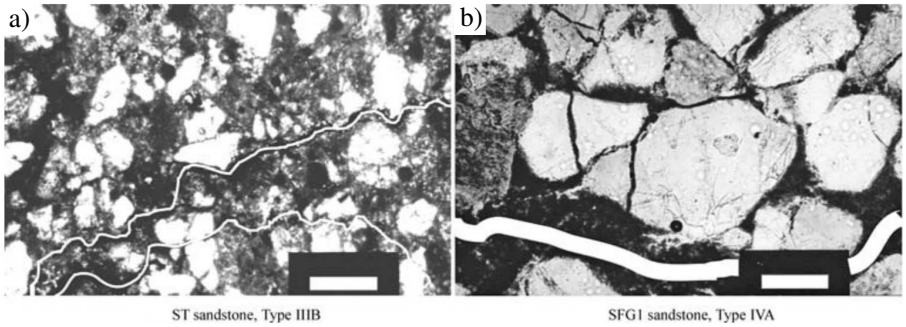

Figure 2.5: Thin-section microphotographs of two different sandstone samples, a) ST sandstone, Type IIIB and b) SFGI sandstone, Type IVA. Type IIIB sample shows intergranular fracturing, whereas higher number of transgranular fracturing is observed in Type IVA sample. Microphotographs adapted from Lin et al. *[5] Copyright (2005), with permission from Springer Nature.*

of microfractures. While intergranular fracturing mostly occured in Type IIIB, Type IVA sample exhibits a larger number of transgranular fractures.

Depending upon the geophysical conditions in the source area, the bulk region of sandstone may also contain secondary phases e.g. rock fragments, clay and grain of other minerals (such as k-feldspar) [95]. These phases with different material properties further impact the fracture paths. Owing to all these heterogeneities and anisotropies at the grain scale, microfracturing in sandstone is considered as a complex phenomenon. Microfractures are the nucleation sites for macrofractures [3], and thereby govern the rock strength, flow-through behavior and storage capacity for hydrocarbons and other fluids. A thorough understanding of microfracturing is highly relevant for the analysis of stress states and petrophysical properties of reservoir rocks. This topic will be revisited with respect to the computational advancements in the modeling of crack propagation at different length scales and the numerical method employed for the present work, in section 2.3.2.

2.3 Numerical approaches

Conventional approaches, particularly rock sample petrography and experimental investigations have played a foundationary role in our current understanding of the phenomena of cementation and fracturing in rocks. However, explicating the evolution of rock microstructure due to these processes through in situ experimental observations is an arduous task, mainly because the spatial distribution of the geological phases (e.g. grains, rock fragments, other minerals) extends beyond the regular two-dimensional representation. Consequently, theoretical treatments are adopted to complement the experimental and field observations for enhancing the understanding of the impact of these physical processes on the rock properties. With the increase in availability of computational resources, the contribution of numerical investigations has been expanding at an increasing pace. The development of spatio-temporal models along with advanced data visualization techniques have further enabled to gain insights of the microstructure evolution, both in space and time, and comprehend the intricacies of underlying processes. As the present work specifically focusses on the phenomena of cementation and fracturing in rocks, a review of the numerical approaches utilized in investigating these processes is presented in the following parts of this section.

2.3.1 Numerical approaches for modeling cementation

Cementation results in the evolution of microstructure and loss of porosity as well as permeability of rocks. For the estimation of porosity reduction during quartz cementation, several empirical laws relating porosity with other physical properties (e.g. grain size, surface area, temperature, etc.) have been proposed in the literature [28, 96–98]. These laws, in the form of analytical equations, have been quite successful in the quantitative estimation of reservoir porosity [99–102]. Similarly, empirical equations for the estimation of permeability as a function of porosity and other rock properties for different types of rocks, and the impact of physical processes on the same, have also been proposed in several works, see the review articles [103–105]. Additionally, their exist diagenetic modeling tools such as *Exemplar* [100] and *Touchstone* [106] that perform quartz cementation on the basis of input physical rock parameters (e.g. available surface area, grain size distribution, nucleation discontinuities). The resulting changes in the available intergranular pore volume due to cementation and also compaction is modeled over time. Recently, these tools have been extended to include the influence of polycrystallinity of quartz aggregates and a growth rate reduction after reaching euhedral faceting on the overgrowth cement volumes [36]. These tools have also been proven as sound basis for predrill predictions [107]. Despite the achievements of empirical equations and abovementioned diagenetic tools, they only take into account the globally averaged data for modeling cementation. As the morphological aspects are not rigorously accounted, these models do not provide any insights into the evolving microstructures as a result of syntaxial overgrowth cementation. For tracing the burial history and making accurate future predictions, a comprehensive understanding of the underlying microstructural processes is imperative. In this regard, spatio-temporal computational models, with the ability to simulate the instantaneous changes locally, could certainly be advantageous and may provide more trustworthy predictions.

2.3.1.1 Sharp interface models for cementation

In the previous decades, numerous spatio-temporal computational models based on the *front-tracking* methods have been developed for simulating cementation under different boundary conditions. They include the simulation packages like *Fringe Growth* [6], *Vein Growth* [7, 79] and *FACET* [108]. With the capabilities to describe grains with straight edges, and simulate the spatio-temporal evolution of grain boundaries according to isotropic as well as anisotropic growth, the abovementioned packages elucidated the complicated grain boundary interference and mechanisms of formation of different vein textures in two dimensions 2-D. A comparative analysis of the algorithms of *Vein Growth* and *FACET*, and their capabilities in recreating vein textures, has been presented by

Nollet et al. [109]. The model of *Fringe Growth* was based on the algorithm of the *Vein Growth*, and was utilized to simulate the incremental growth of crystal fibres in undeformed antitaxial strain fringes. Later on, based on the *cellular automaton* approach, a software package known as *Prism2D* was developed by Lander et al. [36], who simulated quartz overgrowth cementation in realistic 2-D grain packs under different boundary conditions. Subsequently, *Prism2D* was also employed to simulate fracture cementation and formation of crack-seal morphologies in quartz [83] and dolomite [84] veins. In the experimental part of the work of Lander et al. [36], it was found that the growth rate of quartz along the c-axis reduces by a factor of about 20 after the faceting is complete. This particular growth tendency of quartz was also incorporated in *Prism2D*. The numerical investigations of Lander et al. [36] using *Prism2D* reported that growth rates of quartz cement are inversely dependent upon the grain size of aggregates. Moreover, they were able to numerically reproduce the common observation of quartz overgrowths to grow at slower rates on polycrystalline grains as compared to single crystals. These results suggested that slower post-euhedral growth behaviour of quartz is majorly responsible for this observation and the minor impact of mutual hindrance among neighboring overgrowths is also present which predates the euhedral effect. Despite the achievements of all the aforementioned solvers, one major limitation common to all of them was that their scope was restricted to 2-D, owing to the modeling complexities that arise when accounting the third dimension. Thus, these 2-D models can only render a limited understanding of the petrophysical properties such as permeability, which is determined by the nature of the flow pathways in 3-D.

2.3.1.2 Phase-field models for cementation

In the past decade, the *phase-field* method has gained popularity in the computational modeling of anisotropic mineral growth processes in 2-D as well as 3-D [15–18, 110]. Wendler et al. [110] utilized a multiphase-field (MPF) model to simulate the polycrystalline thin-film growth of MFI zeolite and studied the competitive crystal growth in 2-D and 3-D. In the work of Ankit et al. [16], they adapted a MPF model for simulating the vein growth due to precipitation of the Potash Alum, and studied the impact of various parameters (e.g. crack wall roughness, crack opening rate, crack opening trajectory, number of crystal nuclei, etc.) on the resulting vein textures in 2-D and 3-D. Subsequent phase-field works [15, 17, 18] investigated the process of quartz cementation in crack-seal veins under different boundary conditions. All the above-mentioned works have laid a sound foundation for an entirely new generation of cementation models for sedimentary basins and vein growth, based on the phase-field approach. Unlike the conventional front tracking methods [7, 78, 79, 109], the phase-field method inherently captures the motion

of interfaces through the governing equations, thereby obviating the need to track the interfaces explicitly. This feature renders it as a powerful methodology in addressing the boundary value problems in different scientific research fields, particularly materials science [9–12, 111, 112], and others such as fracture mechanics [13, 14], fluid flow [113], biology [114–118], among others. As the numerical investigations of syntaxial overgrowth cementation in the present work are based on phase-field approach, a general overview of the method and its adaptability in different moving boundary problems, are discussed in section 2.3.3.

2.3.2 Numerical approaches for modeling fracture growth

Numerical approaches provide fascinating and powerful tools for describing fracture growth and failure in different materials (e.g. metals, rubber, rocks, etc.), based on the fundamentals of fracture mechanics and materials science. In the geomechanical arena, computational fracture mechanics (CFM) is employed in the predictive failure analysis for a wide variety of rock engineering applications such as rock cutting, underground excavations, among others. CFM also assist in the investigation and characterization of fractured hydrocarbon and geothermal reservoirs.

2.3.2.1 Sharp interface models for fracture

Different numerical approaches have been proposed to address the problem of fracturing in geological systems. Zhang and Jeffrey [119] utilized the Boundary element method for analysing the formation of fracture networks through fluid-driven crack growth in 2-D. However, as only boundary is discretized in this approach, the method faces difficulties in addressing heterogeneities and anisotropies of rocks. Using the Extended finite element method, Wang et al. [120] simulated the interactions between hydraulic and natural fractures, and the formation of fracture networks in 2-D. Moreover, 3-D investigations were conducted by Virgo et al. [121–123] using the Discrete element method (DEM) for analysing the interactions of veins and fractures. DEM based models treat material as an accumulation of spherical particles and track each individual particle and its interactions with the neighbouring particles over time. As an increase in the number of particles n leads to higher computational costs (typically scaling as order of n), these models are not well-suited for large scale numerical simulations. For a comprehensive understanding of the computational methods in fracture mechanics for rocks, interested readers are referred to recent review article by Mohammadnejad et al. [124]. In the above-mentioned numerical approaches, the cracks are treated as sharp material discontinuities, placing these models in the category of so-called *sharp interface* models.

Development of robust algorithms for the update of crack surfaces and their numerical implementation based on the sharp interface approach is a tedious task, especially when dealing with problems such as crack branching and merging and their extensions to 3-D.

2.3.2.2 Phase-field models for fracture

As previously mentioned (in section 2.3.1), phase-field method obviates the need to track the interfaces explicitly. Therefore, phase-field approach to crack propagation has proved to be an elegant methodology in describing brittle and ductile fracturing in different homogeneous as well as heterogeneous materials. Over the past few decades, different phase-field approaches for brittle fracturing have been developed independently in physics [125–130] as well as mechanics [13, 131–137] communities. In physics community, models were developed by adapting the formulation of Ginzburg and Landau [138]. While models developed in mechanics community were based on the variational formulation of Francfort and Marigo [139], later regularized by Bourdin et al. [131], extending the classical *Griffith's theory* of rupture [140]. For a complete review of the phase-field methods for brittle fracturing, interested readers are referred to Ambati et al. [141]. In the field of ductile failure based on the phase-field method, several models have been proposed [142–150]. These models can be cast into a common variational framework, that is similar to the regularized functional of Bourdin et al. [131] but with additional dissipation terms for plastic effects and their coupling with damage, which differ from model to model. A critical comparative review of the above-mentioned phase-field based ductile failure models has done by Alessi et al. [151].

In the geomechanical arena, numerous models coupling the phase-field fracture with mechanics for brittle and ductile geological materials have been developed for addressing different problems e.g. crystallization-induced deformation and fracture in porous material containing crystals growing in pores [152], mixed mode fracture in brittle anisotropic geo-materials [153], coupling of the phase-field fracture with the pressure-sensitive Drucker-Prager plasticity model [154], crystal plasticity model with a phase-field for capturing capture the anisotropy of inelastic and damage behavior in single-crystal halite (rock-salt) [155]. Moreover, several other recent works coupled the flow-physics with phase-field fracture in order to simulate the hydraulic fracturing in porous media [156–161]. It is noteworthy that the aforementioned works [152–154, 156, 157, 159–161], with the exceptions of [155, 158], focussed on fracturing in homogeneous geomaterials, in 2-D as well as 3-D.

In the heterogeneous materials composed of several phases that differ in atleast one physical property (e.g. elastic constants, fracture toughness, anisotropy, etc.), one of the earliest works was published by Wang et al. [162], who addressed the phenomenon

of fracturing in polycrystalline systems. Subsequent works of Abdollahi and Arias [163] and Oshima et al. [164] addressed the phenomenon of intergranular and transgranular crack propagation in polycrystalline materials, that hitherto largely remained unaddressed. The aforementioned works [162–164] considered the isotropic crack resistance of the crystal phases, and thereby, are not applicable to multigrain systems (e.g. sandstones) where each grain has a different crystallographic orientation with preferential cleavage planes due to the direction-dependent fracture toughness. This aspect was addressed in the work of Liu and Juhre [165], who utilized an anisotropy formulation of Clayton and Klap [166]. An extension to this anisotropic formulation was proposed by Nguyen et al. [167], who utilized the Cohesive zone modeling (CZM) approach in the description of grain boundary decohesion, for simulating the intergranular and transgranular fracture. However, in the CZM, the crack paths become mesh dependent as the cohesive surfaces can be present only along the edges of the finite element. Moreover, the anisotropy formulation considered in Clayton and Klap [166], that was adopted in several other works [153, 155, 165, 167], the anisotropy is incorporated only in the gradient damage term of the fracture energy. This causes variable crack interface widths in different crystals. The varying interface widths in different solid phases result in different fracture surface energies, thereby leading to energetic deviations in comparison with the sharp interface results. When the interface widths in different phases differ in orders of magnitude, this further demands larger computational domains for the correct resolution of all the interfaces, and thus, may incur higher computational expenditure. The last part of the dissertation showcases a MPF model for simulating the brittle anisotropic fracturing process in sandstones, with the following two novel aspects: a) the anisotropic treatment of the fracture energy ensures that the crack interface widths remains invariant in different phases, and b) the proposed formulation of interfacial crack resistance interpolation for grain boundary weakening. The complete MPF model is presented in chapter 4. In the next section 2.3.3, a general overview of the phase-field method is discussed.

2.3.3 Phase-field method: A general overview

Phase-field method has shown immense capabilities in describing various physical processes, particularly those which involve moving boundaries (e.g. microstructure evolution during phase transitions, crack propagation, multiphase flow, etc.). The method finds a wide spectrum of applications related to morphological evolution and damage growth in scientific research areas such as materials science, fracture mechanics, structural engineering, geology, physics, biology, among others.

The main idea behind the formulation of a thermodynamically consistent phase-field model is the optimization of a general objective quantity $\mathcal{Q}$ (either energy or entropy)

of the system, that monotonically converges to its optimum value (i.e. minima in the case of free energy minimization, and maxima in the case of entropy maximization). For a multiphase system comprising of N phases, the general objective quantity can be formulated as a sum of volumetric and interfacial contributions, given by

$$\mathcal{Q}(\mathfrak{s}) = \underbrace{\sum_{\alpha=1}^{N} \int_{\mathrm{V}_\alpha} q(\mathfrak{s}) \mathrm{d}V}_{\text{Volumetric}} + \underbrace{\sum_{\alpha<\beta}^{N} \int_{\Gamma_{\alpha\beta}} \sigma(\mathfrak{s}, \mathfrak{n}_{\alpha\beta}) \mathrm{d}\mathfrak{n}}_{\text{interfacial}}, \tag{2.1}$$

where $q(\mathfrak{s})$ denotes the volumetric density and $\sigma(\mathfrak{s}, \mathfrak{n}_{\alpha\beta})$ represents the surface density of the objective quantity, locally. Here $\mathfrak{s}$ denotes a set of state variables and, depending upon the physical process being modeled, can include quantities such as temperature T, composition $\mathfrak{c} = (c_1, \ldots, c_K)$ (for a K component system), chemical potential $\boldsymbol{\mu} = (\mu_1, \ldots, \mu_k)$, deformation field $\boldsymbol{\nabla u}$, among others. V_α denotes the volume of phase α, while $\Gamma_{\alpha\beta}$ represents the interface between phase α and β, as exemplarily illustrated for a two-phase system in figure 2.6a. $\mathfrak{n}_{\alpha\beta}$ denotes a vector oriented perpendicular to the interface $\Gamma_{\alpha\beta}$. In the moving boundary problems, depending upon the physics involved, the interface motion occurs. The physical interface width in such systems may lie in nanoscale or even lower. The discrepancies due to differing length scales of the bulk and the interface regions pose restrictions during the computational treatment of the physical process. In addressing these discrepancies, the regularization of the sharp discontinuities using a diffuse interface description, as illustrated in figure 2.6b, is a convenient approach. In the diffuse interface description, the general objective quantity takes the regularized

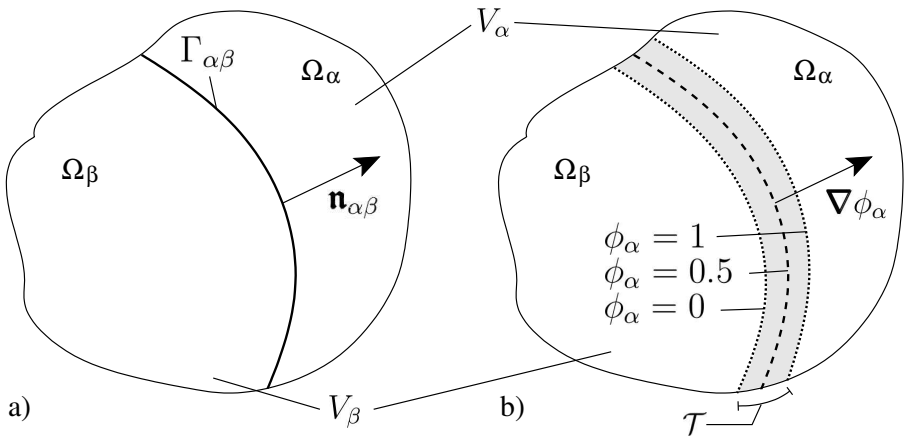

Figure 2.6: a) Sharp interface and b) diffuse interface descriptions of a two-phase system. The phase α occupies the subdomain Ω_α of volume V_α, and phase β occupies the subdomain Ω_β of volume V_β. In the sharp interface description, $\mathfrak{n}_{\alpha\beta}$ is the vector perpendicular to the boundary $\Gamma_{\alpha\beta}$ between the α and β phases. In the diffuse interface description, the interface of finite diffuse interface thickness $\mathcal{T}$ is described by the phase-fields ($\phi_\alpha = 1 - \phi_\beta$), where $\nabla\phi_\alpha$ is the vector perpendicular to the diffuse interface.

form

$$\mathcal{Q}(\boldsymbol{\phi}, \boldsymbol{\nabla}\boldsymbol{\phi}, \boldsymbol{\mathfrak{s}}) = \int_V \underbrace{\left[q(\boldsymbol{\phi}, \boldsymbol{\mathfrak{s}}) + \varepsilon a(\boldsymbol{\phi}, \boldsymbol{\nabla}\boldsymbol{\phi}) + \frac{1}{\varepsilon} w(\boldsymbol{\phi}) \right]}_{(\mathfrak{I})} \mathrm{d}V \tag{2.2}$$

known as *Ginzburg-Landau functional* [138]. In eq. (2.2), the sets of phase-fields $\boldsymbol{\phi}(\boldsymbol{x}, t) = (\phi_1, \ldots, \phi_N)$ and their gradients $\boldsymbol{\nabla}\boldsymbol{\phi} = (\boldsymbol{\nabla}\phi_1, \ldots, \boldsymbol{\nabla}\phi_N)$ enter the formulation, N being the number of phases in the system. Depending upon the physical process under consideration, phase-fields may represent different physical quantities such as phase volume fraction, composition, polarisation, density, among others. While, volumetric density $q(\boldsymbol{\phi}, \boldsymbol{\mathfrak{s}})$ in Ginzburg-Landau formulation (eq. (2.2)) is analogous to its sharp interface description (eq. (2.1)), the quantities $\varepsilon a(\boldsymbol{\phi}, \boldsymbol{\nabla}\boldsymbol{\phi})$ and $\frac{1}{\varepsilon} w(\boldsymbol{\phi})$ represent gradient-type density and potential-type density of the system, which collectively account for the regularization of interfaces. Diffuse interface thickness $\mathcal{T}$ (figure 2.6b) is controlled by the length scale parameter ε. The phase-field variables can be conserved order parameters (e.g. concentration, energy) or non-conserved parameters (e.g. phase-volume fractions). The evolution of both, conserved and non-conserved order parameters can be formulated based on variational principles. The evolution equation for conserved order parameters, popularly known as *Cahn-Hilliard equation* [168], is given by

$$\frac{\partial \phi_\alpha}{\partial t} = \boldsymbol{\nabla} \cdot \left[\mathbf{M}(\boldsymbol{\phi}, \boldsymbol{\nabla}\boldsymbol{\phi}, \boldsymbol{\mathfrak{s}}) \boldsymbol{\nabla} \frac{\delta \mathcal{Q}(\boldsymbol{\phi}, \boldsymbol{\nabla}\boldsymbol{\phi}, \boldsymbol{\mathfrak{s}})}{\delta \phi_\alpha} \right], \quad (\text{for } \alpha = 1, \ldots, N). \tag{2.3}$$

For the problems where the considered order parameter is non-conserved, the evolution equation, popularly known as *Allen-Cahn equation* [169], reads

$$\varepsilon \frac{\partial \phi_\alpha}{\partial t} = \pm \mu(\boldsymbol{\phi}, \boldsymbol{\nabla}\boldsymbol{\phi}, \boldsymbol{\mathfrak{s}}) \frac{\delta \mathcal{Q}(\boldsymbol{\phi}, \boldsymbol{\nabla}\boldsymbol{\phi}, \boldsymbol{\mathfrak{s}})}{\delta \phi_\alpha}, \quad (\text{for } \alpha = 1, \ldots, N). \tag{2.4}$$

The quantities $\mathbf{M}(\boldsymbol{\phi}, \boldsymbol{\nabla}\boldsymbol{\phi}, \boldsymbol{\mathfrak{s}})$ (eq. (2.3)) and $\mu(\boldsymbol{\phi}, \boldsymbol{\nabla}\boldsymbol{\phi}, \boldsymbol{\mathfrak{s}})$ (eq. (2.4)) represent the effective diffusion coefficient and effective mobility, respectively, and are formulated according to the process physics. The variational derivative in eqs. (2.3) and (2.4) is evaluated as

$$\frac{\delta \mathcal{Q}(\boldsymbol{\phi}, \boldsymbol{\nabla}\boldsymbol{\phi}, \boldsymbol{\mathfrak{s}})}{\delta \phi_\alpha} = \frac{\partial \mathfrak{I}}{\partial \phi_\alpha} - \boldsymbol{\nabla} \cdot \frac{\partial \mathfrak{I}}{\partial \boldsymbol{\nabla}\phi_\alpha}, \quad (\text{for } \alpha = 1, \ldots, N), \tag{2.5}$$

where $\mathfrak{I}$ denotes the integrand in eq. (2.2). Depending upon the maximization or minization problem, the sign of eq. (2.4) is chosen. In the presence of a constraint of the form $g(\boldsymbol{\phi}, \boldsymbol{\nabla}\boldsymbol{\phi}) = 0$, the evolution equation modifies to

$$\varepsilon \frac{\partial \phi_\alpha}{\partial t} = \pm \mu(\boldsymbol{\phi}, \boldsymbol{\nabla}\boldsymbol{\phi}, \boldsymbol{\mathfrak{s}}) \left[\frac{\delta \mathcal{Q}(\boldsymbol{\phi}, \boldsymbol{\nabla}\boldsymbol{\phi}, \boldsymbol{\mathfrak{s}})}{\delta \phi_\alpha} - \lambda \frac{\delta g(\boldsymbol{\phi}, \boldsymbol{\nabla}\boldsymbol{\phi})}{\delta \phi_\alpha} \right], \quad (\text{for } \alpha = 1, \ldots, N), \tag{2.6}$$

where λ being the Lagrange multiplier for the constrained optimization problem. Evolution eqs (2.3) and (2.4) describe the motion of interfaces. The physics corresponding

to different processes (e.g. diffusion, advection, momentum balance etc.) is incorporated by coupling the phase-field evolution equation with those of the governing physics. As no additional boundary conditions are required at the moving interfaces, explicit interface tracking, which is an arduous aspect of sharp interface methods, is obviated in the phase-field approach.

In the phase-field models for brittle fracturing, the coupled set of equations essentially includes I) an evolution equation for the crack phase-field and II) a momentum balance equation for the mechanical fields. Moreover, additional equations may be coupled when addressing the multiphysics problems involving e.g. phase-transitions, thermal or magnetic effects, during fracturing. Phase-field models of brittle fracture can be cast into a common variational framework based on the Ginzburg-Landau type free energy functional of the form

$$\mathcal{F}(\phi_c, \boldsymbol{\nabla}\phi_c, \boldsymbol{\varepsilon}(\boldsymbol{u}), \ldots) = \int_{\Omega} \underbrace{f_{\mathrm{el}}(\phi_c, \boldsymbol{\varepsilon}(\boldsymbol{u}), \ldots)}_{\substack{\text{Elastic energy} \\ \text{contribution}}} + \underbrace{G_c(\ldots)\left(\frac{1}{\varepsilon_{\mathrm{c}}} w_{\mathrm{c}}(\phi_c) + \varepsilon_{\mathrm{c}} a(\phi_c, \boldsymbol{\nabla}\phi_c)\right)}_{\substack{\text{Regularized crack surface} \\ \text{energy contribution}}} \mathrm{d}\Omega, \tag{2.7}$$

where minimization of the free-energy governs the process of crack propagation in accordance with the classical *Griffith's theory* of rupture [140]. The symbol $(\ldots)$ in arguments of terms in eq. (2.7) signifies that other fields may appropriately enter the formulation depending upon additional physics, heterogeneities and anisotropies being modeled. ϕ_c denotes the crack phase-field and $\boldsymbol{\varepsilon}(\boldsymbol{u})$ represents the strain field as a function of displacement field $\boldsymbol{u}$. $\mathcal{F}(\phi_c, \boldsymbol{\nabla}\phi_c, \boldsymbol{\varepsilon}(\boldsymbol{u}), \ldots)$ is the free energy of the system, as a sum of an elastic energy contribution and a regularized crack surface energy contribution. $f_{\mathrm{el}}(\phi_c, \boldsymbol{\varepsilon}(\boldsymbol{u}), \ldots)$ denotes the elastic energy density and $G_c(\ldots)$ is the crack resistance of material. In the second contribution, the terms $w_{\mathrm{c}}(\phi_c)$ and $a(\phi_c, \boldsymbol{\nabla}\phi_c))$ represent the potential-type and gradient-type energetic contributions, respectively, regularizing the crack surface energy. Length scale parameter ε_{c} controls the thickness of the transition zone of crack phase. Elastic energy density $f_{\mathrm{el}}(\phi_c, \boldsymbol{\varepsilon}(\boldsymbol{u}), \ldots)$ serves as a coupling term between crack phase-field and deformation fields and is formulated such that it degrades the stress field in the presence of crack phase, see e.g. Bourdin et al. [131]. Different types of fracturing behavior (e.g. anisotropic, elasto-plastic) in homogeneous (i.e. single phase) as well as heterogeneous (i.e. multigrain/multiphase/polycrystalline) materials can be modeled by suitably modifying the existing terms and/or adding new terms and fields in the formulation (eq. (2.7)).

In the upcoming chapters, phase-field models and their adaptations with regards to the processes of syntaxial overgrowth cementation and brittle anisotropic microfracturing in sedimentary rocks are elaborated.

Part II
Methods

Chapter 3

A multiphase-field model for syntaxial overgrowth cementation

We consider a set of $N \in \mathbb{N}$ order parameters called the *phase-fields* $\boldsymbol{\phi}(\boldsymbol{x}, t) = [\phi_1(\boldsymbol{x}, t), \ldots, \phi_N(\boldsymbol{x}, t)]$ in the spatial domain $\Omega \subset \mathbb{R}^d,\ d \in \{1, 2, 3\}$ of the system. Each phase-field $\phi_\alpha : \Omega \times \mathbb{R}_0^+ \to [0, 1]$ describes the presence of a grain or liquid phase at the position $\boldsymbol{x}$ and time t. The part of the domain solely occupied by a single phase α is called the α-*bulk* and is mathematically expressed as $\mathcal{B}_\alpha = \{\boldsymbol{x} \in \Omega \mid \phi_\alpha(\boldsymbol{x}, t) = 1\}$. The surface shared between two phases α and β is described as a diffuse region called the α-β *interface*, defined as $\mathcal{I}_{\alpha\beta} := \{\boldsymbol{x} \in \Omega \mid \phi_\alpha(\boldsymbol{x}, t) + \phi_\beta(\boldsymbol{x}, t) = 1 \text{ and } \phi_\alpha(\boldsymbol{x}, t) \neq 0 \text{ and } \phi_\beta(\boldsymbol{x}, t) \neq 0\}$. The value of the order parameter ϕ_α varies from 1 in the α-bulk to 0 in the β-bulk smoothly and monotonically over the diffuse interface $\mathcal{I}_{\alpha\beta}$. The location and geometry of the α-β interface is determined by the set of spatial points $\{\boldsymbol{x} \in \mathcal{I}_{\alpha\beta} \mid \phi_\alpha(\boldsymbol{x}, t) = \phi_\beta(\boldsymbol{x}, t) = 0.5\}$. The bulk $\mathcal{B}$ and interface $\mathcal{I}$ regions collectively compose the domain Ω, and are given by $\mathcal{B} = \cup_{\alpha \in \mathrm{N}} \mathcal{B}_\alpha$ and $\mathcal{I} = \Omega \setminus \mathcal{B}$, respectively. Figure 3.1 schematically illustrates the sharp and diffuse interface descriptions of a binary solid-liquid system. In the diffuse interface description (figure 3.1b), the spatial variation of the phase-fields for solid ϕ_s and liquid ϕ_l phases in the bulk (i.e. $\mathcal{B}_\mathrm{s}$ and $\mathcal{B}_\mathrm{l}$) and the diffuse interface (i.e. $\mathcal{I}_\mathrm{sl}$) regions is schematically illustrated.

For a multiphase system comprising of N distinct phases at a temperature T, the *Helmholtz free energy* $\mathcal{F}$ is formulated in a generalized manner as

$$\mathcal{F}(\boldsymbol{\phi}, \boldsymbol{\nabla\phi}, \mathfrak{c}, T) = \int_\Omega \left[f(\boldsymbol{\phi}, \mathfrak{c}, T) + \varepsilon a(\boldsymbol{\phi}, \boldsymbol{\nabla\phi}) + \frac{1}{\varepsilon} w(\boldsymbol{\phi}) \right] \mathrm{d}\Omega, \tag{3.1}$$

where $\mathfrak{c}(\boldsymbol{x}, t) = [\mathfrak{c}_1(\boldsymbol{x}, t), \ldots, \mathfrak{c}_K(\boldsymbol{x}, t)]$ represents the set of molar concentrations of K different species. The terms $f(\boldsymbol{\phi}, \mathfrak{c}, T)$, $\varepsilon a(\boldsymbol{\phi}, \boldsymbol{\nabla\phi})$, $\frac{1}{\varepsilon} w(\boldsymbol{\phi})$ denote the *bulk free-*, the *gradient-* and the *potential* energy density contributions. The bulk free energy density of the system

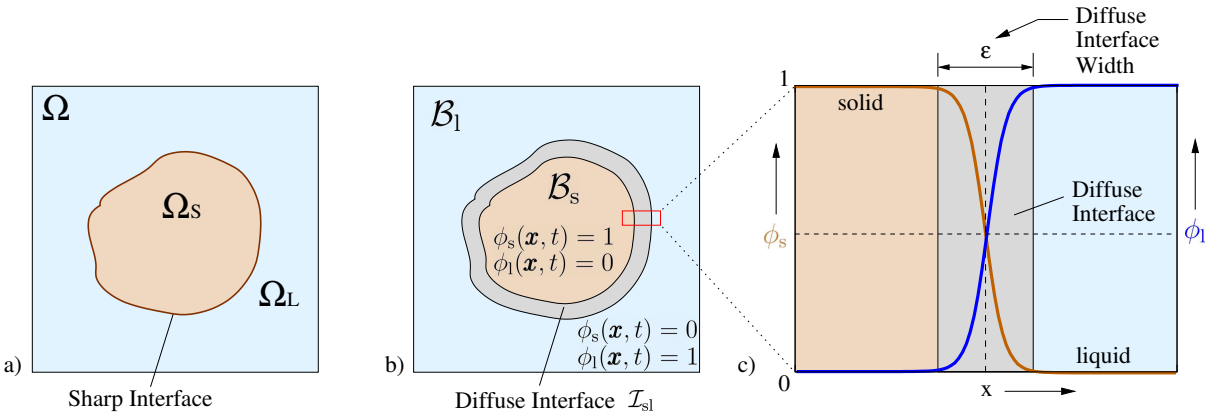

Figure 3.1: a) Sharp interface description of a system with a solid phase dispersed in a liquid phase. b) Diffuse interface description using the phase-fields $\phi_s(\boldsymbol{x},t)$ and $\phi_l(\boldsymbol{x},t)$ corresponding to the solid and liquid phases, respectively. c) Smooth variation of the phase-fields from solid-bulk $\mathcal{B}_s$ to liquid-bulk $\mathcal{B}_l$ over the diffuse interface region $\mathcal{I}_{sl}$.

is given by

$$f(\mathbf{c},T,\boldsymbol{\phi}) = \sum_{\alpha=1}^{N} f_\alpha(\mathbf{c},T)h(\phi_\alpha) \tag{3.2}$$

as an interpolation of the phase-specific bulk free energy densities $f_\alpha(\mathbf{c},T)$ of all the phases. The interpolation function $h(\phi_\alpha)$ should be chosen such that it is continuous and monotonically increasing in the interval $(0,1)$ and fulfils $h(0)=0$ and $h(1)=1$. For the present work, the interpolation function of the form $h(\phi_\alpha)=\phi_\alpha^3(6\phi_\alpha^2-15\phi_\alpha+10)$ was chosen. The difference in the bulk free energy densities between the solid and liquid phases, i.e. $\Delta f_{\mathrm{sl}}(\mathbf{c},T)=f_{\mathrm{s}}(\mathbf{c},T)-f_{\mathrm{l}}(\mathbf{c},T)$, generates a driving force for the crystal growth. In the present thesis, we assume a constant driving force of crystallization for the quartz and calcite cement growth, i.e. $\Delta f_{\mathrm{sl}}=f_{\mathrm{s}}-f_{\mathrm{l}}$. This modeling assumption is valid under the following conditions: I) the solute attachment at the solid-liquid interface is much slower than diffusion and advection, thereby maintaining a constant fluid supersaturation, and II) crystal growth occurs at isothermal conditions. The gradient energy density term serves as an energetic penalty due to the occurrence of diffuse interfaces, and is expressed as

$$\varepsilon a(\boldsymbol{\phi},\boldsymbol{\nabla\phi}) = \varepsilon \sum_{\substack{\alpha,\beta=1\\(\alpha<\beta)}}^{N,N} \gamma_{\alpha\beta}\{a_{\alpha\beta}^{\mathrm{cap}}(\mathbf{q}_{\alpha\beta})\}^2|\mathbf{q}_{\alpha\beta}|^2, \tag{3.3}$$

where $\gamma_{\alpha\beta}$ denotes the surface energy density of the α-β interface. The scalar ε is a length scale parameter that controls the width of the diffuse interface. The vector quantity $\mathbf{q}_{\alpha\beta}$ is a measure of the phase-field gradient and is constructed as $\mathbf{q}_{\alpha\beta}=\phi_\alpha\boldsymbol{\nabla}\phi_\beta-\phi_\beta\boldsymbol{\nabla}\phi_\alpha$ such that it points in the direction perpendicular to the binary α-β interface. The capillary anisotropy function $a_{\alpha\beta}^{\mathrm{cap}}$ is utilized to model the equilibrium crystal shape attained as a

result of surface energy minimization under vanishing driving forces. For the problem of syntaxial overgrowth of quartz and calcite cements resulting in the crystals with sharp edges and flat facets, a piece-wise anisotropy function [170] is utilized only for the solid-liquid interfaces

$$a_{\mathrm{sl}}^{\mathrm{cap}}(\mathbf{q}_{\mathrm{sl}}) = \max_k \left\{ \hat{\mathbf{n}}_{\mathrm{sl}} \cdot \boldsymbol{\eta}_k^{\mathrm{cap}} \right\}, \quad (k = 1, \ldots, n_{\mathrm{cap}}), \tag{3.4}$$

where $\hat{\mathbf{n}}_{\mathrm{sl}} = \mathbf{q}_{\mathrm{sl}}/|\mathbf{q}_{\mathrm{sl}}|$ represents the unit vector perpendicular to the solid-liquid interface. $\{\boldsymbol{\eta}_k^{\mathrm{cap}} \mid k = 1, \ldots, n_{\mathrm{cap}}\}$ is the set of n_{cap} vertex vectors of the capillary anisotropy shape of the solid-liquid interface. For the solid-solid interfaces or the grain boundaries, an isotropic surface energy was assigned, i.e. $a_{\mathrm{ss}}^{\mathrm{cap}} = 1$. A *multiobstacle*-type potential energy density of the form

$$\frac{1}{\varepsilon} w(\boldsymbol{\phi}) = \begin{cases} \dfrac{16}{\varepsilon \pi^2} \displaystyle\sum_{\substack{\alpha,\beta=1 \\ (\alpha<\beta)}}^{N,N} \gamma_{\alpha\beta} \phi_\alpha \phi_\beta + \dfrac{1}{\varepsilon} \sum_{\substack{\alpha,\beta,\delta=1 \\ (\alpha<\beta<\delta)}}^{N,N,N} \gamma_{\alpha\beta\delta} \phi_\alpha \phi_\beta \phi_\delta & \text{if } \boldsymbol{\phi} \in \mathcal{G}, \\ \infty & \text{else} \end{cases} \tag{3.5}$$

is utilized, where the Gibb's simplex $\mathcal{G} = \{\boldsymbol{\phi} \mid \sum_{\alpha=1}^{N} \phi_\alpha = 1 \text{ and } \phi_\alpha \geq 0\}$ enforces the minima in the bulk regions of all the phases. This energy density contribution creates an energetic barrier for the spontaneous phase transitions in the absence of driving forces. The second term in eq. $(3.5)_1$ (proportional to $\phi_\alpha \phi_\beta \phi_\delta$) suppresses the occurrence of spurious phases in a binary α-β interface. The evolution of phase-fields is formulated as

$$\tau \varepsilon \frac{\partial \phi_\alpha}{\partial t} = -\frac{\delta \mathcal{F}}{\delta \phi_\alpha} - \lambda \quad \text{for} \quad \alpha = 1, \ldots, N; \tag{3.6}$$

where the kinetic coefficient τ is the reciprocal of the effective mobility (eq. (2.4) in chapter 2) of the interfaces. In a multiphase/multigrain system, to assign an unequal interface mobility for each α-β interfaces, different formulations can be employed, as discussed in chapters 5 and 7 of this dissertation. Moreover, an anisotropic particle attachment kinetics can be formulated in this term, please refer to the kinetic anisotropy formulation utilized in the modeling of quartz cementation in the polycrystalline system in chapter 7. The term $\delta\mathcal{F}/\delta\phi_\alpha = \partial\mathfrak{I}/\partial\phi_\alpha - \boldsymbol{\nabla} \cdot \left(\partial\mathfrak{I}/\partial(\boldsymbol{\nabla}\phi_\alpha)\right)$ is the variational derivative of the Helmholtz free energy with respect to the phase-field ϕ_α, $\mathfrak{I}$ being the integrand in eq. (3.1). The Lagrange multiplier λ is utilized to locally impose the summation constraint $\left(\sum_{\alpha=1}^{N} \phi_\alpha = 1\right)$ and is computed as $\lambda = -(\sum_{\alpha=1}^{N} \frac{\delta\mathcal{F}}{\delta\phi_\alpha})/N$. Such a formulation ensures that the Helmholtz free energy decreases monotonically with time, rendering thermodynamic consistency to the model. On substituting the expression of eq (3.1) in eq. (3.6) yields the following system of partial differential equations (PDEs)

$$\tau \varepsilon \frac{\partial \phi_\alpha}{\partial t} = \varepsilon \left(\boldsymbol{\nabla} \cdot \frac{\partial a\left(\boldsymbol{\phi}, \boldsymbol{\nabla}\boldsymbol{\phi}\right)}{\partial \boldsymbol{\nabla}\phi_\alpha} - \frac{\partial a\left(\boldsymbol{\phi}, \boldsymbol{\nabla}\boldsymbol{\phi}\right)}{\partial \phi_\alpha} \right) - \frac{1}{\varepsilon} \frac{\partial w\left(\boldsymbol{\phi}\right)}{\partial \phi_\alpha} - \frac{\partial f\left(\boldsymbol{\phi}\right)}{\partial \phi_\alpha} - \lambda \tag{3.7}$$

for $\alpha = 1 \dots N$. The system of PDEs is numerically solved using the finite difference method. The time derivative is approximated using the explicit Euler scheme, and the spatial derivatives are discretized using the second-order accurate central difference scheme. The multiphase-field (MPF) model is implemented in a software package called Pace3D [171] using the programming language C. The code is parallelized on the basis of message passing interface and is optimized with the locally reduced order parameter optimization that reduces the simulation time ($\mathcal{O}(N^3) \rightarrow \mathcal{O}(1)$) and memory usage ($\mathcal{O}(N) \rightarrow \mathcal{O}(1)$) per cell in the computational domain, where N denotes the number of phases. The optimization and parallelization procedures facilitate large scale simulations in multigrain systems. The general structure of the implemented code along with the optimization and parallelization procedures are elaborated in Hoetzer et al. [172].

3.1 A simplified phase-field model for cementation

In this section, a simplified case of the generalized MPF model introduced in the previous section is presented, for the sake of clarity. A two-phase system comprising of a solid and a liquid phase is considered, such that the presence of solid and liquid phases can be described by a single phase-field variable ϕ, where $\phi = \phi_\mathrm{s} = 1 - \phi_\mathrm{l}$, s and l denoting the solid and liquid phases, respectively. Under the assumptions of isotropic and isothermal growth of a solid crystal at the expense of liquid at a constant driving force of crystallization, the expression of the Helmholtz free energy of this binary system is reduced to

$$\mathcal{F}(\phi, \boldsymbol{\nabla}\phi) = \int_\Omega \left[f(\phi) + \varepsilon a(\boldsymbol{\nabla}\phi) + \frac{1}{\varepsilon} w(\phi) \right] \mathrm{d}\Omega. \tag{3.8}$$

The bulk free energy density of this system reads

$$f(\phi) = f_\mathrm{s} h(\phi_\mathrm{s}) + f_\mathrm{l} h(\phi_\mathrm{l}) = f_\mathrm{s} h(\phi) + f_\mathrm{l} h(1 - \phi) \tag{3.9}$$

with $h(\phi) = \phi^3(6\phi^2 - 15\phi + 10)$. The isotropic gradient energy density with $a_{sl}^{\mathrm{cap}} = 1$ is given by

$$\varepsilon a(\boldsymbol{\nabla}\phi) = \varepsilon \gamma_{sl} |\phi_\mathrm{s} \boldsymbol{\nabla}\phi_\mathrm{l} - \phi_\mathrm{l} \boldsymbol{\nabla}\phi_\mathrm{s}|^2 = \varepsilon \gamma_{sl} |\boldsymbol{\nabla}\phi|^2, \tag{3.10}$$

and the obstacle-type potential without the higher order term reads

$$\frac{1}{\varepsilon} w(\boldsymbol{\phi}) = \begin{cases} \dfrac{16}{\varepsilon \pi^2} \gamma_{\mathrm{sl}} \phi_\mathrm{s} \phi_\mathrm{l} = \dfrac{16}{\varepsilon \pi^2} \gamma_{\mathrm{sl}} \phi (1 - \phi) & \text{if } \phi \in [0, 1] \\ \infty & \text{else.} \end{cases} \tag{3.11}$$

Figure 3.2a depicts the plot of obstacle-type potential as a function of the phase-field variable for $\gamma_{\mathrm{sl}} = 1$, illustrating the minima at $\phi = 0$ and $\phi = 1$. The evolution equation

for the phase-field is given by

$$\begin{aligned}\tau\varepsilon\frac{\partial\phi}{\partial t} =& \varepsilon\boldsymbol{\nabla}\cdot\frac{\partial a(\boldsymbol{\nabla}\phi)}{\partial\boldsymbol{\nabla}\phi} - \frac{1}{\varepsilon}\frac{\partial w(\phi)}{\partial\phi} - \frac{\partial f(\phi)}{\partial\phi} \\ =& \underbrace{2\varepsilon\gamma_{\mathrm{sl}}\boldsymbol{\nabla}^2\phi}_{\mathrm{I}} - \underbrace{\frac{16}{\varepsilon\pi^2}\gamma_{\mathrm{sl}}(1-2\phi)}_{\mathrm{II}} - \underbrace{(f_{\mathrm{s}}-f_{\mathrm{l}})h'(\phi)}_{\mathrm{III}}.\end{aligned} \tag{3.12}$$

It is worthy to note that the Lagrange multiplier λ does not enter the evolution eqs. (3.12) because the summation constraint is already incorporated (as $\phi_{\mathrm{s}} = 1 - \phi_{\mathrm{l}}$) in the formulation. The terms I and II in eq. (3.12) represent the interfacial contributions. Depending upon the chosen value of the scalar parameter ε, a diffuse interface is generated. The properties of the diffuse interface (e.g. profile, thickness) also depend upon the chosen form of the potential-type energy density. In the term III, the difference in the bulk free energies (i.e. $\Delta f_{\mathrm{sl}} = f_{\mathrm{s}} - f_{\mathrm{l}}$) provides the driving force of crystallization that results in the interface motion.

3.1.1 Thermodynamic equilibrium

Under the vanishing driving force (i.e. $\Delta f_{\mathrm{sl}} = 0$), a thermodynamic equilibrium is attained when the interface becomes stationary (i.e. $\partial\phi/\partial t = 0$). In this condition, the evolution eq. (3.12) is reduced to the following ordinary differential equation (ODE)

$$2\varepsilon\gamma_{\mathrm{sl}}\boldsymbol{\nabla}^2\phi = \frac{16}{\varepsilon\pi^2}\gamma_{\mathrm{sl}}(1-2\phi). \tag{3.13}$$

In one dimension (1-D), the above eq. (3.13) reads

$$2\varepsilon\gamma_{\mathrm{sl}}\frac{\partial^2\phi}{\partial x^2} = \frac{16}{\varepsilon\pi^2}\gamma_{\mathrm{sl}}(1-2\phi). \tag{3.14}$$

On multiplication of both sides of eq. (3.14) by $\partial\phi/\partial x$ and integrating

$$\int 2\varepsilon\gamma_{\mathrm{sl}}\frac{\partial\phi}{\partial x}\frac{\partial^2\phi}{\partial x^2}\mathrm{d}x = \int\frac{16}{\varepsilon\pi^2}\gamma_{\mathrm{sl}}(1-2\phi)\frac{\partial\phi}{\partial x}\mathrm{d}x \tag{3.15}$$

under the condition of vanishing gradient of the phase-field in the bulk region, i.e. $\partial\phi/\partial x = 0$ at $\phi = 0$ or 1, results in

$$\underbrace{\varepsilon\gamma_{\mathrm{sl}}\left(\frac{\partial\phi}{\partial x}\right)^2}_{\text{gradient energy density}} = \underbrace{\frac{16}{\varepsilon\pi^2}\gamma_{\mathrm{sl}}\phi(1-\phi)}_{\text{potential energy density}} \tag{3.16}$$

As the gradient energy density and the potential energy density are equal at the thermodynamic equilibrium, eq. (3.16) is known as the *Principle of equipartition of energy*.

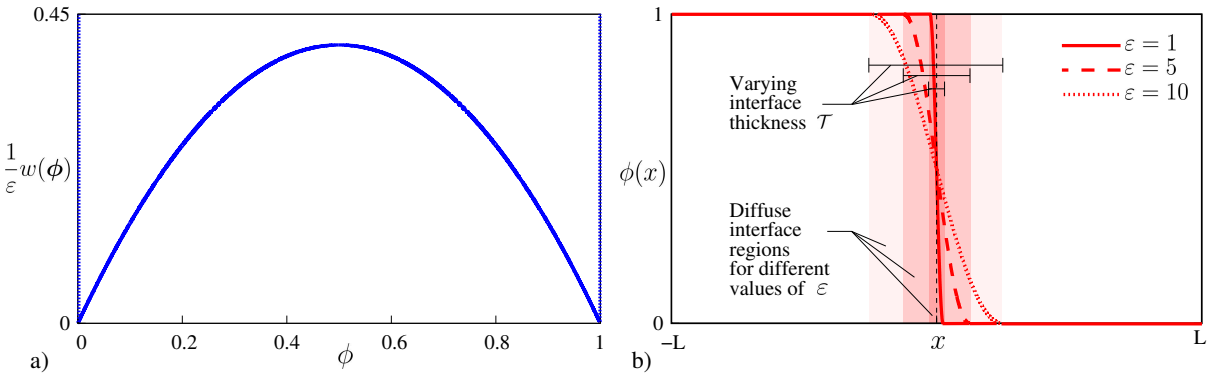

Figure 3.2: a) Plot of obstacle-type potential $w(\phi)/\varepsilon$ with $\gamma_{sl} = 1.0$ as a function of phase-field variable ϕ. b) Equilibrium phase-field profile using the obstacle-type potential in a 1-D domain of length $2L = 100$ for different values of length scale parameter ε. Diffuse interface thickness $\mathcal{T}$ increases with increasing value of ε.

3.1.1.1 Interface properties at the thermodynamic equilibrium

On solving the ODE (eq. (3.16)) under the boundary conditions $\partial\phi/\partial x < 0$ and $\phi(x = 0) = 0.5$, the equilibrium profile of the phase-field $\phi(x)$ is obtained as

$$\phi(x) = \begin{cases} 1 & \text{if } x < -\dfrac{\pi^2\varepsilon}{8} \\ \dfrac{1}{2}\left[1 - \sin\left(\dfrac{4x}{\pi\varepsilon}\right)\right] & \text{if } -\dfrac{\pi^2\varepsilon}{8} \leq x \leq \dfrac{\pi^2\varepsilon}{8} \\ 0 & \text{if } x > \dfrac{\pi^2\varepsilon}{8}. \end{cases} \tag{3.17}$$

Figure 3.2b depicts the equilibrium phase-field profile for different values of the length scale parameter ε. The interface thickness $\mathcal{T}$ with the obstacle-type potential energy density is

$$\mathcal{T} = \frac{\pi^2\varepsilon}{4}. \tag{3.18}$$

Eq. (3.18) implies that that interface thickness increases linearly with increasing value of ε, as also highlighted in figure 3.2b. At the thermodynamic equilibrium, utilizing eqs. (3.8), (3.16) and (3.18), the expression of interfacial energy $\gamma_{\mathcal{I}}$ in 1-D is given by

$$\gamma_{\mathcal{I}} = \int_{-\mathcal{T}/2}^{\mathcal{T}/2} \left(\varepsilon a(\boldsymbol{\nabla}\phi) + \frac{1}{\varepsilon}w(\phi)\right) \mathrm{d}x = \int_{-\pi^2\varepsilon/8}^{\pi^2\varepsilon/8} \frac{2}{\varepsilon}w(\phi)\mathrm{d}x = \int_{-\pi^2\varepsilon/8}^{\pi^2\varepsilon/8} \frac{32\gamma_{\mathrm{sl}}}{\pi^2\varepsilon}\phi(1-\phi)\mathrm{d}x. \tag{3.19}$$

On plugging the expression for the phase-field profile (eq. (3.17)) in the above eq. (3.19) followed by definite integration, the interfacial energy of the solid-liquid interface is recovered as

$$\gamma_I = \gamma_{\mathrm{sl}}. \tag{3.20}$$

Eq. (3.20) showcases the energetic equivalence between the sharp and diffuse interfaces.

3.2 Computational fluid dynamics analysis for the determination of permeability

In order to estimate the flow behaviour of the progressively cemented rock microstructures, numerical data sets corresponding to the pore space of the cemented digital grain packs are extracted at representative time stages. Computational fluid dynamics (CFD) analysis is performed using the steady state *Stokes* equations, given by

$$\begin{aligned} \mu_{\mathrm{f}} \boldsymbol{\nabla}^2 \boldsymbol{v}(\boldsymbol{x},t) - \boldsymbol{\nabla} p(\boldsymbol{x},t) + \boldsymbol{f_b}(\boldsymbol{x},t) = \boldsymbol{0} \quad &\text{(momentum balance)} \\ \boldsymbol{\nabla} \cdot \boldsymbol{v}(\boldsymbol{x},t) = 0 \quad &\text{(mass balance).} \end{aligned} \tag{3.21}$$

The eqs. (3.21) describe the motion of incompressible and viscous fluids undergoing laminar flow under the assumptions of low Reynold number, i.e. $Re << 1$. The physical quantities in eq. (3.21) are the dynamic viscosity μ_{f}, fluid velocity field $\boldsymbol{v}(\boldsymbol{x},t)$, pressure $p(\boldsymbol{x},t)$ and body force $\boldsymbol{f_b}(\boldsymbol{x},t)$. For an applied pressure drop ($\Delta\bar{p} = \bar{p}_2 - \bar{p}_1$) in a given direction ($x_i$ for i=1,2,3), the fluid velocity field is computed based on the free stream boundary conditions [173], given by

$$p - \mu \partial_n v_{\mathrm{n}}|_{\mathcal{S}_k} = \bar{p}_k, \qquad \partial_n v_\tau|_{\mathcal{S}_k} = 0 \qquad \text{for} \;\; k = 1 \text{ and } 2, \tag{3.22}$$

where $\mathcal{S}_{\mathrm{k}}$ represent the plane surface at which a constant pressure $\bar{p}_{\mathrm{k}}$ is applied, the quantities v_{n} and v_τ are the normal and tangential components of the fluid velocity at the plane surface $\mathcal{S}_{\mathrm{k}}$. At the boundaries of the computational domain in the lateral directions, the no-slip conditions i.e.

$$\boldsymbol{v}|_{\mathrm{lateral}} = \boldsymbol{0}, \tag{3.23}$$

were applied. In the extracted geometrical data at different stages of time, the fluid velocities in the solid grain phases are defined to be zero. At the interfaces between the grains and pore space, the no-slip boundary condition is applied, which reads

$$\boldsymbol{v}|_{\mathrm{interfaces}} = \boldsymbol{0}, \tag{3.24}$$

Eqs. (3.21) are numerically solved using the finite difference method on a staggered grid, see e.g. Harlow and Welch [174]. From the obtained fluid velocities, the permeabilities κ_{i} in different directions are computed using the *Darcy's law*, given by

$$\kappa_{\mathrm{i}} = \frac{\mu_{\mathrm{f}} \bar{v}_{\mathrm{i}}}{\Delta\bar{p}/l_{\mathrm{i}}}. \tag{3.25}$$

In eq. (3.25), $\bar{v}_{\mathrm{i}}$ and l_{i} denote the mean velocity and length of computational domain in the direction of the applied pressure drop, respectively. The mean velocity $\bar{v}_{\mathrm{i}}$ is computed by averaging the corresponding velocity component over the entire volume V, i.e.

$$\bar{v}_{\mathrm{i}} = \frac{\int_V u_i \mathrm{d}V}{\int_V \mathrm{d}V}. \tag{3.26}$$

The CFD equations are efficiently implemented in the software package PACE3D [171].

Chapter 4

A multiphase-field model for brittle anisotropic fracture propagation

We consider a set of *phase-fields* $\boldsymbol{\phi}(\boldsymbol{x},t) = [\boldsymbol{\phi}_{\mathrm{s}}(\boldsymbol{x},t), \phi_{\mathrm{c}}(\boldsymbol{x},t)]$ in a domain $\Omega \subset \mathbb{R}^d$, $d \in \{1,2,3\}$. In this set, the subset $\boldsymbol{\phi}_{\mathrm{s}}(\boldsymbol{x},t) = [\phi_1(\boldsymbol{x},t), \ldots, \phi_N(\boldsymbol{x},t)]$ denotes the set of phase-fields of $N \in \mathbb{N}$ solid phases, each $\phi_\alpha \ \forall \ \alpha \in \{1,\ldots,N\}$ describing the presence of the corresponding phase α at position $\boldsymbol{x}$ and time t. In the multigrain system of sandstone composed of e.g. N randomly oriented quartz grains, N solid phase-fields are needed to assign different unique crystallographic orientations (and thereby the direction dependent material properties such as elastic stiffness, fracture toughness, etc.) to distinct grains. The crack is described as a separate phase represented by the crack phase-field ϕ_{c}. The mathematical definitions of bulk $\mathcal{B}$ and interface $\mathcal{I}$ regions, the variation of phase-fields ϕ_α, and the location of interfaces are omitted in this section, as they are discussed in chapter 3. The interface $\mathcal{I}$ contains the diffuse regions describing the grain boundaries (i.e. solid-solid interfaces) and the fracture surfaces (i.e. solid-crack interfaces) in the complete domain. The crack phase-field ϕ_{c} serves as a damage indicator at a material point $\boldsymbol{x}$, where $\phi_{\mathrm{c}} = 1$ and $\phi_{\mathrm{c}} = 0$ imply a completely-damaged and completely-intact material states, respectively. Values in the interval $\phi_{\mathrm{c}} \in (0,1)$ represent the partially damaged states. The summation constraint for all the phase-fields, i.e. $\sum_{\alpha=1}^{N} \phi_\alpha = 1 - \phi_{\mathrm{c}}$, is locally sustained at each material point $\boldsymbol{x}$. Figure 4.1 schematically illustrates the sharp and diffuse interface descriptions of a fractured specimen, along with the spatial variation of the phase-fields ϕ_{s} and ϕ_{c} for the solid and crack phase, respectively. The total free energy of the system is formulated as

$$\mathcal{F}(\boldsymbol{\phi}, \boldsymbol{\nabla}\phi_{\mathrm{c}}, \boldsymbol{\varepsilon}) = \int_{\Omega} \underbrace{\left[G_{\mathrm{c}}(\boldsymbol{\phi}_{\mathrm{s}}, \boldsymbol{\nabla}\phi_{\mathrm{c}}) k \left\{ \varepsilon_{\mathrm{c}} |\boldsymbol{\nabla}\phi_{\mathrm{c}}|^2 + \frac{1}{\varepsilon_{\mathrm{c}}} w_{\mathrm{c}}(\phi_{\mathrm{c}}) \right\} + f_{\mathrm{el}}(\boldsymbol{\phi}, \boldsymbol{\varepsilon}) \right]}_{\mathfrak{I}} \mathrm{d}\Omega, \tag{4.1}$$

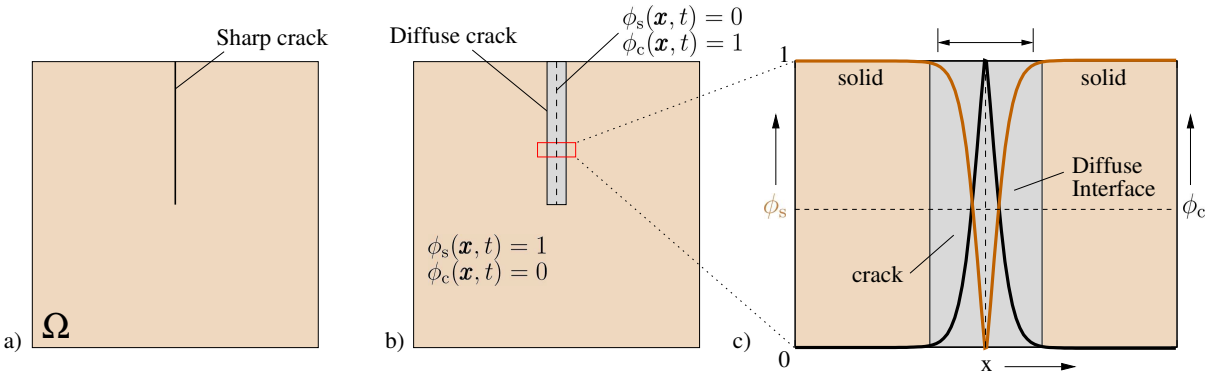

Figure 4.1: a) Sharp interface description of a specimen with a preexisting crack. b) Diffuse interface description using the phase-fields ϕ_s and ϕ_c corresponding to solid and crack phase, respectively. Variation of the phase-fields in a diffuse manner.

where the phase-fields $\boldsymbol{\phi}$, the gradient of the crack phase-field $\boldsymbol{\nabla}\phi_c$ and the local elastic strain tensor field $\boldsymbol{\varepsilon}(\boldsymbol{u})$ are the independent variables. Under the assumption of small strain theory, the local elastic strain in terms of the displacement field $\boldsymbol{u}$ is expressed as

$$\boldsymbol{\varepsilon}(\boldsymbol{u}) = \frac{\boldsymbol{\nabla u} + \boldsymbol{\nabla}^{\mathrm{T}}\boldsymbol{u}}{2}. \tag{4.2}$$

On the right hand side of eq. (4.1), $G_c(\boldsymbol{\phi}_s, \boldsymbol{\nabla}\phi_c)$ denotes the effective crack resistance and $f_{el}(\boldsymbol{\phi}, \boldsymbol{\varepsilon})$ is the effective elastic strain energy density. The curly-bracketed term, comprising of the gradient term $\varepsilon_c|\boldsymbol{\nabla}\phi_c|^2$ and the potential term $w_c(\phi_c)/\varepsilon_c$, describes the energy density of the crack in a regularized manner. For the present work, a *one-sided well* type potential of the form $w_c(\phi_c) = k_w\phi_c^2$ is employed. In the free energy functional, $k = 1/2$ and $k_w = 1$ are the scalar constants whose values are determined by matching the surface energies of the diffuse interface with the sharp interface results, as elaborated in section 4.1.1.1. The scalar parameter ε_c controls the thickness of the solid-crack interface. The effective crack resistance is expressed as

$$G_c(\boldsymbol{\phi}_s, \boldsymbol{\nabla}\phi_c) = \sum_{\alpha=1}^{N} h_s^\alpha(\boldsymbol{\phi}_s) G_c^\alpha(\boldsymbol{\nabla}\phi_c), \tag{4.3}$$

where $h_s^\alpha(\boldsymbol{\phi}_s)$ and $G_c^\alpha(\boldsymbol{\nabla}\phi_c)$ denote the interpolation function and the crack resistance of solid phase α, respectively. The form of crack resistance $G_c^\alpha(\boldsymbol{\nabla}\phi_c)$, well-suited to describe fracture toughness anisotropy in quartz grains, is discussed in section 8.1.1 of chapter 8. The function $h_s^\alpha(\boldsymbol{\phi}_s)$ given by [175]

$$h_s^\alpha(\boldsymbol{\phi}_s) = \frac{\phi_\alpha}{\sum_{\beta=1}^{N} \phi_\beta} \tag{4.4}$$

interpolates the crack resistance of different solid phases along the grain boundaries. In order to model the grain boundary resistance which is lower than the crack resistance

of bulk phases, a reduced interfacial crack resistance interpolation is formulated, which is discussed in section 8.1.2 of chapter 8. Similar to the effective crack resistance, the effective elastic free energy density is given as an interpolation of the phase-specific elastic free energy densities $f_{\mathrm{el}}^{\alpha}(\boldsymbol{\phi}, \boldsymbol{\varepsilon}^{\alpha})$ of all the solid phases

$$f_{\mathrm{el}}(\boldsymbol{\phi}, \boldsymbol{\varepsilon}) = \sum_{\alpha=1}^{N} h_{\mathrm{s}}^{\alpha}(\boldsymbol{\phi}_{\mathrm{s}}) f_{\mathrm{el}}^{\alpha}(\boldsymbol{\phi}, \boldsymbol{\varepsilon}^{\alpha}), \tag{4.5}$$

where $\boldsymbol{\varepsilon}^{\alpha}$ are the phase-specific strains (i.e. corresponding to phase α). The evolution of crack phase-field is formulated as

$$\begin{aligned} \frac{\partial \phi_{\mathrm{c}}}{\partial t} &= -\frac{\mu_{\mathrm{c}}}{\varepsilon_{\mathrm{c}}} \frac{\delta \mathcal{F}(\boldsymbol{\phi}, \boldsymbol{\nabla}\phi_{\mathrm{c}}, \boldsymbol{\varepsilon})}{\delta \phi_{\mathrm{c}}} \\ &= -\frac{\mu_{\mathrm{c}}}{\varepsilon_{\mathrm{c}}} \left(\frac{\partial \mathfrak{I}}{\partial \phi_{\mathrm{c}}} - \boldsymbol{\nabla} \cdot \frac{\partial \mathfrak{I}}{\partial \boldsymbol{\nabla}\phi_{\mathrm{c}}} \right), \end{aligned} \tag{4.6}$$

where μ_{c} is a positive relaxation parameter and $\mathfrak{I}$ denotes the integrand of eq. (4.1). The relaxation parameter μ_{c} controls the crack propagation velocity. In the dynamic models of fracture where the time derivatives of the displacement field in the momentum balance equation are non-negligible, the crack velocity can be controlled by formulating μ_{c} in a suitable manner. In the present work, a quasi-static fracture is assumed. Therefore, the term μ_{c} serves as a constant relaxation parameter, chosen sufficiently large in magnitude such that the simulations are numerically stable. Substitution of eq. (4.1) in eq. (4.6) yields

$$\begin{aligned} \frac{\partial \phi_{\mathrm{c}}}{\partial t} = -\frac{\mu_{\mathrm{c}}}{\varepsilon_{\mathrm{c}}} \Bigg[& \frac{k G_{\mathrm{c}}(\boldsymbol{\phi}_{\mathrm{s}}, \boldsymbol{\nabla}\phi_{\mathrm{c}})}{\varepsilon_{\mathrm{c}}} \frac{\partial w_{\mathrm{c}}(\phi_{\mathrm{c}})}{\partial \phi_{\mathrm{c}}} + \frac{\partial f_{\mathrm{el}}(\boldsymbol{\phi}, \boldsymbol{\varepsilon})}{\partial \phi_{\mathrm{c}}} - \\ & \boldsymbol{\nabla} \cdot \left\{ k \frac{\partial G_{\mathrm{c}}(\boldsymbol{\phi}_{\mathrm{s}}, \boldsymbol{\nabla}\phi_{\mathrm{c}})}{\partial \boldsymbol{\nabla}\phi_{\mathrm{c}}} \left(\varepsilon_{\mathrm{c}} |\boldsymbol{\nabla}\phi_{\mathrm{c}}|^2 + \frac{1}{\varepsilon_{\mathrm{c}}} w_{\mathrm{c}}(\phi_{\mathrm{c}}) \right) + 2k G_{\mathrm{c}}(\boldsymbol{\phi}_{\mathrm{s}}, \boldsymbol{\nabla}\phi_{\mathrm{c}}) \varepsilon_{\mathrm{c}} \boldsymbol{\nabla}\phi_{\mathrm{c}} \right\} \Bigg]. \end{aligned} \tag{4.7}$$

The term $\partial f_{\mathrm{el}}(\boldsymbol{\phi}, \boldsymbol{\varepsilon}) / \partial \phi_{\mathrm{c}}$ provides the elastic driving force for the crack growth. In order to ensure that the crack does not propagate under compressive stress states, that may otherwise result in physically unrealistic fracture patterns, following Miehe et al. [136], a tension-compression split formulation is utilized

$$f_{\mathrm{el}}^{\alpha}(\phi_{\mathrm{c}}, \boldsymbol{\varepsilon}^{\alpha}) = (1 - \phi_{\mathrm{c}})^2 \left[f_{\mathrm{el}}^{\alpha}(\boldsymbol{\varepsilon}^{\alpha}) \right]_{+} + \left[f_{\mathrm{el}}^{\alpha}(\boldsymbol{\varepsilon}^{\alpha}) \right]_{-}. \tag{4.8}$$

Example of unrealistic fracture patterns in compression is presented in e.g. Bourdin et al. [131]. Different formulations of tension-compression split (e.g. [135, 136]) along with a comparative analysis of their performance is presented in Ambati et al. [141]. The terms $\left[f_{\mathrm{el}}^{\alpha}(\boldsymbol{\varepsilon}^{\alpha}) \right]_{\pm}$ represent the positive and negative parts of the phase-specific elastic

strain energy density, and are formulated as

$$\begin{aligned}[f_{\mathrm{el}}^{\alpha}(\boldsymbol{\varepsilon}^{\alpha})]_{\pm} &= \left[\frac{1}{2}\boldsymbol{\varepsilon}^{\alpha} : \mathbb{C}^{\alpha} : \boldsymbol{\varepsilon}^{\alpha}\right]_{\pm} \\ &= \frac{1}{2}\lambda^{\alpha}\langle\epsilon_1^{\alpha}+\epsilon_2^{\alpha}+\epsilon_3^{\alpha}\rangle_{\pm}^2 + \mu^{\alpha}(\langle\epsilon_1^{\alpha}\rangle_{\pm}^2 + \langle\epsilon_2^{\alpha}\rangle_{\pm}^2 + \langle\epsilon_3^{\alpha}\rangle_{\pm}^2).\end{aligned} \tag{4.9}$$

The term $\mathbb{C}^{\alpha} = \lambda^{\alpha}\mathbf{1}\otimes\mathbf{1} + 2\mu^{\alpha}\mathbb{I}$ denotes the phase-specific isotropic stiffness tensor in terms of the phase-specific Lame$^{'}$ parameters λ^{α} and μ^{α}. ϵ_k^{α} for k=1,2,3 represent the three principal strains. The operator $\langle\rangle_{\pm}$, when applied on any scalar quantity s, yields $\langle \mathrm{s}\rangle_{\pm} = (\mathrm{s}\pm|\mathrm{s}|)/2$. The tension-compression split formulation of eq. (4.8) ensures that the propagation of crack is driven solely by the tensile stress states, as only the positive part of the elastic strain energy density enters the evolution equation of the crack phase-field. The evolution of all the solid phase-fields, in the absence of additional solid-solid phase transitions, reads

$$\frac{\partial\phi_{\alpha}}{\partial t} = -h_{\mathrm{s}}^{\alpha}(\boldsymbol{\phi}_{\mathrm{s}})\frac{\partial\phi_{\mathrm{c}}}{\partial t} \quad \text{for} \quad \alpha = 1,\ldots,N. \tag{4.10}$$

For negligible body forces, the equation of balance of linear momentum under the quasi-static assumption (i.e. neglecting the inertia) reads

$$\boldsymbol{\nabla}\cdot\bar{\boldsymbol{\sigma}} = \mathbf{0}, \tag{4.11}$$

where the effective stresses $\bar{\boldsymbol{\sigma}}$ are given by

$$\bar{\boldsymbol{\sigma}} = \sum_{\alpha=1}^{N} h_{\mathrm{s}}^{\alpha}(\boldsymbol{\phi}_{\mathrm{s}})\boldsymbol{\sigma}^{\alpha}. \tag{4.12}$$

as a volumetric interpolation of the phase-specific stresses $\boldsymbol{\sigma}^{\alpha}$. The phase-specific stresses are calculated as

$$\boldsymbol{\sigma}^{\alpha} = (1-\phi_{\mathrm{c}})^2\frac{\partial}{\partial\boldsymbol{\varepsilon}^{\alpha}}\left[\frac{1}{2}\boldsymbol{\varepsilon}^{\alpha} : \mathbb{C}^{\alpha} : \boldsymbol{\varepsilon}^{\alpha}\right] = (1-\phi_{\mathrm{c}})^2\,\mathbb{C}^{\alpha} : \boldsymbol{\varepsilon}^{\alpha}. \tag{4.13}$$

In contrast to the crack driving force, the phase-specific stresses are computed by the degradation of the total elastic strain energy density, in order to retain the linearity of the momentum balance eq. (4.11). Thus, the present formulation is classified as a *Hybrid model* after Ambati et al. [141]. Within the staggered algorithmic approach (as also adopted in the present work, discussed in the next paragraph), hybrid models have shown to predict similar fracture patterns compared to the models where the splitting is utilized for the calculations of the crack phase-field and stresses, however, at lower computational expenditure (by about one order) than the latter [141]. Due to these reasons, a hybrid formulation is chosen for the present work. In the diffuse solid-solid interface regions, the phase-specific stresses are obtained by satisfying the mechanical jump conditions [176, 177].

The phase-field evolution eqs. (4.6) and (4.10) along with the momentum balance eq. (4.11) are solved in a staggered manner. The crack phase-field evolution eq. (4.6) is solved using the finite difference method, where the time derivative is approximated using the explicit Euler scheme and the spatial derivatives are discretized using the central difference scheme. The momentum balance equation, on the other hand, is solved implicitly for the mechanical fields. For the discretization, a rotated staggered grid (RSG) is utilized. The displacements are computed at the corners of the cell, whereas the phase-fields and the stresses are stored at the cell centers. Thus, the present RSG is analogous to a regular finite element mesh with same-sized Q1 elements using full integration. In each time step Δt, the mechanical and phase-fields are inputs for one another. The condition $\dot{\phi}_\mathrm{c} \geq 0$ is locally sustained at each time step. Moreover, in order to reduce the computational expenditure, a critical value of the crack phase-field $\phi_\mathrm{c}^\mathrm{crit} = 0.9$ was set, above which a material point is considered as fully damaged (i.e. $\phi_\mathrm{c} = 1$). This numerical treatment ensures that the values of the crack phase-field ϕ_c always remain in the range of 0 to 1. It is worthy to mention that, in eq. (4.10), the solid phase-fields are updated as the volumetric interpolation of the temporal update of the crack phase-field. This essentially implies that the summation constraint ($\sum_{\alpha=1}^{N} \phi_\alpha = 1 - \phi_\mathrm{c}$) is retained at each time step, provided the constraint is satisfied in the initial configuration of the computational domain. In one mechanical load increment, the balance of linear momentum (eq. (4.11)) and the evolution of crack phase-field (eq. (4.6)) are solved for several relaxation time steps until a steady state for the crack phase-field is reached, i.e. $\partial\phi_\mathrm{c}/\partial t < 10^{-4}$. This numerical treatment results in a minimal impact of the time step size Δt and the relaxation parameter μ_c on the simulation results. The multiphase-field (MPF) model for brittle anisotropic crack propagation is implemented in the highly-parallelized software package, Pace3D [171], using the programming language C. For the details of the general structure and parallelization of the solver, interested readers are referred to Hoetzer et al. [172].

4.1 A simplified phase-field model for fracture

In this section, a simplified case of the generalized MPF model that was introduced in the previous section is presented, for the sake of clarity. A single phase material with a preexisting fracture is considered, where the presence of the crack and solid phases is described by a single phase-field variable ϕ_c, such that $\phi_\mathrm{c} = 1 - \phi_\mathrm{s}$, c and s denoting the crack and solid phases, respectively. Under the assumptions of a constant isotropic crack resistance and utilizing the full degradation of the elastic energy density, the expression

of the free energy of this system reduces to

$$\mathcal{F}(\phi_{\mathrm{c}}, \boldsymbol{\nabla}\phi_{\mathrm{c}}, \boldsymbol{\varepsilon}) = \int_{\Omega} \left[G_{\mathrm{c}} k \left\{ \varepsilon_{\mathrm{c}} |\boldsymbol{\nabla}\phi_{\mathrm{c}}|^2 + \frac{1}{\varepsilon_{\mathrm{c}}} w_{\mathrm{c}}(\phi_{\mathrm{c}}) \right\} + (1-\phi_{\mathrm{c}})^2 f_{\mathrm{el}}(\boldsymbol{\varepsilon}) \right] \mathrm{d}\Omega. \tag{4.14}$$

Figure 4.2a depicts the plot of the one-sided well type potential over the crack phase-field variable for $k_w = 1$. The evolution of crack phase-field is given by

$$\frac{\partial \phi_{\mathrm{c}}}{\partial t} = \frac{\mu_{\mathrm{c}}}{\varepsilon_{\mathrm{c}}} \left[\underbrace{2\varepsilon_{\mathrm{c}} G_{\mathrm{c}} k \boldsymbol{\nabla}^2 \phi_{\mathrm{c}}}_{\mathrm{I}} - \underbrace{\frac{G_{\mathrm{c}} k}{\varepsilon_{\mathrm{c}}} \frac{\partial w_{\mathrm{c}}(\phi_{\mathrm{c}})}{\partial \phi_{\mathrm{c}}}}_{\mathrm{II}} - \underbrace{2(1-\phi_{\mathrm{c}}) f_{\mathrm{el}}(\boldsymbol{\varepsilon})}_{\mathrm{III}} \right]. \tag{4.15}$$

As the terms I and II in eq. (4.15) represent the interfacial contributions for the diffuse fracture surfaces, depending upon the chosen values of the scalar parameter ε_{c}, a diffuse interface between the crack and the solid phase is generated. The properties of the diffuse crack-solid interface (e.g. profile, thickness) also depend upon the chosen form of the potential-type energy density $w_{\mathrm{c}}(\phi_{\mathrm{c}})$. Term III represents the elastic free energy density of the loaded specimen, which is degraded by the crack degradation function $(1-\phi_{\mathrm{c}})^2$ in the presence of the crack phase.

4.1.1 Thermodynamic equilibrium

Under the unloaded state (i.e. $f_{\mathrm{el}}(\boldsymbol{\varepsilon}) = 0$), a thermodynamic equilibrium is attained when the crack interface is stationary (i.e. $\partial\phi_{\mathrm{c}}/\partial t = 0$). Under this condition, the evolution

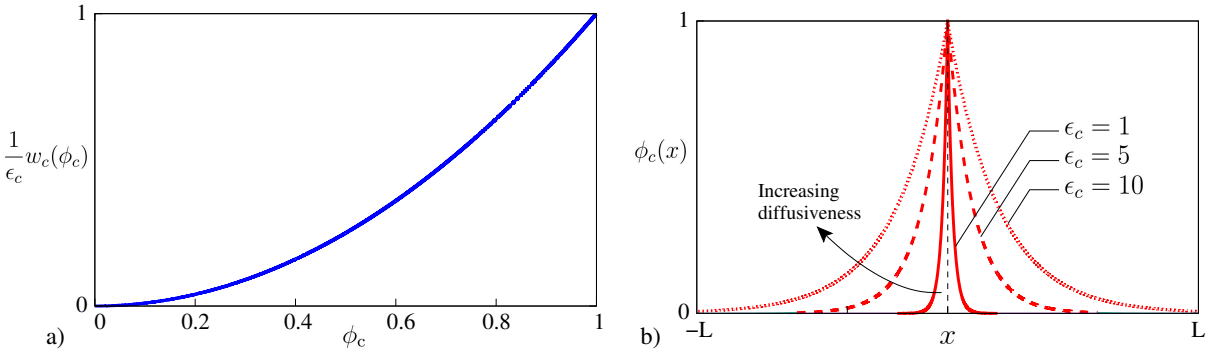

Figure 4.2: a) Plot of one-sided well potential $w_c(\phi_c)/\varepsilon_c$ with $k_w = 1$ as a function of crack phase-field variable ϕ_c. b) Equilibrium crack phase-field profile using the single well-type potential in a 1-D domain of length $2L = 100$ for different values of length scale parameter ε_c. Diffusiveness of the crack phase-field profile increases with increasing value of ε_c.

eq. (4.15) is reduced to the following ordinary differential equation (ODE)

$$2\varepsilon_{\mathrm{c}} G_{\mathrm{c}} k \boldsymbol{\nabla}^2 \phi_{\mathrm{c}} = \frac{G_{\mathrm{c}} k}{\varepsilon_{\mathrm{c}}} \frac{\partial w_{\mathrm{c}}(\phi_{\mathrm{c}})}{\partial \phi_{\mathrm{c}}} \tag{4.16}$$

For the one dimensional (1-D) case, the above eq. (4.16) reads

$$2\varepsilon_{\mathrm{c}} G_{\mathrm{c}} k \frac{\partial^2 \phi_{\mathrm{c}}}{\partial x^2} = \frac{G_{\mathrm{c}} k}{\varepsilon_{\mathrm{c}}} \frac{\partial w_{\mathrm{c}}(\phi_{\mathrm{c}})}{\partial \phi_{\mathrm{c}}}. \tag{4.17}$$

On multiplication of both sides of eq. (4.17) by $\partial\phi_{\mathrm{c}}/\partial x$ and integrating

$$\int 2\varepsilon_{\mathrm{c}} G_{\mathrm{c}} k \frac{\partial \phi_{\mathrm{c}}}{\partial x} \frac{\partial^2 \phi_{\mathrm{c}}}{\partial x^2} \mathrm{d}x = \int \frac{G_{\mathrm{c}} k}{\varepsilon_{\mathrm{c}}} \frac{\partial w_{\mathrm{c}}(\phi_{\mathrm{c}})}{\partial \phi_{\mathrm{c}}} \frac{\partial \phi_{\mathrm{c}}}{\partial x} \mathrm{d}x \tag{4.18}$$

under the condition of vanishing gradient of the crack phase-field in the bulk of the solid phase, i.e. $\partial\phi_{\mathrm{c}}/\partial x = 0$ at $\phi_{\mathrm{c}} = 0$, results in

$$\underbrace{\varepsilon_{\mathrm{c}} G_{\mathrm{c}} k \left(\frac{\partial \phi_{\mathrm{c}}}{\partial x} \right)^2}_{\text{gradient energy density}} = \underbrace{\frac{G_{\mathrm{c}} k}{\varepsilon_{\mathrm{c}}} w_{\mathrm{c}}(\phi_{\mathrm{c}})}_{\text{potential energy density}} \quad . \tag{4.19}$$

Eq. (4.19), showcasing the equality between the potential and the gradient energy density at the equilibrium, represents the *Principle of equipartition of the energy*.

4.1.1.1 Crack interface properties at the thermodynamic equilibrium

On solving the ODE, i.e. eq. (4.19), with $w_{\mathrm{c}}(\phi_{\mathrm{c}}) = k_w \phi_{\mathrm{c}}^2$ under the boundary conditions $\partial\phi_{\mathrm{c}}/\partial x < 0$ and $\phi_{\mathrm{c}}(x = 0) = 1$, the equilibrium profile for the crack phase-field ϕ_{c} is obtained as

$$\phi_{\mathrm{c}}(x) = \exp\left[-\frac{\sqrt{k_w}}{\varepsilon_{\mathrm{c}}} |x| \right]. \tag{4.20}$$

Figure 4.2b depicts the spatial variation of the crack phase-field profile for different values of the length scale parameter ε_{c} for the crack phase. Irrespective of the chosen value of ε_{c}, the crack phase-field tends to zero when x tends to infinity in the positive and negative directions, thereby, implying an infinite crack interface width. However, with the increasing value of ε_{c}, the diffusiveness of the crack interface profile also increases, as illustrated in figure 4.2b. The magnitude of ϕ_{c} represents the extent of damage present at a spatial point x. At the thermodynamic equilibrium, utilizing eqs. (4.14) and (4.19), the expression for the interfacial energy $\gamma_{\mathcal{I}c}$ of the crack surface in 1-D is given by

$$\gamma_{\mathcal{I}c} = \int_{-\infty}^{+\infty} \left[G_{\mathrm{c}} k \left\{ \varepsilon_{\mathrm{c}} |\boldsymbol{\nabla}\phi_{\mathrm{c}}|^2 + \frac{1}{\varepsilon_{\mathrm{c}}} w_{\mathrm{c}}(\phi_{\mathrm{c}}) \right\} \right] \mathrm{d}x = \int_{-\infty}^{\infty} \frac{2 G_{\mathrm{c}} k}{\varepsilon_{\mathrm{c}}} w_{\mathrm{c}}(\phi_{\mathrm{c}}) \mathrm{d}x = \int_{-\infty}^{\infty} \frac{2 G_{\mathrm{c}} k}{\varepsilon_{\mathrm{c}}} k_w \phi_{\mathrm{c}}^2 \mathrm{d}x. \tag{4.21}$$

On plugging the expression for the crack phase-field profile (eq. (4.20)) in the above eq. (4.21) followed by definite integration over the whole interval in a piecewise manner, the interfacial energy of the crack surface reads

$$\gamma_{\mathcal{I}c} = 2G_{\mathrm{c}}k\sqrt{k_w}. \tag{4.22}$$

In order to fulfil the Griffith's criterion [140], the crack interfacial energy in eq. (4.22) should be equal to G_{c}. Griffith's criterion is fulfilled for the following relation between scalars k and k_w,

$$k\sqrt{k_w} = \frac{1}{2}. \tag{4.23}$$

For the present work, the values of scalars $k = 1/2$ and $k_w = 1$ are chosen.

Part III
Syntaxial overgrowth cementation in sedimentary rocks

Chapter 5

Fracture cementation in calcite limestone

Veins are crack-seal microstructures ubiquitously present in the sedimentary rocks, and consist of the fillings of crystallized minerals in the fracture spaces. Veins carry valuable information regarding the fracture opening, cement growth and fluid-flow histories. This chapter deals with the investigation of the formation of different crack-seal vein morphologies during syntaxial calcite cementation in bitaxial veins, using a multiphase-field (MPF) model. In particular, the influence of varying crack opening rates and initial crack aperture size is studied on the following: I) the growth competition between differently oriented calcite crystals on the crack surfaces and II) the resulting vein textures. Finally, the numerically obtained vein textures are compared with the natural calcite vein samples and the structural similarities are discussed.

The chapter is organized as follows. In section 5.1, the numerical aspects of modeling calcite cements, including the modeling assumptions, the numerical setup and the *geometric shift boundary condition*, are presented. The geometric shift boundary condition enables the incremental opening of fracture in the direction perpendicular to the crack surface at adjustable opening rates, during calcite cementation in the fracture space. In section 5.2, the simulation results providing insights on the formation mechanism and growth dynamics of various vein textures are presented. Finally, the chapter is concluded in section 5.3, by recapitulating the findings and highlights, along with a brief outlook on the future research directions based on this work.

5.1 Numerical aspects

For the present numerical investigation, the MPF model described in the chapter 3 is adapted. Section 5.1.1 outlines the modeling assumptions in the context of phase-field modeling of syntaxial calcite cementation. The procedure to adapt the MPF model is elaborated in section 5.1.2. The numerical setup and the algorithm of geometric shift boundary condition are elaborated in sections 5.1.3 and 5.1.4, respectively.

5.1.1 Modeling assumptions

Syntaxial calcite cementation is a highly coupled chemo-thermo-hydro-mechanical phenomenon. In order to constrain this complex process, the MPF model of chapter 3 is adapted under certain assumptions. The assumptions and their relevance in the computational modeling of this process are as follows:

1. Carbonate rocks are known to exhibit heterogeneity at the grain scale [178, 179]. In these rocks, a wide variety of substrates (e.g. crystalline calcite grains, limestone fragments, carbonate fossils and other minerals) can be found. These substrates serve as the deposition sites for cements precipitating from the circulating fluids. In the present work, it is assumed that the fracture surfaces only carry the seeds of crystalline calcite grains, upon which the calcite cement growth takes place epitaxially. The pore space is entirely filled with the formation fluid.

2. During long-range calcite cementation, the fluid supersaturation with respect to calcite may remain invariant when the formation fluids are continuously replenished from other sources [33]. The present work assumes a constant supersaturation and isothermal conditions, and thereby a constant driving force of crystallization at the solid-liquid interface ($\Delta f_{\mathrm{sl}}(\mathfrak{c}, T) = \Delta f_{\mathrm{sl}}$). This assumption is admissible when the solute attachment kinetics is significantly slower than diffusion and advection.

3. The crystal growth shapes result due to an interplay between the surface energy anisotropy and the direction-dependent growth kinetics, under the control of interfacial processes and long-range transport [180]. In the present work, a strong faceted-type anisotropy in the interfacial energy (i.e. capillary anisotropy) is chosen such that the crystal attains the rhombohedral geometry under surface energy minimization. In the absence of any reliable data on the particle attachment kinetics for calcite, the growth kinetics is chosen to be isotropic. This essentially implies that a crystal attains faceting according to the capillary anisotropy shape during the early stages of growth, and further grows while maintaining the shape due to isotropic growth kinetics.

4. The modeling considers the thermal conditions that are sufficiently below the recrystallization temperature of calcite when the grain boundaries remain immobile. Thus, the kinetic mobilities of the grain boundaries (i.e. $\mu_{\mathrm{ss}} = \tau_{\mathrm{ss}}^{-1}$) are chosen to be lower (by two orders in magnitude) than those of the solid-liquid interfaces (i.e. $\mu_{\mathrm{sl}} = \tau_{\mathrm{sl}}^{-1}$).

5.1.2 Modeling calcite cements in the multiphase-field framework

Calcite crystals are observed to exhibit over 800 different growth forms that include acute to obtuse rhombohedra, prisms, tabular, scalenohedral, among others [181]. The most common crystal forms are *rhombohedral* and *scalenohedral* [182]. Thus, the present work focusses on the syntaxial calcite cementation process that results in the formation and growth of rhombohedral crystals, see figure 5.1a for the crystal geometry. For modeling crystal growth such that the solid-liquid interface forms flat facets, sharp edges and pointed corners according to the rhombohedral geometry, a faceted-type anisotropy is incorporated in the interfacial energy using the piece-wise capillary anisotropy function given in eq. (3.4) of chapter 3. The present analysis is restricted to two dimensions (2-D). Therefore, three 2-D projections, namely asymmetric right-handed, symmetric and asymmetric left-handed, are derived, as illustrated in figure 5.1b. For the present work, the asymmetric left-handed projection is chosen so that the influence of asymmetricity of calcite crystals is accounted in the modeling. The chosen set of vertex vectors for the capillary anisotropy shape are

$$\boldsymbol{\eta}_{1,2} = [0, \pm 0.75] \quad \boldsymbol{\eta}_3 = [1, 0.25] = -\boldsymbol{\eta}_4.$$

Figure 5.1c depicts the simulated crystal shape using the above-mentioned set of vertex vectors, using the volume preservation algorithm [183]. In accordance with the assumptions 3 and 4 of section 5.1.1, disparate kinetic mobilities are assigned for the solid-solid and solid-liquid interfaces. The kinetic coefficient τ (eq. (3.7) in chapter 3) is formulated as [184]

$$\tau = \frac{\sum\limits_{\substack{\alpha,\beta=1 \\ (\alpha<\beta)}}^{N,N} \tau_{\alpha\beta}\phi_\alpha\phi_\beta}{\sum\limits_{\substack{\alpha,\beta=1 \\ (\alpha<\beta)}}^{N,N} \phi_\alpha\phi_\beta}. \tag{5.1}$$

The choice of $\tau_{\mathrm{ss}}/\tau_{\mathrm{sl}} = 100$ ensures that the grain boundaries remain immobile, and only the solid-liquid interfaces are in motion when a crystallization driving force is present. The set of phase-field parameters utilized in the present work are given in table 5.1.

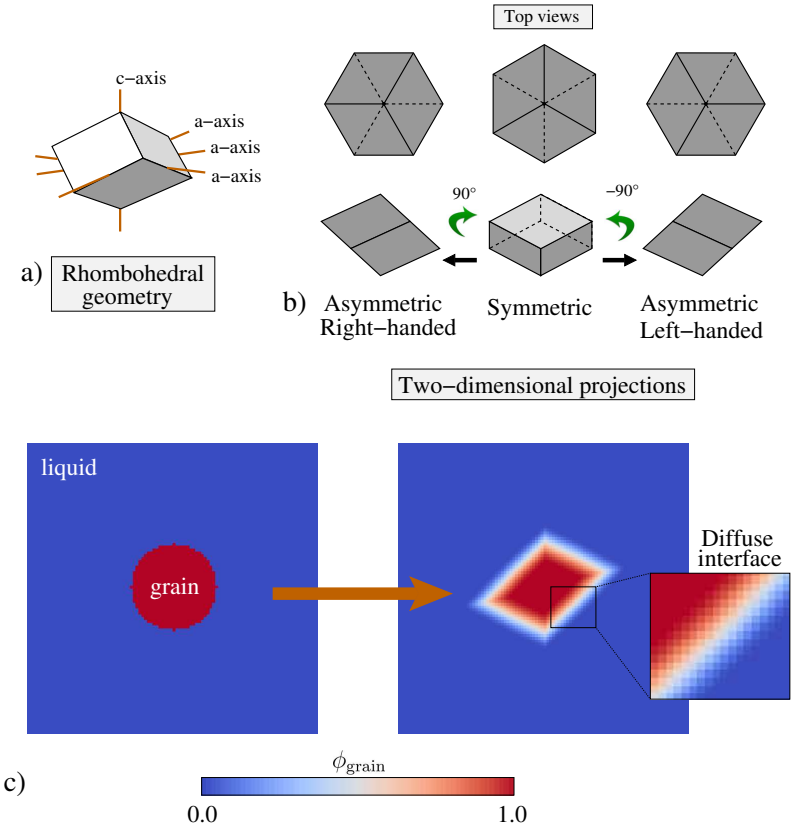

Figure 5.1: a) 3-D Rhombohedral geometry with one c-axis and three a-axes. b) Symmetric and asymmetric 2-D projections along with their top views. c) Validation of faceted-type interfacial energy anisotropy formulation for the chosen set of vertex vectors. A spherical grain embedded in liquid phase evolves to its equilibrium shape, while preserving its volume. At any given time, the location and shape of the grain is determined by the phase-field variable ϕ_{grain}, that varies from 0 in the liquid phase to 1 in the grain phase.

Table 5.1: Values of phase-field model parameters used in the simulations

Model parameters	Non-dimensional value
Grid size Δx	1
Time-step size Δt	0.07
Length scale parameter ε	6.5
Surface energy density $\gamma_{\alpha\beta}$, i.e. γ_{ss} and γ_{sl}	1
Higher order parameter $\gamma_{\alpha\beta\delta}$	10
Kinetic coefficient for solid-solid interface τ_{ss}	100
Kinetic coefficient for solid-liquid interface τ_{sl}	1
Crystallization driving force Δf_{sl}	-0.15

5.1.3 Numerical setup

We consider a 2-D computational domain of size $1000\Delta x \times 1000\Delta x$, filled with a grain structure (in RGB colors) and the so-called *barrier* phase (in grey), see figure 5.2a. The grain structure is generated using the voronoi diagram on the basis of a random set of points. The barrier is treated as an inert phase where the phase-field equations are not solved. A fracture is introduced in the first simulation time step, where the initial crack aperture is given as an input parameter. This results in the formation of two crack surfaces, each hosting the randomly oriented calcite grains, see figure 5.2b. The space between these surfaces is filled with a calcite-supersaturated formation fluid, which is illustrated in yellow color. The applied boundary conditions for the phase-fields are shown in figure 5.2c. The geometric shift boundary condition, which is applied on the lower crack surface, provides the opening increment for the lower crack surface, and is elaborated in section 5.1.4. The crystal orientations of different calcite seed crystals are determined by the orientation colomap shown in figure 5.2d.

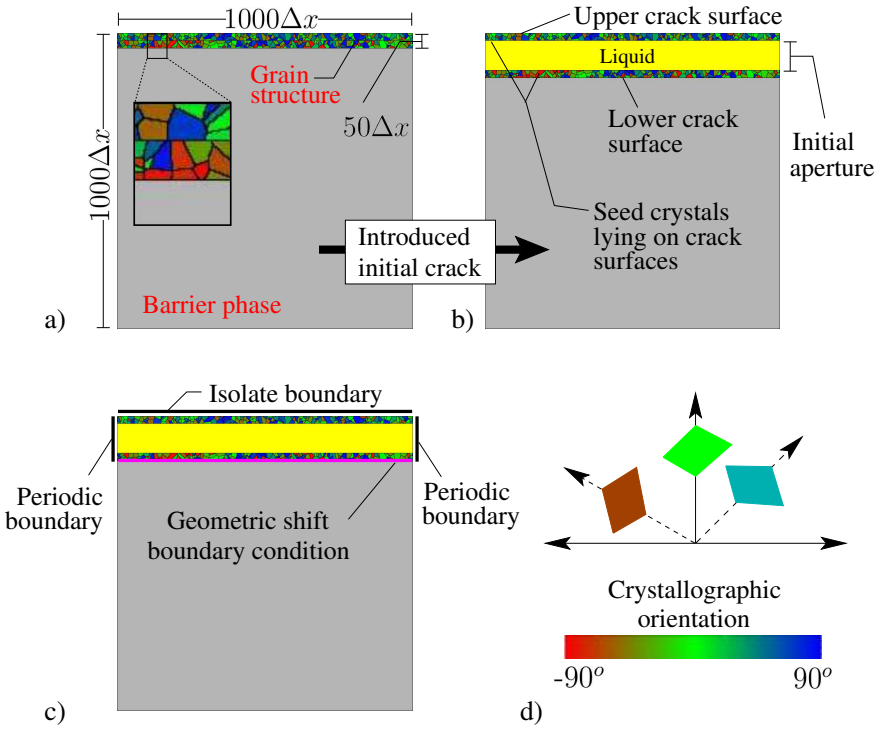

Figure 5.2: a) 2-D computational domain of the given size, filled with the calcite grain structure (in RGB colors) and an inert barrier phase (in grey color). b) A crack of a given aperture is initially introduced, and is filled with liquid phase (in yellow color). c) The boundary conditions applied on the edges of the domain. d) The colormap for identifying the crystallographic orientation of all the calcite seed crystals on the crack surfaces.

5.1.4 Geometric shift boundary condition

For the simulation of an incremental opening of a fracture, a geometric shift boundary condition was implemented. The algorithm shifts the grain phases lying on the lower crack surface by a given vertical displacement after a prescribed number of time steps, and fills the new empty space with the liquid phase. In the diffuse interface region, the phase fraction of liquid is assigned such that summation constraint ($\sum_{\alpha=1}^{N} \phi_\alpha = 1$) is sustained. In this shifting process, the barrier phase is continuously consumed. In the case of crystal bridging or a complete vein closure, the algorithm ensures that the fracture opens along the boundaries between the grains lying on the mutually opposite crack surfaces.

5.2 Results and discussions

The simulation results are presented in sections 5.2.1 and 5.2.2. In particular, the impact of different crack opening rates on the resulting vein textures and the time evolution of porosity during calcite cementation is investigated in section 5.2.1. In section 5.2.2, the influence of initial crack aperture on distinct fibrous vein textures is studied. Finally, the numerically obtained vein morphologies are qualitatively compared with the natural calcite vein samples in section 5.2.3.

5.2.1 Influence of crack opening rate

Utilizing the numerical setup of the computational domain described in section 5.1.3, several simulations were performed for different crack opening rates, while the driving force of crystallization was kept identical. In the physical sense, the crack opening rates can be interpreted as the relative frequency of the episodic crack opening and cement growth processes over geological time scales. the Three cases of the crack opening rates are analysed which are referred as slow, moderate and fast opening rates. An initial crack aperture, of about one order higher magnitude than the mean grain size of seed crystals, is introduced. The numerical values of the crack opening rates and the initial crack aperture are tabulated in table 5.2. All the simulations were performed until the barrier phase is completely disappeared as a result of the downward opening motion of the lower crack surface.

Table 5.2: Crack opening rates and the initial crack aperture for three different cases.

Cases	**Crack opening rate**	**Initial crack aperture**
Slow opening rate	$\Delta x/1000\Delta t$	$100\Delta x$
Moderate opening rate	$\Delta x/200\Delta t$	$100\Delta x$
Fast opening rate	$\Delta x/100\Delta t$	$100\Delta x$

5.2.1.1 Vein textures

The temporal evolution of the simulated vein microstructures for the three cases is analysed as follows:

- **Slow opening rate**: In this case, the applied crack opening rate is observed to be smaller than the minimum potential growth of calcite crystals. Different stages of vein growth are depicted in figure 5.3b-d. In the early stages, the presence of a large initial crack aperture for the free growth of crystals on both the surfaces, results in the occurrence of growth competition among the differently oriented calcite crystals, see figure 5.3b at $t = 1190$. Subsequently, at $t = 3850$ (figure 5.3c), the growing crystals fill the crack completely. This stage marks the suppression of growth competition, as the subsequent growth occurs such that almost all the crystals grow equally into the fracture space introduced during each opening increment (Δx). This increment-dependent growth results in the formation of the so-called *fibrous* vein texture (figure 5.3d), comprising of elongated crystals (or fibers) of nearly-constant width and the length parallel to the direction of crack opening displacement, see figure 5.3e.

- **Moderate opening rate**: In this case, the applied crack opening rate is observed to lie between the maximum and the minimum potential growth of calcite crystals. Figure 5.3f-h illustrates the different stages of vein growth. Due to the availability of sufficient pore space for a larger period of time as compared to the previous case, the growth competition amongst the crystals lying on the same crack surface is intense. It is worthy to mention that, as the aspect ratio of the calcite geometry is close to one, the fastest growing grains do not exhibit any preferred orientation. The growth of these grains is completely decided by their interactions with the neighbouring crystals. Since the competitive crystal growth proceeds on both surfaces, crystal bridges begin to form, as illustrated in figure 5.3f. Further growth is constrained by the crystals growing on the mutually opposite surfaces, leading to the formation of the so-called *partially-open* veins, as highlighted in figure 5.3g. At the final stages, when complete pore space is occluded by calcite cements, the resulting vein microstructures exhibit the well-known *elongate-blocky* textures, characterized by

the crystals with an increasing width along the length, as depicted in figure 5.3h,i.

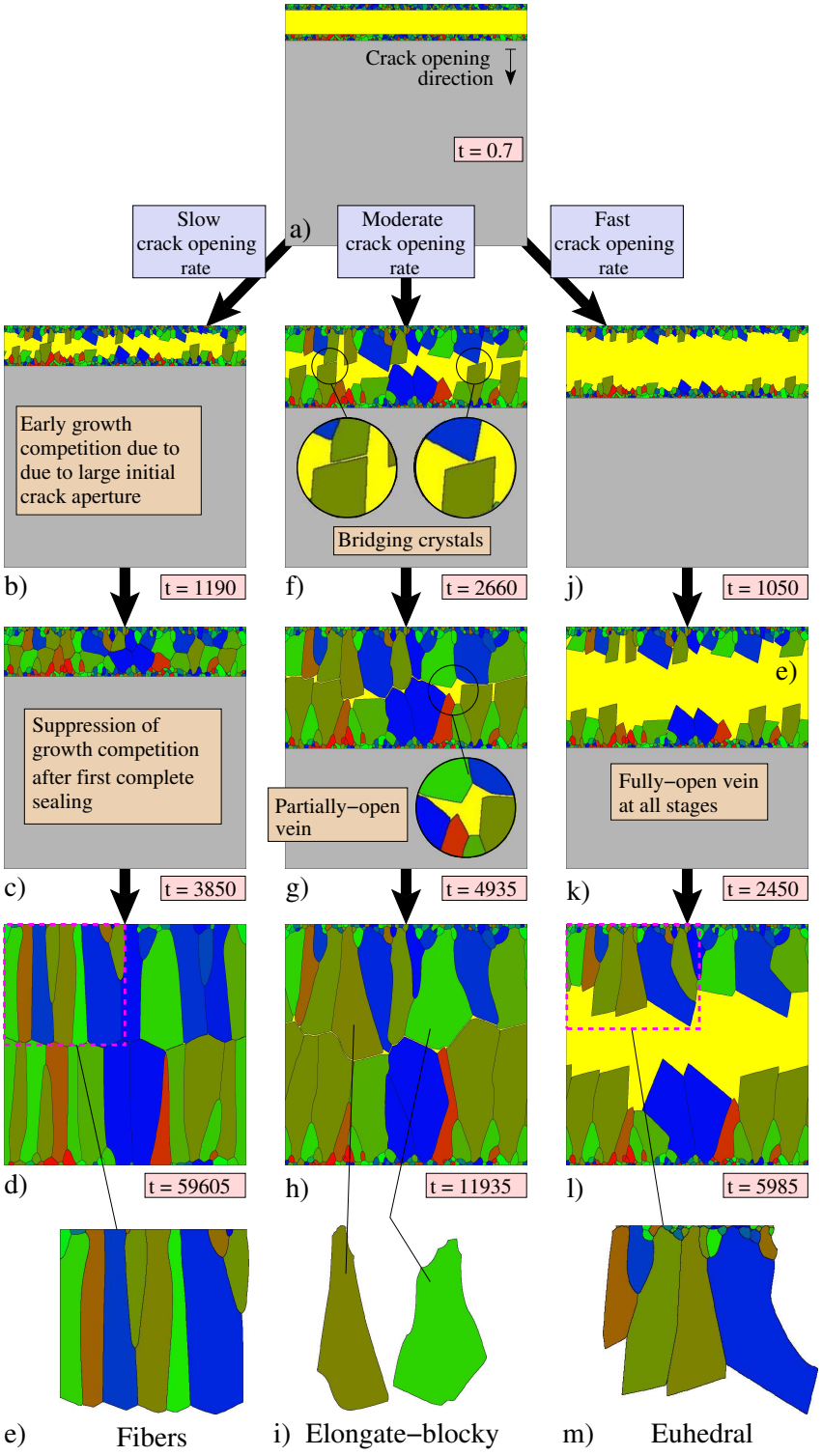

Figure 5.3: a) Simulation domain with a grain structure and an initial crack aperture of 100 Δx. Simulated bitaxial growth of crystals for b)-e) slow ($\Delta x/1000\Delta t$), f)-i) moderate ($\Delta x/200\Delta t$) and j)-m) fast opening rates ($\Delta x/100\Delta t$).

- **Fast opening rate**: In this case, the crack opening rate is larger compared to the maximum potential growth of calcite crystals. Figure 5.3j-l depicts the different stages of growth for one such case. Similar to the former cases, the initial growth competition is present in this case. However, as the crystal bridging cannot occur, the veins remain open at all stages of growth. This results in the appearance of well-developed *euhedral* crystals, characterized by straight edges and sharp corners in the pore spaces, as shown in figure 5.3l,m. The simulated texture exhibit structural similarities with the rind morphologies described in the work of Lander & Laubach [83].

5.2.1.2 Porosity evolution

The phase-field simulations, in addition to elucidating the processes controlling the formation of different vein morphologies based on the considered growth conditions, can further be utilized to speculate the histories and future evolution of fracture porosities, for different opening rates. In this section, we analyse the temporal evolution of porosity for the simulations presented in section 5.2.1.1. An additional simulation corresponding to the crack opening rate of $\Delta x/50\Delta t$ with the same initial crack aperture (i.e. $100\Delta x$) was performed resulting in euhedral vein textures, as expected. The porosity evolution for this simulation is also analysed under the case of fast opening rate. The colored solid lines in figure 5.4 depict the temporal evolution of porosity for different crack opening rates. The dash-dotted plots correspond to the porosity evolution in the absence of crystal growth, and are linear according to the constant crack opening rates. The initial and final stages of simulation are illustrated for all the cases. We analyse each case one-by-one as follows:

- **Slow opening rate** (crack opening rate = $\Delta x/1000\Delta t$): The temporal evolution of porosity exhibits a monotonically decreasing behavior. The early growth competition due to the presence of a large initial crack aperture leads to the slow initial decrease of porosity. After the first complete sealing, somewhere near $t = 3850$ (simulation stage illustrated in figure 5.3c), the opening increment (Δx) of crack takes place along the grain boundaries of the crystals lying on the opposite surfaces. The subsequent porosity evolution is dependent upon the opening increment. As a result periodic oscillatory behavior is exhibited by the porosity-time curve, owing to the occurrence of alternative events of crack-opening and vein-sealing, depicted in the zoomed inset image of figure 5.4.

- **Moderate opening rate** (crack opening rate = $\Delta x/200\Delta t$): In the early stages, the porosity increases monotonically with time due to a higher crack opening rate

in comparison with the previous case. The initial growth competition leads to the occlusion of unfavorably oriented crystals. Subsequent growth of the remaining grains with a higher growth potential results in an increase in the overall crystal growth rates. Thus, the porosity-time curve attains a maximum (at around $t = 1225$, highlighted in figure 5.43), eventually exhibiting a monotonically decreasing behavior. In comparison with the previous case, the first complete crack sealing (when the porosity drops to zero) occurs at a later stage in this case, due to a higher opening rate.

- **Fast opening rate** (crack opening rate = $\Delta x/100\Delta t$ and $\Delta x/50\Delta t$): The temporal evolution of fracture porosity exhibits a monotonically increasing behavior with respect to time. With further increase in the crack opening rates (e.g for the case of $\Delta x/50\Delta t$), the porosity-time plot becomes steeper. It is worthy to mention that the upper bound for the porosity-time plot is defined by the dash-dotted lines (when no crystal growth occurs) of figure 5.4. Thus, the porosity-time curves in these cases, although exhibiting a monotonically increasing pattern, remain concave with respect to time.

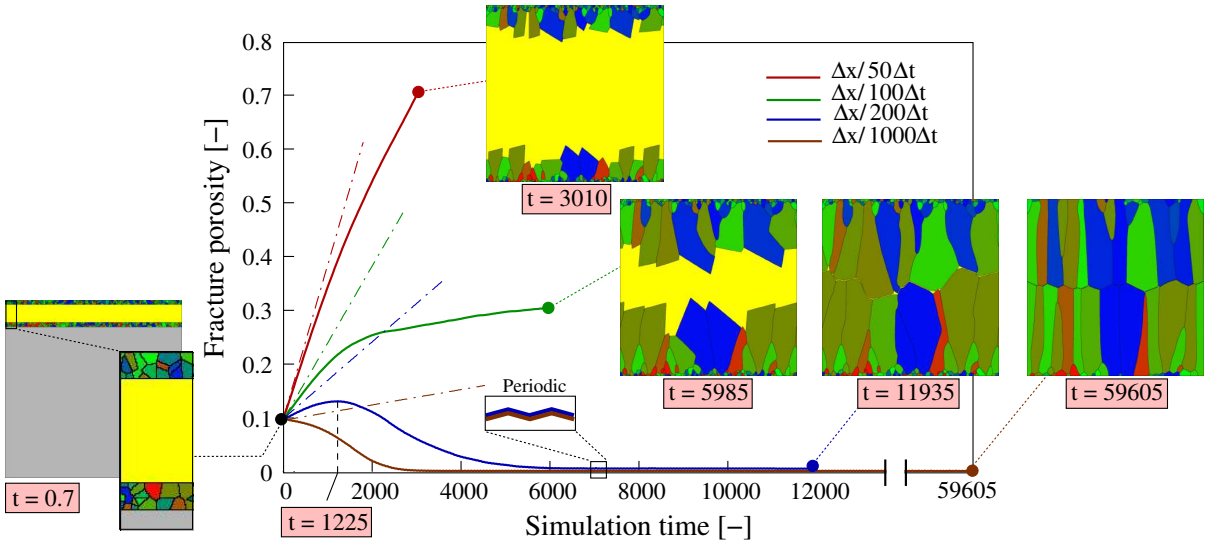

Figure 5.4: Plots of fracture porosity over simulation time for different crack opening rates. Linear dash-dotted lines, shown in same color as the solid lines, describe the fracture porosity evolution in the absence of crystal growth. The inset pictures illustrate the simulated crystal growth at initial and final stages for each case.

5.2.2 Influence of initial crack aperture

The case of slow crack opening rate presented in section 5.2.1 indicates that slow opening rate suppresses the growth competition after vein sealing, leading to the formation of

Table 5.3: Initial crack aperture and the crack opening rates for the simulations.

Cases	Crack opening rate	Initial crack aperture
Small crack aperture	$\Delta x/1000\Delta t$	$5\Delta x$
Large crack aperture	$\Delta x/1000\Delta t$	$100\Delta x$

fibrous veins. However, the presence of an initial large crack aperture (with magnitude one order higher than the grain size) facilitates the growth competition among the crystals, and thereby, the occlusion of unfavorably oriented grains. In this section, for decoupling the impact of the initial crack aperture on the resulting fibrous textures during slow opening rates, the following two cases are considered: I) small and II) large initial crack apertures, with the numerical parameters given in table 5.3.

- **Small crack aperture**: In this case, the width of the open fracture space is of the

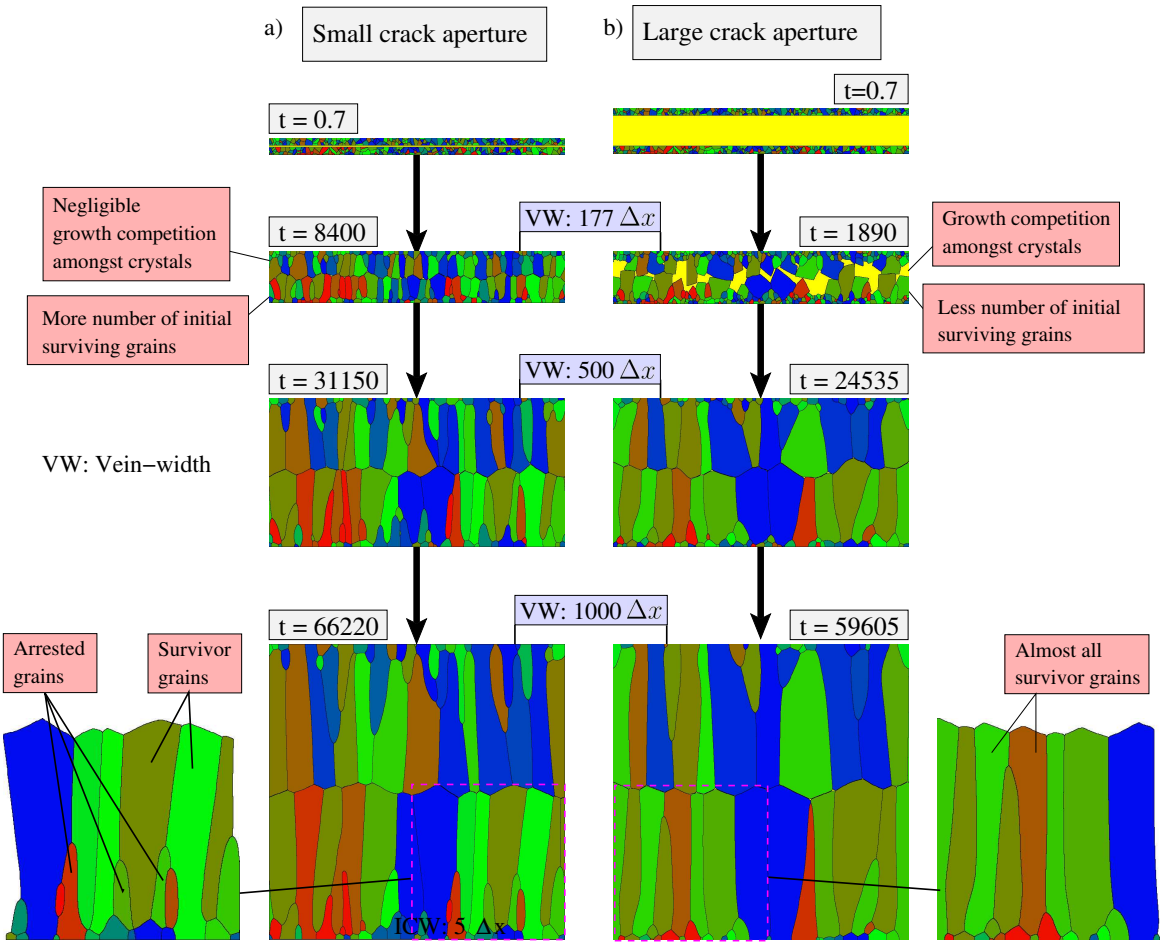

Figure 5.5: Different stages of the simulated bitaxial calcite cementation for a) small crack aperture (=5Δx) and b) large crack aperture (100Δx). The progression is shown at representative vein-width (VW).

same order as the mean grain size. Thus, the suppression of growth competition occurs in the early stages itself, leading to the growth of a large fraction of the initial grains, as depicted in figure 5.5a at $t = 8400$. As the cementation progresses, the occlusion of less favorably oriented crystals occurs gradually, resulting in the formation of so-called *arrested* fibers, at $t = 31150$ in figure 5.5a. The resulting vein at $t = 66220$ exhibits *non-uniform fibrous* morphology, comprising of *arrested* and *survivor* fibres of different lengths.

- **Large crack aperture**: As the magnitude of initial crack aperture in this case is one order larger than the mean grain size, the initial growth competition occurs, resulting in the occlusion of a higher number of less favorably oriented crystals in the very beginning, see figure 5.5b at $t = 1890$. The remaining favorably oriented *survivor* grains, shown in figure 5.5b at $t = 24535$, experience relatively less competition for growth. This results in the formation of *uniform fibrous* vein textures, comprising of almost all non-occluded fibers of nearly same length.

Figure 5.6a shows the plot of fracture porosity over time for the two cases. For the case of small crack aperture, the crystal growth becomes dependent upon the opening increment in the very beginning. As a result, the porosity-time curve begins to exhibit a periodic behavior at an earlier stage as compared to the case of large crack aperture. Figure 5.6b depicts the plot of number of survivor grains over vein-width. It is observed that, for the case of large crack aperture, a lower number of survivor grains are present at an initial stage (vein width = 200 Δx) as compared to the small crack aperture, due to the occurrence of an early growth competition in the former. For the case of large crack aperture, as a higher number of unfavorably oriented grains are already occluded, the subsequent reduction in the number of survivor grains is less steep, when compared with the case of small crack aperture. It is worthy to mention that, at later stages, the number of survivor grains is similar for both the cases. To this end, it is deduced that, while slow crack opening rates is a mandatory condition for the formation of fibrous vein morphologies, the presence of uniform vein fibers is indicative of the presence of large crack apertures in the early growth stages. Similarly, the occurrence of fibers of different lengths indicate that the crack apertures are small during all the stages.

5.2.3 Comparison of simulated vein textures with natural samples

Naturally occurring calcite veins exhibit a wide variety of textures that can be directly linked with the simulated microstructures. Figure 5.7 demonstrate the resemblance of the simulated vein textures with four different natural calcite vein samples from the

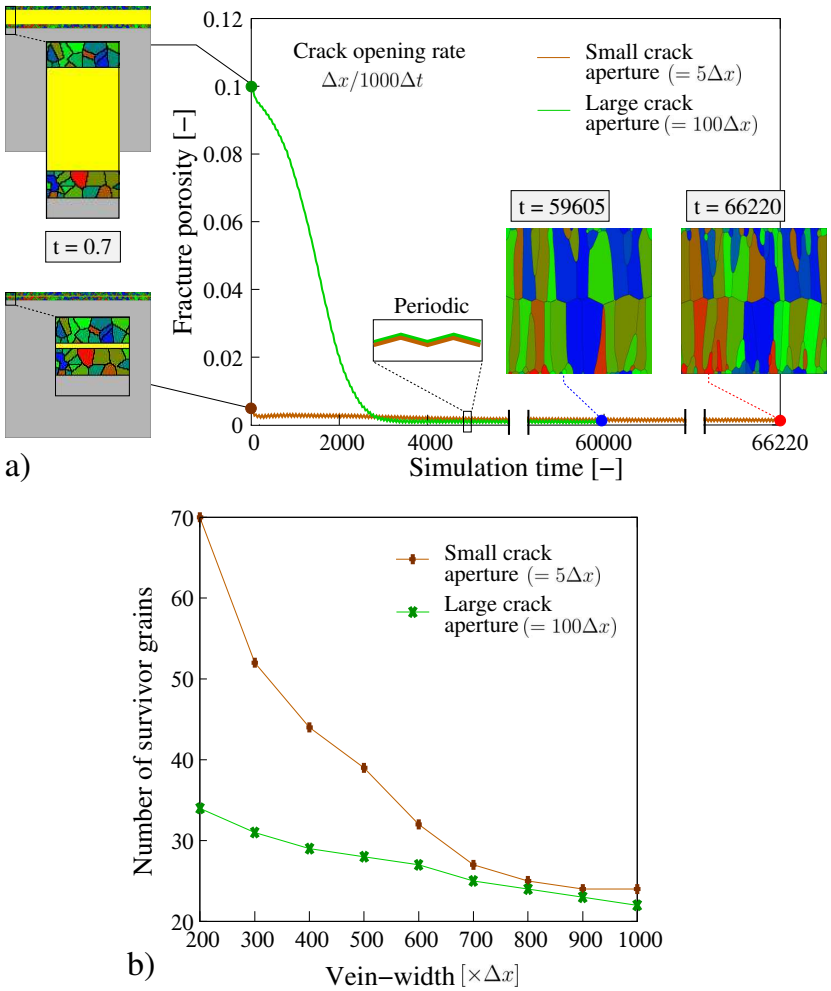

Figure 5.6: a) Plots of fracture porosity over simulation time for different initial crack apertures. The initial and final vein textures are illustrated in the inset pictures. b) Plots of the number of survivor grains as a function of the vein-width for different initial crack apertures.

Jurassic limestones of southern England. The microphotographs of the natural samples (shown in figure 2.4 in chapter 2) and their sketches in figure 5.7 were provided by Dr. Benjamin Busch and Prof. Christoph Hilgers from the Institute of Applied Geosciences (AGW-SGT) at the Karlsruhe Institute of Technology. The euhedral vein morphology, exhibiting straight edges in the pore spaces, shows a good match between natural and simulated examples. Further, the growth competition, as indicated by the occluded grains near the host rock, is also recovered by the simulations. The partially-open vein microstructure, formed during an intermediate stage of the simulation with the moderate crack-opening rate, exhibits clear similarities with the respective natural sample. These similarities include I) the competitive growth fabric near the host rock, II) irregular grain boundary contacts between the bitaxial growth of crystals on opposite crack surfaces and III) occasional open spaces with the possibility of euhedral facets, as depicted in figure 5.7b. The simulated elongate-blocky texture at the final stages of the moderate

opening rates, characterized by crystals with increasing width towards the pore, matches well with the corresponding natural example, see figure 5.7c. The simulated non-uniform fibrous crystals, under slow opening rates and small initial crack aperture, also show good agreement with the morphologies observed in natural fibrous vein textures, as depicted in figure 5.7d.

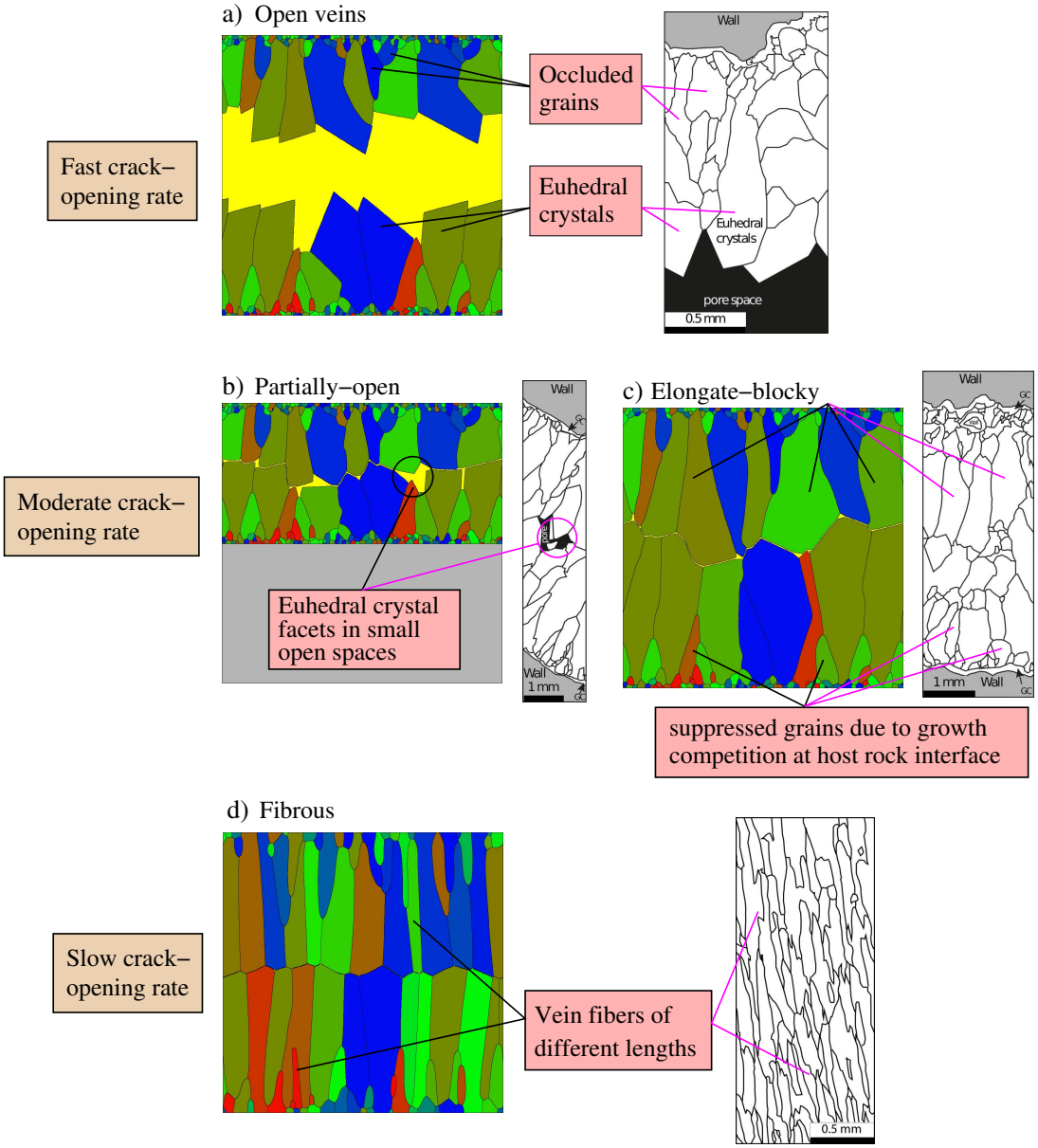

Figure 5.7: Comparison of different vein textures obtained in the simulations with natural calcite vein morphologies. The sketches illustrated in grey scale are drawn from the thin-section images of the calcite vein samples of Jurassic limestones from southern England, depicted in figure 2.4.

5.3 Concluding remarks

In the recent years, several phase-field investigations have been conducted for the study of quartz cementation process in sandstones (e.g. [15, 17, 18]). The present study is amongst the first works, demonstrating the application of phase-field method in modeling calcite cementation in limestones. Motivated from the earlier works of Bons [7] and Hilgers et al. [79], the present study further adds to their analysis. The phase-field simulations are able to recreate four important vein textures (i.e. euhedral, partially-open, elongate-blocky and fibrous) that are extensively observed in the naturally occurring calcite veins, while elucidating their growth dynamics and some of the boundary conditions that can lead to their formation. In addition, the present study sheds light on the mechanisms of formation of uniform and non-uniform fibrous vein textures depending upon the initial crack apertures. All the simulated vein morphologies presented in this work show clear similarities with the natural samples. With the aid of innovative post-processing techniques, the present model allows to speculate the temporal evolution of fracture porosity. In the presented examples, although a continuous crack opening is simulated, it is remarked that the geometric shift boundary condition, in its current form, is capable of simulating the intermittent and episodic opening of fractures normal to crack surfaces. The geometric shift boundary condition can be extended to simulate the shear opening of fractures and other complex curved opening trajectories. Therefore, this work paves the way for the exploration of different vein formation mechanisms depending upon the possible range of boundary conditions. The present work is restricted to 2-D. However, as the phase-field approach doesnot require explicit tracking of interfaces, the model extension to 3-D is fairly straight-forward, albeit with additional computational expenditure. With extensions to 3-D, the simulated vein morphologies can be further utilized to study the flow behavior through the analysis of the evolving physical properties (e.g. permeability, tortuosity, pore size distributions). The model and the proposed extensions, can also potentially assist in the the design and analysis of engineered geothermal energy systems.

Chapter 6

Pore space cementation in quartz sandstone

In the present chapter, the dynamics of syntaxial quartz cementation in sandstones from the supersaturated siliceous formation fluids is investigated using a multiphase-field model MPF. First, a two-dimensional (2-D) euhedral shape of quartz is derived from the three-dimensional geometry (3-D). Thereafter, 2-D unitaxial growth of quartz in open geological fractures is simulated for assessing the impact of misorientations and the crystal c- to a-axis ratio (c/a) in the formation of *bridge* morphologies that are extensively observed in nature. On the basis of this sensitivity analysis and taking into consideration the previous experimental findings, a realistic value of c/a was chosen for simulating the syntaxial growth of quartz cements in the intergranular pore spaces of sandstones in 3-D. Under identical growth conditions, several simulations were performed for different-sized grain packs. The simulated microstructures were qualitatively compared with the thin-section microphotographs of natural sandstone samples. Thereafter, the generated numerical data sets in the simulations were post-processed for analysing the impact of grain size of quartz aggregates on the evolution of porosity, permeability and pore size distributions and their dynamic correlations in comparison with the existing literature.

This chapter is organized as follows. Section 6.1 presents the numerical aspects of modeling syntaxial quartz cements along with a procedure for the generation of 3-D grain packs of different grain sizes. In section 6.2, the simulation results of quartz cementation and their discussions are presented. The chapter is concluded in section 6.3, by recapitulating the findings and insights derived from this numerical analysis.

6.1 Numerical aspects

For the present numerical investigation, the MPF model discussed in the chapter 3 is adapted for simulating syntaxial quartz cementation. Section 6.1.1 outlines the procedure to adapt the MPF model, along with the considered growth conditions. In section 6.1.2, the preprocessing algorithm for the generation of different-sized digital grain packs, analogous to sandstones, is elaborated.

6.1.1 Modeling quartz cements in the multiphase-field framework

Depending upon the physical and geochemical conditions, quartz can exhibit a wide variety of growth habits (e.g. Muzo, Trigonal, Hexagonal, Maderan, Cumberland, Needle), see The Quartz Page [185] for example. In the present work, the *Maderan* crystal habit, also called *Prismatic* or *Normal* habit, is considered as it is one of the most common morphologies observed in nature [38, 39]. Figure 6.1a depicts the 3-D geometry of the prismatic habit possessing the so-called r $\{01\bar{1}1\}$, z $\{1\bar{1}01\}$ and m $\{10\bar{1}0\}$ facets. The following three 2-D projections are derived for the 2-D investigations: asymmetric left-handed, symmetric, and asymmetric right-handed, as shown in figure 6.1b. In the context of phase-field method, in order to model the interfaces that form flat facets, sharp edges and pointed corners, we assume a faceted-type anisotropy in the interfacial energy using the formulations given in eq. (3.4) of chapter 3. Figure 6.1c depicts the simulated Asymmetric right-handed 2-D shape, using the volume preservation technique [183]. Similar to calcite cementation modeling formulation of chapter 5, an isotropic growth kinetics is assumed in the present work by choosing a constant value of the inverse mobilities of the solid-liquid interfaces τ_{sl}. The value of solid-solid interfacial inverse mobility is chosen according to $\tau_{\mathrm{ss}} = 100\tau_{\mathrm{sl}}$, such that the grain boundaries remain rigid. The inverse mobilities are interpolated according to the formulation in eq. (5.1) of chapter 5. The chosen set of phase-field parameters in the present study are given in table 6.1. The parameters utilized in the fluid-flow simulations, for the computation of permeabilities, are also given in table 6.1. The set of vertex vectors for the 2-D and 3-D euhedral shape, that were chosen based on the sensitivity analysis presented in section 6.2.1, are given in sections 6.2.1 and 6.2.2, respectively.

6.1.2 Generation of 3-D grain packs

A 3-D *periodic distribution generator* tool [186] was developed to generate a distribution of spherical grains of a given radius in a 3-D computational domain of any size. The

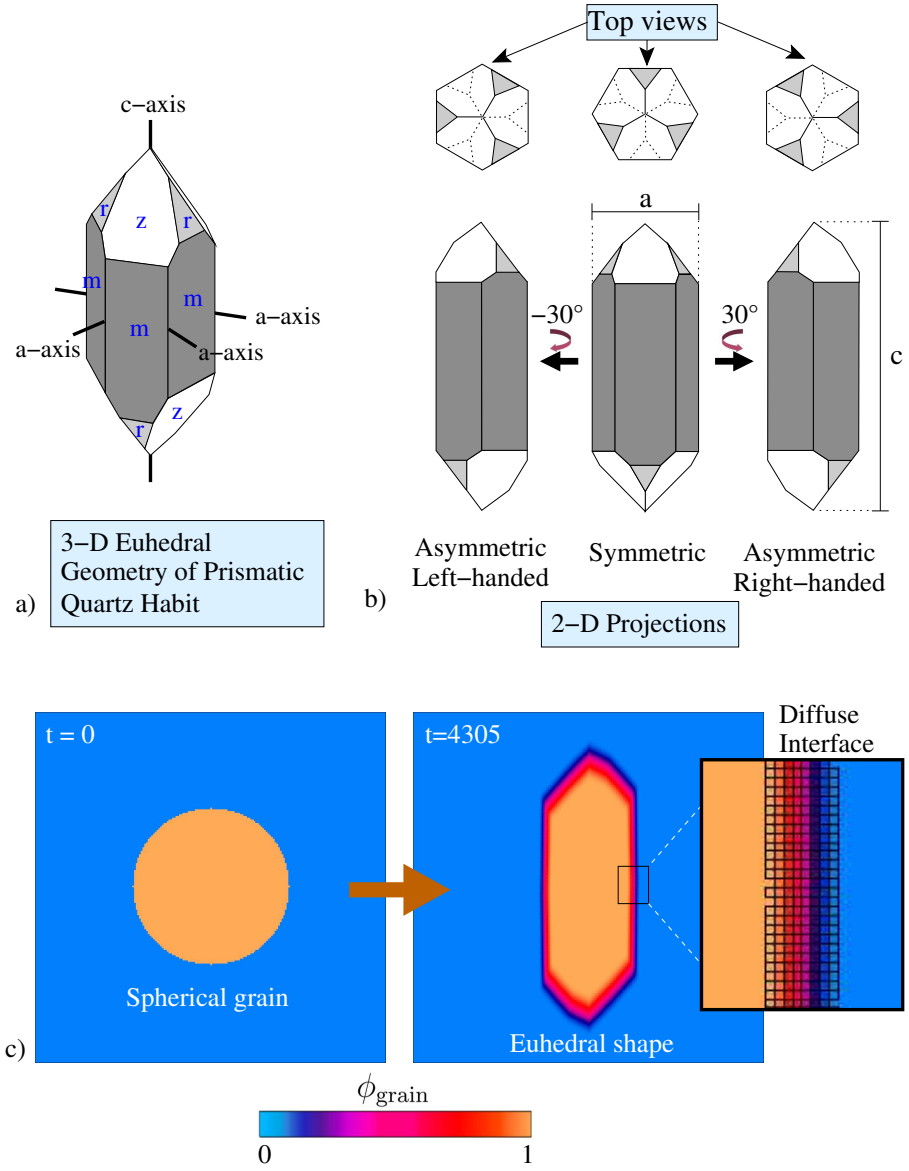

Figure 6.1: a) 3-D Euhedral shape of the prismatic growth habit of quartz. The different families of facets, i.e. z-, r- and m- facets, are shown in different shades of grey. b) Schematics illustrating the procedure of deriving the 2-D equilibrium shapes, i. e. Asymmetric left-handed, Symmetric and Asymmetric right-handed, from the 3-D geometry, for the 2-D simulations. c) Validation of the faceted-type interfacial energy anisotropy formulation. An initial spherical quartz grain (yellow) embedded in a liquid phase (navy blue), evolves to its euhedral shape (Asymmetric right-handed projection in this case) with diffuse interface, while preserving its volume. The grain phase-field ϕ_{grain} varies from 0 outside the grain to 1 inside the grain over a diffuse interface region.

tool generates the coordinates of the centre of spheres that represent quartz grains, using a random number generator. The spheres at the edges or corners of the domain are generated in a periodic manner such that the part of a grain lying outside of the domain

Table 6.1: Non-dimensional phase-field parameters and their dimensional values used in the simulations

Parameter	Symbol	Non-dim. value	Dim. value
Phase-field simulations			
Grid cell size	Δx	1.0	$1\mu m$
Time step size	Δt	0.07	$81s$
Length scale parameter	ε	6.5	$6.5\mu m$
Interface energy density	$\gamma_{\alpha\beta}$	1.0	$0.36 J/m^2$
Higher order parameter	$\gamma_{\alpha\beta\delta}$	10.0	$3.6 J/m^2$
Solid-liquid interfacial kinetic coefficient	τ_{sl}	1.0	$4.18 \times 10^{14} J\text{-}s/m^4$
Solid-solid interfacial kinetic coefficient	τ_{ss}	100.0	$4.18 \times 10^{16} J\text{-}s/m^4$
Driving force for crystallization	Δf_{sl}	-0.3	$-10^5 J/m^3$
Fluid-flow simulations			
Pressure drop	Δp	0.2	$8Pa$
Dynamic viscosity	μ	0.2	$0.0010026 Pa\text{-}s$

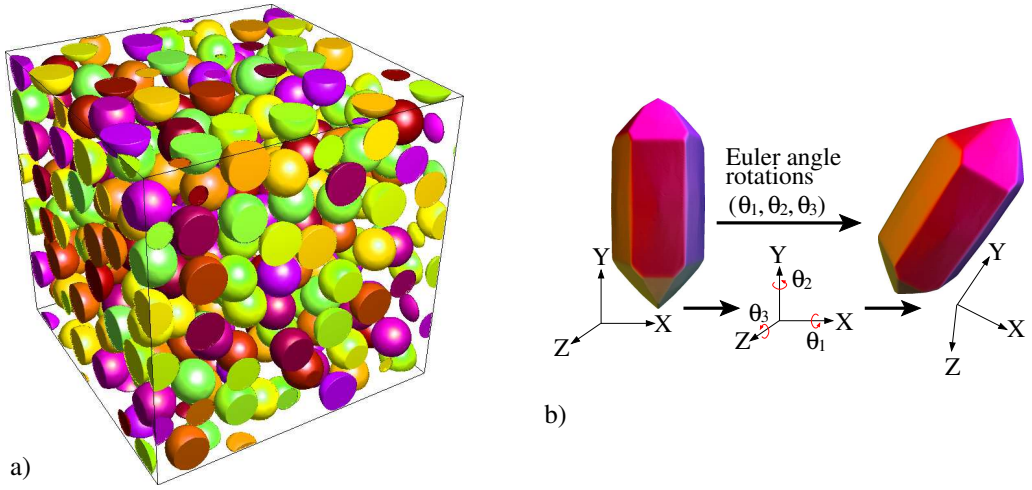

Figure 6.2: a) Cubic computational domain of size $300\Delta x \times 300\Delta x \times 300\Delta x$ consisting of 265 identical spherical grains of diameter $40\Delta x$. b) Schematics illustrating the Euler angle rotations of a quartz crystal for the assignment of a distinct crystallographic orientation to each grain in the domain.

appears on the opposite edges or corners of the domain. During the generation process, the spheres that overlap the already generated ones are filtered out. This process of generation and filtering out continues until there is no more possibility of inserting a new sphere in the computational domain. As a result, the numerical data set representing a distribution of touching (or nearly touching) spherical grains is obtained. Utilizing this tool, a 3-D grain pack comprising of 265 grains of grain size (or grain diameter) 40 Δx in a cubic domain of size $300\Delta x \times 300\Delta x \times 300\Delta x$ (Δx being the grid size) is generated, as shown in figure 6.2a. The remaining space of the domain is filled with the liquid phase that represents a supersaturated siliceous formation fluid. Each quartz grain in the pack is assigned a random crystallographic orientation that is defined by the Euler angle rotations (θ_1, θ_2, θ_3), as depicted in figure 6.2b. Moreover, based on this grain pack, four additional geometrically similar grain packs composed of grains with an initial grain size of $50\Delta x$, $60\Delta x$, $70\Delta x$ and $80\Delta x$ were generated, see figure 6.3. For maintaining an identical relative position of the grains in the grain packs for different grain sizes, the coordinates of centre of the spherical grains were scaled in proportion to the initial grain size. That is, if the coordinates of the centre of a spherical grain of diameter (or initial grain size) $d\Delta x$ in a grain pack of edge length $N\Delta x$ are (x, y, z), than for a grain pack with an edge length of $2N\Delta x$ and an initial grain size of $2d\Delta x$, the coordinates of the corresponding grain are ($2x$, $2y$, $2z$).

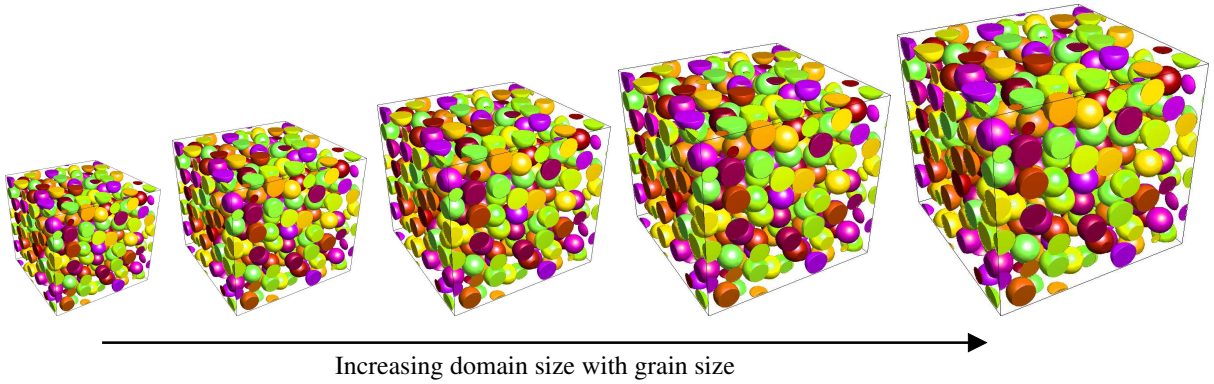

Figure 6.3: Five geometrically similar digital grain packs, each comprising of 265 grains, for different grain sizes. The crystallographic orientation of each grain G_n in all the digital grain packs is kept identical.

6.2 Results and discussions

This section is divided into two parts. The first part deals with the 2-D numerical studies of unitaxial quartz cement growth in an open fracture space, presented in section 6.2.1. The numerical setup for this study is described in subsection 6.2.1.1. The role of c- to a-

axis ratio of the equilibrium crystal shape of quartz, on the formation of quartz bridge structures during unitaxial growth in veins, is studied in subsection 6.2.1.2. Based on the numerical results obtained in this part, the 3-D geometrical parameters pertaining to the capillary anisotropy are chosen in the MPF model. In the second part of the results presented in section 6.2.2, the calibrated MPF model is employed to investigate syntaxial quartz overgrowth cementation in the intergranular pore spaces of sandstones. As a model test case, in subsection 6.2.2.1, the unrestricted growth of different-sized spherical crystals was simulated for analysing the model-predicted growth tendencies of quartz, in comparison with the existing literature. There after, in subsection 6.2.2.2, quartz cementation was simulated in a multigrain digital grain pack, analogous to sandstone, and the simulated crystal morphologies were qualitatively analysed in comparison with the thin-section microphotographs of natural samples, provided by Dr. Benjamin Busch and Prof. Christoph Hilgers from the Institute of Applied Geosciences (AGW-SGT) at the Karlsruhe Institute of Technology. Further, numerous simulations were performed in geometrically similar, but different-sized digital grain packs, for analysing the impact of initial grain size on the evolution of different rock properties. The impact of grain size on the porosity loss and sealing kinetics is discussed in subsection 6.2.2.3. The implications on the pore size statistics are elaborated in subsection 6.2.2.4. Finally, in subsection 6.2.2.5, a relationship between porosity and permeability is numerically established for different grain sizes, and analysed in comparison with the existing literature and a previously proposed empirical law.

6.2.1 Unitaxial quartz growth in open fractures in 2-D

Quartz bridge morphologies are extensively observed in the natural crack-seal veins [68], and have been discussed in the numerical investigations of [15, 17, 83]. With the aim of calibrating the capillary anisotropy shape in the phase-field model based on the crystal bridging tendency during unitaxial growth, 2-D simulations were performed for different values of the crystal c- to a-axis (c/a) ratio of the shape, hereafter denoted by the symbol $R_{\mathrm{c/a}}$. The vertex vectors for the 2-D simulations were chosen such that the internal angles of the equilibrium shape are preserved for different values of $R_{\mathrm{c/a}}$. The chosen set of vertex vectors in terms of $R_{\mathrm{c/a}}$ is tabulated in table 6.2.

6.2.1.1 Numerical setup

A 2-D computational domain of size $2500\Delta x \times 200\Delta x$ comprising of 50 randomly oriented spherical quartz grains lying on the lower edge was considered, see figure 6.4a. The colormap (figure 6.4b) describes the crystallographic orientation of each grain. The rest

Table 6.2: Set of vertex vectors for the 2-D right-handed euhedral shape of quartz as a function of the c- to a-axis ratio $R_{c/a}$.

Vertex	x	y
1	0.432	$0.5R_{\mathrm{c/a}} - 0.377$
2	0.187	$0.5R_{\mathrm{c/a}} - 0.094$
3	0.0	$0.5R_{\mathrm{c/a}}$
4	-0.432	$0.5R_{\mathrm{c/a}} - 0.475$
5	-0.432	$-0.5R_{\mathrm{c/a}} + 0.377$
6	-0.187	$-0.5R_{\mathrm{c/a}} + 0.094$
7	0.0	$-0.5R_{\mathrm{c/a}}$
8	0.432	$-0.5R_{\mathrm{c/a}} + 0.475$

of the space is filled with the liquid phase (in white color). The boundary conditions applied on the edges of the domain are illustrated in figure 6.4a. A *moving boundary condition* is applied at the upper edge of the domain, using a *boundary shifting* algorithm. This algorithm begins to add new horizontal layers of cells filled with the liquid phase on the top of the existing domain as soon as a growing crystal reaches the upper edge. As a result, the height of the 2-D domain increases with time. This algorithm provides

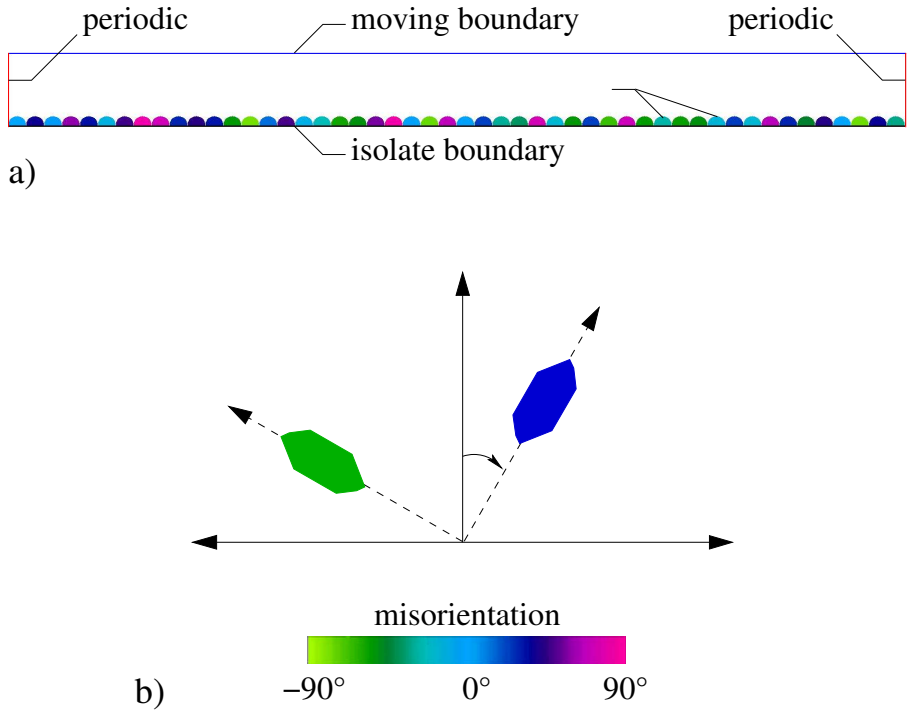

Figure 6.4: a) The computational domain filled with quartz grains (RGB colors) and liquid phase (white), along with the applied boundary conditions. b) Schematics and colormap determining the crystallographic orientation of the individual quartz grains in the domain.

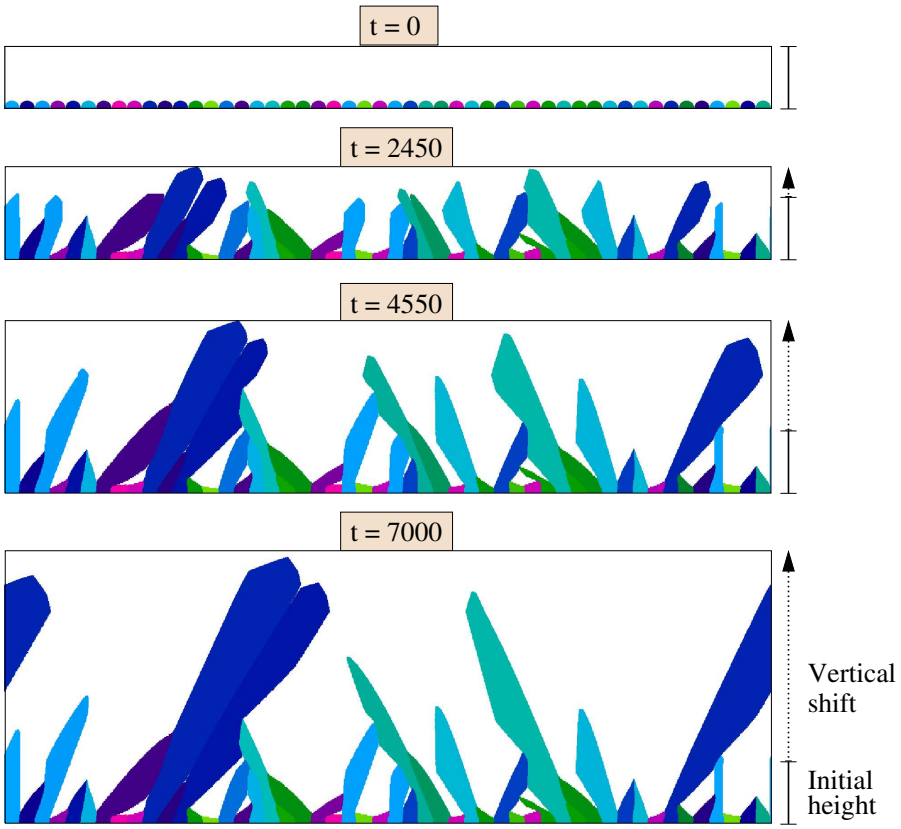

Figure 6.5: Simulated unitaxial quartz growth for $R_{c/a} = 3$. The progression is shown at representative growth stages. The moving boundary condition on the upper edge of the simulation domain leads to the vertical shift of the upper edge of the domain.

computational efficiency, as it allows to choose smaller initial domains and imparts the flexibility of increasing the dimensions of the domain based on the crystal growth. Using the phase-field simulation parameters provided in table 6.1 , simulations were performed for different values of the c/a ratio. Figure 6.5 depicts the different stages of unitaxial quartz growth for the case $R_{\mathrm{c/a}} = 3$, highlighting the temporal evolution of the domain height (= initial height + vertical shift) with the growth of crystals.

6.2.1.2 Impact of c- to a-axis ratio of the capillary shape of quartz

Figure 6.6a-f depicts the simulated unitaxial quartz growth for different values of the c/a ratio $R_{\mathrm{c/a}}$ after an equal amount of time $t = 7000$. The plot of domain height over $R_{\mathrm{c/a}}$ is shown in figure 6.7. When the c/a ratio is close to unity, a distinct crystal-liquid growth front is observed to evolve irrespective of the distinct crystallographic orientations of the grains, as highlighted in figure 6.6a. Moreover, in this case, the final height of domain (at $t = 7000$), which is directly proportional to the maximum vertical reach of the crystals and indicates the fracture spanning potential, is small. As $R_{\mathrm{c/a}}$ increases from 1.05 to

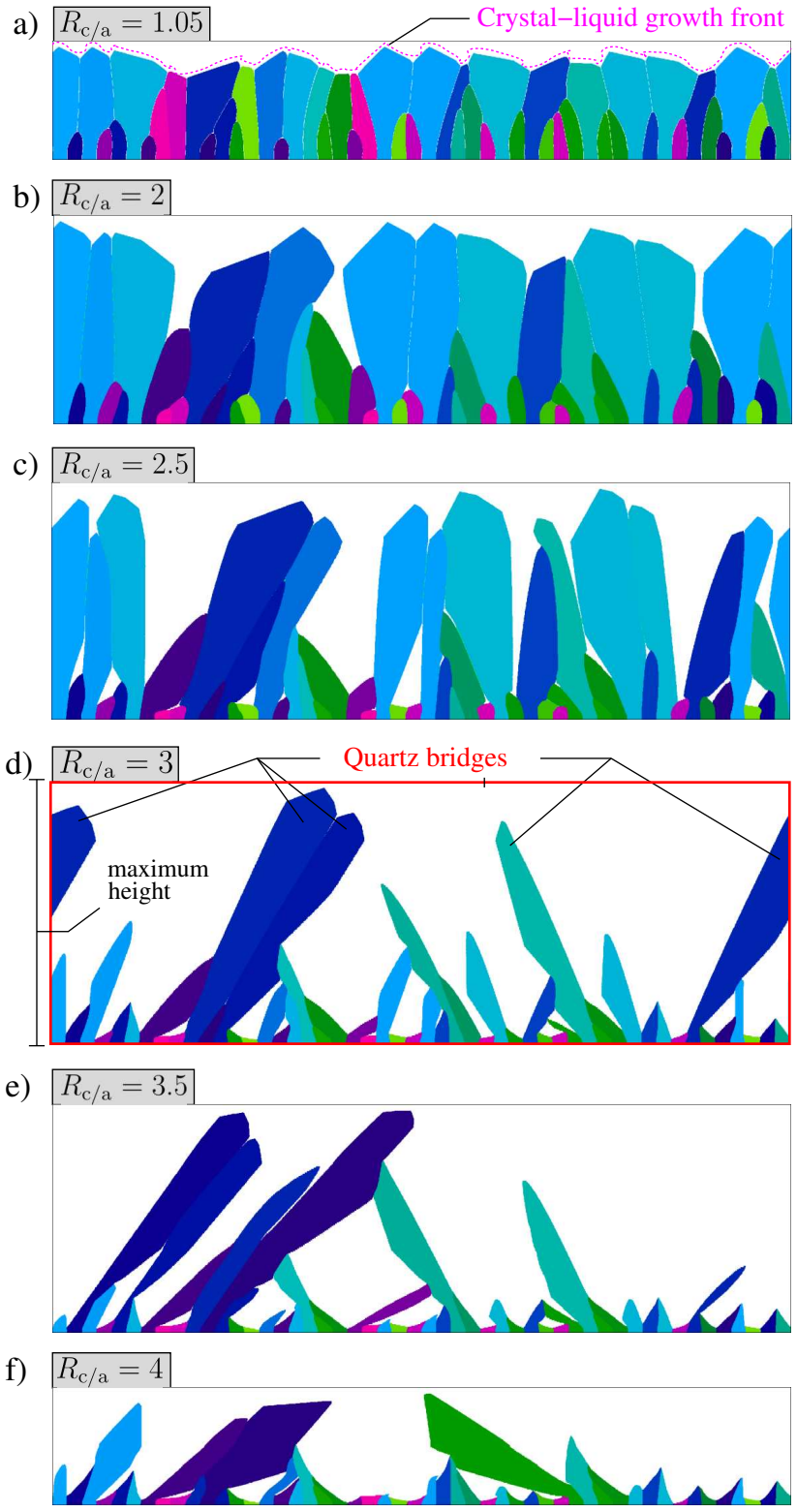

Figure 6.6: a)-f) Simulated unitaxial quartz growth at the time t = 7000 for different values of c/a ratios ($R_{c/a}$)

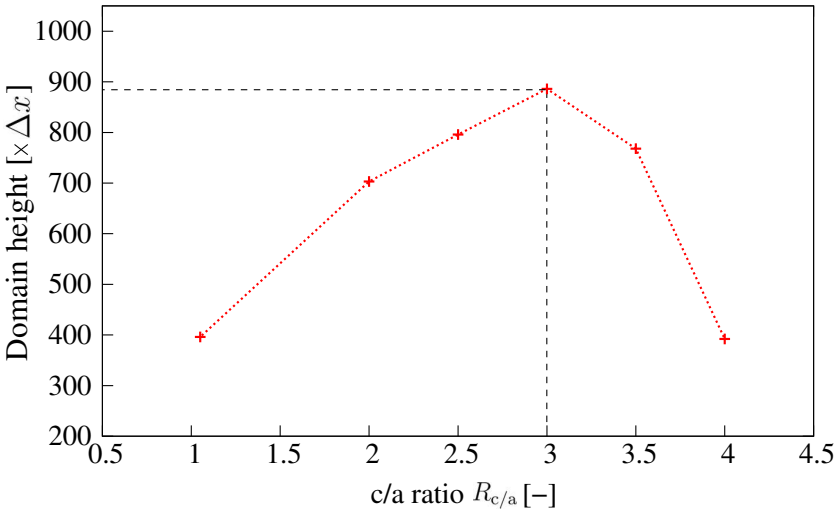

Figure 6.7: Plot of domain height [×Δx] over c/a ratio ($R_{c/a}$) for the simulations presented in subsection 6.2.1.2.

3.0, the following growth behavior is observed, see also figure 6.6a-d: I) the front forming tendency decreases due to the increasing growth competition between the neighbouring crystals and II) final height of the domain increases. At $R_{c/a} = 3$, the tendency of the surviving crystals to form the so-called *quartz bridges* (between the fracture space) is observed to be intense. Moreover, for this case, the height of domain attains a maximum, as highlighted in figure 6.6d. Further increasing the c/a ratio results in a reduction in the crystal bridging tendency as well as the domain height. Lander and Laubach [83], based on the hydrothermal experiments [36], reported the ratio of growth rates of quartz along the non-euhedral c- and a-axis growth surfaces of $1/0.31 \approx 3.2$. In a different set of hydrothermal experiments pertaining to the laboratory synthesis of quartz veins, Okamoto and Sekine [48] reported an average value of 2.9 for the aspect ratio of the well-grown quartz crystals that bridged the fracture, regardless of the grain size. The simulation results presented in this section provide a fair understanding of the role of crystal geometry on the bridging behavior in quartz. Further, on analysing the different stages of simulated growth for $R_{c/a} = 3$, as shown in figure 6.5, it is deduced that the growth competition causes the occlusion of grains with c-axis parallel to the crack surface (i.e. greenish and pinkish), while the survivor or bridging crystals are mostly subnormal to the crack surface (i.e. bluish). These results are in qualitative agreement with the petrographic investigation of natural samples [187] and laboratory-synthesized quartz veins [83], who suggested that the bridge forming crystals were those with c-axis orientation nearly perpendicular to the vein-wall. On the basis of these simulation results and their link with the previous experimental and field findings [36, 48, 83, 187], it is reasonable to choose the value of $R_{c/a} = 3$ for the modeling of syntaxial overgrowth quartz cementation in the intergranular pore spaces of sandstones.

6.2.2 Syntaxial quartz overgrowth cementation in sandstone

The 3-D simulation studies presented in this section are performed using the phase-field parameters listed in table 6.1. Based on the 2-D analysis of section 6.2.1.2, a c/a ratio of 3.0 is chosen for the 3-D capillary anisotropy shape. Figure 6.8 depicts the simulated capillary Wulff shape using the volume preservation technique [183], along with the anisotropy function plot illustrating the variation of the surface energy in different spatial directions. The set of vertex vectors used to generate the simulated shape and the surface energy plot are given in table 6.3.

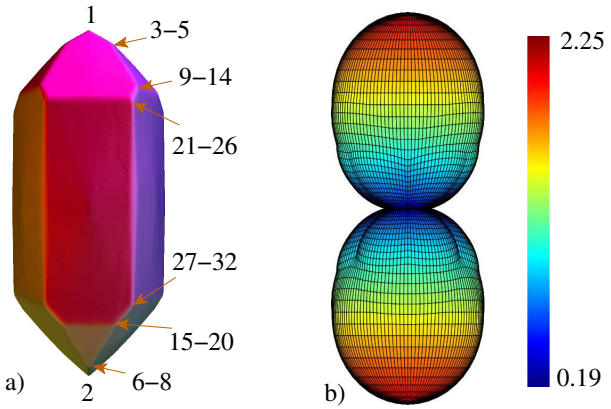

Figure 6.8: a) Simulated capillary Wulff shape of the prismatic habit of quartz using the volume preservation technique in 3-D. Different facets are depicted in different colors based on the surface normal direction, for the sake of visualization. b) The 3-D capillary anisotropy function plot in spherical coordinate system.

Vertex	x	y	z
1,2	0.000	0.000	±1.500
3,4	± 0.152	-0.088	1.389
5	0.000	0.175	1.389
6	0.000	-0.175	-1.389
7,8	± 0.152	0.088	-1.389
9,10	± 0.152	0.437	1.056
11, 12	± 0.455	-0.088	1.056
13,14	± 0.303	-0.350	1.056
15,16	± 0.152	-0.437	-1.056
17,18	± 0.455	0.088	-1.056
19, 20	± 0.303	0.350	-1.056
21, 22	± 0.505	0.000	0.944
23, 24	0.253	± 0.437	0.944
25, 26	-0.253	± 0.437	0.944
27, 28	± 0.505	0.000	-0.944
29, 30	0.253	± 0.437	-0.944
31, 32	-0.253	± 0.437	-0.944

Table 6.3: Chosen set of vertex vectors for the 3-D capillary Wulff shape of quartz with a c-to a-axis ratio $R_{c/a} = 3.0$.

6.2.2.1 Formation of crystal facets during unrestricted cement growth

Hydrothermal experiments [36] suggest that for a given initial grain shape, the rate of facet formation of quartz aggregates as a result of syntaxial quartz cementation is strongly dependent upon the grain size. Coarse grains attain their euhedral shape at a slower rate in comparison to the finer ones, as the overgrowth volume needed to achieve complete faceting is directly proportional to the initial grain size. As a model validation,

Table 6.4: Initial grain size (i.e. diameter) and domain size for the unrestricted single grain growth.

Case	Grain size	Domain size
fine	$40\Delta x$	$200\Delta x \times 200\Delta x \times 200\Delta x$
medium	$60\Delta x$	$300\Delta x \times 300\Delta x \times 300\Delta x$
coarse	$80\Delta x$	$400\Delta x \times 400\Delta x \times 400\Delta x$

simulations pertaining to undisturbed growth of single crystals were performed for three different-sized spherical grains. For the sake of convenience, these grains are referred as fine, medium and coarse. For the chosen grain size (or diameter) and domain size listed in the table 6.4, the initial volume fraction of liquid $\mathrm{F_{liquid}}$ in the computational domain remains the same in all the three cases. Figure 6.9 depicts the temporal evolution of liquid volume fraction for different cases. The initial ($t = 0$) and final ($t = 175$) stages of growth are presented as the inset pictures. The colormap at the final stage describes the curvature of the grain-liquid isosurface, numerically computed as $\kappa_{\mathrm{c}} = \nabla \cdot (\mathbf{q}_{\alpha\beta}/|\mathbf{q}_{\alpha\beta}|)$. It is observed that the fine grain has attained its euhedral form, as indicated by the sharp edges (reddish) and corners (yellowish), whereas the coarser ones have flattened edges and blunt corners (bluish) and require more time to reach the euhedral shape. With the increasing grain size, the rate of loss of liquid volume fraction decreases, as indicated in the plot of figure 6.9. These plots along with the simulation results essentially imply that finer grains attain their equilibrium shape more rapidly as compared to coarser ones, in qualitative agreement with previous experiments [36]. In the present phase-field simulations, the grains growth is governed by a crystallization driving force, that can be directly related to the fluid supersaturation. For the chosen value of the crystallization driving force (i.e. $\Delta f_{\mathrm{sl}} = -0.3$), the opposing model-inherent curvature-induced force [188] is significantly smaller. Therefore, the motion of interfaces in the direction of growth is nearly independent of the initial grain size for the considered growth condition and the size of aggregates. As the overgrowth volume and the distance from the initial interface location required to achieve the faceting is higher for coarser grains, they need more time to reach their euhedral shape.

6.2.2.2 Formation of crystal morphologies during restricted cement growth in multigrain systems

A 3-D computational domain of size $300\Delta x \times 300\Delta x \times 300\Delta x$ comprising of 265 spherical grains of diameter $40\Delta x$ each was considered, as shown in figure 6.2a. The domain was generated by utilizing the 3-D periodic distribution generator tool [186], described in section 6.1.2, such that the grains located on the faces, edges and corners of the domain

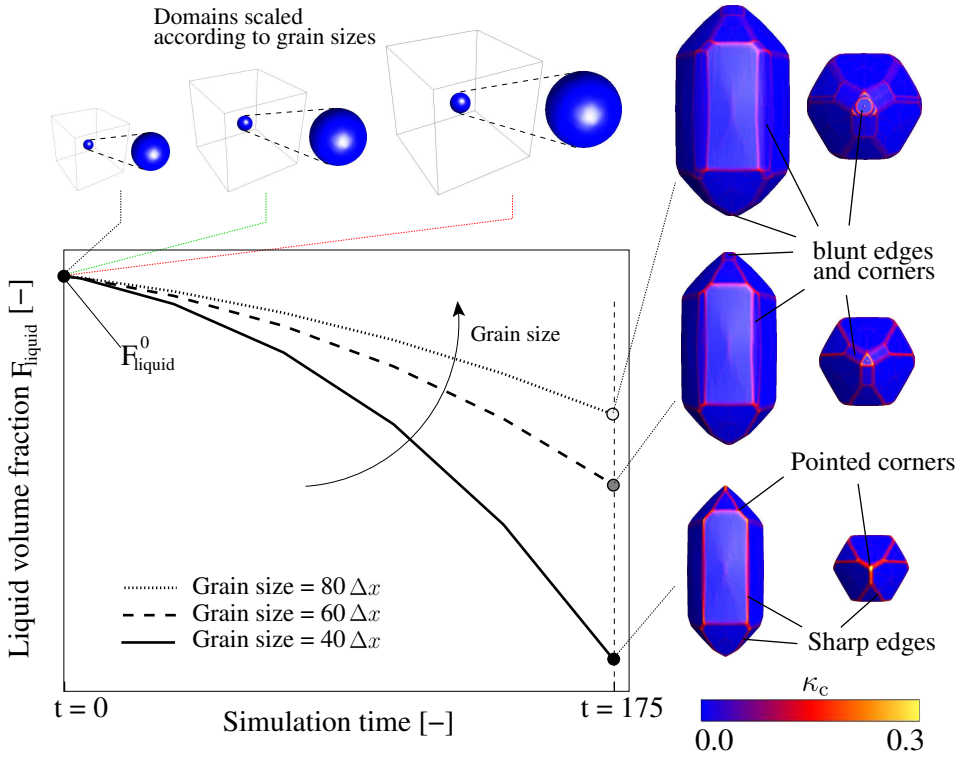

Figure 6.9: Temporal evolution of liquid volume fraction F_{liquid} for the simulated unrestricted quartz cement growth for spherical grains with different initial grain sizes. The inset pictures depict the initial and final grain geometries. The colormap describes the curvature κ_c of the interfaces, and thus determines the sharpness of corners and edges of the crystals. Fine grains, with flat facets, pointed corners and sharp edges, attain their euhedral shape faster when compared to coarser ones, as illustrated at $t = 175$.

exhibit periodicity. All the boundaries of the computational domain were rendered as periodic with respect to the phase-fields. Each grain was assigned a random crystallographic orientation, defined by the Euler angle rotations (θ_1, θ_2, θ_3), schematically illustrated in figure 6.2b. Syntaxial quartz cementation was simulated in this digital grain pack, using the phase-field simulation parameters given in table 6.1. Representative stages of the simulated growth (in BRY colors) and the pore space (in gray) are depicted in figure 6.10a,b. We analyze the simulated crystal morphologies along a central plane of the grain pack at two different stages, as shown in figure 6.10c. The intermediate stage exhibits clear microstructural similarities with the natural sandstone sample from north England in terms of crystal morphologies and the remaining pore space, as highlighted in figure 6.10c at t=245. In particular, the following three characteristic similarities are drawn:

1. Well-developed facets (pyramidal and prismatic) according to the euhedral shape of quartz are formed when sufficient pore space is present for the syntaxial growth of cements.

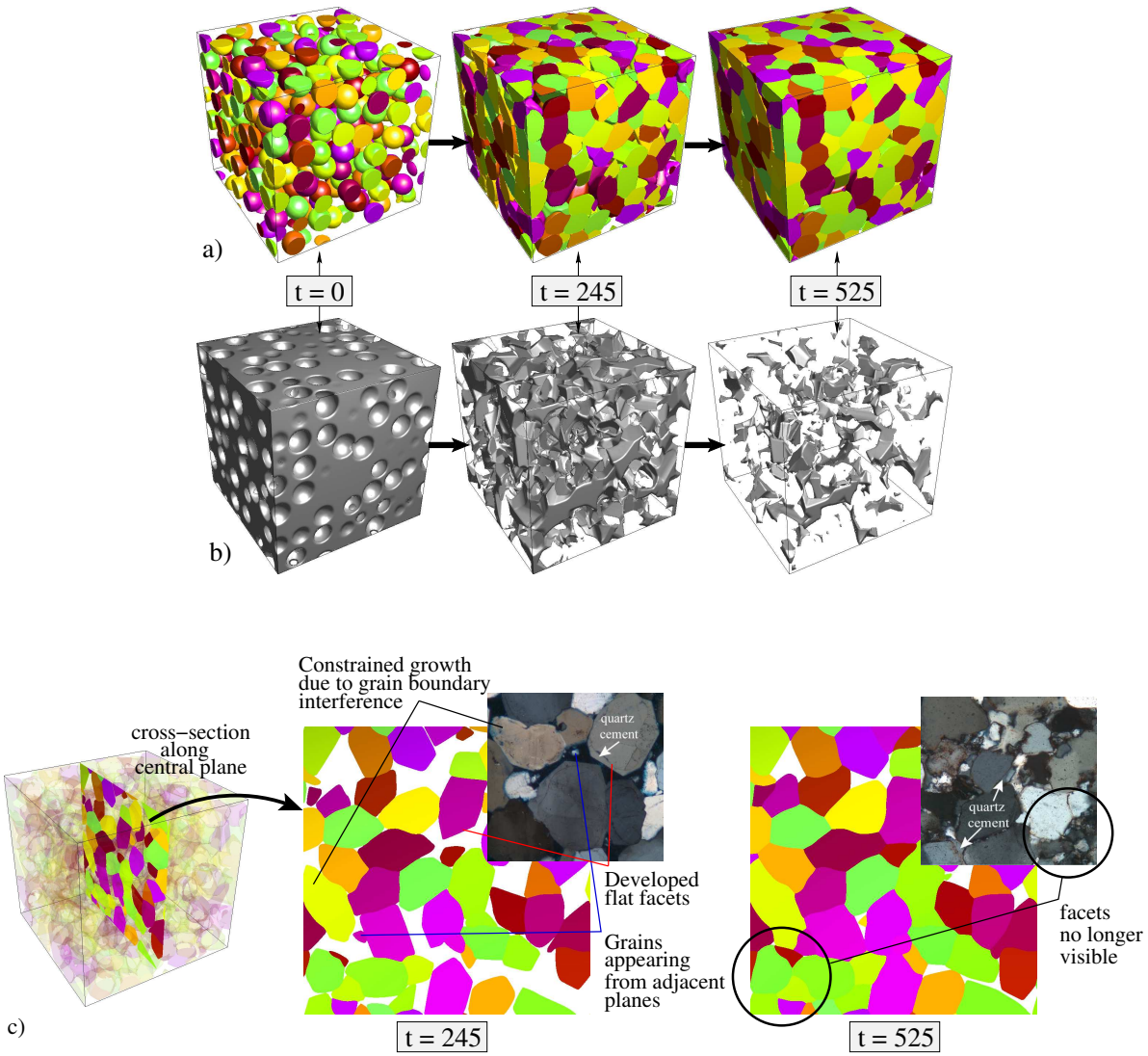

Figure 6.10: a) Simulated syntaxial quartz cementation in multigrain digital grain pack at representative stages. The different grains are shown in different BRY colors. b) Evolution of pore space at the corresponding stages in gray. c) Visualization of the simulated crystal growth along the central plane for qualitative comparison with the natural samples of Busch et al. *[42].*

2. When enough pore space is not present, constrained cement growth occurs due to the mutual interference amongst the neighboring overgrowths, consequently resulting in randomly shaped crystals.

3. The pore space in a thin-section is also occluded by overgrowths growing on the grains lying in the adjacent planes. This morphological attribute can only be captured in the 3-D simulations.

At later stages, when the pore space cementation has extensively occurred, the facets are no longer distinguishable, both in the 3-D simulation and the 2-D thin section of the

Table 6.5: Initial grain sizes (or diameter) and the corresponding domain sizes of the five digital grain packs.

Initial grain size	Domain size
$40\Delta x$	$300\Delta x \times 300\Delta x \times 300\Delta x$
$50\Delta x$	$375\Delta x \times 375\Delta x \times 375\Delta x$
$60\Delta x$	$450\Delta x \times 450\Delta x \times 450\Delta x$
$70\Delta x$	$525\Delta x \times 525\Delta x \times 525\Delta x$
$80\Delta x$	$600\Delta x \times 600\Delta x \times 600\Delta x$

natural sample of sandstone from north Germany, as illustrated in figure 6.10c at t=525. The aforementioned similarities between the simulations and the natural samples demonstrate that the adapted MPF model is capable of recreating the syntaxial overgrowth textures and their temporal evolution in optical continuity with the substrate grains.

6.2.2.3 Impact of initial grain size on the rate of porosity loss

In this section, the influence of initial grain size of quartz aggregates on the rates of cementation and porosity reduction is investigated, and discussed in comparison with the existing literature. Five geometrically similar digital grain packs generated using the procedure discussed in section 6.1.2 were considered for this analysis. The grain size and domain sizes of the digital grain packs are listed in table 6.5. The initial porosity of these grain packs is around 67%, which is higher than the naturally observed depositional porosities (39-47% for eolian sediments [189]). However, it is remarked that under the geometrically similar setting of digital grain packs, the impact of the initial grain size on the kinetics of pore space sealing can be safely extracted, without significant effects of the initial porosity. For the numerical parameters given in table 6.1, quartz cementation simulations were performed in these grain packs. Figure 6.11 depicts the plot of porosity over time for different grain sizes. The porosity-time curves are observed to be convex with respect to time, as also suggested by Wangen [97]. Moreover, the rate of porosity loss decreases with the increasing initial grain size. This essentially implies that coarse-grained samples are cemented at slower rates as compared to the finer ones, in agreement with the hydrothermal experiments [36, 44]. In order to analyze the growth of grains in the digital grain packs, we visualize the evolution of six neighboring grains, namely G_1-G_6, in isolation with the rest of the grain pack for the grain sizes $40\Delta x$ and $80\Delta x$. Different stages of the evolution are shown in figure 6.12. It is observed that:

1. At $t = 0$, the relative configuration of the grains in both the packs is identical.
2. At $t = 105$, two non-interacting neighbouring grain pairs (G_3-G_4, G_5-G_6) are present

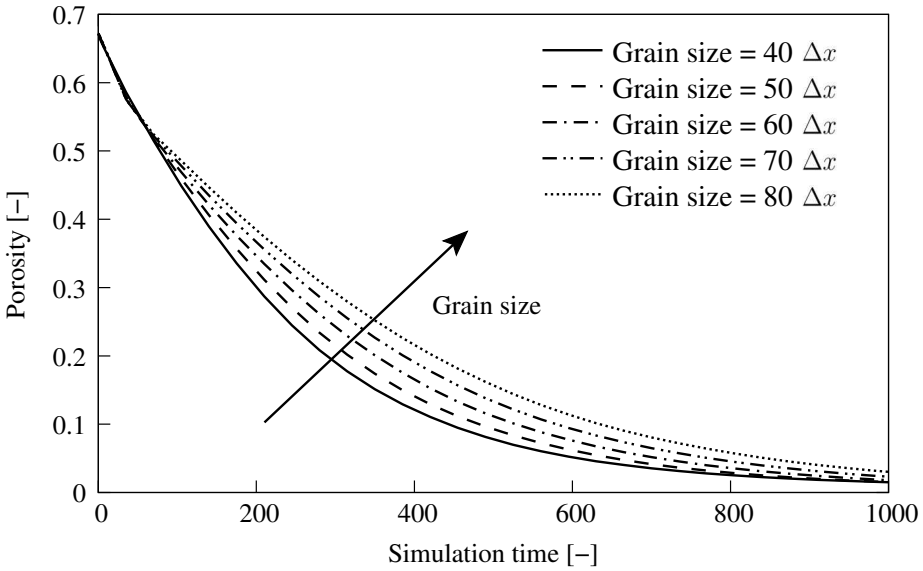

Figure 6.11: Plot of porosity over simulation time for different grain sizes (or diameter). The rate of reduction of porosity increases with decreasing initial grain size.

in the coarse-grained pack, whereas the fine-grained pack has one non-interacting neighbouring grain pair (G_5-G_6).

3. At $t = 455$, coarse-grained pack has one non-interacting neighbouring grain pair (G_5-G_6), while the visualized grains in the fine-grained pack form a closed loop.

4. At $t = 1050$, a closed loop is established in both the cases, resulting in nearly similar spatial grain configurations.

In order to quantify the similarity of the numerically cemented grain packs at different stages of growth, a *similarity index* [190] is utilized for the comparison between the two simulation data sets, which is given by

$$\text{Similarity index} = \frac{\text{Number of matching grid points}}{\text{Total number of grid points}}. \tag{6.1}$$

A similarity index of one implies a perfect match of all the grid points, while the value of zero indicate a complete mismatch at all the grid points of the numerical domain. Figure 6.13 shows the plot of temporal evolution of similarity index obtained by the comparison of simulated cementation in the digital grain packs with the initial grain sizes of $40\Delta x$ and $80\Delta x$. Since the computational domain of the coarse-grained pack is 8 times larger (2 times in each dimensions) as compared to the fine-grained pack, every second grid point in the former case is compared with each grid point of the latter. Starting with an initial value of about 0.95, the similarity index drastically decreases and attains a minimum, indicating a significant difference in the sealing kinetics, as also observed in

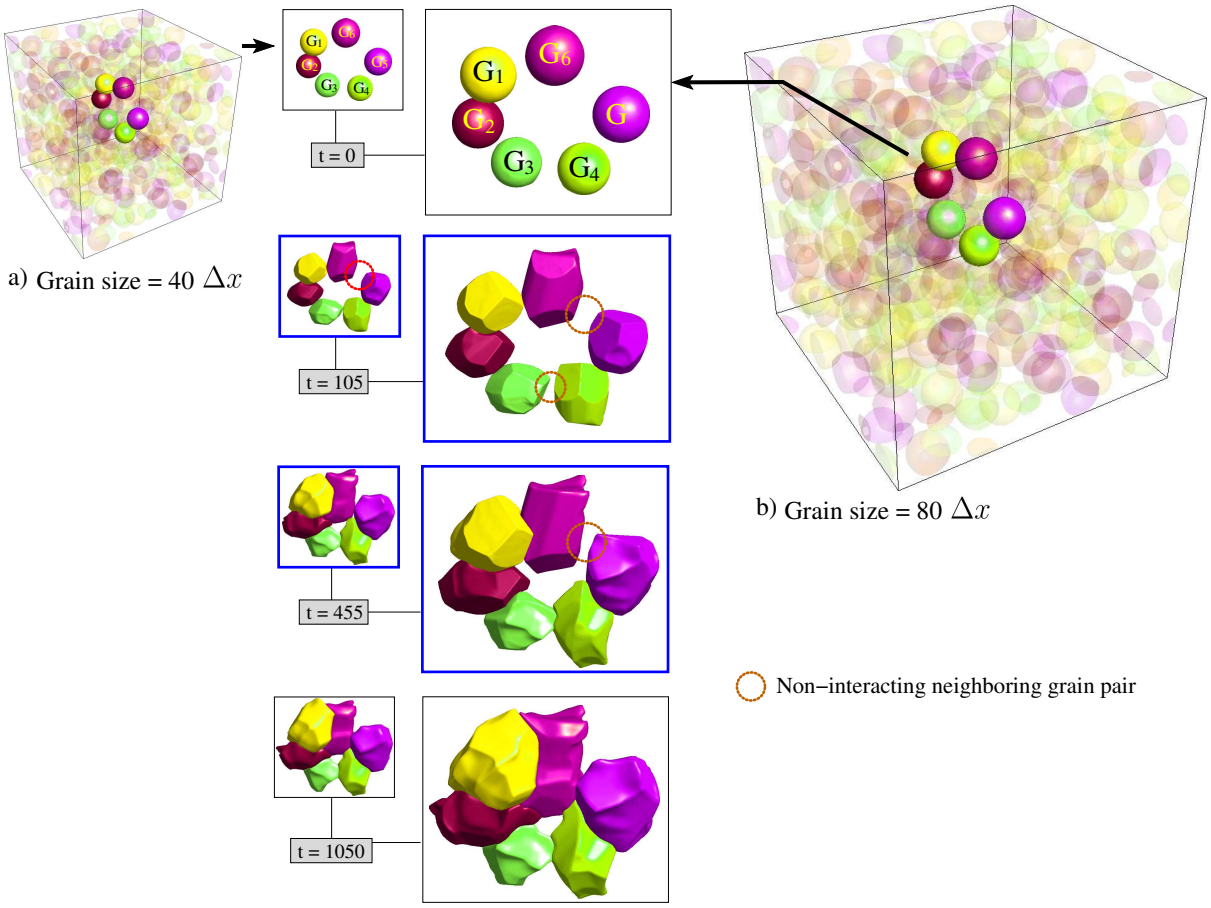

Figure 6.12: Evolution of 6 neighbouring grains of the grain packs for grain sizes a) $40\Delta x$ and b) $80\Delta x$ at four representative stages of growth. The red dotted circles highlight the non-interacting neighbouring grain pairs. At intermediate stages (t=105 and t=455), a significant difference is observed in the evolution of grains for different grain sizes, as illustrated in the inset pictures in the blue boxes.

figure 6.12 at $t = 105$. With further time, the similarity index increases monotonically and converges towards one, thereby indicating a near-similarity in the numerically cemented grain packs, as also inferred in figure 6.12 at $t = 1050$. The plots in figure 6.11 and 6.13 suggest that the impact of initial grain size on the kinetics of pore space sealing is intense in the intermediate stages, and dwindles at the later stages. The pore space sealing behavior described in the figure 6.11 can be rationalized on the basis of the arguments of unrestricted growth (subsection 6.2.2.2). The additional complexities arising due to the interference of overgrowths in a multigrain system do not impact the direction of movement of the solid-liquid interfaces (that move such that the grains grow). Thus, although the kinetics may differ due to these complexities, but the principle behavior of the sealing curve for coarser grains lying above the finer ones remains the same.

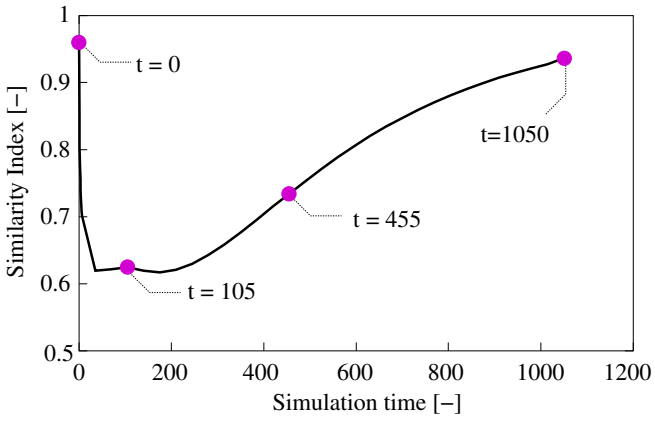

Figure 6.13: Plot of similarity Index over simulation time for the numerically cemented digital grain packs with the initial grain sizes of $40\Delta x$ and $80\Delta x$.

6.2.2.4 Impact of syntaxial overgrowth cementation on pore size distributions

For the simulation of syntaxial quartz cementation in the digital grain pack of initial grain size of $40\Delta x$ (section 6.2.2.3), numerical data sets of the digital pore space were extracted at five representative stages of time. The chosen stages are highlighed by different colored points in the porosity-time plots of figure 6.14a. Utilizing the post-processing tool chain

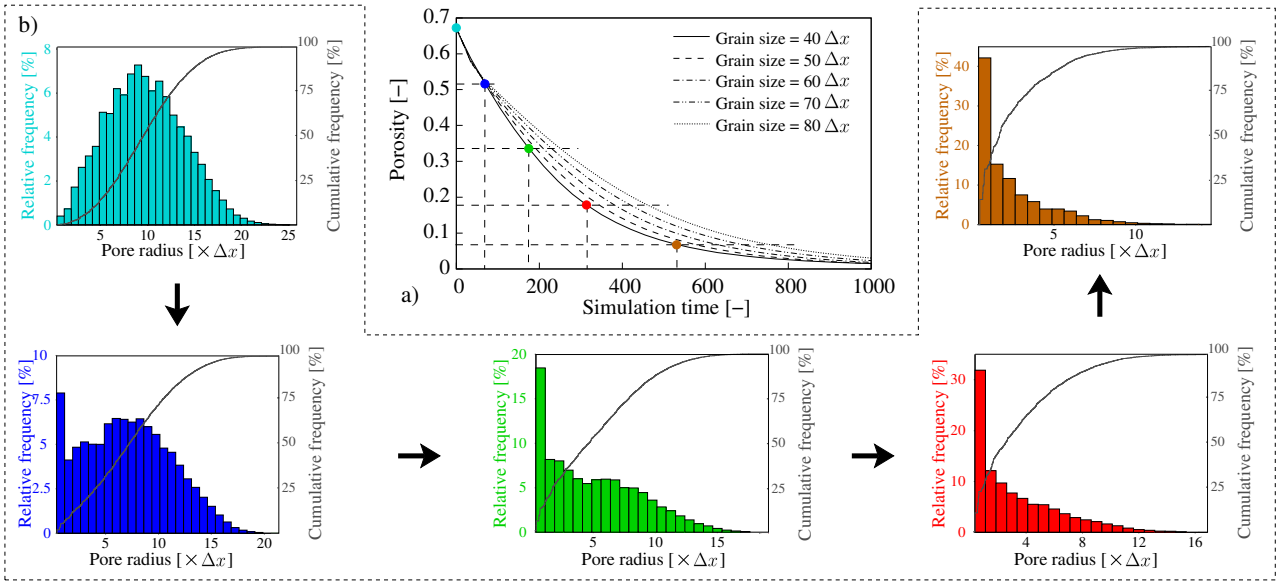

Figure 6.14: Five representative data points (in different colors) on the porosity-time curve for the digital grain pack with an initial grain size $40\Delta x$ where the digital pore space data was analysed. b) Temporal evolution of the relative pore size distribution (as colored histograms) and cumulative pore size distribution (smoothed curves in grey). The color of the each histogram corresponds to the time stage depicted in the same colored point on the porosity-time plot.

of PACE3D [171, 172], the medial axis transform (MAT) was computed for each digital pore space. This numerical technique generates the complete set of discretization grid points lying on the medial axis, and assigns the radius of the largest pore that can be inserted at that grid point. This MAT data was utilized to estimate the pore size distribution of the porous rock structures. Figure 6.14b depicts the plots of relative and cumulative (smoothed) pore size frequency distributions at different stages of time. The color of each plot corresponds to the time highlighted by the same colored points in figure 6.14a. Figure 6.15a,b depict the combined plots (with smoothing) of relative and cumulative pore size frequency distributions. The relative pore size distribution for the initial pore geometry ($t = 0$), corresponding to the spherical grains, exhibits a 'bell-shaped' curve. Such a normal distribution is expected for clean and well-sorted sandstones, as suggested by NETTO [191]. As the cementation progresses, the pore sizes reduce. At $t = 70$, a bimodal relative frequency distribution is observed, where a second peak appears near a smaller value of pore radius, indicating a significant fraction of smaller pores. Further, the first peak lying at a higher pore radius also shifts towards the left, signifying the decrease in the overall pore sizes due to cementation. Subsequently at $t = 175, 315$ and 525, the fraction of smaller pores increases, as indicated by the second peak in figure 6.15a and reflected in the cumulative frequency plot in figure 6.15b. The relative pore size distribution eventually evolves into a log-normal kind of pattern ($t = 525$), generally exhibited by the reservoir sandstones [191]. In the presented set of simulations in section 6.2.2.3, at a given porosity, the pore size statistics of the digital grain pack with the initial grain size of $80\Delta x$ can be directly inferred by scaling the pore-radius axis by a factor of 2, and accordingly for other intermediate packs. As these packs are geometrically similar, the evolution of pore size distributions for rest of the cases (i.e. grain size $50\Delta x - 80\Delta x$) will follow the exact same path illustrated by arrows in figure 6.14b, and the rates of evolution will decrease with the increasing grain size in

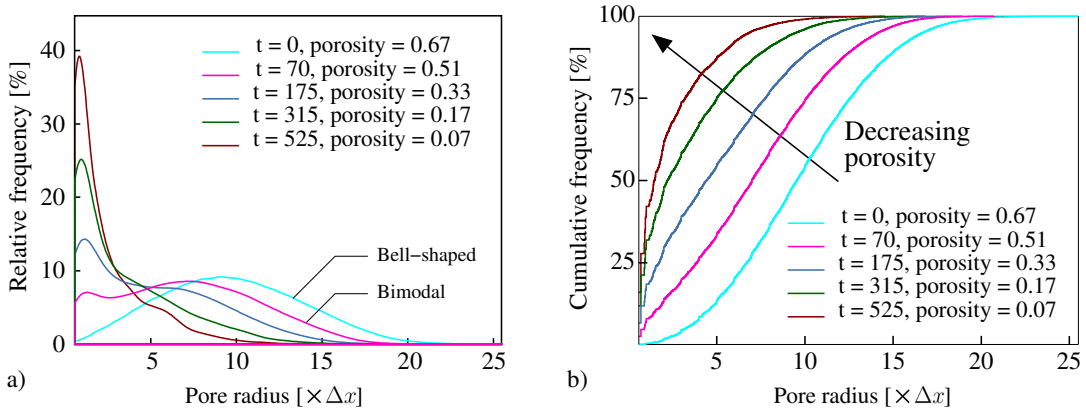

Figure 6.15: Smoothed plots of relative and cumulative pore size frequency distributions at five representative stages of time.

accordance with the kinetics of pore space sealing.

6.2.2.5 Impact of syntaxial overgrowth cementation on permeability-porosity relationships

For the simulations of syntaxial quartz cementation in different-sized grain packs reported in the section 6.2.2.3, data sets of the digital pore space were extracted at different stages of time. With an objective to compute the numerical permeabilities during progressive cementation, viscous fluid flow was numerically simulated through the digital pore space. The utilized fluid dynamical model is elaborated in section 3.2 of chapter 3. For each simulation, a constant pressure drop was applied on the basis of the free-steam boundary conditions (eq. (3.22) in chapter 3) at the 2-D faces of the computational domain in the x-direction. The numerical values of the flow parameters are given in table 6.1. With the vanishing body force (i.e. $\boldsymbol{f_b}(\boldsymbol{x}, t) = \mathbf{0}$ in eq. (3.21)), the velocity fields were computed. Figure 6.16a,b depicts the velocity stream lines at three different stages of cementation in the digital grain packs with initial grain sizes of $40\Delta x$ and $80\Delta x$, respectively. The fine-grained pack exhibits lower fluid velocities at each time step than the coarser one,

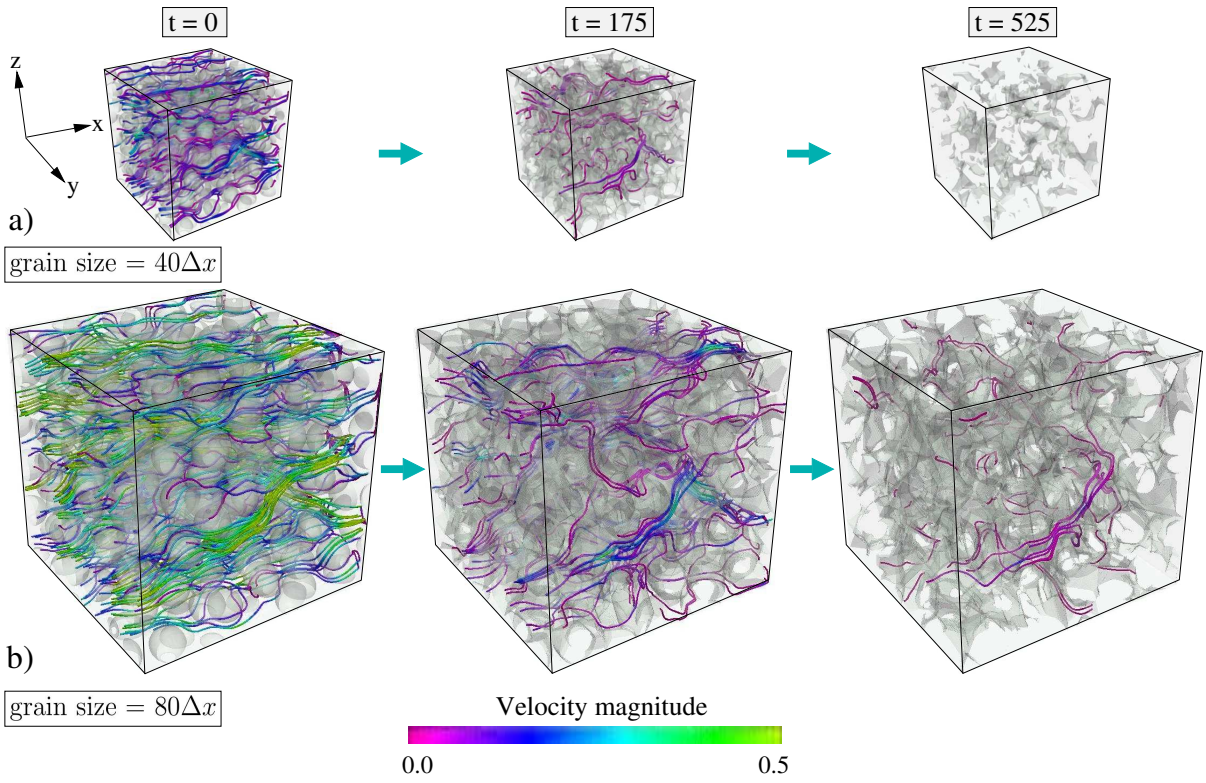

Figure 6.16: Stream lines depicting the magnitude of velocity in the flow simulations at three different stages of quartz cementation in digital grain packs of initial grain size a) 40 Δx and b) 80 Δx.

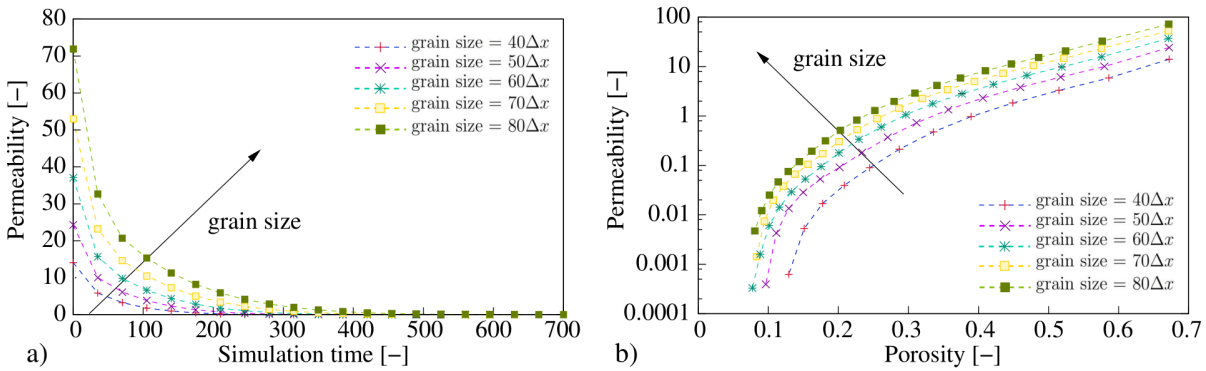

Figure 6.17: Plots of a) permeability versus simulation time and b) permeability versus porosity (in semi-log scale) for digital grain packs with different initial grain sizes.

due to a lower pore space volume in the former. Thus, at each stage of time, the permeabilities of coarser packs are higher than those of the finer ones, as depicted in the permeability-time plots in figure 6.17a. For the chosen length scale, the computed numerical permeabilities in the simulations lie in the range of $5 - 7200$ mD. Utilizing the data sets shown in figures 6.11 and 6.17a, permeability-porosity relationships were derived for different initial grain sizes, see figure 6.17b. Experiments [192] suggest that finer sands are less permeable than the coarser ones at same porosities. The porosity-permeability relationship obtained in the simulations (figure 6.17b) are in qualitative agreement with these experimental investigations. Based on the analysis and fitting of the experimental data of natural samples from different geological settings, several empirical equations (e.g. Kozeny-Carman, Timur's, etc.) relating permeability with porosity and other physical rock properties (e.g. mean grain size, surface area, sorting, irreducible water saturation) have been proposed, see the review article [103] for a detailed analysis. Many models including the *Timur's model* [193] suggest a power-law relationship between the porosity φ and permeability κ (i. e. $\kappa \propto \varphi^n$, n being an empirical constant) and additional physical parameters. Thus, for the numerically obtained permeability-porosity data of the present work, a power-law fitting ($\kappa = a\varphi^n$) was employed. For different initial grain sizes, the

Table 6.6: Fitting parameters for the permeability-porosity data corresponding to the power-law fitting.

Initial grain size	a	n
$40\Delta x$	106.35	5.08
$50\Delta x$	125.21	4.45
$60\Delta x$	193.27	4.36
$70\Delta x$	248.79	4.18
$80\Delta x$	312.16	4.05

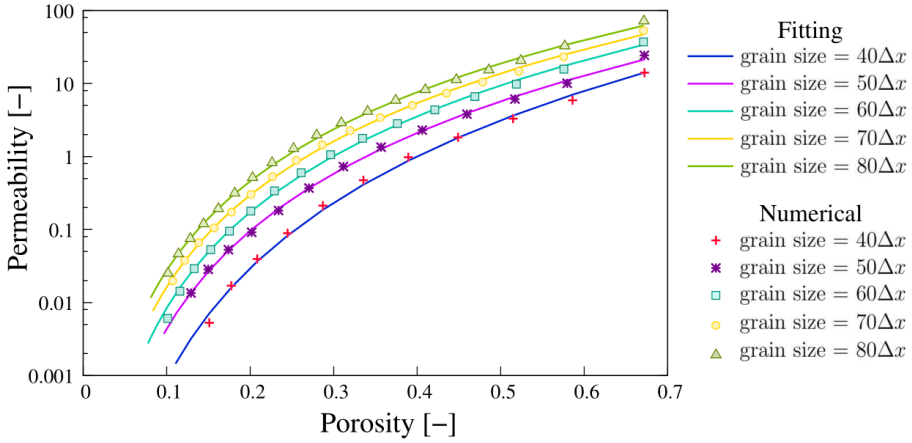

Figure 6.18: Numerical permeability-porosity data (discrete points) along with the fitted curves (continuous lines) in semi-log scale.

values of the proportionality constant a and the exponent n generating the best fit are tabulated in table 6.6. The fitted curves along with the numerical data are plotted in a semi-log scale, see figure 6.18. Timur's model [193], given by

$$\kappa = \frac{k_1 \varphi^n}{S_{wi}^2} \tag{6.2}$$

mathematically relates the permeability κ with porosity φ, irreducible water saturation S_{wi} and two empirical constants k_1 and n. Timur reported that the exponent varies between $3 - 5$ depending upon the data and still produces good fits. Although S_{wi} cannot be constrained separately in the present numerical approach, it is reasonable to assume that the power-law behavior is valid. It is noteworthy that the exponent n (see table 6.6) lie within the range proposed by Timur.

6.3 Concluding remarks

In this work, a MPF model was adapted to simulate the syntaxial quartz cementation in sandstones. The 2-D numerical experiments of unitaxial quartz cement growth in an open fracture indicate that the bridge structures are formed for the crystals possessing a c/a ratio of about 3.0 under undisturbed growth conditions and most of the bridging crystals are oriented sub-normal to the fracture surface, coherent with the hydrothermal experiments [36] as well as other numerical investigations [83, 187]. Utilizing this value of the c/a ratio in the model, 3-D phase-field simulations were performed for investigating the impact of syntaxial pore space cementation on the evolving rock properties of quartz sandstones. Based on the analysis of the simulation results, the following inferences are drawn:

1. Unrestricted quartz cement growth simulations on the single spherical crystals of different initial grain sizes indicate that coarse grains attain their euhedral shape at a slower rate in comparison to finer ones, in agreement with the experimental findings [36].

2. Simulated quartz cementation in the digital grain packs, when visualized along a central plane exhibits similarities with the thin sections of natural sandstone samples from Busch et al.[42]. Based on this analysis, the following inferences about the formation of crystal morphologies and pore geometries are drawn:

   (a) Flat facets, sharp edges and pointed corners are formed according to the euhedral shape of quartz, when sufficient pore space is present for the overgrowths.

   (b) Randomly shaped grains are formed in the absence of enough pore space, as the interference of neighbouring overgrowth leads to constrained growth.

   (c) Pore space as visible in a 2-D plane is also occluded by the overgrowths growing from adjacent planes, advocating the advantage of 3-D numerical studies over the 2-D counterparts.

3. Simulated quartz overgrowth cementation in the digital packs comprising of same-sized spherical grains within each pack but distinct initial grain sizes in different packs, elucidate two important aspects about the rates of porosity loss in sandstones:

   (a) The temporal reduction of porosity for each digital grain pack exhibits a convex behavior with respect to time, as also suggested in the work of Wangen [97].

   (b) The porosity reduces at a slower rate in the coarse-grained packs as compared to the finer ones. This essentially implies that finer sands are cemented faster than the coarser ones, in agreement with the previous experimental findings [36, 44].

4. The pore size statistics, analysed at different stages of the numerically cemented grain packs, reveal that the relative pore size distribution evolves from an initial bell-shaped curve to lognormal patterns at the later stages.

5. The permeabilities, that were computed through the flow simulations of the digital pore space at different stages of cementation, elucidate two important aspects about the permeability-porosity relationships:

   (a) At same porosity, fine-grained sandstones possess lower permeabilities than the coarser ones, in agreement with the existing literature [192].

(b) The numerically obtained permeability-porosity relationships follow a power-law relationship with the exponents lying in the range of $3-5$, as also suggested by the empirical relation of Timur [193].

Chapter 7

Towards more accurate quartz cementation models

Despite the achievements of the adapted multiphase-field model (MPF) in the previous chapter 6 in recreating the realistic cement textures and capturing several aspects of the quartz cementation process in sandstones, the model suffered from the following two main limitations:

1. The euhedral shape was generated by considering a faceted-type anisotropy in the interface energy, while the kinetics was assumed to be isotropic. This essentially implies that a quartz crystal achieves the faceting in the initial growth phase according to the capillary anisotropy shape. Once this shape is attained, the crystal further grows while maintaining that shape due to isotropic growth kinetics. However, it has been found that different facets of the prismatic quartz grow at different rates relative to each other [52]. Further, the growth along the c-axis is more rapid as compared to the a-axis [46, 50]. Moreover, the hydrothermal growth experiments of Lander et al. [36] reported that the growth of quartz cements occur at different rates during the pre- and the post-euhedral stages. All the above quartz growth tendencies cannot be rigorously accounted by considering the anisotropy in the interfacial energy alone.

2. A simple interpolation of the inverse mobilities of the solid-solid τ_{ss} and solid-liquid τ_{sl} interfaces was utilized (i.e. $\tau = \sum_{\alpha<\beta}^{N} \tau_{\alpha\beta}\phi_\alpha\phi_\beta / \sum_{\alpha<\beta}^{N} \phi_\alpha\phi_\beta$). When the mobilities differ in orders of magnitude, this interpolation creates an artificial pinning of the triple-junctions shared between two solid and one liquid phase.

In order to overcome the above-mentioned limitations, the previous MPF model is extended in this chapter, based on the work of Wendler et al. [15]. Further, the

phase-field parameter set is determined at the temperature and pressure that corresponds to common reservoir conditions. Moreover, a novel procedure to generate realistic 3-D digital grain packs, that represent natural sandstones in terms of grain shapes, size distributions and depositional porosity, is presented. The obtained digital grain packs are then utilized for the simulation of syntaxial quartz cementation in the digital grain packs varying in the fraction of polycrystalline grains. Finally, the numerical data sets are post-processed and analysed to study the impact of quartz cementation and polycrystallinity of the aggregates on the cement volumes, porosity and permeability of the rock structures, in comparison with the measured permeability of the reference natural sample (experimental data provided by Dr. Benjamin Busch and Prof. Christoph Hilgers, Institute of Applied Geosciences (AGW-SGT) at Karlsruhe Institute of Technology) as well as the exisiting empirical, experimental and numerical literature.

This chapter is organized as follows. Section 7.1 includes the petrographic and petrophysical analysis of a natural sample that was used as a reference for the present numerical investigations. Moreover, the methodologies utilized for extracting the rock sample information are elaborated. Section 7.2 presents the numerical aspects of modeling syntaxial quartz cements. In this section, the procedure utilized to determine the phase-field parameter set, and the growth conditions they correspond to, is elaborated. Further, in the same section, the preprocessing methodology for generating realistic 3-D digital grain packs is elaborated. In section 7.5, the simulation results of quartz cementation and their discussions are presented. The chapter is concluded by recapitulating the findings and insights derived from the present investigation in section 7.6.

7.1 Analysis of a natural sample: Methodology and information

To support the numerical investigations presented in this chapter, the petrographical and petrophysical information of a natural sandstone sample (BQ_1 of Busch et al. [42]) was provided by Dr. Benjamin Busch and Prof. Christoph Hilgers from Institute of Applied Geosciences (AGW-SGT) at Karlsruhe Institute of Technology. A thin section microphotograph of the sample is shown in figure 7.4a. The rock sample was extracted from the dune foreset in Bowscar Quarry, north of Penrith, and was a part of a Permian aeolian sandstone from the Penrith Sandstone Formation, outcropping in the Vale of Eden, Cumbria, North England. Sample's detrital composition was determined using point counting (300 steps) on a grid adjusted to the largest grain size. The grain sizes were petrographically determined as the long axis of atleast 100 grains per sample. Sorting was computed after Trask [194]. Helium pycnometry (micromeritics AccuPyc II 1340)

was utilized for measuring the porosity. For the permeability measurements, a Westphal air permeameter was employed at a 1.2 MPa confining pressure.

The sample exhibits pinstripe lamination which is a sedimentary characteristic arising due to the deposition of finer and coarser grains in distinct layers in the eolian dune deposits [195]. The sand is moderately sorted and the average grain size is 0.349 mm. Based on the grain percentage, the sample contains 68.3 % quartz grains, 2.7 % K-feldspar grains, and 0.3 % volcanic rock fragments. Amongst the quartz grains, 77.07% are unicrystalline, while the rest are polycrystalline aggregates. The authigenic minerals in the sample include 20.7 % quartz cement, 0.3 % K-feldspar cement, and 2.3 % replacements after K-feldspar (illite and kaolinite). On the basis of grain composition, the sandstone comprises of 95.8 % quartz, 3.8 % K-feldspar, and 0.4 % volcanic rock fragments. The rock sample falls in the category of quartzarenite after Folk [196]. As the sample contains a major portion of detrital quartz grains, both single crystals as well as polycrystalline aggregates, this sandstone is a suitable natural example for the present numerical investigation. The petrophysically determined porosity of the sample is 19.8% and the Klinkenberg-corrected permeability is 1044 mD.

7.2 Numerical aspects

Section 7.3 delineates the procedure of adapting the MPF model (discussed in chapter 3) for the simulation of quartz cementation. In section 7.3.1, the phase-field parameter set along with the methodology employed to generate them at the considered growth conditions (p, $\mathfrak{c}$, T) is presented in a systematic manner. Finally, the preprocessing procedures for the generation of realistic 3-D digital grain packs composed of different fractions of unicrystalline and polycrystalline grains is discussed in section 7.4.

7.3 Modeling quartz cements in the multiphase-field framework

Like the previous chapter 6, the prismatic growth habit of quartz is also considered in the present chapter. However, as delineated in the beginning of this chapter, the modeled quartz cementation in the previous chapter was devoid of some important quartz growth tendencies. In order to address those limitations, the following extensions were incorporated in the MPF model. Firstly, in addition to a faceted-type anisotropy in the interfacial energy using the piece-wise function $a_{\mathrm{sl}}^{\mathrm{cap}}$ for the solid-liquid interfaces (eqs. (3.3) and (3.4) in chapter 3), an anisotropic growth kinetics was incorporated by

formulating the effective kinetic mobility μ [which is related to the kinetic coefficient τ (eq. (3.6) in chapter 3) as $\mu = 1/\tau$] in the following generalized form [15]

$$\mu(\boldsymbol{\phi}, \boldsymbol{\nabla\phi}) = \sum_{\substack{\alpha,\beta=1 \\ (\alpha<\beta)}}^{N,N} \mu^0_{\alpha\beta} \mathfrak{g}_{\alpha\beta}(\boldsymbol{\phi}) a^{\text{kin}}_{\alpha\beta}(\mathbf{q}_{\alpha\beta}). \tag{7.1}$$

Here $\mu^0_{\alpha\beta}$ denotes the kinetic mobility of the α-β interface. $a^{\text{kin}}_{\alpha\beta}(\mathbf{q}_{\alpha\beta})$ represents a kinetic anisotropy function of the form [15]

$$a^{\text{kin}}_{\text{sl}}(\mathbf{q}_{\text{sl}}) = \left[1 + \delta\left(\max_k\left\{\hat{\mathbf{n}} \cdot \boldsymbol{\eta}^{\text{kin}}_k\right\} - \max_{k-1}\left\{\hat{\mathbf{n}} \cdot \boldsymbol{\eta}^{\text{kin}}_k\right\}\right)\right] \cdot \max_k\left\{\hat{\mathbf{n}} \cdot \boldsymbol{\eta}^{\text{kin}}_k\right\}, \quad (k = 1, \ldots, n_{\text{kin}}). \tag{7.2}$$

Here $\hat{\mathbf{n}} = \mathbf{q}_{\text{sl}}/|\mathbf{q}_{\text{sl}}|$ is the unit vector perpendicular to the solid-liquid interface, $\{\boldsymbol{\eta}^{\text{kin}}_k |\ k = 1, \ldots, n_{\text{kin}}\}$ denotes the set of n_{kin} vertex vectors of the resulting kinetic anisotropy shape of the solid-liquid interface. $\max_k$ and $\max_{k-1}$ are the functions, that take the input of the inner product [denoted by the symbol $(\cdot)$] of two vectors, and return the largest and second largest argument in the braces, respectively. δ is the kinetic anisotropy strength parameter that controls the pre-euhedral growth of a crystal. The kinetic anisotropy function (eq. (7.2)) serves the following dual purposes:

1. When the chosen set of vertex vectors $\boldsymbol{\eta}^{\text{kin}}_k$ for the kinetic anisotropy shape are compatible with the corresponding set $\boldsymbol{\eta}^{\text{cap}}_k$ for the capillary anisotropy shape, the kinetic anisotropy accounts for the different relative growth rates of distinct facets during the post-euhedral growth phase (i.e. after the faceting is complete).

2. The kinetic anisotropy strength parameter δ provides an adjustable growth rate prior to faceting (i.e. during pre-euhedral growth stage) and can be calibrated to match the known pre-euhedral growth tendencies of any mineral.

The interpolation function $\mathfrak{g}_{\alpha\beta}(\boldsymbol{\phi})$ is formulated as [15]

$$\mathfrak{g}_{\alpha\beta}(\boldsymbol{\phi}) = \begin{cases} 0 & \text{if } \alpha \text{ and } \beta \text{ are solid phases and } \phi_{\text{liquid}} > 0, \\ \dfrac{\phi_\alpha \phi_\beta}{\sum^{N,N}_{\substack{\alpha,\beta=1 \\ (\alpha<\beta)}} \phi_\alpha \phi_\beta} & \text{else,} \end{cases} \tag{7.3}$$

in order to prevent the artificial pinning of the triple junctions between the two solid and a liquid phase, when the mobilities of the solid-solid and solid-liquid interfaces differ by orders of magnitude. Figure 7.1a depicts the schematics of a diffuse three-phase region with two solid phases and a liquid phase. The variation of effective kinetic mobility along the red line (in figure 7.1a) according to the previous interpolation of Vondrous et al. [184] (eq. (5.1) of chapter 5, also utilized in chapter 6) and the present interpolation of

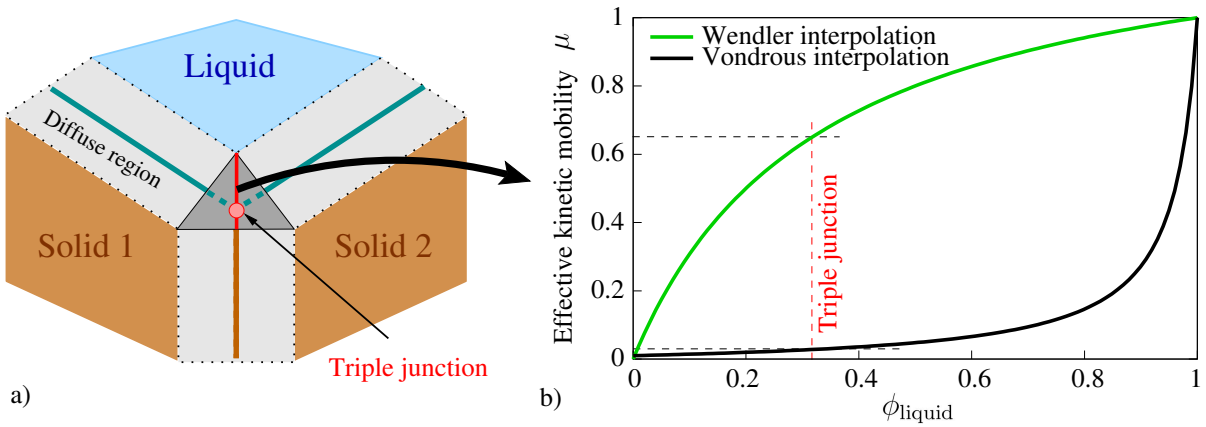

Figure 7.1: a) Schematics illustrating the three-phase diffuse region (grey triangle) for a solid-solid-liquid system, where all the three phase-fields (i.e. ϕ_{solid1}, ϕ_{solid2} and ϕ_{liquid}) are non-zero. b) The variation of mobility along the red line with the liquid phase-field for the interpolations proposed by Vondrous et al. *[184] and* Wendler et al. *[15], for the case $\mu_{sl}/\mu_{ss} = 100$ and $a_{sl}^{kin}(\mathbf{q}_{sl}) = 1$.*

Wendler et al. [15] (eq. (7.3)) for the case of $\mu_{\text{sl}}/\mu_{\text{ss}} = 100$ and $a_{\text{sl}}^{\text{kin}}(\mathbf{q}_{\text{sl}}) = 1$ is plotted in figure 7.1b. Clearly, the mobilities along the red line in the three-phase region computed using the present interpolation function [15] are significantly higher as compared to the previously used formulation [184]. The utility of the present interpolation is illustrated in the numerical example presented in section 7.5.1.3.1. Finally, the anisotropic kinetic mobility formulation (eq. (7.1)) enters the evolution equation of the phase-field as follows

$$\varepsilon \frac{\partial \boldsymbol{\phi}}{\partial t} = \mu(\boldsymbol{\phi}, \boldsymbol{\nabla}\boldsymbol{\phi}) \left(-\frac{\delta \mathcal{F}}{\delta \boldsymbol{\phi}} - \lambda \right), \tag{7.4}$$

The chosen set of the vertex vectors for the capillary and kinetic anisotropy functions are provided in the upcoming section 7.3.1.4.

7.3.1 Determination of phase-field parameters for quartz growth

In this section, the method utilized to generate the parameter set for the MPF model along with their mapping to the corresponding physical values is elucidated. A temperature of 423 K (150^{o}C) is considered, as all the required physical parameters of quartz growth are readily available in the literature [49]. With the increasing depth from the earth's surface, the temperature increases at about 30^{o}C/km [197]. Therefore, in a geological system, a temperature of 423 K is expected at the depth of 4.5 Km, when a surface temperature of 298 K is assumed. The expected hydrostatic pressure at such depths is about 44 MP, according to Bourgoyne et al. [198] (equation 4.2b in the book chapter 4.1). Hence, in the present work, the above-mentioned temperature and pressure conditions

are chosen for the quartz cementation. For a detailed discussion about the equations that are presented in the following part of this section, their assumptions and applicability, the interested readers are referred to WENDLER ET AL. [15] and the references therein.

7.3.1.1 Surface energies

The interfacial energy of the quartz-water interface is chosen to be $\gamma_{\mathrm{sl}} = 0.36$ J/m^2 from PARKS [199], where s and l denote the solid (quartz in this case) and liquid phases, respectively. The grain boundary energy or the solid-solid interface energy γ_{ss} is related to γ_{sl} and the dihedral angle φ_{d} through the equation of textural equilibrium, known as the *Young's law*, that reads

$$2\cos\left(\frac{\varphi_{\mathrm{d}}}{2}\right) = \frac{\gamma_{\mathrm{ss}}}{\gamma_{\mathrm{sl}}}. \tag{7.5}$$

HOLNESS [200] reported a linear relationship between the dihedral angle and temperature, with $\varphi_{\mathrm{d}} = 80^o$ at T $= 600^o$C and $\varphi_{\mathrm{d}} = 60^o$ at T $= 400^o$C. Hence, at a temperature of 150^oC (or 423 K), the ratio $\gamma_{\mathrm{ss}}/\gamma_{\mathrm{sl}} = 1.91$ and the grain boundary energy $\gamma_{ss} = 0.6876$J/m^2 are obtained.

7.3.1.2 Crystallization driving force

Quarz growth is phenomenologically governed by the precipitation and dissolution of silica (SiO_2), that is given by the chemical reaction

$$SiO_2(s) + 2H_2O(l) \leftrightarrow H_4SiO_4(aq), \tag{7.6}$$

where (aq) denotes the dissolved phase. The Gibbs free energy change during the crystallization of one mole of quartz from the solution is given by [201]

$$\Delta G = RT \ln \mathcal{S}, \tag{7.7}$$

where R is the Gas constant, T denotes the temperature in Kelvins and $\mathcal{S}$ represents the fluid supersaturation index $\mathcal{S}$ with respect to silica. The crystallization driving force is calculated as [15]

$$\Delta f_{\mathrm{sl}} = (\mathfrak{c}_{H_4SiO_4} - \mathfrak{c}^{\mathrm{eq}}_{H_4SiO_4}) \frac{RT}{V_{\mathrm{m}}^{H_2O}} \ln\left[\frac{\mathfrak{c}_{H_4SiO_4}}{\mathfrak{c}^{\mathrm{eq}}_{H_4SiO_4}}\right] \tag{7.8}$$

$$= \mathfrak{c}^{\mathrm{eq}}_{H_4SiO_4} \frac{RT(\mathcal{S}-1)\ln \mathcal{S}}{V_{\mathrm{m}}^{H_2O}} \tag{7.9}$$

where $\mathfrak{c}_{H_4SiO_4}$ and $\mathfrak{c}^{\mathrm{eq}}_{H_4SiO_4}$ denote the molar and equilibrium concentrations of orthosilicic acid (H_4SiO_4), respectively. $V_{\mathrm{m}}^{H_2O}$ represents the molar volume of water. The equations (7.8) and (7.9) are based on the following approximations:

- The mechanical work (i.e. $p\Delta V = \Delta G - \Delta \mathcal{F}$) of the process is negligible in comparison with the Gibb's free energy change, such that it is admissible to directly utilize eq. (7.7) in deriving the driving force expression, which in the phase-field model is based on the Helmholtz free energy $\mathcal{F}$.

- The fluid possesses a low salinity and its behavior can be well-estimated with that of an ideal solution. In this case, the fluid supersaturation index can be approximated as

$$\mathcal{S} \approx \frac{\mathfrak{c}_{\mathrm{H_4SiO_4}}}{\mathfrak{c}^{\mathrm{eq}}_{\mathrm{H_4SiO_4}}}. \tag{7.10}$$

The equilibrium concentration of silica at a temperature of 423 K is $\mathfrak{c}^{\mathrm{eq}}_{\mathrm{H_4SiO_4}} = 60.8$ ppm [from Table A1 in Okamoto et al. 49]. The mechanical work during the crystallization at a pressure of $p = 44$ MPa is $p\Delta V = p(V_{\mathrm{m}}^{\mathrm{Qtz}}\text{-}V_{\mathrm{m}}^{\mathrm{H_4SiO_4(aq)}}) \approx 206$ J/mol, where $V_{\mathrm{m}}^{\mathrm{Qtz}}$ and $V_{\mathrm{m}}^{\mathrm{H_4SiO_4(aq)}}$ denote the molar volumes of quartz and aqueous orthosilicic acid solution, respectively. At a supersaturation index of $\mathcal{S} = 1.1$ (or $\mathfrak{c}_{\mathrm{H_4SiO_4}} = 66.88$ ppm, a Gibb's free energy change of $\Delta G = 335.2$ J/mol is calculated. For this case, the mechanical work and the Gibb's free energy change are comparable in magnitude, and the mechanical work should be included in the calculation of the driving force. Taking the contribution of mechanical work into account, a driving force of 43 J/m^3 is obtained. In the present modeling, as an explicit time update scheme is utilized for computing the phase-fields, the scheme is conditionally stable. Thus, there is an upper limit on the choice of the numerical time step width Δt above which the simulations become unstable. As the value of kinetic mobility increases, the maximum allowable time step width decreases. Moreover, in the present model, the mobility formulation is dependent upon the the kinetic anisotropy strength parameter δ that is calibrated through the simulations. At $\delta = 115$, the experimentally reported pre- and post-euhedral growth behavior of quartz cements is recovered, which is discussed in detail in section 7.5.1.1. At this value of δ, the value of the maximum allowable time step width of $\Delta t = 0.0058$ is found. For a fluid supersaturation of $\mathcal{S} = 1.1$ and $\delta = 115$, the simulation time required to carry out the desired amount of quartz cementation in the digital grain packs (i.e. reduction of porosity from 38 % to <10 %) is unfeasibly large. In order to deal with this computational limitation, the fluid supersaturation can be increased that would cause more rapid cementation. It should be noted that, at higher fluid supersaturations, the role of the model-inherent curvature effects, which account for the inability of the crystals above a certain curvature to grow at a given fluid supersaturation, is suppressed. As a consequence, at higher supersaturations, the microquartz and chert grains might also grow, that would otherwise stop growing or even dissolve at lower supersaturations. To the best of my knowledge, the extent to which this curvature-dependent driving force influences the crystal morphologies in polycrystalline sandstones is not reported in the

literature. Thus, in the absence of any reliable data and for the computational feasibility, a supersaturation index $\mathcal{S} = 6$ ($\mathfrak{c}_{H_4SiO_4} = 364.8$ ppm) is selected for the present work, and the fluid is assumed to follow the ideal solution behavior. At this growth condition, i.e. $p = 44$ MPa, $\mathfrak{c}_{H_4SiO_4} = 364.8$ ppm and $T = 423$ K, a driving force of around 10^5 J/m^3 is obtained. It is remarked that such high values of the fluid supersaturation may be found in the lower crust under supercritical conditions, and are less likely to be present in the upper crust. Further, the physical time scale of the quartz cementation process decreases by a factor of about 18 at $\mathcal{S} = 6$ in comparison with the corresponding value at $\mathcal{S} = 1.1$. Finally, it is worth mentioning that pore waters during quartz cementation may be highly saline [202], when the low salinity approximation (eq. (7.10)) will no longer be applicable. Hence, when accounting for the real solution behavior, the driving force formulation should be appropriately modified.

7.3.1.3 Kinetic mobilities

The solid-liquid interface velocity v_{sl} during quartz crystal growth is given by [201]

$$v_{sl} = \frac{V_m^{Qtz} k_- (\mathcal{S} - 1)}{A_s/M}, \tag{7.11}$$

as a function of reaction rate constant k_- of the system comprising of 1 kg solute and 1 m^2 of quartz surface area, and the area to mass ratio A_s/M at a given temperature. At higher supersaturations, when the curvature effects in the phase-field model are negligible in comparison with the crystallization driving force, the kinetic mobility of the solid-liquid interface reads [15]

$$\mu_{sl}^0 = \frac{v_{sl}}{\Delta f_{sl}} = \frac{V_m^{Qtz} V_m^{H_2O} k_-}{\mathfrak{c}_{H_4SiO_4}^{eq} (A_s/M) RT \ln \mathcal{S}}. \tag{7.12}$$

The values of all the parameters in eq. (7.12) at a temperature of $T = 423$ K are given in Okamoto et al. [49]. Thus, the kinetic mobility of the solid-liquid interface $\mu_{sl}^0 = 4.65 \times 10^{-17}$ m^4/(J-s) is obtained. For ensuring immobile grain boundaries, a two order lower value for the kinetic mobility of the solid-solid interface is chosen, i.e. $\mu_{ss}^0 = 4.65 \times 10^{-19}$ m^4/(J-s).

7.3.1.4 Set of vertex vectors for the anisotropy functions

The complete set of vertex vectors for quartz growth was determined by Wendler et al. [15], on the basis of a detailed analysis of their experimental sample. They chose the z-facet as their reference for which $a_{sl}^{cap}(z) = a_{sl}^{kin}(z) = 1$ was set, and the values of the anisotropy functions in other directions were varied based on the set of vertex vectors. With the assumption that the anisotropies in surface energy and growth kinetics are

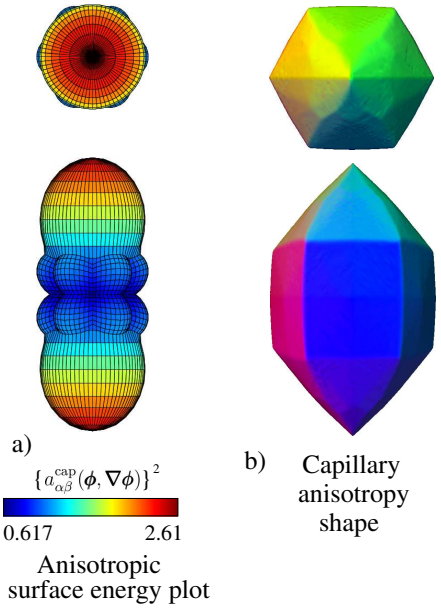

Figure 7.2: a) Capillary anisotropy function (squared) plot in spherical coordinate system. b) Simulated 3-D capillary anisotropy shape using the volume preservation technique. For the sake of visualization, different facets are depicted in different colors based on the surface normal direction.

x	y	z
0	0	± 1.6165
0.4536	0.7856	± 0.6187
-0.4536	0.7856	± 0.6187
-0.9072	0	± 0.6187
-0.4536	-0.7856	± 0.6187
0.4536	-0.7856	± 0.6187
0.9072	0	± 0.6187

Table 7.1: Chosen set of vertex vectors for the 3-D capillary anisotropy shape.

invariant with respect to the physical growth conditions of (p, $\mathfrak{c}$, T), in the present work, the sets of 3-D vertex vectors for the capillary and kinetic anisotropy shape are adopted from Wendler et al. [15]. The set of vertex vectors for the capillary and kinetic anisotropy shape are given in tables 7.1 and 7.2. The 3-D polar plot of the capillary (squared) and kinetic anisotropy functions in the spherical coordinate system and the corresponding crystal shapes simulated using the volume preservation technique [183] are depicted in figures 7.2 and 7.3.

7.4 Work-flow for generating realistic 3-D digital grain packs

Natural and experimental samples of rocks can be broadly characterized based on I) grain shapes and II) size distributions. In this section, a preprocessing procedure to generate the digital grain packs is presented, which takes into account the above-mentioned parameters. For the characterization of grain geometry from a thin section of the same sample [i.e. BQ_1 from Busch et al. 42, in figure 7.4a], the original 2-D grain shapes

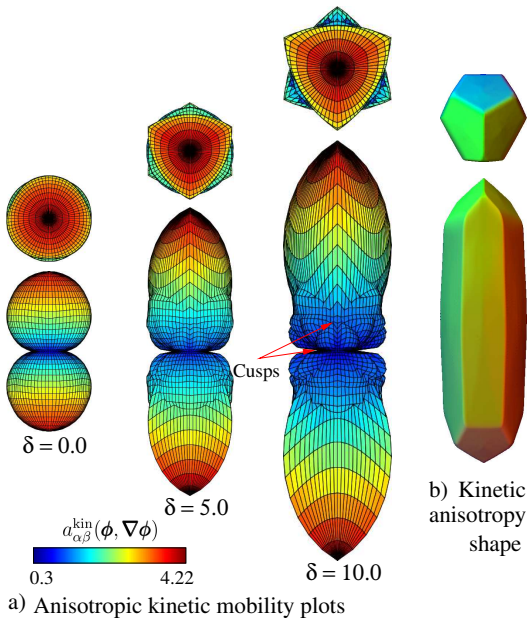

Figure 7.3: a) Kinetic anisotropy function plot in spherical coordinate system for different values of the strength parameter δ. b) Simulated 3-D kinetic anisotropy shape using the volume preservation technique. For the sake of visualization, different facets are depicted in different colors based on the surface normal direction.

x	y	z
0	0	±1.6165
0.2204	∓0.1273	±1.4549
-0.2204	∓0.1273	±1.4549
0	± 0.2546	±1.4549
0.0262	± 0.3	±1.3971
-0.0262	± 0.3	±1.3971
0.2467	∓0.1727	±1.3971
-0.2467	∓0.1727	±1.3971
0.2729	∓0.1273	±1.3971
-0.2729	∓0.1273	±1.3971
0.1732	0.3	±1.2355
0.1732	-0.3	±1.2355
-0.1732	0.3	±1.2355
-0.1732	-0.3	±1.2355
0.3464	0	±1.2355
-0.3464	0	±1.2355

Table 7.2: Chosen set of vertex vectors for the 3-D kinetic anisotropy shape.

(as revealed by the reddish dust rims) were reconstructed from a segment of the thin section, see figure 7.4b. Next, four different digital grain geometries were chosen from a repository of 3-D digital grains, that fairly represent the quartz grains in the thin section, when projected in a 2-D plane. The digital grains in the repository were obtained using a preprocessing algorithm which generates different-sized spheres in close vicinity based on a random function generator, followed by extraction of the inner overlapping region and finally a smoothening of the 3-D surface, resulting in randomly shaped 3-D grains. Next, a representative grain size distribution was obtained by measuring the maximum distance between the two points lying on the grain boundary in the thin section, and was approximated using a lognormal distribution, as illustrated in figure 7.4c. With the parameters of the lognormal distribution and the four digital grain geometries at hand, a simplified grain deposition (i.e. free fall) was simulated by utilizing the software package Blender [203], using the following four-step preprocessing algorithm:

1. Implementation of the mathematical function for the grain size distribution.

2. Generation of a given number of particles following the grain size distribution.

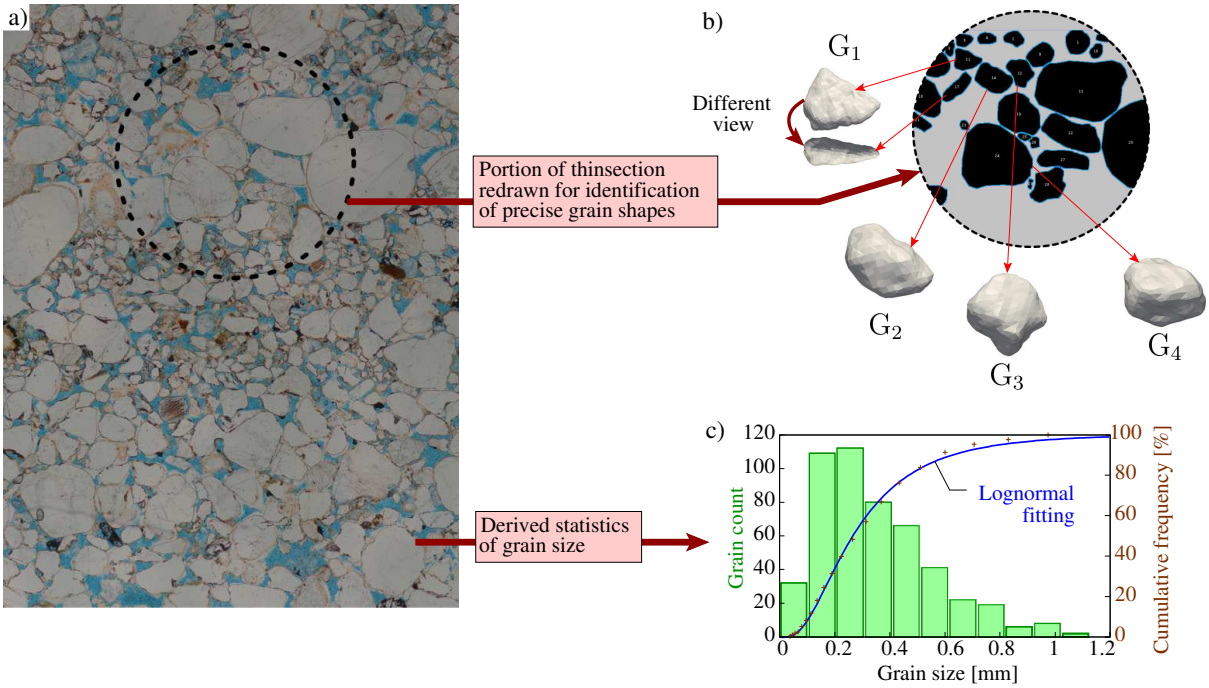

Figure 7.4: Schematics of the work flow for generating a realistic digital grain pack comprising of unicrystalline grains. a) Thin-section microphotograph of the natural sample, BQ_1 from Bowscar Quarry, provided by Dr. Benjamin Busch and Prof. Christoph Hilgers. b) A representative segment of the microphotograph was analysed for deriving the information of grain shapes. Four digital 3-D grain geometries referred as G_1, G_2, G_3 and G_4 were selected, such that when projected in a 2-D plane, they resemble the grains that are visible in the thin-section. c) The grain size distribution was derived based on the measurements of about 500 grains of the thin-section.

3. Random assignment of the four selected digital grain geometries to particles.

4. Simulation of deposition of grains driven by gravity.

The generated particle distribution comprises of the digital grains (with the geometries randomly assigned from the four digital geometries) and satisfies the grain size distribution corresponding to the mathematical distribution function. Deposition was simulated by allowing this particle distribution to fall in a 3-D domain of a fixed base area under the action of gravity. During this simulation, the grains were further allowed to rearrange via tilting and rotation after colliding with each other at the bottom, until a steady state is attained. As a result, an unconsolidated digital grain pack comprising of unicrystalline grains is obtained, see figure 7.5a. Further, a representative cubic volume of size 425 μm $\times$ 425 μm $\times$ 425 μm (Figure 7.5b) was cut out for the sake of computational feasibility. The numerical data was converted to the phase-field compatible data such that each grain in the pack was assigned a phase-field with a unique phase-index. After this process, the

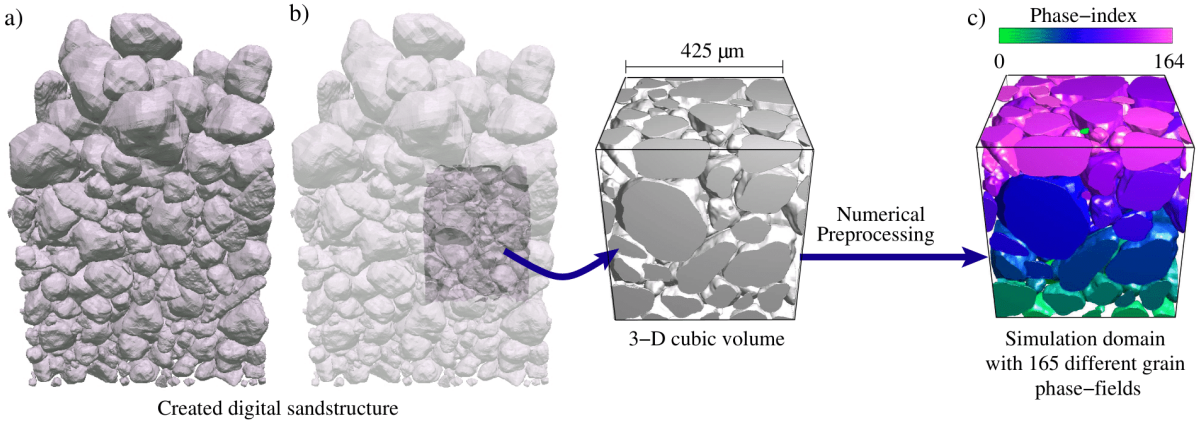

Figure 7.5: a) The created digital pack through the simulation of deposition. b) A representative cubic portion, extracted from the digital pack and post-processed into the phase-field compatible data where c) the simulation domain comprises of 165 grain phases each having a unique phase-field and phase-index.

final digital grain pack shown in figure 7.5c consists of 165 grains and exhibits a porosity of about 38 % (close to the observed porosities of 39-47 % for the eolian sediments at the time of deposition [189]). In order to study the influence of polycrystallinity of quartz grains on the dynamics of quartz cementation, two separate digital grain packs, namely polycrystalline and mixed packs, were generated by preprocessing the unicrystalline grain pack and a voronoi structure, as shown in figure 7.6. The obtained polycrystalline pack comprises of quartz polycrystals with an average subgrain size of about 25μm. The mixed pack represents an intermediate case of the other two packs, as it comprises of an equal number of unicrystalline and polycrystalline grains. The three digital grain packs possess an identical particle distribution, and thereby, a same initial pore structure as well as porosity. In the upcoming section 7.5, these three digital grain packs are utilized for the simulation of syntaxial quartz cementation followed by a detailed analysis of the generated data sets.

7.5 Results and discussions

Through the analysis presented in section 7.3.1, the set of phase-field parameters for the simulations was determined, as listed in table 7.3. The non-dimensional values of some parameters are not given because they are only used for calculating the driving force of crystallization and the kinetic mobility of the interfaces. The simulation results of syntaxial quartz cementation are elaborated in the sections 7.5.1 and 7.5.2. In section 7.5.1, the simulation results of undisturbed cement growth on single unicrystalline and polycrystalline grains are presented. Section 7.5.2 includes a systematic simulation study

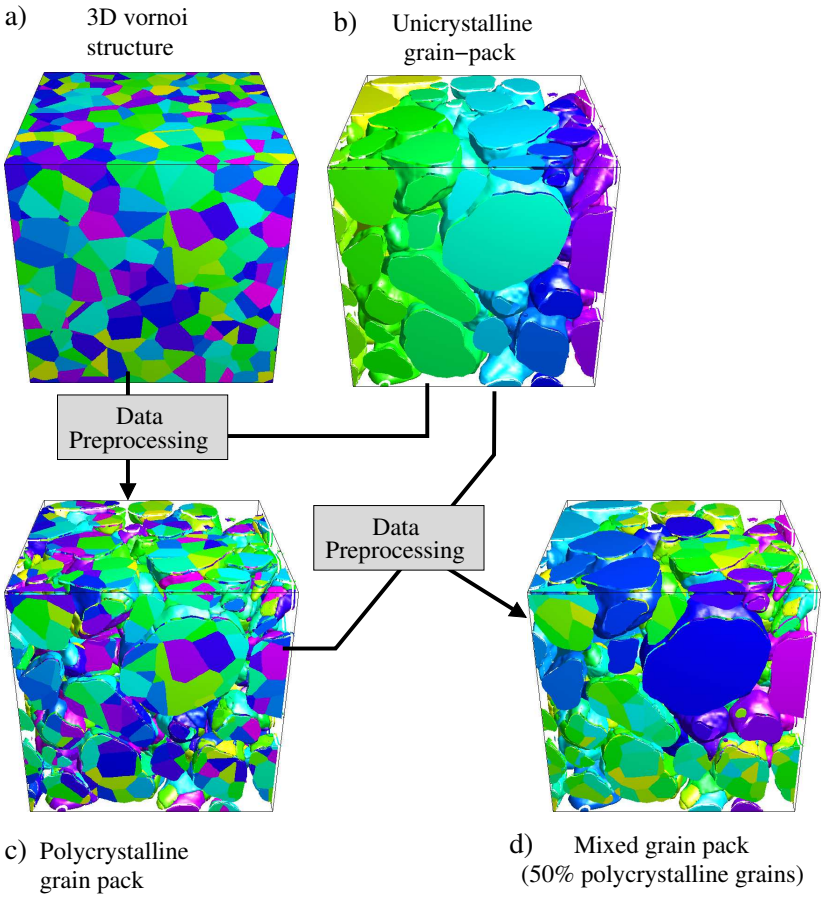

Figure 7.6: Work flow illustarting the procedure for the generation of polycrystalline and mixed digital grain packs. By preprocessing the numerical data of a) the 3-D voronoi structure and b) the previously obtained unicrystalline digital grain pack, c) a polycrystalline pack is created, Using the numerical data of the unicrystalline and polycrystalline grain packs, d) a mixed pack is obtained.

investigating the impact of syntaxial overgrowth cementation and polycrystallinity of quartz grains on the development of crystal morphologies and the evolving rock properties such as porosity, overgrowth cement volumes and permeability.

7.5.1 Simulation study: Unrestricted syntaxial quartz cement growth

Quartz grains in natural sandstones rarely achieve fully euhedral forms owing to the limited pore space for growth and the underlying mutual hindrances amongst the overgrowths originating on the neighboring grains. Numerical simulations of unrestricted growth on single crystals can be utilized for the parameter calibration and model validation. Utilizing an identical set of phase-field model parameters given in table 7.3, simulations of

Table 7.3: Parameter set used for the present work.

Model parameters	Symbol	Non-dim. value	Dim. value
For Phase-field Simulation			
Grid cell size	Δx	1.0	1 μm
Time step size	Δt	0.0058	350 s
Length scale parameter	ε	5.5	5.5 μm
Solid-liquid interface energy density	γ_{sl}	1.0	0.36 J/m^2
Solid-solid interface energy density	γ_{ss}	1.91	0.6876 J/m^2
Higher order parameter	$\gamma_{\alpha\beta\delta}$	25.0	9.0 J/m^2
Driving force for crystallization	Δf_{sl}	-0.294	-1.0×10^5 J/m^3
Solid-liquid interface mobility	μ^0_{sl}	1.0	4.65×10^{-17} m^4/J-s
Solid-solid interface mobility	μ^0_{ss}	0.01	4.65×10^{-19} m^4/J-s
Pressure	p		44 MPa
H_4SiO_4 equilibrium concentration	$\mathfrak{c}^{eq}_{H_4SiO_4}$		60.8×10^{-6}
H_4SiO_4 concentration of the solution	$\mathfrak{c}_{H_4SiO_4}$		364.8×10^{-6}
Precipitation rate coefficient for quartz	k_(T)		7.62×10^{-7} $1/s$
Quartz surface area to mass ratio	A_s/M		17.5 m^2/kg
Temperature	T		150 ^{o}C
For Fluid flow simulations			
Pressure drop	Δp	0.2	8 Pa
Dynamic viscosity	μ	0.90876	0.0011004 Pa-s

undisturbed syntaxial overgrowth cementation were performed for different types and sizes of grains that are tabulated in table 7.4. The physical size of the computational domain for each simulation is also listed in the same table. Each domain was discretized into a regular 3-D grid of cell size $\Delta x = 1\mu m$. As a starting point, the impact of kinetic anisotropy strength on the growth tendencies of quartz grains is investigated. Based on comparison of the simulation results with the experimentally reported quartz growth behaviour, the strength parameter δ is determined. After this calibration procedure, the complete set of phase-field parameters is utilized to study the influence of initial grain size and the polycrystallinity of aggregates on the growth tendencies of quartz cements.

7.5.1.1 Effect of kinetic anisotropy strength

The numerical setup comprises of a spherical unicrystalline grain of diameter 90μm in a computational domain of size given in table 7.4, as shown in figure 7.7 at $t = 0$. The liquid phase occupies rest of the domain and is not shown for the sake of visualization.

Table 7.4: Details of the numerical setup for the unrestricted cement growth simulations on various types of grains.

Grain type	Grain size (diameter)	Computational domain size
1. Unicrystalline		
a) Small	32 μm	75 μm $\times$ 75 μm $\times$ 200 μm
b) Medium	90 μm	150 μm $\times$ 150 μm $\times$ 400 μm
c) Large	130 μm	200 μm $\times$ 200 μm $\times$ 400 μm
2. Bicrystalline		
a) Orientation difference 180^o	130 μm	200 μm $\times$ 200 μm $\times$ 400 μm
b) Orientation difference 135^o	130 μm	250 μm $\times$ 180 μm $\times$ 300 μm
c) Orientation difference 90^o	130 μm	350 μm $\times$ 175 μm $\times$ 300 μm
3. Polycrystalline (all cases)	130 μm	300 μm $\times$ 300 μm $\times$ 300 μm

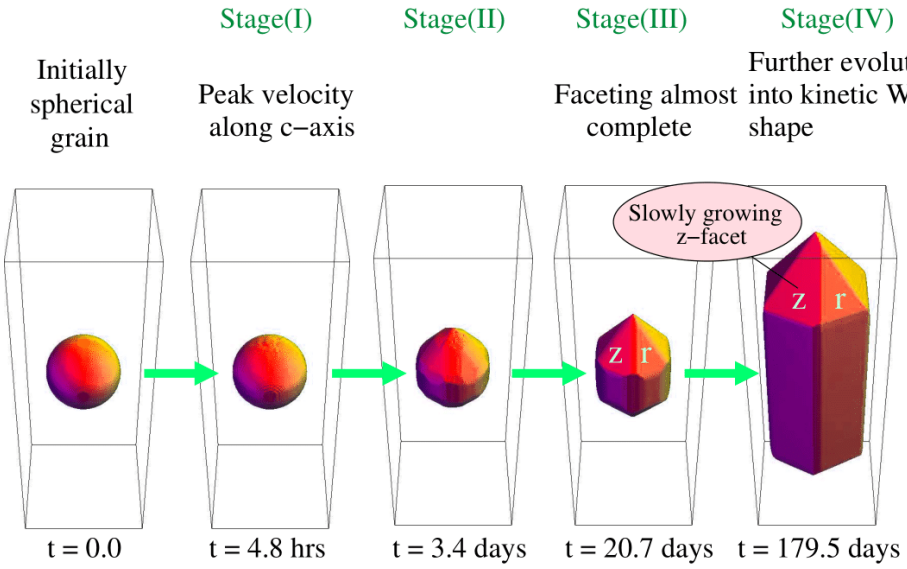

Figure 7.7: Simulated unrestricted quartz growth on a spherical grain of size 90μm *for the kinetic anisotropy strength parameter* $\delta = 115$. *The progression is shown at representative stages of time, also highlighted in figure 7.8.*

By utilizing the phase-field parameter set of table 7.3 and the set of vertex vectors for the capillary and kinetic anisotropy given in tables 7.1 and 7.2, simulations were performed for different value of the kinetic anisotropy strength parameter δ. The evolution of velocity along the crystallographic c-axis of the grain with respect to time is plotted in figure 7.8a. In the initial stages (i.e. $<$ 10 days) for all cases, the velocity along the c-axis exhibits a maximum value, and magnitude of the peak increases with increasing value of δ. After a growth period of about 20 days in the simulations, a constant velocity of

6.3×10^{-4} mm/day along the c-axis is achieved for all the cases. The pictures of figure 7.7 depict the simulated unrestricted growth of a single spherical grain for the case of $\delta = 115$ at five representative stages of time. As the syntaxial overgrowth cementation proceeds, the facets begin to appear ($t = 3.4$ days) and the velocity along the c-axis reduces. As soon as complete faceting occurs (somewhere close to $t = 20.7$ days), the velocity reaches a constant value. Hydrothermal experiments [36] report that the growth rate along the c-axis drops by a factor of around 20 when faceting is complete. In the present set of simulations, this growth behaviour of quartz is recovered for $\delta = 115$ at the growth conditions (table 7.3) considered in this work. Values of the initial velocity along the non-euhedral c-face and the post-euhedral velocity are 1.24×10^{-2} mm/day and 6.3×10^{-4} mm/day, respectively. The velocities of different directions/facets are listed in table 7.5. The simulated growth velocity of the reference z-facet matches well (around 7% difference) with the expected theoretical value determined using eq. (7.11) at the considered growth conditions. Due to the chosen set of vertex vectors for the kinetic anisotropy (from Wendler et al. [15]), that corresponds to a 3-D quartz crystal of prismatic habit having r-, m- and z- facets with a high-aspect ratio, the fastest growth is obtained along the c-axis, in coherence with the reported literature [50–52]. Consequently, an elongated crystal measuring 0.37 mm along the c-axis and 0.136 mm along the a-axis is obtained after around 180 days. Moreover, the anisotropy in kinetics, which accounts for the non-equivalent pyramidal facets (i.e. r- and z- facets) leads to the appearance of these facets at later stages due to a faster growth of r-facet as compared to the z-facet. This tendency of the pyramidal facets (i.e. higher growth rate of r-facet

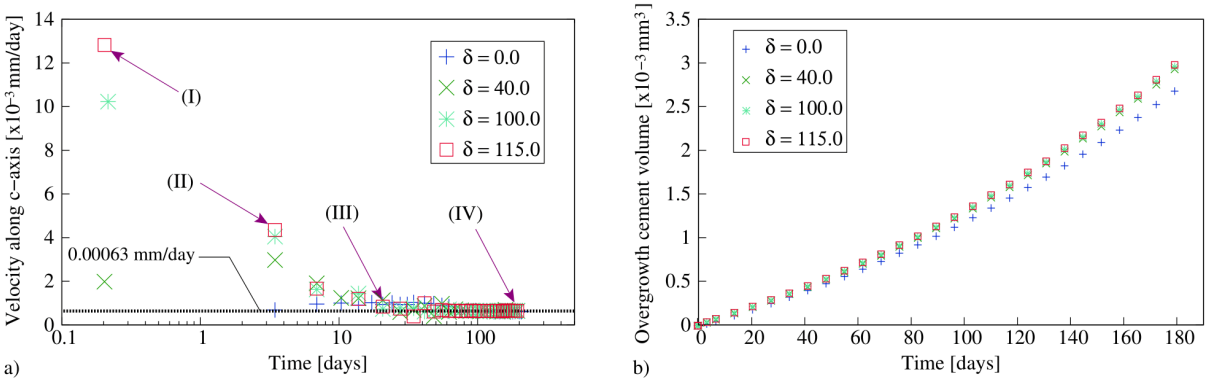

Figure 7.8: a) Plot of solid-liquid interface velocity along the c-axis over time in the simulated quartz crystal growth for different values of kinetic anisotropy strength parameter δ. A velocity drop by a factor of about 20 is obtained for $\delta = 115$. The highlighted points on the plot correspond to different stages of simulation shown in figure 7.7. b) Plot of overgrowth cement volume over time for different values of δ. Cement growth rate and volume increases with increase in the value of δ.

than z-facet) was reported in the early work of Ballman and Laudise [52] and later confirmed in the micro-infrared spectroscopic studies of Ihinger and Zink [53] and the hydrothermal experiments of Lander et al. [36]. Furthermore, the simulated quartz growth for $\delta = 115$ is in quantitative agreement with the theoretical value and the sequence of growth velocities is in qualitative agreement with the existing literature [36, 50–53].

In contrast to the unrestricted cement growth, overgrowths in the pore spaces mostly do not have sufficient distance for growth before reaching their euhedral form. Thus, the choice of δ, which controls the pre-euhedral growth in the simulations, plays a crucial role in predicting cement volumes in multigrain systems. Figure 7.8b depicts the plot of overgrowth cement volume over time for different values of δ, during free growth. As expected, an increase in the value of δ increases the overgrowth volume and the growth rate. This influence may increase in the multigrain systems where overgrowths on a large number of quartz grains grow simultaneously, while interfering with each other. Hence, the value of $\delta = 115$ is chosen for the remaining simulation studies in the forthcoming sections. The numerical time step Δt in table 7.3 is the maximum allowable value for $\delta = 115$, at which the simulations are numerically stable.

Table 7.5: Growth velocities predicted by the present phase-field model for $\delta = 115$.

Crystal facet or direction	velocity [$\times 10^{-4}$mm/day]
During pre-euhedral growth phase	
1. Non-euhedral c-face	124
During post-euhedral growth phase	
2. along c-axis	6.3
3. m $\{10\bar{1}0\}$	0.87
4. r $\{01\bar{1}1\}$	4.1
5. z $\{1\bar{1}01\}$	3.9
Theoretical	
6. z $\{1\bar{1}01\}$ (eq. (7.11))	4.1

7.5.1.2 Effect of grain size

The hydrothermal experiments of Lander et al. [36] reported that quartz cementation takes place at a slower rate on fine grains as compared to the coarser ones. The overgrowths on finer grains require lesser amount of cement volume and smaller distance to grow before reaching their euhedral shape. Therefore, smaller grains have a disadvantage of a shorter duration of growth on the faster growing non-euhedral surfaces, resulting

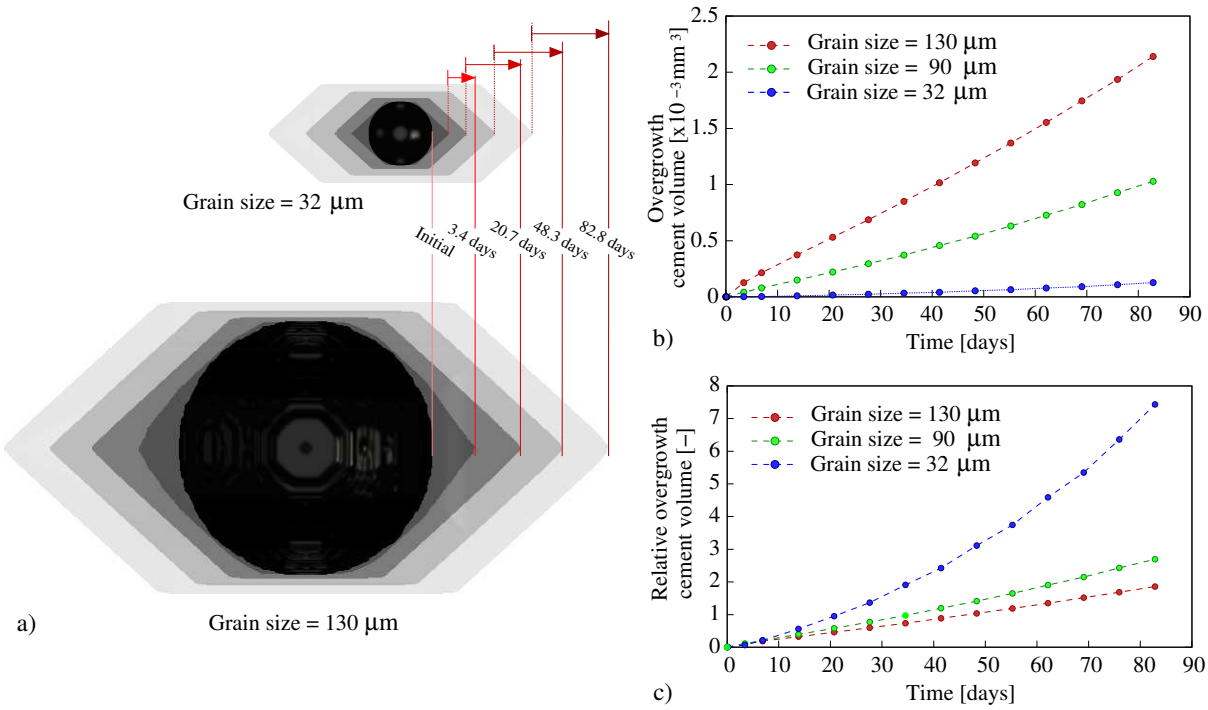

Figure 7.9: Undisturbed quartz cement growth simulations of spherical grains of different grain sizes. Different colored isosurfaces are shown at different stages of time. Plots depicting the temporal evolution of b) absolute and c) relative overgrowth cement volumes for different grain sizes.

in this size-dependency of growth rates. Under identical growth conditions, quartz cementation was simulated on two different-sized spherical grains as shown in figure 7.9a. Different stages of growth are shown in different colored isosurfaces for the two grains. The plots of temporal evolution of absolute and relative overgrowth cement volume are depicted in figure 7.9b,c. The relative overgrowth cement volume is defined as the overgrowth cement volume scaled by the initial volume of the grain. From the simulation results, the following inferences are drawn:

1. After 3.4 days, faceting is finished in the smaller grain while the larger one needs more time to develop flat facets.

2. As the quartz cementation proceeds, the gap between the overgrowths on the smaller and larger grain increases, as illustrated by the colored arrows in figure 7.9a.

3. The quartz cement growth rate and the overgrowth cement volumes decreases with decreasing grain size, as depicted in figure 7.9b.

4. The relative cement growth rate and the relative overgrowth cement volumes increases with decreasing grain size, see figure 7.9c. As the grain size decreases, the

surface area per unit volume increases at a rate that outstrips the rate reduction as a result of earlier faceting of smaller grains.

These numerical results demonstrate that the present model is capable of capturing the size-dependent growth behavior of quartz cements reported in the experiments [36].

7.5.1.3 Effect of polycrystallinity

Polycrystalline quartz aggregates are composed of multiple subdomains of quartz crystals known as the subgrains. Each subgrain possesses a distinct crystallographic orientation. In this section, the role of the crystallographic orientations of subgrains on the polycrystalline cement overgrowth volumes and growth rates is numerically analysed. For this purpose, the following two sets of quartz cement growth simulations were performed: spherical polycrystalline grains composed of I) two and II) eight equal subgrains. The simulated growth of these polycrystalline aggregates is then compared with that of an equal-sized unicrystalline grain.

7.5.1.3.1 Role of c-axis orientations of subgrains: Unicrystalline versus bicrystalline grains A single spherical grain and a bicrystalline grain with equal-sized subgrains differing in the c-axis orientations were considered. For the growth of bicrystalline grain, the following three different cases of the c-axis orientation difference (COD) of the subgrains were studied:

1. COD = 180^o: C-axes are anti-parallel to each other when the least possible hindrances can be expected. This system physically corresponds to the case of misaligned a-axis and parallel c-axes resulting in a grain boundary between the subgrains.

2. COD = 90^o: C-axes are perpendicular to each other when maximum interference is expected.

3. COD = 135^o: Intermediate case between the above two.

The isosurfaces at four representative stages of the simulated growth are shown in figure 7.10a-d, where the time lapsed at each stage in all the cases is highlighted in figure 7.10d. Figure 7.11 shows the plot of temporal evolution of overgrowth cement volume for all the cases. It is observed that the volume of overgrowth cement on the unicrystalline and the bicrystalline grain with anti-parallel c-axes is almost equal, see figures 7.10a,b and 7.11. In the latter case, the difference in the solid-solid and solid-liquid interface energies (i.e. $\gamma_{ss} = 1.91\gamma_{sl}$) results in the presence of local curvatures near the triple-junctions

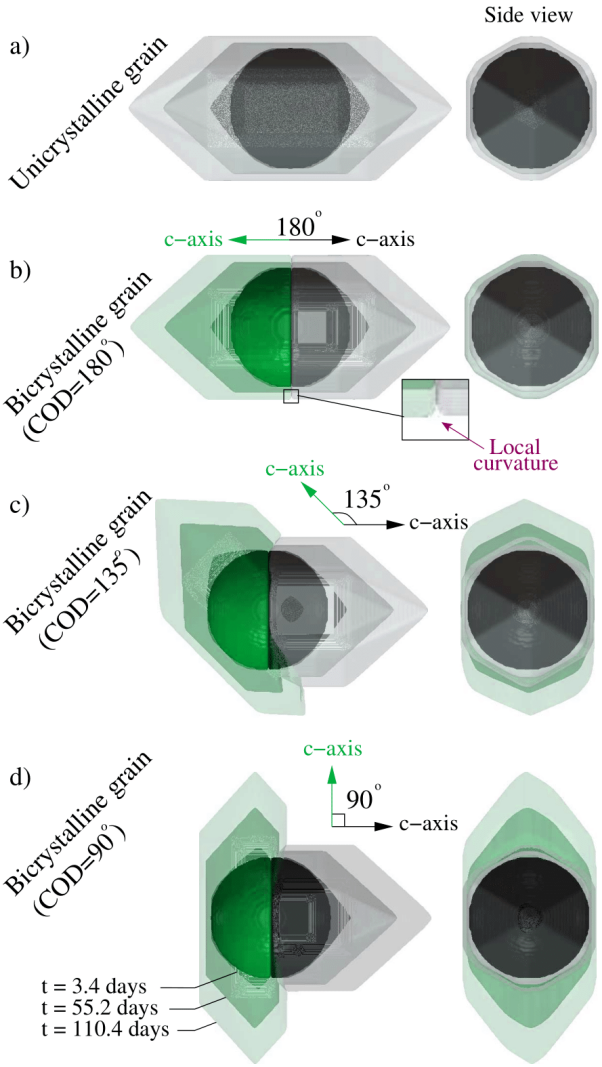

Figure 7.10: Undisturbed quartz cementation simulated on spherical a) unicrystalline and b)-d) three bicrystalline grains of same-sized subgrains possessing distinct c-axes orientations as given in the figure.

between the two solids and liquid phase, as highlighted in the zoomed inset picture of figure 7.10b. Nevertheless, the impact of curvatures on the overgrowth cement volumes is negligible, as reflected in the plot of figure 7.11. On comparison of the cement volumes for the three bicrystalline cases, a small but systematic deviation is observed. For the grain with the COD of 90^o, the cement volume is lower in the initial stages as compared to the one with a COD of 135^o. At later stages, this trend reverses, as depicted in the inset pictures of figure 7.11. The above-mentioned behavior can be rationalized on the basis of two opposing factors which are: I) level of mutual interference and II) the area of unhindered pyramidal facets (r- and z-facets). While the first factor causes the suppression of cement growth, the second one facilitates growth as the pyramidal facets grow at faster rates compared to the prismatic ones. The plots of cement volume versus

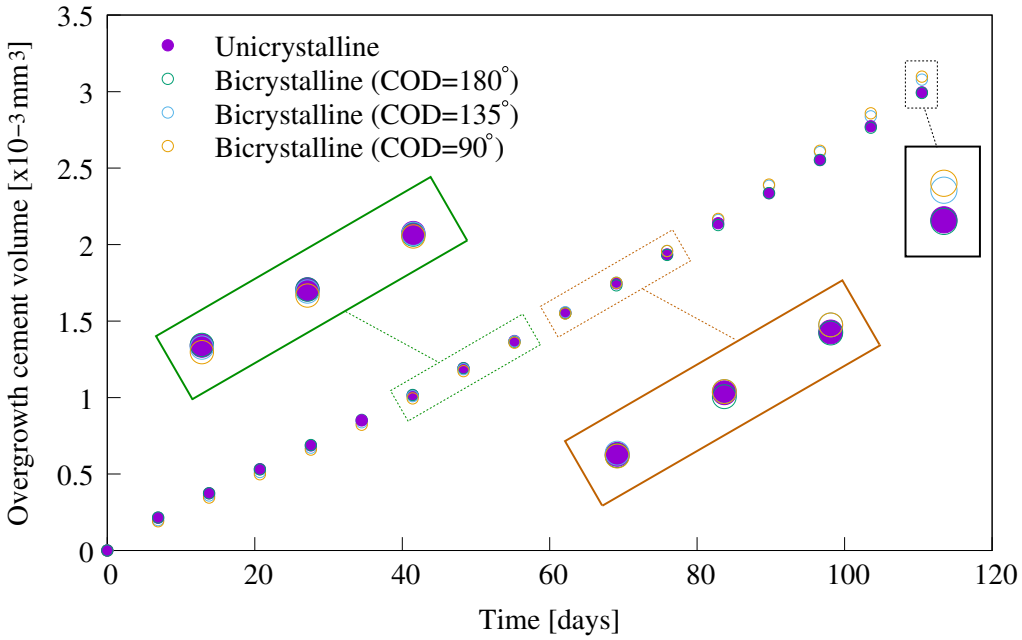

Figure 7.11: Temporal evolution of overgrowth cement volume for the undisturbed quartz cementation simulations for unicrystalline and bicrystalline grains. The cement volume is controlled by the mutual interference between the subgrains and the area of the unhindered pyramidal facets.

time (figure 7.11) indicate that the impact of mutual interference is intense in the early stages, resulting in a growth rate retardation when the c-axis are perpendicular to each other. On a comparative analysis of the simulated growth of the third (COD = 135^o) and the last case (COD = 90^o), it is further deduced that despite the occurance of a higher level of mutual hindrance in the last case, the impact of a higher number of freely growing pyramidal facets outstrips the rate retardation effect of the mutual hindrance, thereby resulting in a larger cement volume at the later stages in the last case. The simulation results reveal that an interplay of the two factors control the cement volumes on bicrystalline aggregates, and the cement volumes on some bicrystals might even be higher than on single crystals if the impact of the growth facilitating factor dominates the effect of growth retarding one.

7.5.1.3.2 Role of c-axis orientations of subgrains: Unicrystalline versus polycrystalline grains For a spherical polycrystalline grain composed of eight equal subgrains, the following three cases of the c-axis orientations of the subgrains were considered:

1. *Favorably oriented*: All subgrains can grow with the least possible hindrance from their neighbors.

2. *Unfavorably oriented*: All subgrains experience the maximum possible hindrance from their neighbors.

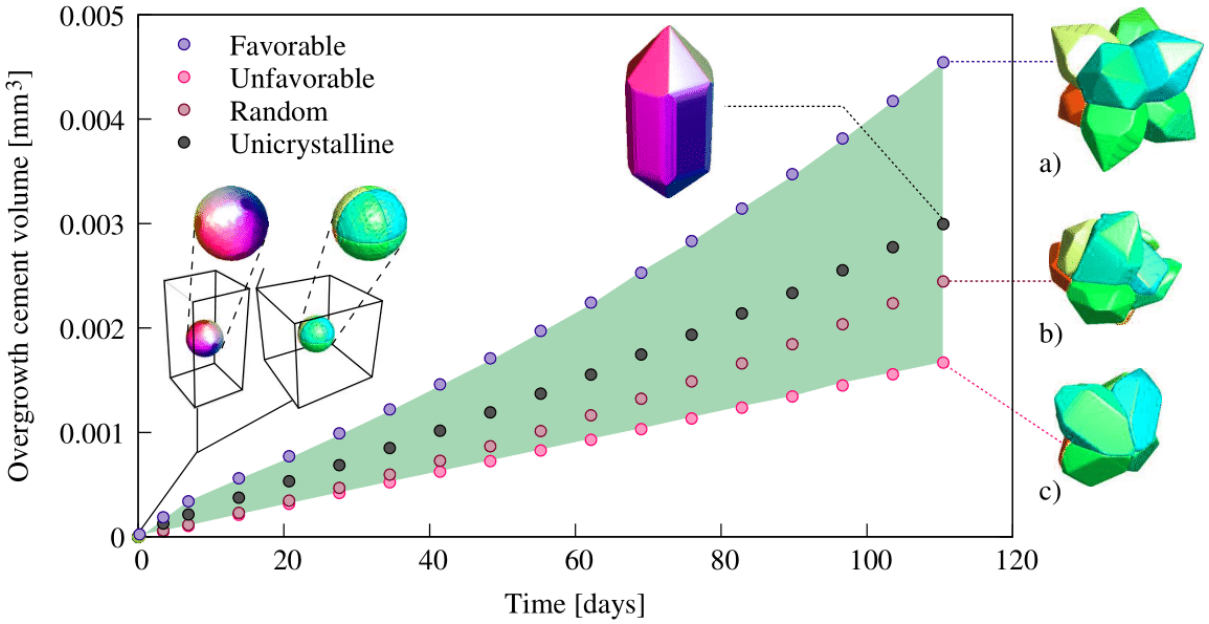

Figure 7.12: Temporal evolution of overgrowth cement volume for the simulations of undisturbed quartz cementation on the same-sized spherical I) unicrystalline and II) polycrystalline grains with eight equal subgrains for the cases of a) favorable, b) random and c) unfavorable orientation states of the subgrains. For the sake of visualization, different subgrains are illustrated in distinct colors and the liquid is not shown.

3. *Randomly oriented*: An intermediate configuration with randomly chosen c-axis orientation for all the subgrains.

Figure 7.12 depicts the plot of overgrowth cement volume versus time for the three polycrystalline cases along with a same-sized unicrystalline grain. The initial and final stages of the simulated growth for all the cases are depicted as inset pictures. It is observed that the cement volume for the favorable polycrystal is significantly higher than that of the unfavorable case. For the favorable case, the mutual hindrances are lowest and the surface area of more rapidly growing pyramidal facets is the largest, collectively accounting for the fastest quartz cement growth rate (therefore, the highest cement volume), and vice versa for the unfavorable case. As compared to the bicrystalline grain, for the polycrystalline grain, the difference in the cement volume and growth rate between the favorable and unfavorable cases is significantly larger. It can be deduced that, depending on the mutual hindrance and the area of unhindered faster growing surfaces, the growth rate and cement volume of all the intermediate orientation states of the subgrains, including the presented case of random configuration, would lie between the bounds defined by the favorable and unfavorable cases. The blue region in figure 7.12 depicts the regime of all the intermediate states. It is worthy to note that despite a higher pre-euhedral growth of the unicrystalline grain as compared to that on the relatively smaller individ-

ual subgrains of a same-sized polycrystalline one, the model-predicted growth rate of the favorable polycrytalline case is higher than the single crystal. This result indicates that the impact of a large number of faster growing surfaces outstrips the influence of higher pre-euhedral growth rate in the single crystal. Finally, on comparing the simulation results of bicrystalline and polycrystalline grains, it can be concluded that the maximum possible deviation in the overgrowth cement volume and the growth rate, originating due to the difference in the subgrain orientations, increases with increasing number of subgrains.

7.5.2 Simulation study: Quartz cementation in sandstones

Unlike free growth, syntaxial overgrowth quartz cementation in natural sandstones occurs in a complex manner, as it involves the interference of overgrowths growing on the neighbouring grains. For the sandstones containing polycrystalline grains, the additional interference of overgrowths growing on the subgrains of the same aggregate is also present. In order to evaluate the impact of cementation and polycrystallinity of aggregates on the evolving physical properties of sandstones, simulations were performed in three digital grain packs, namely unicrystalline, polycrystalline and mixed packs. For the simulations, identical parameters were chosen, see table 7.3. These packs were generated through the procedure elaborated in section 7.4. Figure 7.13 depicts the simulated microstructures visualized along a 2-D plane at three representative stages of growth. The colormap showing the *axial tilt* of the c-axis of each grain with respect to the positive z-axis is illustrated in figure 7.13l. The crystallographic orientations of the grains in the mixed pack are same as the corresponding grains of the unicrystalline and polycrystalline packs. The crystal morphologies and pore geometries for the three packs are analysed at an intermediate stage (t = 20.7 days). Cement growth on the unicrystalline grains results in the flat-faceted crystals surrounding the pores, see figure 7.13j. While, in the polycrystalline pack, overgrowths resulting in the partially as well as fully developed euhedral forms on the subgrains surround the pores, see figure 7.13k. Moreover, when the crystallographic orientations of two subgrains of the adjacent polycrystalline grains are identical, their overgrowths merge with each other without any grain boundary, as depicted in the growth of grains 1 and 2 in figures 7.13d-f,k. In the mixed packs, depending upon the crystalline structure of the neighboring grains, pores surrounded by the overgrowths of both unicrystalline as well as polycrystalline grains are present, see figure 7.13n. The simulated microstructures of the unicrystalline and mixed packs at the shown intermediate stage exhibit clear similarities with the natural textures (samples BQ_1 and BQ_2 from Busch et al. [42]) in terms of crystal morphologies and the remaining pore space, as highlighted in figure 7.13m,n. Figure 7.13n further illustrates a grain appearing from an

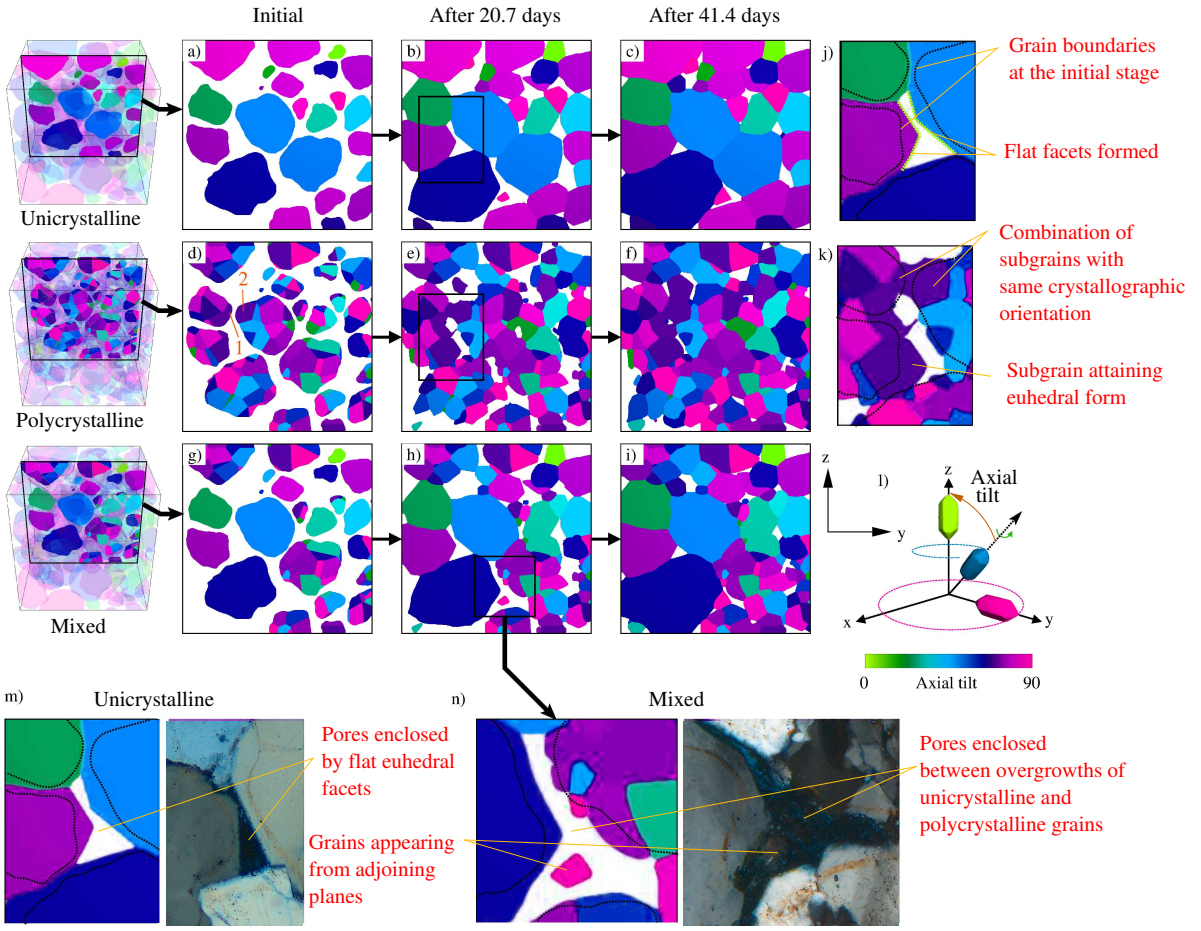

Figure 7.13: Visualization of the simulated textures along a 2-D plane for a)-c) unicrystalline, d)-f) polycrystalline and g)-i) mixed pack at three representative stages of growth. At the initial stage, all the grain packs exhibit an identical particle distribution, but different crystalline structure of grains. After 20.7 days, overgrowths on j) unicrystalline grains results in flat-faceted crystals, while in the k) polycrystalline pack, partially and fully euhedral overgrowths on individual subgrains are present. Overgrowths growing on neighbouring crystals merge with each other when their crystallographic orientations are identical. Due to a higher number of mutual interference and grain boundary interactions, polycrystalline pack exhibit a lower volume of cements than the unicrystalline pack at same stage of time, while the cement volume in mixed packs lie between the other two packs. l) Colormap defining the c-axis tilt or the axial-tilt of the grains. m)-n) Comparison of the simulated textures with the thin-section microphotographs of natural samples.

adjacent plane in the thin-section, that cannot be realised in similar 2-D studies, thereby advocating the utility of 3-D numerical investigations.

7.5.2.1 Impact on porosity and cement volumes

From the numerical data sets generated in the simulations reported in section 7.5.2, the temporal evolution of overgrowth cement volume and porosity for different grain packs is plotted in figure 7.14. The cement volume and porosity reduction are found to be inversely related to the polycrystalline composition of the packs. For an identical particle distribution, sandstones containing polycrystalline grains have a larger number of differently oriented crystals than the unicrystalline counterparts. Therefore, a higher level of mutual interference is expected in polycrystalline sandstones than unicrystalline ones, due to a larger number of grain boundary interactions in the former case. More rapid pre-euhedral cement growth on coarser grains may further account for the higher cement volumes on larger single crystals of unicrystalline sandstones in comparison with the individual overgrowths on relatively smaller subgrains of polycrystalline aggregates. Even if the total surface area of the unhindered faster growing pyramidal facets in the polycrystalline sandstones is higher than in the unicrystalline counterparts, these facets will have

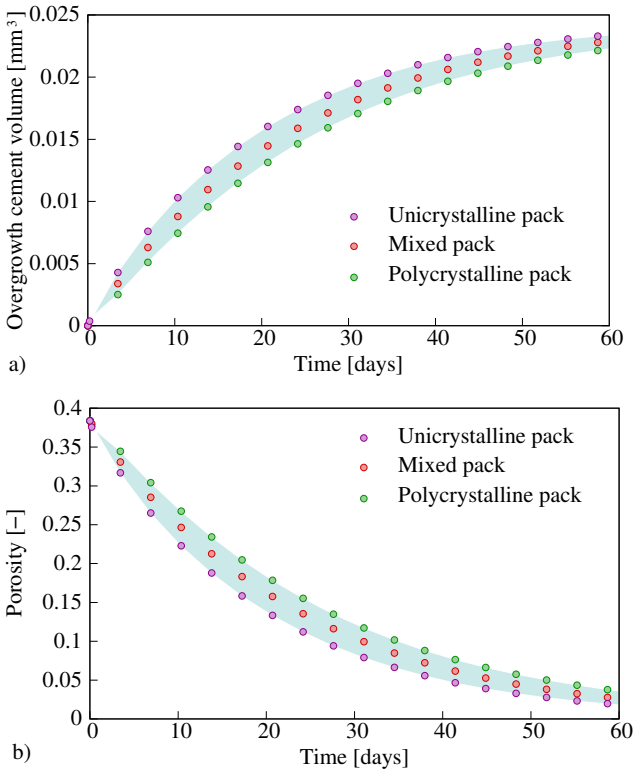

Figure 7.14: Temporal evolution of a) overgrowth cement volume and b) porosity for the unicrystalline, polycrystalline and mixed packs. The rate of porosity loss and cement growth are observed to be inversely dependent on the number of mutually interfering overgrowths. The porosity and cement volume of all the intermediate packs lie within the limits imposed by the unicrystalline and polycrystalline packs, as highlighted by the blue regions.

a limited distance to grow in the multigrain systems in order to outstrip the impact of the growth inhibiting factors. Owing to these reasons, the numerically cemented unicrystalline pack exhibits higher overgrowth cement volumes and thereby lower porosities than the polycrystalline one at all the stages of time. The abovementioned temporal behavior is in qualitative agreement with the hydrothermal experiments of quartz cementation in unicrystalline and polycrystalline sands performed by Heald and Renton [44]. It can be directly rationalized that in all the grain packs exhibiting an identical particle distribution but differing in the fraction of polycrystalline aggregates, the temporal evolution of the overgrowth cement volume and the porosity would lie within the grey regions of figures 7.14a,b. The presented mixed pack is one such case. Moreover, it is worthy to note that the curves of cement volume versus time exhibit a concave and monotonically increasing behavior. Previous numerical investigations of Lander et al [36] reported similar patterns in their results of quartz cements versus time for different-sized grain packs. The present work, additionally reveals that a similar kinetic behavior is expected for sandstones comprising of polycrystalline aggregates, but at lower cement volumes than the unicrystalline ones.

7.5.2.2 Impact on porosity-permeability correlations

In order to compute the permeability of the progressively cemented packs, digital pore structure was extracted at selected time stages by post-processing the numerical data sets of cement growth in the digital grain packs, generated in section 7.5.2. For each digital pore structure, fluid-flow simulation was performed using the Stokes equations (outlined in section 3.2 of chapter 3). From the computed fluid velocity field in the direction of the applied pressure drop, and utilizing the Darcy's law, permeability of each structure was obtained. Figure 7.15a depicts the temporal evolution of permeability for the three

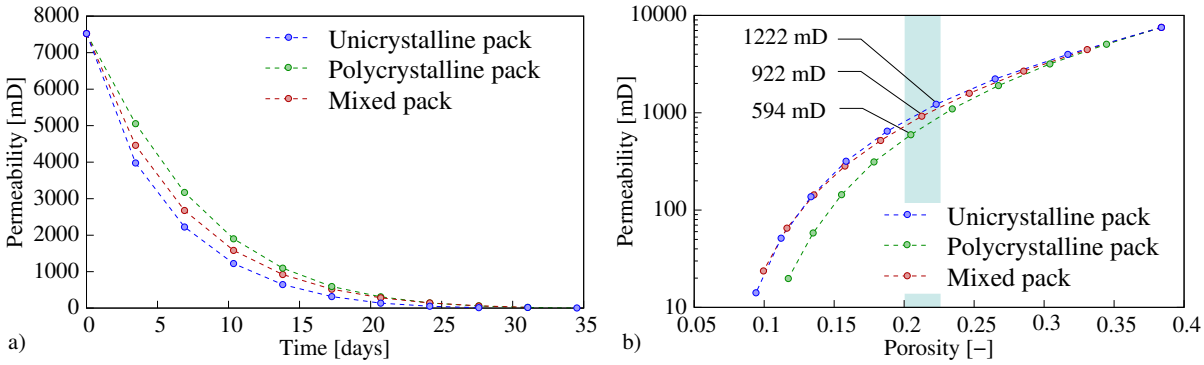

Figure 7.15: a) Permeability versus time and b) permeability versus porosity for the simulated quartz cementation in unicrystalline, polycrystalline and mixed packs. At equal porosity, packs with higher fraction of polycrystalline aggregates exhibit lower values of permeability.

digital grain packs. The rate of permeability reduction in response to cementation is found to be inversely related to the fraction of polycrystalline aggregates in the pack, consistent with the model predicted patterns for porosity versus time in figure 7.14b. In figure 7.15b, the plot of permeability versus porosity is shown for the three digital grain packs, where the permeability is plotted in logarithmic scale. The simulated quartz cementation causes a porosity reduction from an initial value of about 38 % in all the packs to different final values. The corresponding permeabilities are reduced from 7523 mD for the initial pore structure to the lowest values of about 10 mD. For the BQ_1 sample with about 77.07% unicrystalline and remaining polycrystalline grains (figure 7.4a), the experimentally measured porosity and permeability are 19.8 % and 1044 mD, respectively. The present numerical results suggest that at the above grain composition and porosity, the permeabilities of the grain pack are expected to lie between 922 mD (for mixed pack with 50% polycrystals) and 1222 mD (unicrystalline pack). For the sandstones with no intergranular clay, Walderhaug et al. [204] proposed a *modified Kozeny equation* that reads

$$\kappa = 8000 \frac{\varphi^3}{(100-\varphi)^2} d^2, \tag{7.13}$$

based on the data fitting analysis of 66 Norwegian continental shelf samples. In eq. (7.13), κ represents the permeability in milli Darcy (mD), φ denotes the porosity in percentage (%) and d is the grain size in millimeter (mm). For the BQ_1 sample with a porosity of 19.8 % and a mean grain size of 0.349 mm, a permeability of 1176 mD is predicted by eq. (7.13). It is worthy to note that, although the modified Kozeny equation does not take into account the impact of polycrystallinity of the aggregates, the sample permeability is well-estimated by this equation. These results show agreement between the permeability values predicted by experiments, simulations and the empirical modified Kozeny relation, thereby underpinning the efficacy of the procedure for generating the digital grain packs and the cementation modeling approach. From the plot shown in figure 7.15b, it is further deduced that at same porosity, sandstones composed of smaller number of polycrystalline aggregates are expected to be more permeable than those with a larger polycrystalline grain population. The same inference can also be derived from the fluid velocity fields for the three digital grain packs at similar porosity (i.e. 20-22.5 %), see figure 7.16. At same porosity, the permeability of a structure depends upon the geometrical parameters such as surface area, pore connectivity and tortuosity of the flow pathways. The porosity-permeability patterns observed in figure 7.15b are a result of the difference in the connected pore geometries of the progressively cemented packs.

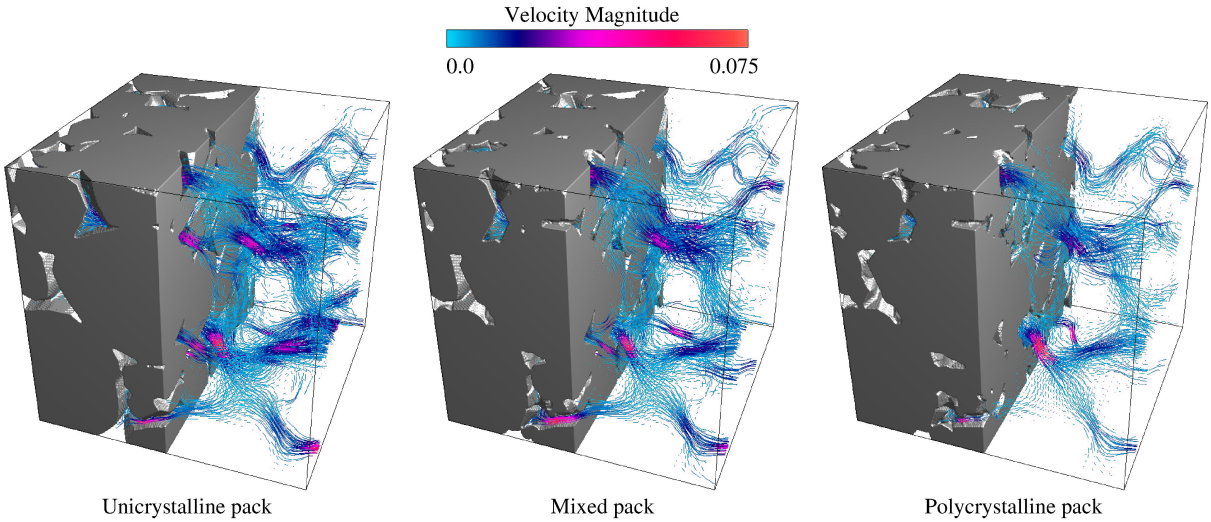

Figure 7.16: Visualization of the fluid velocity field component in the direction of the applied pressure drop for the three packs at 20-22.5 % porosity. Fluid velocities are higher for unicrystalline pack and decreases with increasing fraction of polycrystalline grain population.

7.6 Concluding remarks

Present work demonstrates a systematic approach of constraining the process of syntaxial quartz overgrowth cementation in sandstones which are composed of aggregates exhibiting a wide range of sizes, geometries and polycrystalline content at grain scale. As a starting point, the set of phase-field parameters was determined for the temperature and pressure matching the common reservoir diagenesis. In order to expedite the cementation in the simulations, the fluid supersaturation with respect to silica was chosen significantly higher than the actual values (i.e. close to unity), as the simulation time at the values close to unity was impractically large. The geometrical parameters controlling the quartz crystal shape and the relative growth rates of different facets were adopted from Wendler et al. [15]. From the unrestricted growth simulations on single crystals, a pre-euhedral to post-euhedral growth rate ratio of about 20 (as reported in the hydrothermal experiments of Lander et al. [36]) was recovered for the kinetic anisotropy strength parameter $\delta = 115$. The z-facet velocity obtained during the post-euhedral growth phase in the simulation matches well ($\sim$ 7% difference) with the theoretical value. Moreover, the sequence of the growth velocity of different facets of quartz is consistent with the existing literature [36, 50–53]. The present model while accounting for the pre-euhedral growth tendency of the quartz cements is able to capture the influence of grain size on the grain rates. Based on the simulation results of undisturbed growth on bicrystalline and polycrystalline aggregates for different cases of crystallographic orientations of subgrains, it is found that the net overgrowth cement volume is controlled by an interplay of two opposing factors. One, the mutual hindrance

originating due to the difference in the crystallographic orientations of the neigbouring crystals, suppressing the growth. Two, the area of unhindered faster growing pyramidal facets, that facilitates the growth. In the polycrystalline quartz aggregates, as the number of subgrains increases, the maximum possible difference in the net cement volume for different crystallographic orientations also increases. Analysis of the simulated unrestricted cement growth on same-sized unicrystalline and the favorably oriented polycrystalline grain reveal that, in spite of the impact of grain size that causes more rapid cementation of larger single crystals than the relatively smaller individual subgrains of a polycrystalline aggregate, the net cement volume on the latter might be higher if the subgrains are favorably orientated.

In the next part, a systematic methodology was presented for the generation of digital grain packs analogous to natural sandstones in terms of grain geometries, size distribution and depositional porosity. Simulations of syntaxial quartz cementation in these grain packs are able to recover several petrophysical and petrographical aspects of the process in natural sandstones, which are summarized as follows:

1. Microstructures of the numerically cemented digital grain packs show clear similarities with the natural samples [42] in terms of crystal morphologies and pore geometries.

2. Quartz cement growth rate decreases with increasing fraction of the population of polycrytalline quartz aggregates in sandstone, consistent with the previous experimental findings [44]. In the grain packs comprising of polycrystalline aggregates, the cement overgrowths have to compete with those growing on the same as well as the neighboring grains. The present simulation results indicate that two important growth inhibiting factors collectively contribute to the slower cementation in polycrystalline sandstones, which are as follows: I) mutual interference among the overgrowths and II) earlier attainment of euhedral shape of relatively smaller subgrains in polycrystalline aggregates. During the post-euhedral growth stages, even if the polycrystalline overgrowths possess a larger net surface area of unhindered faster growing pyramidal facets, these surfaces will have a limited intergranular space to grow in order to surpass the impact of the above-mentioned growth retarding factors.

3. For the simulated quartz cementation in the digital grain packs, the obtained cement volume versus time plots exhibit a concave non-linear behavior for all the packs. Previous numerical investigations of Lander et al. [36] predicted concave patterns in the temporal evolution of quartz cements for unicrystalline packs. The present work further reveals that similar concave patterns are expected for

sandstones composed of different populations of polycrystalline aggregates, albeit at lesser cement volumes.

The fluid-flow simulations through the digital pore space of the packs for computing the permeabilites at different stages of time, reveal that:

1. Sandstones composed of larger fractions of single crystals are more permeable than equally porous sandstones that contain larger populations of polycrystalline aggregates, which can be attributed to the complex pore geometries in the latter case.

2. The calculated porosity and permeability values of the numerically cemented digital grain packs are in agreement with the experimentally obtained values corresponding to the natural sample.

The present model, in its current form, can be utilized to simulate the growth of different minerals (e.g. alum, calcite, etc.), while accounting for the impact of inert surfaces (e.g. clay coats etc.). As the employed explicit time update scheme for the phase-fields is conditionally stable thereby imposing the computational constraints, it is imperative to develop unconditionally stable schemes that may relax the restriction on the choice of numerical time step. This would, in turn, allow the setting of lower and more realistic fluid supersaturations in the phase-field model. Moreover, the model is presently devoid of the impact of fluid salinity, and can be extended by modifying the driving force of crystallization in an appropriate manner such that the deviation of the fluid from the ideal solution behavior is accounted. The above-mentioned extensions, when implemented in the MPF model, would enable the simulation of quartz cementation at realistic fluid supersaturations in the sandstones comprising of large number of microquartz and chert grains. With these future directions, the present work paves the way for more advanced cementation models for the purpose of reservoir quality modeling prediction.

Part IV
Fracture propagation in sandstone

Chapter 8

Brittle anisotropic fracture propagation in sandstone

At microscale, quartz arenites are majorly composed of detrital quartz grains along with a minor fraction (usually less than 10%) of other minerals (e.g. feldspar, lithic fragments) [205]. These grains and other minerals are cemented together due to the precipitation of authigenic cement phases (e.g. silica, calcite) [30, 87, 88]. Each quartz grain exhibits a unique crystallographic orientation, thereby resulting in the presence of grain boundaries between differently oriented grains. The material properties of quartz vary depending upon the crystallographic direction. For the quartz crystals exhibiting the prismatic growth habit (figure 8.1a) the fracture toughness has been experimentally reported to differ along the c-axis and the a-axes [89–93], thereby resulting in the presence of preferred cleavage planes for fracture growth within each quartz grain [see e.g. chapter 4 of Guéguen and Boutéca 4]. Moreover, when the grain boundaries between different grains offer a lower resistance for the crack propagation due to e.g. grain boundary corrosion from the chemically active fluids [94] or the presence of a weaker binding mineral, intergranular fracture propagation may take place. Thus, as the crack tip reaches a grain boundary, based on the local stress state and the fracture toughness in the locality of the tip, the following three types of fracturing may occur [4, 5, 94]:

1. **Intergranular**: Fracturing along the grain boundaries.
2. **Transgranular**: Fracturing through the grains.
3. **Mixed**: Combination of the above two modes.

Crack pathways are also affected by the presence of other mineral phases exhibiting different material properties. Owing to these material heterogeneities and anisotropies at grain scale, the process of microfracturing in sandstones is a highly complicated phenomenon.

In this chapter, a multiphase-field (MPF) model is adapted for simulating the process of brittle and anisotropic crack propagation in quartz sandstones at micro-to-mesoscopic length scales. In this phase-field based approach, the grain boundaries between the different geological solid phases (i.e. quartz grains, other minerals) and the crack surfaces are treated as diffuse interfaces. The two novel aspects of the present work include the formulations of *anisotropic* and *reduced interfacial* crack resistance. The anisotropic crack resistance formulation accounts for preferred cleavage planes for fracture growth within the bulk region of each quartz grain, and the relevant parameters are calibrated based on fracture toughness values along the c-axis and the a-axes, which are provided in literature [91, 92]. Moreover, in order to assign lower fracture toughness along the grain boundaries, the reduced interfacial crack resistance formulation is incorporated, that may result in intergranular fracturing. With these two novelties, the present MPF model of fracture is able to simulate the competition between intergranular and transgranular crack propagation, depending upon the grain boundary attributes, while also exhibiting preferential cleavage planes for fracture growth within each grain. The present MPF model, in the full parameter space, can serve as a powerful computational tool for the analysis of complex crack propagation processes in polycrystalline systems composing of grains with distinct elastic properties, fracture toughness, cleavage planes and nature of grain boundaries. The capabilities of the present model are demonstrated in a systematic manner through a set of representative numerical examples.

The present chapter is organized as follows. In section 8.1, the numerical aspects of modeling fracture propagation within the MPF framework, including the anisotropic and the reduced interfacial crack resistance formulations, are elaborated. The set of representative numerical examples showcasing the performance and capabilities of the two above-mentioned formulations are presented in section 8.2. The chapter is concluded in section 8.3 with a brief summary of the present numerical investigation and an outlook on the directions for further work.

8.1 Numerical aspects

For the numerical investigations of this present chapter, the MPF model of fracture discussed in chapter 4 is adapted. The material parameters of quartz utilized in the simulations are listed in table 8.1. Quartz exhibits an elastic anisotropy as reported in literature [206, 207]. However, for the present work, in order to account for the tension-compression split [136] which was formulated for the materials obeying isotropic elastic behavior, the quasi-isotropic elastic constants, determined by Heyliger et al. [206], were chosen. The Lamé's parameters λ^{α} and μ^{α}, which enter the computation of phase-

Table 8.1: Quartz material parameters

Parameter	Symbol	Value	Reference
Young's modulus	E	99.45 GPa	[206]
Poisson's ratio	ν	0.06	[206]
Lamé's first parameter for quartz	λ^{Qtz}	6.39 GPa	-
Lamé's second parameter for quartz	μ^{Qtz}	46.91 GPa	-
Fracture toughness along c-axis	$K_{\mathrm{Ic}}^{\text{c-axis}}$	2.4 MN m$^{-3/2}$	[91]
Fracture toughness along a-axis	$K_{\mathrm{Ic}}^{\text{a-axis}}$	2.14 MN m$^{-3/2}$	[92]
Crack resistance along c-axis	$G_{\mathrm{c}}^{\text{c-axis}}$	57.71×10^{-6} J/mm^2	-
Crack resistance along a-axis	$G_{\mathrm{c}}^{\text{a-axis}}$	45.87×10^{-6} J/mm^2	-

specific isotropic stiffness tensor $\mathbb{C}^{\alpha}$, are calculated as $\lambda^{\alpha} = E\nu/[(1+\nu)(1-2\nu)]$ and $\mu^{\alpha} = E/[2(1+\nu)]$. For keeping the computational costs low, the present investigation is limited to 2-D. All the simulations were performed under the plane-strain assumption. Therefore, the crack resistance G_{c} is computed as $G_{\mathrm{c}} = K_{\mathrm{Ic}}^2(1-\nu^2)/E$. The phase-field parameter set utilized for the simulations is given in table 8.2. The anisotropic crack resistance formulation, its suitability for the multigrain system of quartz sandstones, and adaptation procedure are elucidated in section 8.1.1. Section 8.1.2 elaborates the reduced interfacial crack resistance formulation for controlling the fracture toughness along the grain boundaries.

8.1.1 Anisotropic crack resistance formulation

In the quartz grains of prismatic growth habit (with one c-axis, three a-axes and the families of $m\{10\bar{1}0\}$ $z\{1\bar{1}01\}$ and $r\{01\bar{1}1\}$ facets, see figure 8.1a), the fracture tough-

Table 8.2: Numerical and phase-field model parameters.

Parameter	Symbol	Value
Grid spacing	Δx	1.0
Time step width	Δt	1.0
Length scale parameter for crack surface	ε_{c}	4.0
Relaxation parameter	μ_{c}	2166.0
Critical crack phase-field	$\phi_{\mathrm{c}}^{\mathrm{crit}}$	0.9
Scalar constant 1	k	0.5
Scalar constant 2	k_w	1

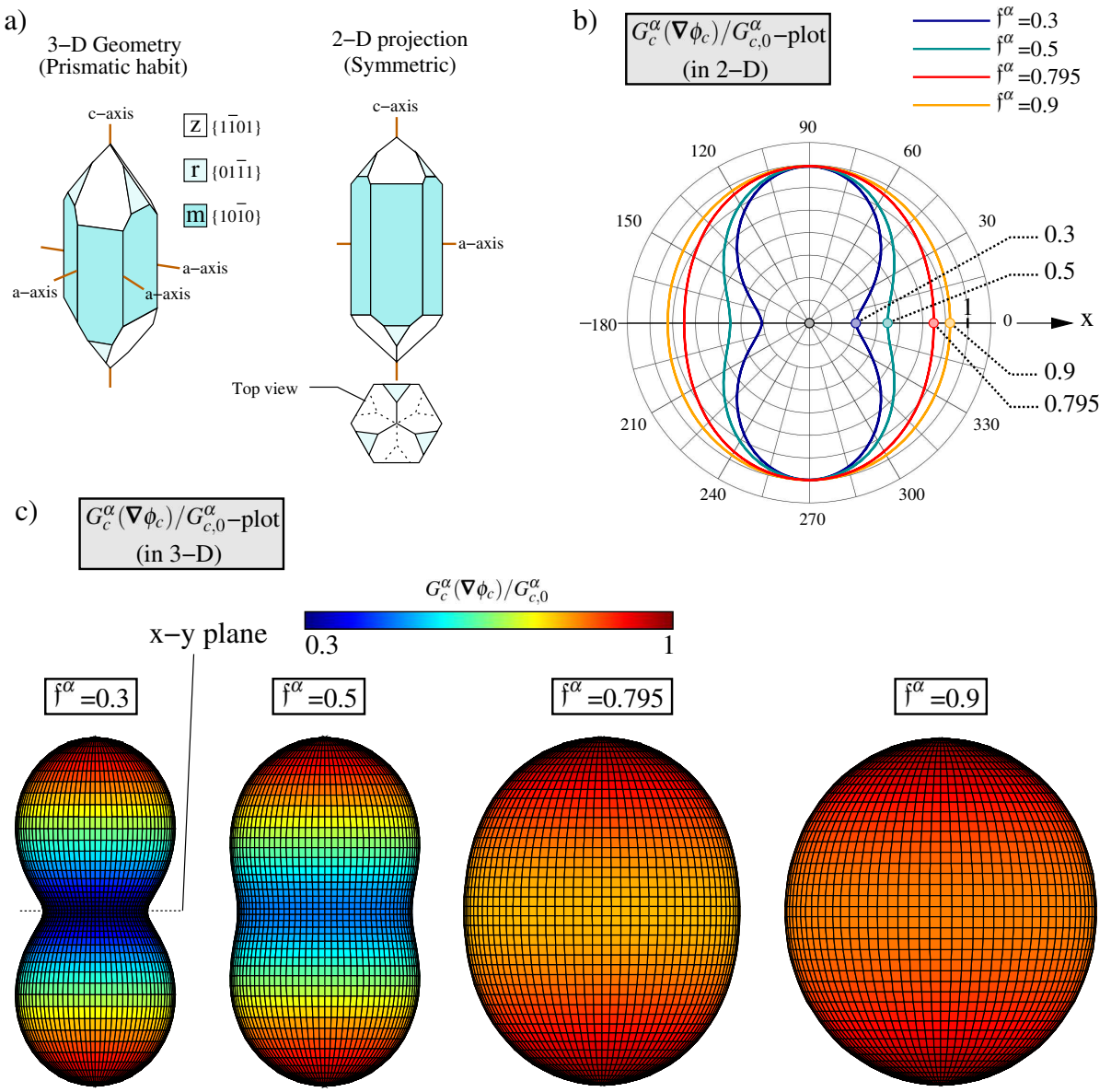

Figure 8.1: a) 3-D geometry of the euhedral form of a quartz crystal according to the prismatic growth habit, along with its symmetric 2-D projection. This geometry contains one c-axis, three a-axes and families of m-, z- and r-facets (six in each family). Polar plots of normalized crack resistance ($G_c^\alpha(\nabla\phi_c)/G_{c,0}^\alpha$) for different values of the anisotropy strength factor $\mathfrak{f}^\alpha$ in b) 2-D and c) 3-D. The lowest values of the normalized crack resistance are found in the x-y plane for the 3-D plots (along the x-axis for the 2-D plots), which correspond to the a-axes plane of the prismatic quartz crystal in 3-D (a-axis direction in 2-D).

ness has been reported to vary with the crystallographic direction [89–93]. Table 8.1 lists the values of fracture toughness and crack resistance along the c- and the a-axis of quartz, provided in the works of Norton & Atkinson [91] and Ferguson et al. [92], respectively. As this growth form of quartz possesses three a-axes lying in a plane perpendicular to the c-axis, an isotropic crack resistance is assumed in the a-axes plane.

In order to model this transversely anisotropic behavior, an anisotropy function of the following mathematical form is chosen for the spatial variation of the crack resistance within each quartz grain:

$$G_{\mathrm{c}}^{\alpha}(\boldsymbol{\nabla}\phi_{\mathrm{c}}) = G_{\mathrm{c},0}^{\alpha}\Big[\mathfrak{f}_{\mathrm{x}}^{\alpha}\left\{\mathfrak{n}_{\mathrm{c,x}}^{\alpha}(\boldsymbol{\nabla}\phi_{\mathrm{c}})\right\}^2 + \mathfrak{f}_{\mathrm{y}}^{\alpha}\left\{\mathfrak{n}_{\mathrm{c,y}}^{\alpha}(\boldsymbol{\nabla}\phi_{\mathrm{c}})\right\}^2 + \left\{\mathfrak{n}_{\mathrm{c,z}}^{\alpha}(\boldsymbol{\nabla}\phi_{\mathrm{c}})\right\}^2\Big] \tag{8.1}$$

Here, the prefactor $G_{\mathrm{c},0}^{\alpha}$ represents the crack resistance of phase α and the term in square brackets incorporates the crack resistance anisotropy in phase α. In this term, $\mathfrak{n}_{\mathrm{c,x}}^{\alpha}(\boldsymbol{\nabla}\phi_{\mathrm{c}})$, $\mathfrak{n}_{\mathrm{c,y}}^{\alpha}(\boldsymbol{\nabla}\phi_{\mathrm{c}})$ and $\mathfrak{n}_{\mathrm{c,z}}^{\alpha}(\boldsymbol{\nabla}\phi_{\mathrm{c}})$ denote the x-, y- and z- components, respectively, of the rotated unit vector $\mathfrak{n}_{\mathrm{c}}^{\alpha}(\boldsymbol{\nabla}\phi_{\mathrm{c}})$, which is computed as

$$\mathfrak{n}_{\mathrm{c}}^{\alpha}(\boldsymbol{\nabla}\phi_{\mathrm{c}}) = -\boldsymbol{Q}^{\alpha}\frac{\boldsymbol{\nabla}\phi_{\mathrm{c}}}{|\boldsymbol{\nabla}\phi_{\mathrm{c}}|}. \tag{8.2}$$

In eq. (8.2), $\boldsymbol{Q}^{\alpha}$ denotes the phase-specific rotation matrix that describes the solid-phase anisotropy according to the crystallographic orientation of each quartz grain. The scalar parameters $\mathfrak{f}_{d}^{\alpha}, \in [0,1]$ for $d = x$ and y represent the phase-specific anisotropic strength factors. These factors, when chosen in the range (0,1), reduce the crack resistance in their respective directions in the rotated coordinate system. Setting $\mathfrak{f}_{\mathrm{x}}^{\alpha} = \mathfrak{f}_{\mathrm{y}}^{\alpha} = \mathfrak{f}^{\alpha} \in (0,1)$ lowers the crack resistance isotropically in the x-y plane (or x-axis in case of 2-D) that corresponds to the a-axes plane (or along the a-axis direction in case of 2-D) of a randomly orientated quartz grain. The choice $G_{\mathrm{c}}^{\alpha,\text{c-axis}} = G_{\mathrm{c},0}^{\alpha}$ along the c-axis results in a crack resistance value of $G_{\mathrm{c}}^{\alpha,\text{a-axis}} = \mathfrak{f}^{\alpha}G_{\mathrm{c},0}^{\alpha}$ in the a-axes plane, leading to preferred directions for fracture propagation. For different values of the anisotropic strength factor $\mathfrak{f}^{\alpha}$, the 2-D and 3-D polar plots of the normalized crack resistance $G_{\mathrm{c}}^{\alpha}(\boldsymbol{\nabla}\phi_{\mathrm{c}})/G_{\mathrm{c},0}^{\alpha}$ are depicted in figures 8.1b and 8.1c-f, respectively. The choice $\mathfrak{f}^{\alpha} = 1$ represents the case of isotropic crack resistance with the value $G_{\mathrm{c},0}^{\alpha}$ in all the crystallographic directions, and the normalized polar plot for this case would represent a sphere of unit radius. The choice $\mathfrak{f}^{\alpha}$=0.795 corresponds to the case of Brazilian quartz calculated using the reported fracture toughness values along the c- and a-axis as follows

$$\mathfrak{f}^{\mathrm{Qtz}} = \frac{G_{\mathrm{c}}^{\text{a-axis}}}{G_{\mathrm{c}}^{\text{c-axis}}} = \left[\frac{K_{\mathrm{Ic}}^{\text{a-axis}}}{K_{\mathrm{Ic}}^{\text{c-axis}}}\right]^2 = 0.795. \tag{8.3}$$

In contrast to the works of Nguyen et al. [167] and Liu and Juhre [165], the present formulation (eq. (8.1)) introduces an anisotropy in both, potential and gradient, terms of the diffuse crack surface energy, thereby resulting in a near-uniform interface width in different anisotropic solid phases. For the present case, where a non-zero crack phase-field is expected in the entire computational domain (due to the chosen one-sided well potential), if the interface width is defined between the isosurfaces (isolines in case of 2-D) $\phi_{\mathrm{c}} = 0.15$ and $\phi_{\mathrm{c}} = 0.85$, the presented anisotropic formulation ensures a near-constant interface width.

8.1.2 Reduced interfacial crack resistance formulation

In a diffuse α-β interface, the normal interpolation according to eqs. (4.3) and (4.4) in chapter 4 yields the following expression for the effective crack resistance

$$\begin{aligned} G_c(\phi_\alpha, \phi_\beta, \nabla\phi_c) &= \phi_\alpha G_c^\alpha(\nabla\phi_c) + \phi_\beta G_c^\beta(\nabla\phi_c) \\ &= G_c^\alpha(\nabla\phi_c) + (G_c^\beta(\nabla\phi_c) - G_c^\alpha(\nabla\phi_c))\phi_\beta \end{aligned} \tag{8.4}$$

in terms of the crack resistances $G_c^\alpha(\nabla\phi_c)$ and $G_c^\beta(\nabla\phi_c)$ of the α and β phase, respectively. For the spatial variation of the phase-fields ϕ_α and ϕ_β (figure 8.2a), a sinusoidal profile was utilized, as illustrated in figure 8.2b. In order to model a lower crack resistance along the grain boundaries, a modified interpolation of the following mathematical form

$$\begin{aligned} G_c^{\text{red}}(\phi_\alpha, \phi_\beta, \nabla\phi_c) &= G_c(\phi_\alpha, \phi_\beta, \nabla\phi_c) \\ &\quad - 4\phi_\alpha\phi_\beta\left[G_c(\phi_\alpha, \phi_\beta, \nabla\phi_c) - \frac{\zeta}{2}\left\{G_c^\alpha(\nabla\phi_c) + G_c^\beta(\nabla\phi_c)\right\}\right] \end{aligned} \tag{8.5}$$

is incorporated. The modified interpolation (eq. (8.5)) renders the crack resistance a third order polynomial function of ϕ_α or ϕ_β. ζ is an interfacial crack resistance reduction factor

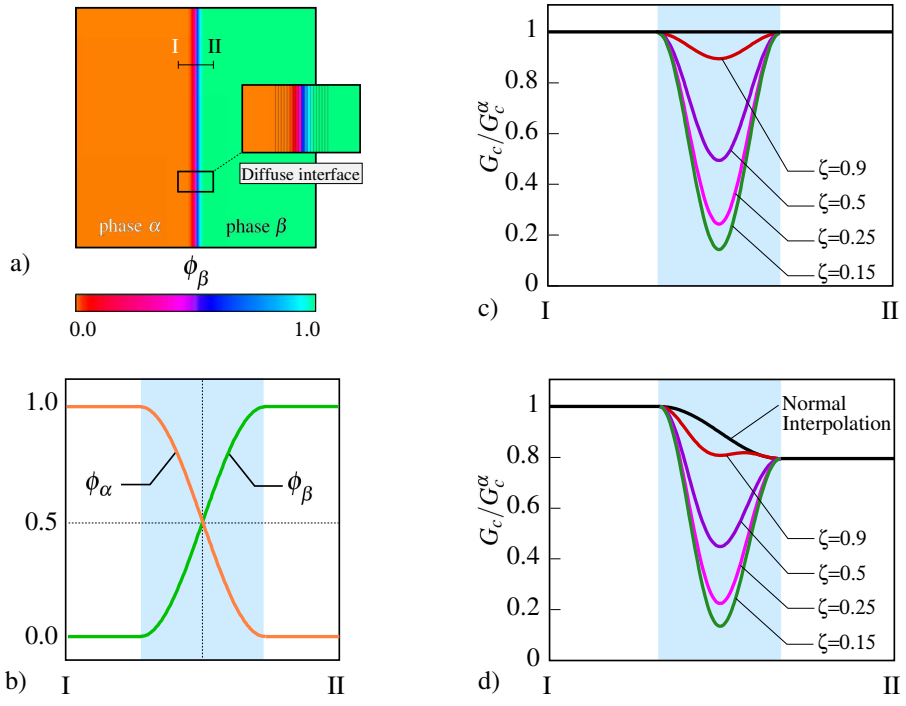

Figure 8.2: a) A two-phase specimen comprising of solid phases α and β with a diffuse grain boundary. b) Spatial variation of solid phase-fields ϕ_α and ϕ_β along the line joining the points I and II, illustrating a smooth and monotonic transition in the diffuse interface region (in blue). Spatial variation of the normalized crack resistance ϕ_α and ϕ_β for different values of the interfacial crack resistance reduction factor ζ along the line I-II for the case of c) G_c^β/G_c^α=1.0 and d) G_c^β/G_c^α=0.795.

that determines the magnitude of the crack resistance along the isosurface $\phi_\alpha = \phi_\beta = 0.5$ of the α-β interface. For different values of ζ, the plot of normalized crack resistance $G_{\mathrm{c}}^{\mathrm{red}}(\phi_\alpha, \phi_\beta, \boldsymbol{\nabla}\phi_{\mathrm{c}})/G_{\mathrm{c}}^{\alpha}(\boldsymbol{\nabla}\phi_{\mathrm{c}})$ along the line I-II (of figure 8.2a) according to eq. (8.5), when $G_{\mathrm{c}}^{\beta}/G_{\mathrm{c}}^{\alpha}$=1, is depicted in figure 8.2c. The reduced interfacial interpolation for the case of quartz, where the maximum difference in the crack resistance between the two different grains can be 0.795 (as elaborated in section 8.1.1), is depicted in figure 8.2d. The variation of the normally interpolated crack resistance according to eq. (8.4) is also depicted in black color in figure 8.2d. In the present work, a reduction of the interfacial crack resistance, in a smooth and continuous manner, is realized due to the diffuse interface description of the grain boundaries, thereby highlighting the utility of the MPF approach with separate phase-fields for each grain.

8.2 Representative numerical examples

Section 8.2.1 presents a detailed analysis of the simulation results of crack propagation in a two-phase specimen with different but isotropic crack resistances. In the next section 8.2.2, the numerical results showcasing the performance of the crack resistance anisotropy formulation are presented. Subsequently, the impact of lower grain boundary resistance based on the reduced interfacial crack resistance formulation of section 8.1.2 is elucidated through the simulations in section 8.2.3. Finally, in section 8.2.4, applications of the two formulations for simulating fracture growth in exemplary geological structures are presented. In the numerical settings of all the presented examples, the solid and crack phase-fields are initialized such that the summation constraint $\left(\sum_{\alpha=1}^{N} \phi_\alpha = 1 - \phi_{\mathrm{c}}\right)$ is locally satisfied.

8.2.1 Two-phase specimen with unequal isotropic crack resistances

A two-phase specimen with a pre-existing crack is considered as shown in figure 8.3a. At the upper edge of the computational domain, an incremental displacement loading is applied. The two solid phases of the specimen, namely α and β, differ in magnitude of crack resistance, while their elastic properties (i.e. E and ν) are assumed to be identical and are same as those given in table 8.1. The crack is described using a diffuse crack phase-field ϕ_{c} as illustrated in figure 8.3b. The crack resistance for phase α is set to $G_{\mathrm{c}}^{\alpha} = (K_{\mathrm{Ic}}^{\text{c-axis}})^2(1-\nu^2)/E = 57.71 \times 10^{-6}$ J/mm^2, corresponding to the c-axis fracture toughness of quartz. For varying values of the crack resistance G_{c}^{β} of phase β, simulations were performed. For the sake of convenience, a crack resistance ratio $R_{\mathrm{c}} = G_{\mathrm{c}}^{\beta}/G_{\mathrm{c}}^{\alpha}$

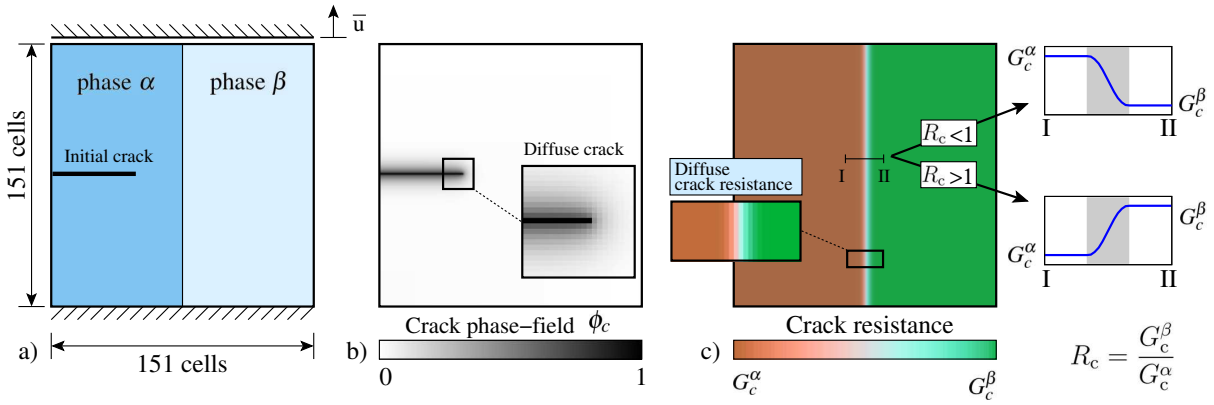

Figure 8.3: a) Geometry and boundary conditions of the two-phase specimen with a preexisting crack under uniaxial tension. b) Diffuse interface description of fracture using crack phase-field $\phi_c \in [0, 1]$. c) Diffuse interface description of grain boundary along which the crack resistance varies from G_c^α in phase α to G_c^β in phase β, smoothly and monotonically.

is defined for the present set of simulations. For the variation of the crack resistance along the diffuse grain boundary, a sinusoidal profile was generated, see figure 8.3c. For different values of R_c, the crack growth occurs along a horizontal straight line, which is perpendicular to the direction of the applied displacement loading, see figure 8.4a. When the fracture tip reaches the position (III) during propagation, the contour plots of displacement, crack driving force and stress fields are shown in figure 8.4b-f. As the crack resistance is isotropic in both the phases, all the above-mentioned fields remain symmetric with respect to the line passing through the fracture path (i.e. white dashdoted line in figure 8.4a) at all the stages of propagation. At any stage, in all the simulations, the following inferences regarding the above-mentioned fields are drawn:

1. The displacement field u_{22}, in figure 8.4b, exhibits a sharp transition between the separated parts (i.e on the left side of the fracture tip), whereas it varies smoothly on the unfractured side (i.e. on the right of fracture tip).

2. A symmetric crack driving force field is sustained near the fracture tip, causing the crack to follow a horizontal path, as shown in figure 8.4c.

3. The normal components of the stress, i.e σ_{11} and σ_{22} in figure 8.4d-e, exhibit peak values near the fracture tip.

4. Magnitude of the shear component of stress, i.e. σ_{12} in figure 8.4f, exhibits peak values just above and below the fracture tip.

When the crack is about to propagate while the fracture tip is still at its initial position (i.e. (I) in figure 8.4a), the variation of a) the normal stress components along the white

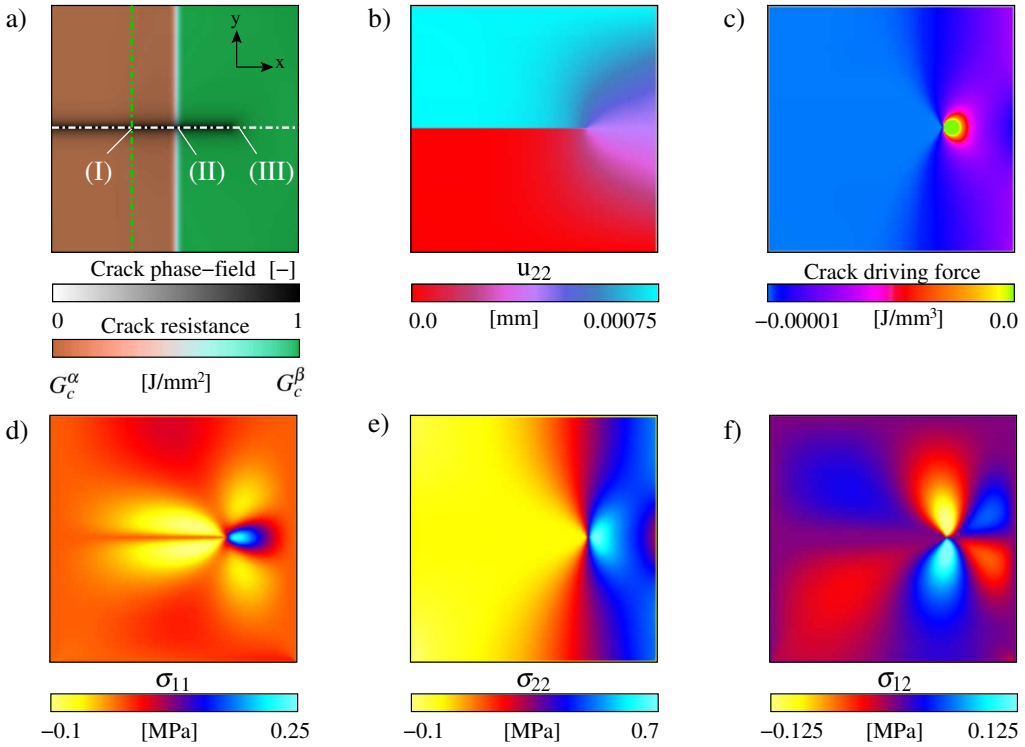

Figure 8.4: a) Fracture growth occurs along a straight horizontal path from phase α to phase β due to isotropic crack resistance of both the phases. For the case of $R_c = 3$, the contour plots of b) displacement field u_{22} in the direction of the applied loading (i.e. y direction), c) crack driving force field and the stress components: d) normal stress σ_{11} in x-direction, e) normal stress σ_{22} in y-direction, and f) shear stress σ_{12}, when the fracture tip is located it at position (III).

dash-dotted line (highlighted in figure 8.4a), and b) the shear stress component along the green dash-dotted line (figure 8.4a), is analysed as shown in figure 8.5a-c. For different values of R_c, the location and magnitude of the peaks for all the stress components are found to be invariant. The magnitude of normal stress components in phase β increases with increasing value of R_c. The variation of shear stress component along the green dash-dotted line shows negligible dependency on the crack resistance of phase β. Figure 8.5d depicts the load-displacement response for different values of R_c. The following two regimes are observed:

1. Green regime for $R_c \leq 1$: As displacement increases, the load increases monotonically while the fracture tip is still at its initial location (i.e. (I) in figure 8.4a). When crack growth is about to begin, the load-displacement curves attain their first maxima, i.e. (I) in figure 8.5d. As R_c decreases, the softening tendency of the load-displacement curve increases due to the crack resistance-dependent normal stress components (shown in figure 8.5a,b). As soon as fracture growth commences, the

load immediately drops to zero without any additional displacement increment.

2. Brown regime for $R_c > 1$: A monotonically increasing load-displacement behavior is observed until a maximum is attained (at (I)) followed by a drop in the load when the crack growth begins, similar to the case of $R_c \leq 1$. However, the lowering of load stops as soon as the fracture tip reaches the α-β interface at position (II) in figure 8.4a. At this stage, as the crack resistance of the phase β is higher for these cases, the fracture growth temporarily stops while the load begins to increase monotonically with the displacement increments, until it attains a second maximum (i.e. (II) in figure 8.5d). Finally, as soon as the crack growth begins in phase β, the load drops to zero without further displacement increments. Moreover, as expected, the magnitude of load at the second peak is directly proportional to the value of R_c.

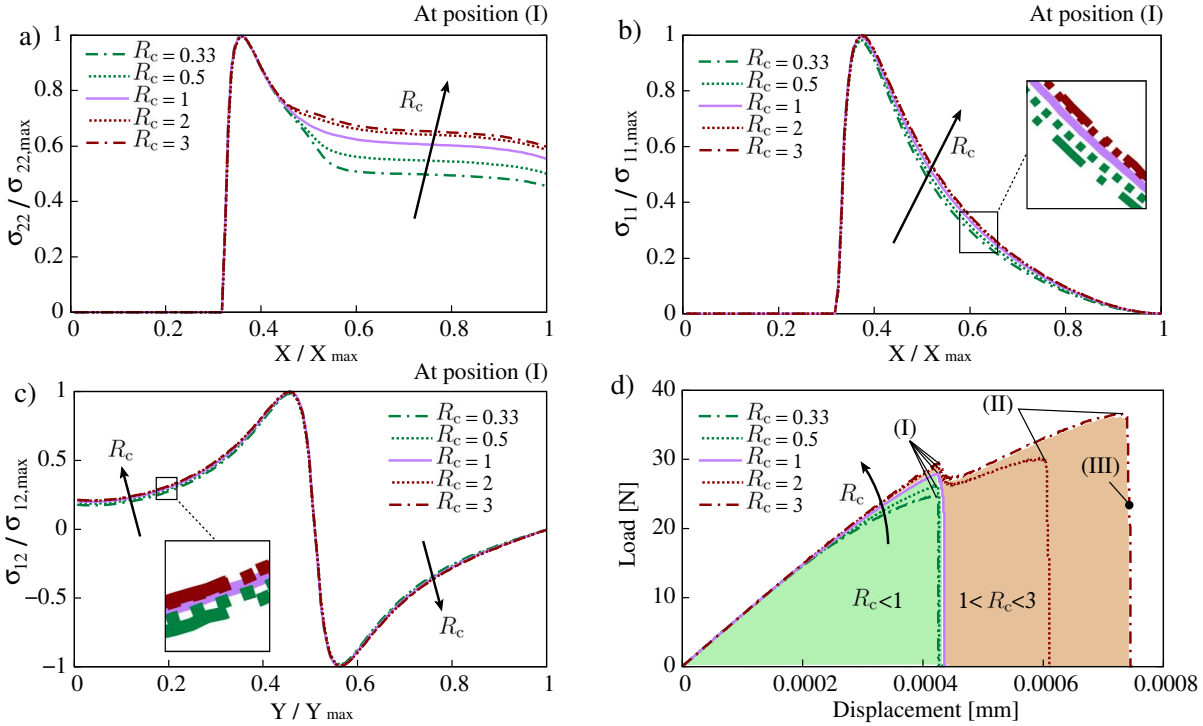

Figure 8.5: When the fracture tip is located at position (I), plots of the normalized stress components a) $\sigma_{22}/\sigma_{22,max}$, b) $\sigma_{11}/\sigma_{11,max}$ along the white dash-dotted line and c) $\sigma_{12}/\sigma_{12,max}$ along the green dash-dotted line (highlighted in Fig. 8.4a) for different values of the crack resistance ratio $R_c = G_c^{\beta}/G_c^{\alpha}$. d) Plot of the load-displacement response for different values of R_c.

8.2.2 Anisotropic crack resistance

Figure 8.6a-b depicts the numerical setup of a single phase specimen with a pre-existing fracture and exhibiting an anisotropic fracture toughness according to the formulation

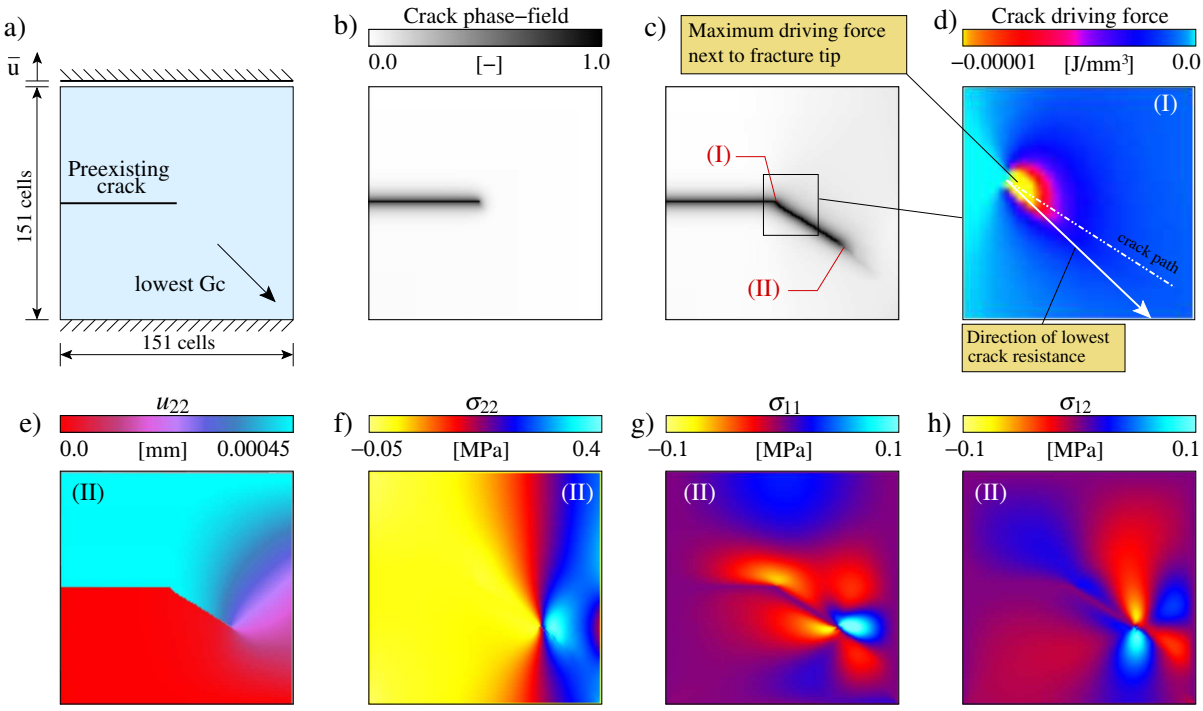

Figure 8.6: a) Geometry and boundary conditions for a fractured single phase specimen with anisotropic crack resistance. b) Diffuse interface description of crack using the crack phase-field ϕ_c. c) An intermediate state of the simulated fracture growth for the case of phase-specific anisotropy strength factor $\mathfrak{f}^{\alpha} = 0.5$. d) Zoomed inset picture of the crack driving force field developed in the vicinity of fracture tip when it was at position (I) just before the commencement of crack propagation. Contour plots of e) displacement field u_{22}, the stress components f) σ_{22}, g) σ_{11} and h) σ_{12}, showing asymmetricity as a result of anisotropic crack resistance.

discussed in section 8.1.1. The chosen values of elastic constants (i.e. E and ν) for the specimen are given in table 8.1. The crystallographic orientation of the specimen is set such that the direction of lowest crack resistance is inclined at an angle of -45^o with respect to the horizontal, see figure 8.6a. Crack resistance in the direction perpendicular to that of minimum crack resistance is set to $G_c = 57.71 \times 10^{-6}$ J/mm^2, corresponding to the value along the c-axis for quartz. For the case of $\mathfrak{f}^{\alpha} = 0.5$, figure 8.6c depicts the simulated fracture path along the preferred plane at an intermediate stage. The path of fracture is governed by the crack driving force field developed in the vicinity of fracture tip, which is dependent upon the stress state and the crack resistance along different crystallographic directions at a material point. As the crack resistance anisotropy is present in the specimen, the driving force field developed near the crack tip is asymmetric, see figure 8.6d. Fracturing takes place in the direction pointed out by this field. At the above-mentioned intermediate stage when the crack tip is at position (II), the displacement in the direction of loading (i.e. u_{22}) and the stress component fields (i.e. σ_{11}, σ_{22} and σ_{12}) are depicted in figure 8.6e-h. Due to the crack resistance anisotropy, all the

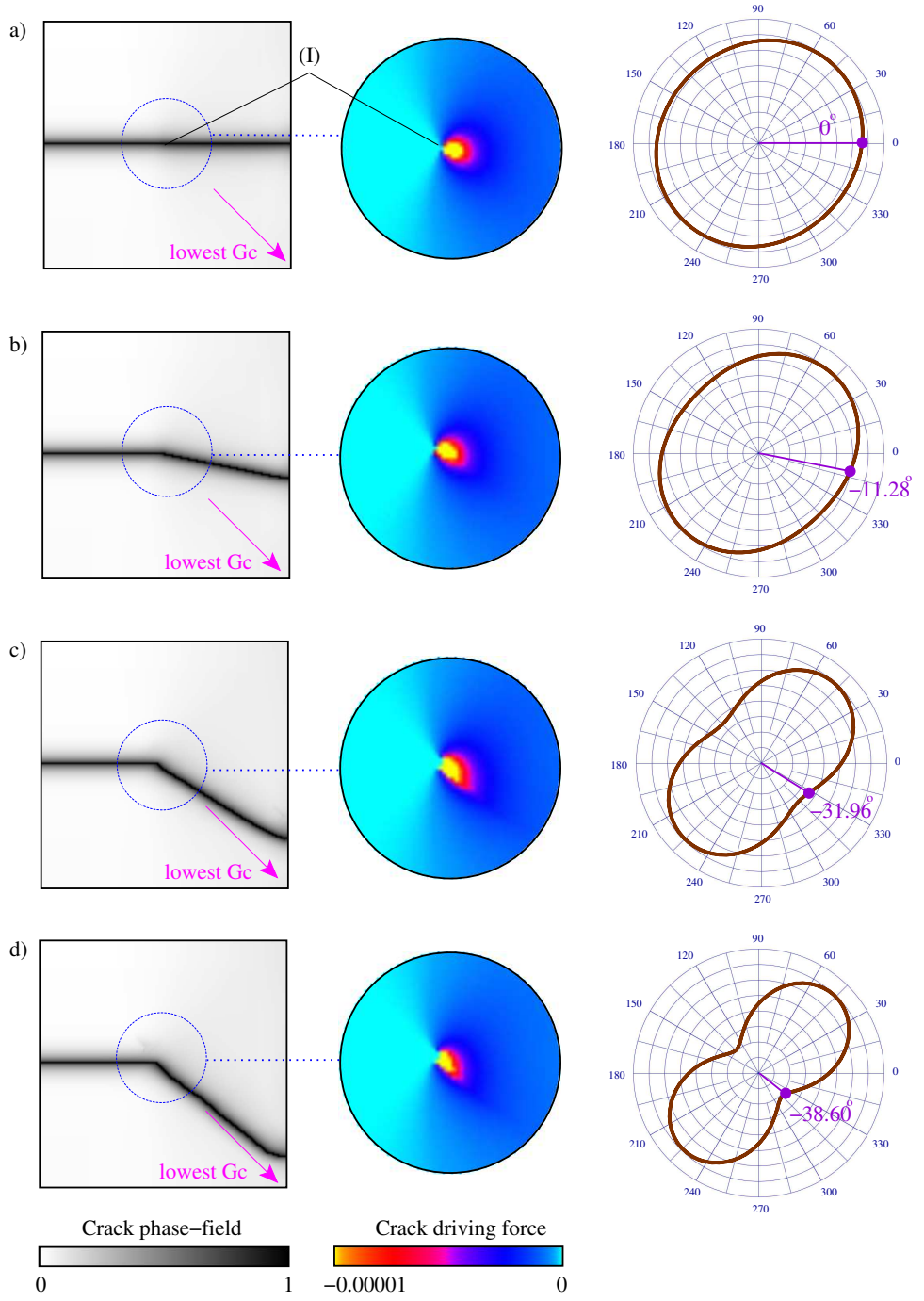

Figure 8.7: Simulation results of fracture propagation and the polar plots of anisotropic crack resistance for a) $\mathfrak{f}^{\alpha} = 0.9$, b) $\mathfrak{f}^{\alpha} = 0.795$ (for quartz), c) $\mathfrak{f}^{\alpha} = 0.5$ and d) $\mathfrak{f}^{\alpha} = 0.3$. First column: The simulated fracture geometries. Second column: Driving force field developed in the vicinity of the crack tip when the tip is at position (I) and the fracture growth is about to commence. Third column: The polar plots of the anisotropic crack resistance G_c. Increasing the value of $\mathfrak{f}^{\alpha}$ increases the asymmetricity of the developed crack driving force field near the fracture tip, thereby leading to increase in the angle of deflection of the crack.

fields exhibit an asymmetricity.

Using the numerical setup of figure 8.6a-b, several simulations were performed for different values of the phase-specific anisotropy strength factor $\mathfrak{f}^{\alpha}$, while keeping the other parameters identical. For different cases, the model-predicted fracture paths are shown in the first column of figure 8.7. The crack driving force field developed next to the fracture tip, right before the beginning of fracture growth, is shown in the second column of figure 8.7. As the strength of anisotropy increases (i.e. with the decreasing value of $\mathfrak{f}^{\alpha}$), the asymmetricity of the crack driving force field also increases, thereby leading to a larger deflection in the fracture path. The 2-D polar plots of the crack resistance and the angle of crack deflection for different values of $\mathfrak{f}^{\alpha}$ are shown in the third column of figure 8.7. In all the cases, a mean crack interface width, determined between the isolines ϕ_c=0.15 and ϕ_c=0.85, of about 9-10 cells is obtained. For the case of quartz, the phase-specific anisotropy strength parameter $\mathfrak{f}^{\alpha}$ is computed using the reported values of the fracture toughness along the c- and a- axes (table 8.1), as follows

$$\mathfrak{f}^{\text{Qtz}} = \frac{G_{\text{c}}^{\text{a-axis}}}{G_{\text{c}}^{\text{c-axis}}} = \left[\frac{K_{\text{Ic}}^{\text{a-axis}}}{K_{\text{Ic}}^{\text{c-axis}}}\right]^2 = 0.795. \tag{8.6}$$

For this value, small crack deflections are expected within each quartz grain in sandstones as predicted by the present model, see figure 8.7b.

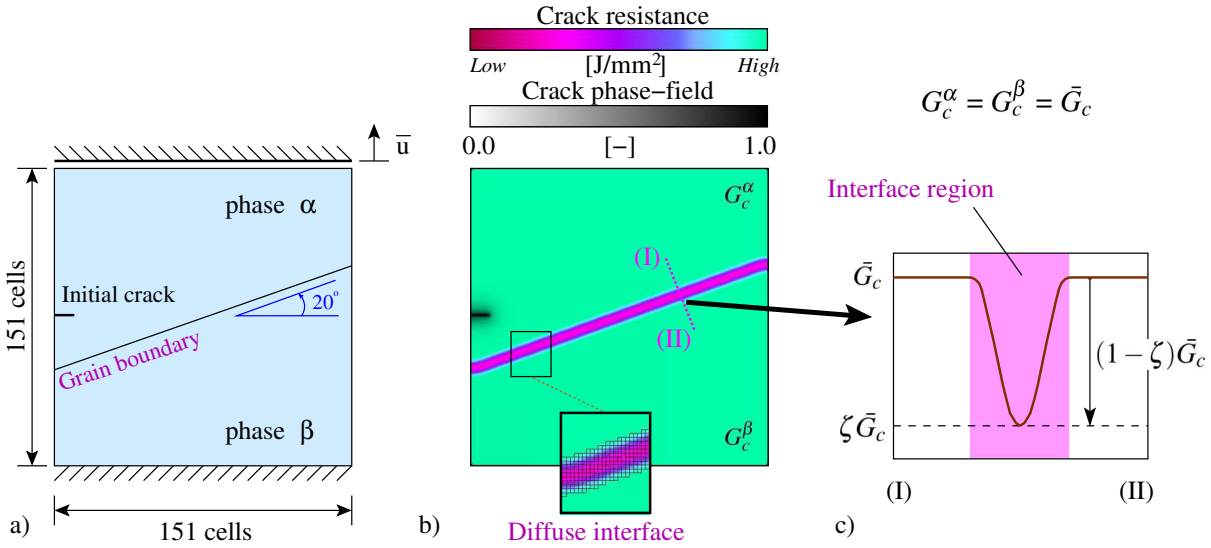

Figure 8.8: a) Geometry and boundary conditions of a two-phase specimen with an existing crack. The grain boundary is inclined at an angle of 20° from the horizontal. Diffuse interface description of 1) the crack using the crack phase-field ϕ_c and 2) the grain boundary where the crack resistance is reduced in a smooth and continuous manner. c) Schematics illustrating the spatial variation of crack resistance with a reduction factor ζ, along the line (I)-(II) passing through the solid-solid interface

8.2.3 Reduced grain boundary resistance

A two-phase specimen with an inclined grain boundary and a pre-existing crack is considered, see the numerical setup in figure 8.8a. The crack is described by a crack phase-field ϕ_c, see figure 8.8b. Crack resistance in the bulk regions of phase α and β are chosen to be isotropic and equal to the value along the c-axis of quartz, i.e. $G_c^\alpha = G_c^\beta = \bar{G}_c = 57.71 \times 10^{-6}$ J/mm^2. Crack resistance of the grain boundary is lowered in a smooth and continuous manner (see figure 8.8b-c) by utilizing the reduced crack resistance formulation elaborated in section 8.1.2. The chosen elastic properties (i.e. Young's modulus E and Poisson's ration ν) correspond to quartz and are given in table 8.1.
For different values of reduction factor ζ, the simulated fracture paths are shown in the first row of figure 8.9. When fracture tip reaches the diffuse grain boundary region, the developed crack driving force field in the tip's vicinity is shown as inset pictures in the second row of figure 8.9. Decreasing the value of ζ increases the asymmetricity of crack driving force field in the interface region, consequently resulting in a transition from transgranular to intergranular mode of fracturing. When the reduction factor is close to unity ($\zeta = 0.9$), the driving force field is nearly symmetric, and therefore, no visible deflection in the fracture path is observed, see figure 8.9a. On decreasing the value of ζ, a transition to the mixed mode of fracturing is observed, due to the increase in the asymmetricity of the driving force field that, in turn, increases the tendency of crack to deflect along the grain boundary. As a result, partial crack deflections are observed along the grain boundary for the cases of $\zeta = 0.5$ and 0.25, as shown in figure 8.9b-c. For $\zeta = 0.15$, a complete deflection along the grain boundary is observed, thereby resulting in an intergranular mode of fracturing, see figure 8.9d. It is worthy to mention that the crack interface width of about $9 - 10$ cells is maintained in all the simulations.

8.2.4 Fracture growth in exemplary geological structures

A multigrain system analogous to a geological vein structure with 10 crystals is considered. The digital vein structure was taken from Prajapati et al. [2]). The elastic properties (i.e E and ν) of all the vein crystals are set to the corresponding values for quartz, given in table 8.1. For demonstrating the performance of the two crack resistance formulations discussed in sections 8.1.1 and 8.1.2, the following four cases of the crack resistance field in the computational domain are considered:

1. **Domain I**: Isotropic crack resistance in the complete simulation domain comprising of quartz grains and the grain boundaries, see figure 8.10a. The grain boundaries are shown in grey color for the sake of visualization. Value of the crack resistance in the entire domain is determined by the crack resistance colormap.

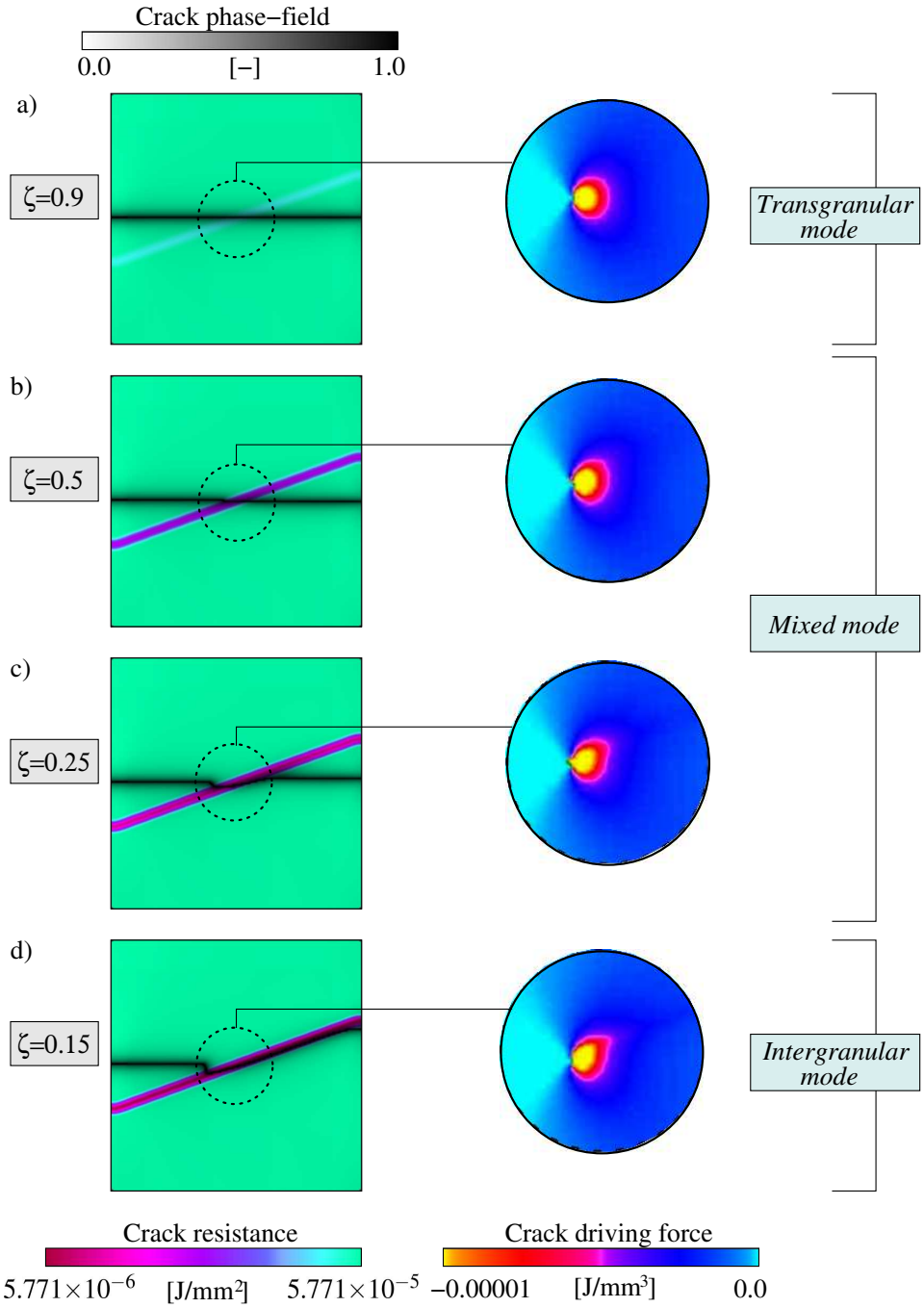

Figure 8.9: Simulation results of fracture propagation for different values of the reduction factor ζ. First column: Simulated fracture path. Second column: Driving force field developed in the vicinity of the fracture tip when the tip is in the grain boundary region. A transition from intragranular to mixed fracturing and finally to intergranular mode is observe for decreasing values of ζ.

2. **Domain II**: Isotropic crack resistance of same magnitude for all the grains, but a lower grain boundary crack resistance by setting a reduction factor of $\zeta = 0.2$, as shown in figure 8.10b. Here also, the value of crack resistance in the entire domain

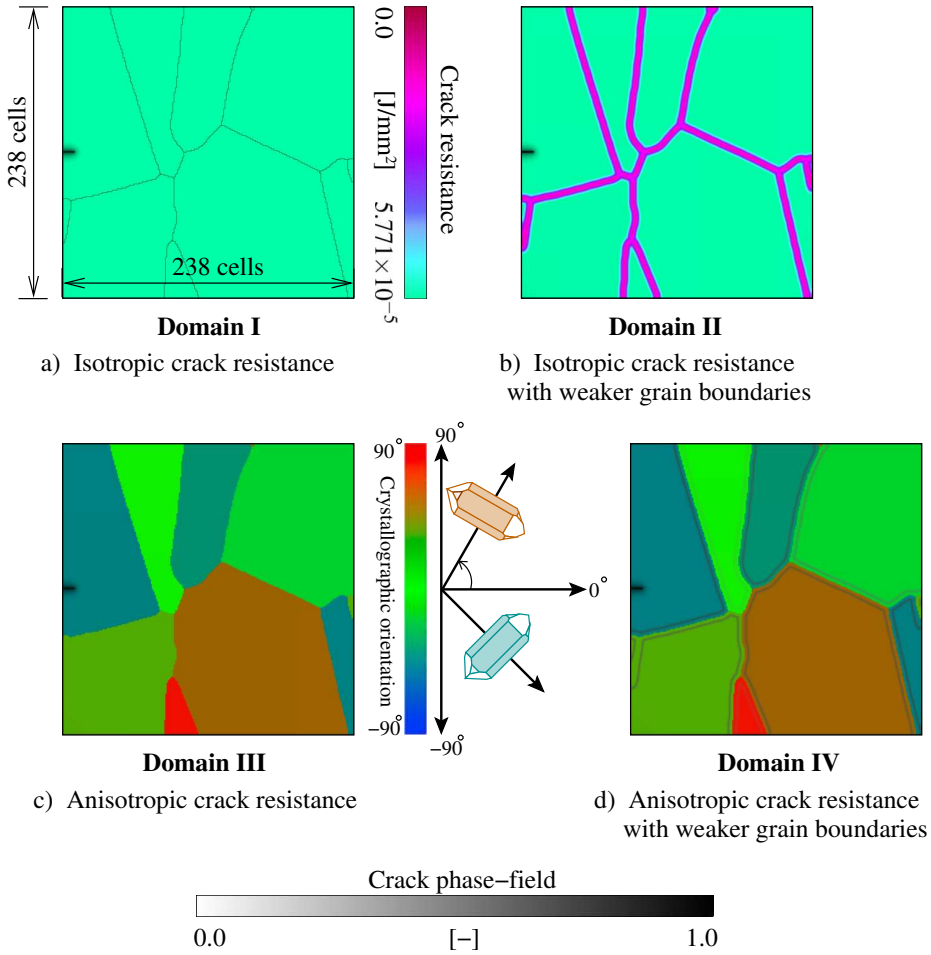

Figure 8.10: Exemplary geological structure comprising of several quartz grains with a) isotropic crack resistance, b) isotropic crack resistance of bulk phases and weaker grain boundaries, c) anisotropic crack resistance of grains and d) anisotropic crack resistance of grains with weaker grain boundaries. All the structures possess an initial fracture illustrated in grey scale. In the fourth case, the crack resistance reduction is applied in the diffuse interface region illustrated by the grey lines parallel to the grain boundaries.

is determined by the crack resistance colormap.

3. **Domain III**: Anisotropic crack resistance with an anisotropy strength factor $\mathfrak{f}^{\mathrm{Qtz}} = 0.795$ for each randomly oriented quartz grain. The crystallographic orientation of each grain is determined by the orientation colormap, see figure 8.10c.

4. **Domain IV**: Anisotropic crack resistance with $\mathfrak{f}^{\mathrm{Qtz}} = 0.795$ for each randomly oriented quartz grain, and reduced grain boundary crack resistance with the reduction factor $\zeta = 0.2$, as depicted in figure 8.10d. Here also, the crystallographic orientation of each grain is determined by the same orientation colormap. The reduction of crack resistance is applied along the diffuse interface region lying between the

grey lines parallel to the grain boundaries, as shown in the figure.

The size of computational domains for all the above cases is $238\Delta x \times 238\Delta x \times 1\Delta x$. Similar to the previous numerical examples, identical boundary conditions of uniaxial tension are applied in all the simulations, and an initial crack phase is present shown in grey scale in all the domains in figure 8.10. Different representative stages of the simulated fracture growth are depicted in figure 8.11. The inset pictures in the intermediate stages showcase the crack driving force field developed next to the fracture tip. For the first case with a homogeneous crack resistance, as the crack driving force field remains symmetric at all the stages, fracturing occurs along a straight line perpendicular to the direction of loading, see figure 8.11a. In the second case, a lower value of crack resistance along the grain boundaries than the bulk of grains induces an asymmetricity in the crack driving force field when the fracture tip is in the diffuse grain boundary regions, see the inset pictures in figure 8.11b. As a result, both partial as well as complete crack deflections occur at different spatial points in the computational domain along the grain boundaries, as highlighted at the last stage in figure 8.11b. In the third case with an anisotropic crack resistance shown in figure 8.11c, the fracture deflects in the direction of lowest crack resistance, according to the crystallographic orientation of each grain. As the anisotropy strength of quartz is weak (i.e. with $\mathfrak{f}^{\alpha} = 0.795$), the observed deflections in different grains are small. It is worthy to note that, in different grains, a nearly constant crack interface width (calculated between the isolines $\phi_{\mathrm{c}} = 0.15$ and $\phi_{\mathrm{c}} = 0.85$) of about 16-18 cells is maintained as shown in the last stage of figure 8.11c. For the final case with an anisotropic crack resistance of the grains and a lower crack resistance in the grain boundaries according to the reduction factor $\zeta = 0.2$, the crack driving force field and the crack path are controlled by the interplay of both the factors.

8.3 Conclusion and outlook

The present work showcases a generalized and rigorous MPF model for fracture propagation in polycrystalline systems based on the Griffith's theory of rupture [140]. The MPF model was adapted to address the phenomenon of brittle anisotropic microfracturing in sandstones. To this end, two novel formulations, namely anisotropic and reduced interfacial crack resistance, were proposed for simulating the interplay of intergranular and transgranular crack propagation, while accounting for the preferred cleavage planes within each randomly oriented quartz grain for intragranular fracturing. With the incorporated anisotropy in the crack resistance, a nearly constant crack interface width is ensured in all the quartz grains. The reduced interfacial crack resistance formulation provides a general framework to lower the crack resistance by a given factor along the

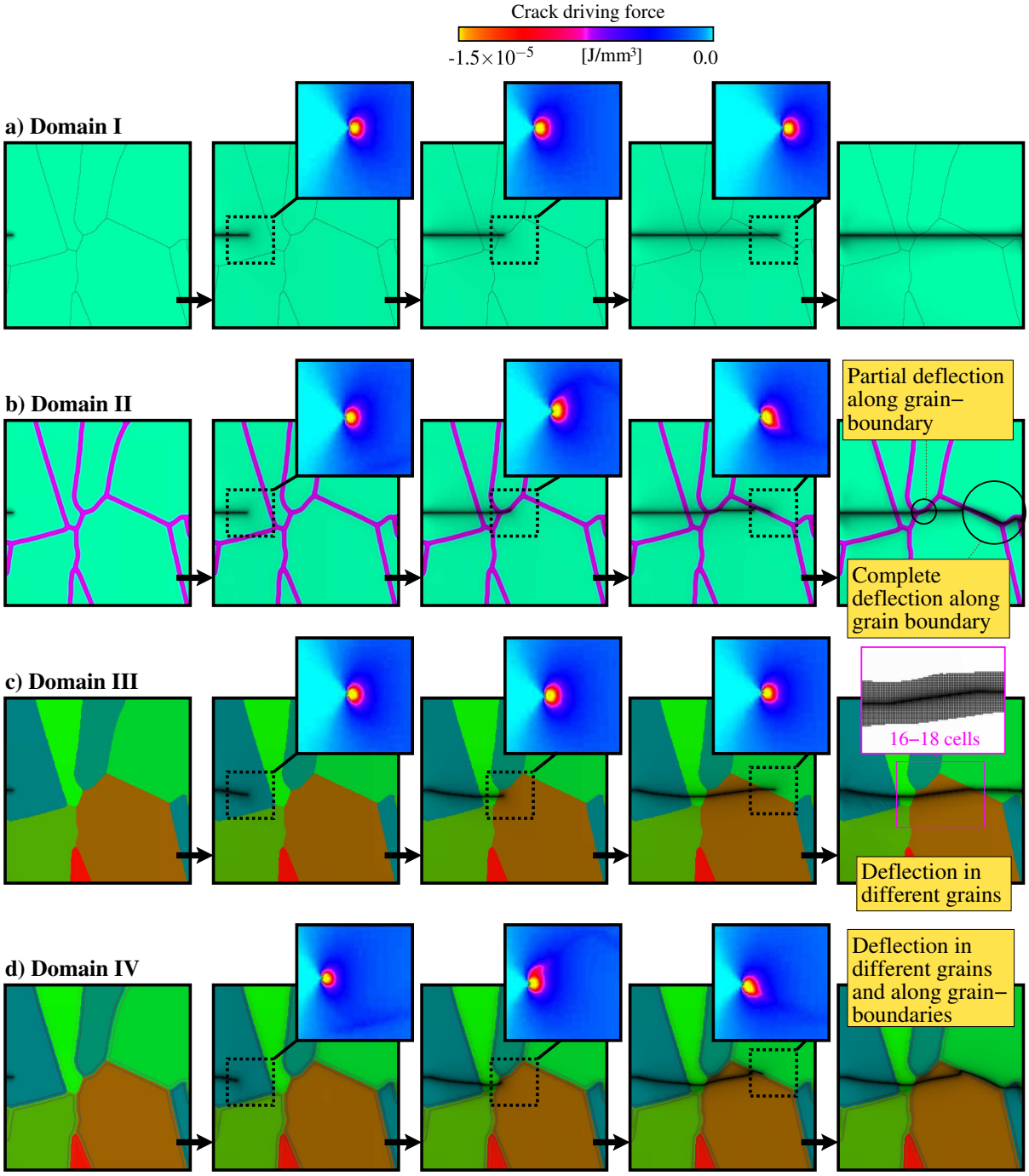

Figure 8.11: Simulated fracture path in exemplary geological vein structures with a) isotropic crack resistance, b) isotropic crack resistance with weaker grain boundaries, c) anisotropic crack resistance and d) anisotropic crack resistance with weaker grain boundaries. The driving force field developed near the fracture tip is shown in the inset pictures at all the intermediate stages.

grain boundaries in a smooth and continuous manner. Using the full parameter space of the two crack resistance formulations, more complex anisotropies in the bulk region and along the grain boundaries can be incorporated. In order to demonstrate the model performance, a uniaxial load was applied in all the presented numerical examples. The following conclusions are drawn from the simulation results:

1. The crack driving force field developed near the tip of fracture governs the crack path. This field is dependent upon the stress state and the crack resistance at a material point.

2. In materials with an anisotropic crack resistance, the crack driving force field exhibits an asymmetricity pointing in the direction of lowest crack resistance, and thus accounts for preferred cleavage planes within the bulk region of a material.

3. In the polycrystalline materials exhibiting a lower crack resistance along the grain boundaries, the crack driving force field points along the grain boundary, thereby, facilitating intergranular fracture propagation.

Simulated fracture patterns in the numerical examples show consistency with respect to the variation of relevant parameters, which is elucidated as follows:

1. With a decreasing crack resistance along the grain boundaries, the tendency of fracture to propagate along the grain boundaries increases.

2. With an increasing crack resistance anisotropy strength in a prescribed direction, the magnitude of crack deflection in the direction of lowest crack resistance increases.

In the present work, the chosen set of material parameters corresponds to quartz, and was adopted from the previous literature [91, 92, 206]. However, it is remarked that the model parameters are chosen keeping into consideration the computational costs and the numerical stability, and may not correspond to real geological systems. The present work, although limited to 2-D, can be extended to 3-D in a fairly straight-forward manner, the analyses of which would essentially require more computational resources. Future works would aim at extending the model that can account for fracturing under more complex mechanical boundary conditions (e.g. fluid pressurization and hydraulic fracturing). In loading states where a large portion of the material is expected to be in compressive stress states, the irreversibility condition for the crack phase-field (i.e. $\dot{\phi}_{\mathrm{c}} \geq 0$) should be relaxed and suitable conditions for the crack closure must be implemented. When precise information is available about the rock structures, material properties at grain scale, anisotropic behavior, loading conditions in e.g. experiments, the model parameters

can be calibrated to precisely imitate real fracture patterns in multigrain/polycrystalline systems. The present MPF model can also be applied to simulate fracture propagation at macroscopic length scales in the materials comprising of large regions of different solid phases. At this point, a coupling of present model with the macrosopic plasticity models (e.g. von Mises, Mohr-Coulomb, Drucker-Prager, etc. can be done, so as to describe the plastic flow behavior of certain phases in a multiphase system.

Chapter 9

Conclusion

In section 9.1, a concise summary of the findings, highlights and the objectives fulfilled in this research work is presented. Finally, the dissertation is concluded in section 9.2 with a brief outlook on the future directions and possible extensions of the presented work.

9.1 Summary

In this work, two different geophysical processes in sedimentary rocks, namely syntaxial overgrowth cementation and brittle anisotropic microfracturing, were studied. To this end, two multiphase-field (MPF) models were adapted. The feasibility of the phase-field method in capturing the essential physics of the two problems and tackling the microstructure evolution efficiently and elegantly was amply demonstrated. The results of syntaxial overgrowth cementation, while reproducing the previously known microstructural patterns, significantly enhance our current understanding of the process controls and their implications on the petrographical and petrophysical rock properties. Moreover, the results of fracturing advocate the versatility and robustness of the adapted MPF model of fracture in capturing the impact of grain-scale heterogeneities and anisotropies of sedimentary rocks on the crack geometries. The findings, highlights and the objectives fulfilled in the present dissertation are summarized as follows:

In chapter 5, the effect of physical boundary conditions such as the relative crack opening rates and initial crack aperture in modulating the morphologies of calcite veins in limestones was studied. For this purpose, a MPF model based on the time-dependent Ginzburg-Landau (TDGL) theory was employed. Although the model is phenomenological in a sense that it lacks the details of the molecular interactions, it is now well-established that the crystal morphologies observed experimentally and in naturally occuring rocks can be reproduced by the methodology [15–18, 110]. The numerically obtained

vein textures in two dimensions 2-D were qualitatively compared with the natural calcite vein samples with good agreement. Although the role of the interplay of crack opening rates and cement growth rates in the formation of different vein textures was first proposed by MÜGGE [80], and later numerically explored using a front tracking approach by HILGERS ET AL. [79], the results presented in chapter 5 serve as the first report elucidating a novel transition from uniform to non-uniform fibrous vein morphologies based on the initial crack apertures. The numerical results and the studied boundary conditions can further serve as a guideline regarding the appropriate selection of process parameters for the experimentalists as well as in the development projects of engineered geothermal systems.

In chapter 6, the MPF model of cementation was adapted for simulating the anisotropic quartz cement growth in sandstones in three dimensions (3-D). The numerical data sets generated in the phase-field simulations were utilized to study the role of grain size of unicrystalline quartz aggregates on the evolving physical properties of sandstones during cementation. As a direct extension to this study, the impact of quartz cementation in sandstones composing of varying fractions of polycrystalline quartz aggregates on the physical properties was investigated in chapter 7. To this end, the MPF model utilized in the previous chapter 6 was extended based on the work of WENDLER ET AL. [15]. With the extensions, the faceting-dependent growth tendencies of quartz cements were more rigorously accounted. Further, a phenomenologically more appropriate prescription for the motion of triple junctions (shared between the solid-solid-liquid phases) was adopted, as it plays an important role in modulating the polycrystalline cement morphologies. Moreover, the set of phase-field parameters was determined at a temperature and pressure matching the common reservoir conditions, based on the procedure proposed by WENDLER ET AL. [15], while a previously unknown kinetic parameter was calibrated using the simulations of unrestricted growth and an experimentally reported growth tendency of quartz cements [36]. Furthermore, a novel procedure for generating the realistic 3-D digital grain packs that fairly represent natural sandstones in terms of grain shapes, size distributions and depositional porosity was presented. The numerical data sets generated through the simulated quartz cementation in these packs were postprocessed and analysed for the role of polycrystallinity of quartz aggregates on the evolving physical properties of sandstones. The phase-field simulations of chapters 6 and 7, while producing unicrystalline as well as polycrystalline quartz cement textures that exhibit clear similarities with the corresponding morphologies observed in the thin-section microphotographs of natural sandstone samples, recovered several petrophysical aspects of the process. In particular, the numerically derived relationships between the petrophysical properties (such as cement volumes, porosity, permeability and pore size distributions) and their variation in sandstones, differing on the basis of the grain size and

fraction of polycrystalline quartz aggregates, showed good agreement with the previous hydrothermal experiments [36, 44] and the empirical equations [193, 204].

In chapter 8, a separate MPF model of fracture, also based on the TDGL theory, was adapted to simulate the brittle anisotropic microfracturing in sandstones. To this end, two novel formulations, namely a) anisotropic and b) reduced interfacial crack resistance, were proposed and incorporated for simulating the interplay of intergranular and transgranular fracturing, while exhibiting preferred cleavage planes within each quartz grain. It was shown that the MPF model with these formulations predicted consistent fracture patterns in the multigrain sandstones. Within the full parameter space of the two formulations, the presented MPF model can simulate more complex material behavior based on fracture toughness (e.g. other directional dependencies in the bulk of grains, stiffer grain boundaries).

9.2 Future directions

Although the work presented in this dissertation is complete in its own right, several interesting extensions are possible.

The work in chapter 5 explores only the bitaxial crack-seal mechanism in syntaxial calcite veins under normal crack opening increments in 2-D. However, a whole range of vein growth mechanisms based on different combinations of growth directions (e.g. unitaxial, antitaxial), location of new fractures (e.g. ataxial), cement type (e.g. calcite, quartz, dolomite), relative frequency of crack and seal events (e.g. elongate-blocky, fibrous, euhedral) and crack opening trajectories (e.g. curved, blade-like crystals) [35] can be readily investigated in a straightforward manner, even in 3-D [15, 17, 18]. Numerical studies of vein growth in 3-D would further allow the investigation of flow properties of different vein structures and their controlling factors [208]. The systematic work-flow of chapters 6 and 7 can be extrapolated, while adapting and improvising the model formulation, for computationally investigating the impact of other relevant factors such as grain coatings [209] and hetergeneities arising due to other mineral phases on the evolving rock morphologies and physical properties.

In the scope of this thesis, a constant fluid supersaturation was considered, which is a reasonable assumption when a) the particle attachment kinetics is much slower than diffusion and advection, b) the fluid is continuously replenished with solute and c) the temperature is invariant. However, in physical systems where the above-mentioned conditions are not met, a coupling with diffusion, temperature and/or flow equations needs to be incorporated. From the algorithmic point of view, numerical computations in the adapted MPF models of cementation in chapters 5, 6 and 7 were performed based on the

explicit time update of phase-fields, which renders the algorithm as conditionally stable, thereby imposing an upper bound on the choice of numerical time step width. This constraint may be relaxed with effective and efficient implementation of implicit schemes, that would subsequently allow numerical investigations at more realistic fluid supersaturations (in case of quartz), which is currently not possible with the present modeling. These extensions, when effectively implemented, will accentuate a faster bridging between simulations, experiments and reservoir quality prediction.

The work in chapter 8 showcases a rigorous and generalized MPF model of fracture, adapted specifically for modeling the brittle crack growth in sandstones, which are essentially anisotropic polycrystalline systems at grain-scale. However, application to other multiphase / multigrain / polycrystalline systems at different length scales, where distinct phases may differ in terms of elastic properties, crack resistance in the bulk region and along the grain boundaries along with their associated anisotropies, is fairly straightforward. When addressing the process at macroscopic scale, the model can be extended to account for inelastic response of certain phases of a multiphase system, based on different plasticity models (e.g. Drucker-Prager, von Mises, Mohr-Coulomb). Further, the model should be extended to account for large deformations using e.g. the logarithmic strain space formulation [210]. From the algorithmic point of view, the update of mechanical and phase-fields in the present MPF model of fracture is performed in a staggered manner. Efforts in the direction of development of faster monolithic schemes, where these fields are updated simultaneously in each time increment [see e.g. 211], in the MPF framework could be beneficial with respect to the convergence characteristics, while addressing the aforementioned model extensions.

The work-flow, results and analysis procedures demonstrated in this thesis can serve as guidelines for the proposal, development and execution of multidisciplinary research projects, where experimental investigations are conducted in parallel to numerical simulations. With the availability of exact experimental data which can then be utilized to extend, calibrate and validate the MPF models, a more precise and quantitative modeling of these processes can be achieved.

Bibliography

[1] N. Prajapati, M. Selzer, B. Nestler, B. Busch, C. Hilgers, and K. Ankit. Three-dimensional phase-field investigation of pore space cementation and permeability in quartz sandstone. *Journal of Geophysical Research: Solid Earth*, 123(8):6378–6396, 2018.

[2] N. Prajapati, M. Selzer, B. Nestler, B. Busch, and C. Hilgers. Modeling fracture cementation processes in calcite limestone: a phase-field study. *Geothermal Energy*, 6(1):7, 2018.

[3] M. H. Anders, S. E. Laubach, and C. H. Scholz. Microfractures: A review. *Journal of Structural Geology*, 69:377–394, 2014.

[4] Y. Guéguen and M. Boutéca. *Mechanics of fluid-saturated rocks*. Elsevier, Amsterdam, 2004.

[5] M.-L. Lin, F. Jeng, L. Tsai, and T. Huang. Wetting weakening of tertiary sandstonesmicroscopic mechanism. *Environmental Geology*, 48(2):265–275, 2005.

[6] D. Koehn, C. Hilgers, P. D. Bons, and C. W. Passchier. Numerical simulation of fibre growth in antitaxial strain fringes. *Journal of Structural Geology*, 22(9):1311–1324, 2000.

[7] P. Bons. Development of crystal morphology during unitaxial growth in a progressively widening vein: I. The numerical model. *Journal of Structural Geology*, 23(6-7):865–872, 2001.

[8] S. Mohammadi. *Extended finite element method: for fracture analysis of structures*. Blackwell Publishing Ltd, Oxford, 2008.

[9] L.-Q. Chen. Phase-field models for microstructure evolution. *Annual Review of Materials Research*, 32(1):113–140, 2002.

[10] W. J. Boettinger, J. A. Warren, C. Beckermann, and A. Karma. Phase-field simulation of solidification. *Annual Review of Materials Research*, 32(1):163–194, 2002.

[11] N. Moelans, B. Blanpain, and P. Wollants. An introduction to phase-field modeling of microstructure evolution. *Calphad*, 32(2):268–294, 2008.

[12] B. Nestler and A. Choudhury. Phase-field modeling of multi-component systems. *Current Opinion in Solid State and Materials Science*, 15(3):93–105, 2011.

[13] C. Miehe, F. Welschinger, and M. Hofacker. A phase field model of electromechanical fracture. *Journal of the Mechanics and Physics of Solids*, 58(10):1716–1740, 2010.

[14] D. Schneider, M. Selzer, J. Bette, I. Rementeria, A. Vondrous, M. J. Hoffmann, and B. Nestler. Phase-field modeling of diffusion coupled crack propagation processes. *Advanced Engineering Materials*, 16(2):142–146, 2014.

[15] F. Wendler, A. Okamoto, and P. Blum. Phase-field modeling of epitaxial growth of polycrystalline quartz veins in hydrothermal experiments. *Geofluids*, 16(2):211–230, 2016.

[16] K. Ankit, B. Nestler, M. Selzer, and M. Reichardt. Phase-field study of grain boundary tracking behavior in crack-seal microstructures. *Contributions to Mineralogy and Petrology*, 166(6):1709–1723, 2013.

[17] K. Ankit, J. L. Urai, and B. Nestler. Microstructural evolution in bitaxial crack-seal veins: A phase-field study. *Journal of Geophysical Research: Solid Earth*, 120(5):3096–3118, 2015.

[18] K. Ankit, M. Selzer, C. Hilgers, and B. Nestler. Phase-field modeling of fracture cementation processes in 3-d. *Journal of Petroleum Science Research*, 4:79, 2015.

[19] E. H. Oelkers, P. A. Bjorkum, and W. M. Murphy. A petrographic and computational investigation of quartz cementation and porosity reduction in North Sea sandstones. *American Journal of Science*, 296(4):420–452, 1996.

[20] S. Paxton, J. Szabo, J. Ajdukiewicz, and R. Klimentidis. Construction of an intergranular volume compaction curve for evaluating and predicting compaction and porosity loss in rigid-grain sandstone reservoirs. *AAPG Bulletin*, 86(12):2047–2067, 2002.

[21] M. Kennedy. Petrophysical Properties. In *Developments in Petroleum Science*, volume 62, pages 21–72. Elsevier, Amsterdam, 2015.

[22] F. J. Lucia. Petrophysical rock properties. In *Carbonate reservoir characterization: An integrated approach*, pages 1–27. Springer Science & Business Media, Berlin, 2007.

[23] O. K. M. Sajed and P. W. Glover. Dolomitisation, cementation and reservoir quality in three Jurassic and Cretaceous carbonate reservoirs in north-western Iraq. *Marine and Petroleum Geology*, 115:104256, 2020.

[24] I. Becker, B. Koehrer, M. Waldvogel, W. Jelinek, and C. Hilgers. Comparing fracture statistics from outcrop and reservoir data using conventional manual and t-Lidar derived scanlines in ca2 carbonates from the Southern Permian Basin, Germany. *Marine and Petroleum Geology*, 95:228–245, 2018.

[25] B. WAUGH. Formation of quartz overgrowths in the Penrith Sandstone (Lower Permian) of northwest England as revealed by scanning electron microscopy. *Sedimentology*, 14(3-4):309–320, 1970.

[26] O. Walderhaug. Precipitation rates for quartz cement in sandstones determined by fluid-inclusion microthermometry and temperature-history modeling. *Journal of Sedimentary Research*, 64(2a):324–333, 1994.

[27] O. Walderhaug. Temperatures of quartz cementation in Jurassic sandstones from the Norwegian continental shelf; evidence from fluid inclusions. *Journal of Sedimentary Research*, 64(2a):311–323, 1994.

[28] O. Walderhaug. Kinetic modeling of quartz cementation and porosity loss in deeply buried sandstone reservoirs. *AAPG Bulletin*, 80(5):731–745, 1996.

[29] O. Walderhaug. Modeling quartz cementation and porosity in Middle Jurassic Brent Group sandstones of the Kvitebjørn field, northern North Sea. *AAPG Bulletin*, 84(9):1325–1339, 2000.

[30] R. Worden and S. Morad. Quartz cementation in oil field sandstones: a review of the key controversies. *Special Publication-International Association of Sedimentologists*, 29:1–20, 2000.

[31] R. Worden and S. Burley. Sandstone diagenesis: the evolution of sand to stone. *Sandstone Diagenesis: Recent and Ancient*, 4:3–44, 2003.

[32] T. Taylor, R. Stancliffe, C. Macaulay, and L. Hathon. High temperature quartz cementation and the timing of hydrocarbon accumulation in the Jurassic Norphlet Sandstone, offshore Gulf of Mexico, USA. *Geological Society, London, Special Publications*, 237(1):257–278, 2004.

[33] R. G. Bathurst. *Carbonate sediments and their diagenesis*, volume 12. Elsevier, Amsterdam, 1972.

[34] C. Hilgers and S. Sindern. Textural and isotopic evidence on the fluid source and transport mechanism of antitaxial fibrous microstructures from the Alps and the Appalachians. *Geofluids*, 5(4):239–250, 2005.

[35] P. D. Bons. The formation of veins and their microstructures. *Journal of the Virtual Explorer*, 2:12, 2000.

[36] R. H. Lander, R. E. Larese, and L. M. Bonnell. Toward more accurate quartz cement models: The importance of euhedral versus noneuhedral growth rates. *AAPG Bulletin*, 92(11):1537–1563, 2008.

[37] The quartz page. `http://www.quartzpage.de/crs_habits.html`. Accessed: 2020-03-5.

[38] C. Frondel. Dana's system of mineralogy. In *Silica minerals*, volume 3. John Wiley and Sons, New York, 7^{th} edition, 1962.

[39] R. Rykart. *Quarz-Monographie: Die Eigenheiten von Bergkristall, Rauchquarz, Amethyst, Chalcedon, Achat, Opal und anderen Varietäten*. Ott-Verlag, Thun, 1995.

[40] B. Busch, C. Hilgers, R. H. Lander, L. M. Bonnell, and D. Adelmann. Reservoir quality and burial model evaluation by kinetic quartz and illite cementation modeling: Case study of Rotliegendes, north Germany. *AAPG Bulletin*, 102(2):293–307, 2018.

[41] E. F. McBride. Quartz cement in sandstones: a review. *Earth-Science Reviews*, 26(1-3):69–112, 1989.

[42] B. Busch, C. Hilgers, L. Gronen, and D. Adelmann. Cementation and structural diagenesis of fluvio-aeolian Rotliegend sandstones, northern England. *Journal of the Geological Society*, 174(5):855–868, 2017.

[43] N. Prajapati, A. Abad Gonzalez, M. Selzer, B. Nestler, B. Busch, and C. Hilgers. Quartz cementation in polycrystalline sandstone: Insights from phase-field simulations. *Journal of Geophysical Research: Solid Earth*, page e2019JB019137, 2020.

[44] M. Heald and J. Renton. Experimental study of sandstone cementation. *Journal of Sedimentary Research*, 36(4):977–991, 1966.

[45] W. James, G. C. Wilmar, and B. G. Davidson. Role of quartz type and grain size in silica diagenesis, Nugget sandstone, south-central Wyoming. *Journal of Sedimentary Research*, 56(5):657–662, 1986.

[46] L. Thomas, N. Wooster, and W. Wooster. The hydrothermal synthesis of quartz. *Discussions of the Faraday Society*, 5:341–345, 1949.

[47] C. Cecil and M. Heald. Experimental investigation of the effects of grain coatings on quartz growth. *Journal of Sedimentary Research*, 41(2):582–584, 1971.

[48] A. Okamoto and K. Sekine. Textures of syntaxial quartz veins synthesized by hydrothermal experiments. *Journal of Structural Geology*, 33(12):1764–1775, 2011.

[49] A. Okamoto, H. Saishu, N. Hirano, and N. Tsuchiya. Mineralogical and textural variation of silica minerals in hydrothermal flow-through experiments: Implications for quartz vein formation. *Geochimica et Cosmochimica Acta*, 74(13):3692–3706, 2010.

[50] E. D. Pittman. Diagenesis of quartz in sandstones as revealed by scanning electron microscopy. *Journal of Sedimentary Research*, 42(3):507–519, 1972.

[51] G. Van Praagh. Synthetic quartz crystals. *Geological Magazine*, 84(2):98–100, 1947.

[52] A. Ballman and R. Laudise. Hydrothermal growth. In *J.J. Gilman(Ed.), The art and science of growing crystals*, pages 231–251. John Wiley and Sons, New York, 1963.

[53] P. D. Ihinger and S. I. Zink. Determination of relative growth rates of natural quartz crystals. *Nature*, 404(6780):865, 2000.

[54] K. Bjørlykke and J. Jahren. Sandstones and sandstone reservoirs. In *Petroleum Geoscience*, pages 119–149. Springer, Berlin, 2015.

[55] C. Hilgers, D. Kirschner, J.-P. Breton, and J. Urai. Fracture sealing and fluid overpressures in limestones of the Jabal Akhdar dome, Oman mountains. *Geofluids*, 6(2):168–184, 2006.

[56] P. D. Bons, M. A. Elburg, and E. Gomez-Rivas. A review of the formation of tectonic veins and their microstructures. *Journal of Structural Geology*, 43:33–62, 2012.

[57] D. D. McNamara, A. Lister, and D. J. Prior. Calcite sealing in a fractured geothermal reservoir: Insights from combined EBSD and chemistry mapping. *Journal of Volcanology and Geothermal Research*, 323:38–52, 2016.

[58] L. Plummer. Critical review of the kinetics of calcite dissolution and precipitation. *Chemical Modeling in Aqueous Systems.*, pages 539–573, 1979.

[59] J. S. Herman and M. M. Lorah. Calcite precipitation rates in the field: measurement and prediction for a travertine-depositing stream. *Geochimica et Cosmochimica Acta*, 52(10):2347–2355, 1988.

[60] J. Girard, B. Sanjuan, I. Czernichowski-Lauriol, and C. Fouillac. Diagenesis of the Oseberg Sandstone Reservoir (North Sea): an example of integration of core, formation fluid and geochemical modelling studies. In *Conference: Annual convention of the AAPG, Inc. and the Society for Sedimentary Geology: global exploration and geotechnology*, volume 5 (CONF-960527-), San Diego, 1996.

[61] A. Gutjahr, H. Dabringhaus, and R. Lacmann. Studies of the growth and dissolution kinetics of the CaCO3 polymorphs calcite and aragonite I. growth and dissolution rates in water. *Journal of Crystal Growth*, 158(3):296–309, 1996.

[62] D. Durney. Incremental strains measured by syntectonic crystal growths. In *Gravity and Tectonics (edited by De Jong, K.A. and Scholten, R.)*, pages 67–96. John Wiley and Sons, New York, 1973.

[63] J. G. Ramsay. The crack–seal mechanism of rock deformation. *Nature*, 284(5752):135, 1980.

[64] S. Cox and M. Etheridge. Crack-seal fibre growth mechanisms and their significance in the development of oriented layer silicate microstructures. *Tectonophysics*, 92(1-3):147–170, 1983.

[65] S. E. Laubach. Subsurface fractures and their relationship to stress history in East Texas Basin sandstone. *Tectonophysics*, 156(1-2):37–49, 1988.

[66] D. M. Fisher and S. L. Brantley. Models of quartz overgrowth and vein formation: deformation and episodic fluid flow in an ancient subduction zone. *Journal of Geophysical Research: Solid Earth*, 97(B13):20043–20061, 1992.

[67] C. Hilgers and J. L. Urai. Microstructural observations on natural syntectonic fibrous veins: implications for the growth process. *Tectonophysics*, 352(3-4):257–274, 2002.

[68] S. E. Laubach, R. M. Reed, J. E. Olson, R. Lander, and L. Bonnell. Coevolution of crack-seal texture and fracture porosity in sedimentary rocks: cathodoluminescence observations of regional fractures. *Journal of Structural Geology*, 26(5):967–982, 2004.

[69] C. Dezayes, A. Genter, and B. Valley. Structure of the low permeable naturally fractured geothermal reservoir at Soultz. *Comptes Rendus Geoscience*, 342(7-8):517–530, 2010.

[70] S. Haffen, Y. Géraud, M. Diraison, and C. Dezayes. Fluid-flow zones in a geothermal sandstone reservoir: localization from thermal conductivity and temperature logs, borehole eps1 (Soultz-sous-forêts, France). *Geothermics*, 46:32–41, 2013.

[71] J. F. Gale, S. E. Laubach, R. A. Marrett, J. E. Olson, J. Holder, and R. M. Reed. Predicting and characterizing fractures in dolostone reservoirs: Using the link between diagenesis and fracturing. *Geological Society, London, Special Publications*, 235(1):177–192, 2004.

[72] C. Hilgers, S. Nollet, J. Schonherr, and J. Urai. Paleo-overpressure formation and dissipation in reservoir rocks. *Oil Gas European Magazine*, 32(2):68, 2006.

[73] J. Lamarche, A. P. Lavenu, B. D. Gauthier, Y. Guglielmi, and O. Jayet. Relationships between fracture patterns, geodynamics and mechanical stratigraphy in Carbonates (South-East Basin, France). *Tectonophysics*, 581:231–245, 2012.

[74] P. Wuestefeld, M. De Medeiros, B. Koehrer, D. Sibbing, L. Kobbelt, and C. Hilgers. Automated workflow to derive LIDAR fracture statistics for the DFN modelling of a tight gas sandstone reservoir analog. In *78th EAGE Conference and Exhibition 2016*, pages 1–5. European Association of Geoscientists & Engineers, 2016.

[75] S. Becker, P. Eichhubl, S. E. Laubach, R. M. Reed, R. Lander, and R. Bodnar. A 48 my history of fracture opening, temperature, and fluid pressure: Cretaceous Travis Peak Formation, East Texas basin. *GSA Bulletin*, 122(7-8):1081–1093, 2010.

[76] S. Taber. The origin of veinlets in the Silurian and Devonian strata of central New York. *The Journal of Geology*, 26(1):56–73, 1918.

[77] W. Means and T. Li. A laboratory simulation of fibrous veins: some first observations. *Journal of Structural Geology*, 23(6-7):857–863, 2001.

[78] J. L. Urai, P. Williams, and H. Van Roermund. Kinematics of crystal growth in syntectonic fibrous veins. *Journal of Structural Geology*, 13(7):823–836, 1991.

[79] C. Hilgers, D. Koehn, P. Bons, and J. Urai. Development of crystal morphology during unitaxial growth in a progressively widening vein: II. Numerical simulations of the evolution of antitaxial fibrous veins. *Journal of Structural Geology*, 23(6-7):873–885, 2001.

[80] O. Mügge. Über die Entstehung faseriger Minerale und ihrer Aggregationsformen. *Neues Jahrbuch für Mineralogie, Geologie und Paläontologie A*, 58:303–438, 1928.

[81] S. E. Laubach, R. Lander, L. Bonnell, J. E. Olson, and R. M. Reed. Opening histories of fractures in sandstone. *Geological Society, London, Special Publications*, 231(1):1–9, 2004.

[82] J. Hooker, L. Gomez, S. E. Laubach, J. Gale, and R. Marrett. Effects of diagenesis (cement precipitation) during fracture opening on fracture aperture-size scaling in carbonate rocks. *Geological Society, London, Special Publications*, 370(1):187–206, 2012.

[83] R. Lander and S. E. Laubach. Insights into rates of fracture growth and sealing from a model for quartz cementation in fractured sandstones. *GSA Bulletin*, 127(3-4):516–538, 2015.

[84] J. F. Gale, R. H. Lander, R. M. Reed, and S. E. Laubach. Modeling fracture porosity evolution in dolostone. *Journal of Structural Geology*, 32(9):1201–1211, 2010.

[85] E. Ukar and S. E. Laubach. Syn-and postkinematic cement textures in fractured carbonate rocks: Insights from advanced cathodoluminescence imaging. *Tectonophysics*, 690:190–205, 2016.

[86] C. W. Passchier and R. A. Trouw. *Microtectonics*. Springer Science & Business Media, Berlin, 2005.

[87] P. A. Bjørkum and O. Walderhaug. Geometrical arrangement of calcite cementation within shallow marine sandstones. *Earth-Science Reviews*, 29(1-4):145–161, 1990.

[88] K. Bjorlykke and P. Egeberg. Quartz cementation in sedimentary basins. *AAPG Bulletin*, 77(9):1538–1548, 1993.

[89] N. Hartley and T. Wilshaw. Deformation and fracture of synthetic α-quartz. *Journal of Materials Science*, 8(2):265–278, 1973.

[90] B. Atkinson and V. Avdis. Fracture mechanics parameters of some rock-forming minerals determined using an indentation technique. In *International Journal of Rock Mechanics and Mining Sciences & Geomechanics Abstracts*, volume 17(6), pages 383–386. Pergamon-Elsevier Sceince Ltd., Oxford, 1980.

[91] M. Norton and B. Atkinson. Stress-dependent morphological features on fracture surfaces of quartz and glass. *Tectonophysics*, 77(3-4):283–295, 1981.

[92] C. C. Ferguson, G. E. Lloyd, and R. J. Knipe. Fracture mechanics and deformation processes in natural quartz: a combined vickers indentation, SEM, and TEM study. *Canadian Journal of Earth Sciences*, 24(3):544–555, 1987.

[93] B. K. Atkinson. Subcritical crack propagation in rocks: theory, experimental results and applications. *Journal of Structural Geology*, 4(1):41–56, 1982.

[94] R. L. Kranz. Microcracks in rocks: a review. *Tectonophysics*, 100(1-3):449–480, 1983.

[95] S. Boggs Jr. *Principles of sedimentology and stratigraphy*. Pearson Education, Upper Saddle River, New Jersey, 5^{th} edition, 2014.

[96] M. Canals and J. D. Meunier. A model for porosity reduction in quartzite reservoirs by quartz cementation. *Geochimica et Cosmochimica Acta*, 59(4):699–709, 1995.

[97] M. Wangen. Modeling porosity evolution and cementation of sandstones. *Marine and Petroleum Geology*, 15(5):453–465, 1998.

[98] M. Wangen. Modelling quartz cementation of quartzose sandstones. *Basin Research*, 11(2):113–126, 1999.

[99] P. A. Bjørkum, E. H. Oelkers, P. H. Nadeau, O. Walderhaug, and W. M. Murphy. Porosity prediction in quartzose sandstones as a function of time, temperature, depth, stylolite frequency, and hydrocarbon saturation. *AAPG Bulletin*, 82(4):637–648, 1998.

[100] R. H. Lander and O. Walderhaug. Predicting porosity through simulating sandstone compaction and quartz cementation. *AAPG Bulletin*, 83(3):433–449, 1999.

[101] A. M. Marchand, R. S. Haszeldine, P. C. Smalley, C. I. Macaulay, and A. E. Fallick. Evidence for reduced quartz-cementation rates in oil-filled sandstones. *Geology*, 29(10):915–918, 2001.

[102] S. Sliaupa. Predicting porosity through simulating quartz cementation of Middle Cambrian sandstones, West Lithuania. *Geological Quarterly*, 50(2):247–256, 2010.

[103] P. H. Nelson et al. Permeability-porosity relationships in sedimentary rocks. *The Log Analyst*, 35(3):38–62, 1994.

[104] Y. Bernabé, U. Mok, and B. Evans. Permeability-porosity relationships in rocks subjected to various evolution processes. *Pure and Applied Geophysics*, 160(5-6):937–960, 2003.

[105] J. Ma. Review of permeability evolution model for fractured porous media. *Journal of Rock Mechanics and Geotechnical Engineering*, 7(3):351–357, 2015.

[106] A. Makowitz, R. H. Lander, and K. L. Milliken. Diagenetic modeling to assess the relative timing of quartz cementation and brittle grain processes during compaction. *AAPG Bulletin*, 90(6):873–885, 2006.

[107] J. M. Ajdukiewicz and R. H. Lander. Sandstone reservoir quality prediction: The state of the art. *AAPG Bulletin*, 94(8):1083–1091, 2010.

[108] J. Zhang and J. B. Adams. FACET: a novel model of simulation and visualization of polycrystalline thin film growth. *Modelling and Simulation in Materials Science and Engineering*, 10(4):381, 2002.

[109] S. Nollet, J. L. Urai, P. D. Bons, and C. Hilgers. Numerical simulations of polycrystal growth in veins. *Journal of Structural Geology*, 27(2):217–230, 2005.

[110] F. Wendler, C. Mennerich, and B. Nestler. A phase-field model for polycrystalline thin film growth. *Journal of Crystal Growth*, 327(1):189–201, 2011.

[111] R. Qin and H. Bhadeshia. Phase field method. *Materials Science and Technology*, 26(7):803–811, 2010.

[112] H. Johannes, K. Michael, S. Philipp, and N. Britta. Applications of the phase-field method for the solidification of microstructures in multi-component systems. *Journal of the Indian Institute of Science*, 96(3):235–256, 2016.

[113] J. Kim. Phase-field models for multi-component fluid flows. *Communications in Computational Physics*, 12(3):613–661, 2012.

[114] Q. Du, C. Liu, and X. Wang. A phase field approach in the numerical study of the elastic bending energy for vesicle membranes. *Journal of Computational Physics*, 198(2):450–468, 2004.

[115] T. Biben, K. Kassner, and C. Misbah. Phase-field approach to three-dimensional vesicle dynamics. *Physical Review E*, 72(4):041921, 2005.

[116] X. Wang and Q. Du. Modelling and simulations of multi-component lipid membranes and open membranes via diffuse interface approaches. *Journal of Mathematical Biology*, 56(3):347–371, 2008.

[117] C. Peco, A. Rosolen, and M. Arroyo. An adaptive meshfree method for phase-field models of biomembranes. Part II: A Lagrangian approach for membranes in viscous fluids. *Journal of Computational Physics*, 249:320–336, 2013.

[118] E. Lima, J. Oden, and R. Almeida. A hybrid ten-species phase-field model of tumor growth. *Mathematical Models and Methods in Applied Sciences*, 24(13):2569–2599, 2014.

[119] X. Zhang and R. G. Jeffrey. Role of overpressurized fluid and fluid-driven fractures in forming fracture networks. *Journal of Geochemical Exploration*, 144:194–207, 2014.

[120] X. Wang, F. Shi, C. Liu, D. Lu, H. Liu, and H. Wu. Extended finite element simulation of fracture network propagation in formation containing frictional and cemented natural fractures. *Journal of Natural Gas Science and Engineering*, 50:309–324, 2018.

[121] S. Virgo, S. Abe, and J. L. Urai. Extension fracture propagation in rocks with veins: Insight into the crack-seal process using Discrete Element Method modeling. *Journal of Geophysical Research: Solid Earth*, 118(10):5236–5251, 2013.

[122] S. Virgo, S. Abe, and J. L. Urai. The evolution of crack seal vein and fracture networks in an evolving stress field: Insights from Discrete Element Models of fracture sealing. *Journal of Geophysical Research: Solid Earth*, 119(12):8708–8727, 2014.

[123] S. Virgo, S. Abe, and J. L. Urai. The influence of loading conditions on fracture initiation, propagation, and interaction in rocks with veins: Results from a comparative Discrete Element Method study. *Journal of Geophysical Research: Solid Earth*, 121(3):1730–1738, 2016.

[124] M. Mohammadnejad, H. Liu, A. Chan, S. Dehkhoda, and D. Fukuda. An overview on advances in computational fracture mechanics of rock. *Geosystem Engineering*, 7:1–24, 2018.

[125] I. Aranson, V. Kalatsky, and V. Vinokur. Continuum field description of crack propagation. *Physical Review Letters*, 85(1):118, 2000.

[126] A. Karma, D. A. Kessler, and H. Levine. Phase-field model of mode III dynamic fracture. *Physical Review Letters*, 87(4):045501, 2001.

[127] V. Hakim and A. Karma. Laws of crack motion and phase-field models of fracture. *Journal of the Mechanics and Physics of Solids*, 57(2):342–368, 2009.

[128] R. Spatschek, E. Brener, and A. Karma. Phase field modeling of crack propagation. *Philosophical Magazine*, 91(1):75–95, 2011.

[129] L. Eastgate, J. Sethna, M. Rauscher, T. Cretegny, C.-S. Chen, and C. Myers. Fracture in mode I using a conserved phase-field model. *Physical Review E*, 65(3):036117, 2002.

[130] H. Henry and H. Levine. Dynamic instabilities of fracture under biaxial strain using a phase field model. *Physical Review Letters*, 93(10):105504, 2004.

[131] B. Bourdin, G. A. Francfort, and J.-J. Marigo. Numerical experiments in revisited brittle fracture. *Journal of the Mechanics and Physics of Solids*, 48(4):797–826, 2000.

[132] B. Bourdin, G. A. Francfort, and J.-J. Marigo. The variational approach to fracture. *Journal of Elasticity*, 91(1-3):5–148, 2008.

[133] C. Kuhn and R. Müller. A phase field model for fracture. In *PAMM: Proceedings in Applied Mathematics and Mechanics*, volume 8(1), pages 10223–10224. Wiley Online Library, Berlin, 2008.

[134] C. Kuhn and R. Müller. A continuum phase field model for fracture. *Engineering Fracture Mechanics*, 77(18):3625–3634, 2010.

[135] H. Amor, J.-J. Marigo, and C. Maurini. Regularized formulation of the variational brittle fracture with unilateral contact: Numerical experiments. *Journal of the Mechanics and Physics of Solids*, 57(8):1209–1229, 2009.

[136] C. Miehe, F. Welschinger, and M. Hofacker. Thermodynamically consistent phase-field models of fracture: Variational principles and multi-field FE implementations. *International Journal for Numerical Methods in Engineering*, 83(10):1273–1311, 2010.

[137] M. J. Borden, T. J. Hughes, C. M. Landis, and C. V. Verhoosel. A higher-order phase-field model for brittle fracture: Formulation and analysis within the isogeometric analysis framework. *Computer Methods in Applied Mechanics and Engineering*, 273:100–118, 2014.

[138] L. D. Landau and V. Ginzburg. On the theory of superconductivity. *Zh. Eksp. Teor. Fiz.*, 20:1064, 1950.

[139] G. A. Francfort and J.-J. Marigo. Revisiting brittle fracture as an energy minimization problem. *Journal of the Mechanics and Physics of Solids*, 46(8):1319–1342, 1998.

[140] A. A. Griffith. VI. The phenomena of rupture and flow in solids. *Philosophical Transactions of the Royal Society of London. Series A, Containing Papers of a Mathematical or Physical Character*, 221(582-593):163–198, 1921.

[141] M. Ambati, T. Gerasimov, and L. De Lorenzis. A review on phase-field models of brittle fracture and a new fast hybrid formulation. *Computational Mechanics*, 55(2):383–405, 2015.

[142] R. Alessi, J.-J. Marigo, and S. Vidoli. Gradient damage models coupled with plasticity and nucleation of cohesive cracks. *Archive for Rational Mechanics and Analysis*, 214(2):575–615, 2014.

[143] R. Alessi, J.-J. Marigo, and S. Vidoli. Gradient damage models coupled with plasticity: variational formulation and main properties. *Mechanics of Materials*, 80:351–367, 2015.

[144] R. Alessi, J.-J. Marigo, C. Maurini, and S. Vidoli. Coupling damage and plasticity for a phase-field regularisation of brittle, cohesive and ductile fracture: one-dimensional examples. *International Journal of Mechanical Sciences*, 149:559–576, 2018.

[145] M. Ambati, T. Gerasimov, and L. De Lorenzis. Phase-field modeling of ductile fracture. *Computational Mechanics*, 55(5):1017–1040, 2015.

[146] M. Ambati, R. Kruse, and L. De Lorenzis. A phase-field model for ductile fracture at finite strains and its experimental verification. *Computational Mechanics*, 57(1):149–167, 2016.

[147] M. J. Borden, T. J. Hughes, C. M. Landis, A. Anvari, and I. J. Lee. A phase-field formulation for fracture in ductile materials: Finite deformation balance law derivation, plastic degradation, and stress triaxiality effects. *Computer Methods in Applied Mechanics and Engineering*, 312:130–166, 2016.

[148] F. P. Duda, A. Ciarbonetti, P. J. Sánchez, and A. E. Huespe. A phase-field/gradient damage model for brittle fracture in elastic–plastic solids. *International Journal of Plasticity*, 65:269–296, 2015.

[149] C. Kuhn, T. Noll, and R. Müller. On phase field modeling of ductile fracture. *GAMM-Mitteilungen*, 39(1):35–54, 2016.

[150] C. Miehe, S. Teichtmeister, and F. Aldakheel. Phase-field modelling of ductile fracture: a variational gradient-extended plasticity-damage theory and its micromorphic regularization. *Philosophical Transactions of the Royal Society A: Mathematical, Physical and Engineering Sciences*, 374(2066):20150170, 2016.

[151] R. Alessi, M. Ambati, T. Gerasimov, S. Vidoli, and L. De Lorenzis. Comparison of phase-field models of fracture coupled with plasticity. In *Advances in computational plasticity*, pages 1–21. Springer, Cham, 2018.

[152] J. Choo and W. Sun. Cracking and damage from crystallization in pores: Coupled chemo-hydro-mechanics and phase-field modeling. *Computer Methods in Applied Mechanics and Engineering*, 335:347–379, 2018.

[153] E. C. Bryant and W. Sun. A mixed-mode phase field fracture model in anisotropic rocks with consistent kinematics. *Computer Methods in Applied Mechanics and Engineering*, 342:561–584, 2018.

[154] J. Choo and W. Sun. Coupled phase-field and plasticity modeling of geological materials: From brittle fracture to ductile flow. *Computer Methods in Applied Mechanics and Engineering*, 330:1–32, 2018.

[155] S. Na and W. Sun. Computational thermomechanics of crystalline rock, part I: A combined multi-phase-field/crystal plasticity approach for single crystal simulations. *Computer Methods in Applied Mechanics and Engineering*, 338:657–691, 2018.

[156] A. Mikelić, M. F. Wheeler, and T. Wick. Phase-field modeling of a fluid-driven fracture in a poroelastic medium. *Computational Geosciences*, 19(6):1171–1195, 2015.

[157] A. Mikelić, M. F. Wheeler, and T. Wick. A quasi-static phase-field approach to pressurized fractures. *Nonlinearity*, 28(5):1371, 2015.

[158] S. Lee, M. F. Wheeler, and T. Wick. Pressure and fluid-driven fracture propagation in porous media using an adaptive finite element phase field model. *Computer Methods in Applied Mechanics and Engineering*, 305:111–132, 2016.

[159] Z. A. Wilson and C. M. Landis. Phase-field modeling of hydraulic fracture. *Journal of the Mechanics and Physics of Solids*, 96:264–290, 2016.

[160] Y. Heider and B. Markert. A phase-field modeling approach of hydraulic fracture in saturated porous media. *Mechanics Research Communications*, 80:38–46, 2017.

[161] C. Chukwudozie, B. Bourdin, and K. Yoshioka. A variational phase-field model for hydraulic fracturing in porous media. *Computer Methods in Applied Mechanics and Engineering*, 347:957–982, 2019.

[162] Y. U. Wang, Y. M. Jin, and A. G. Khachaturyan. Phase field microelasticity theory and simulation of multiple voids and cracks in single crystals and polycrystals under applied stress. *Journal of Applied Physics*, 91(10):6435–6451, 2002.

[163] A. Abdollahi and I. Arias. Numerical simulation of intergranular and transgranular crack propagation in ferroelectric polycrystals. *International Journal of Fracture*, 174(1):3–15, 2012.

[164] K. Oshima, T. Takaki, and M. Muramatsu. Development of multi-phase-field crack model for crack propagation in polycrystal. *International Journal of Computational Materials Science and Engineering*, 3(02):1450009, 2014.

[165] Z. Liu and D. Juhre. Phase-field modelling of crack propagation in anisotropic polycrystalline materials. *Procedia Structural Integrity*, 13:787–792, 2018.

[166] J. Clayton and J. Knap. Phase field modeling of directional fracture in anisotropic polycrystals. *Computational Materials Science*, 98:158–169, 2015.

[167] T.-T. Nguyen, J. Rethore, J. Yvonnet, and M.-C. Baietto. Multi-phase-field modeling of anisotropic crack propagation for polycrystalline materials. *Computational Mechanics*, 60(2):289–314, 2017.

[168] J. W. Cahn and J. E. Hilliard. Free energy of a nonuniform system. I. Interfacial free energy. *The Journal of Chemical Physics*, 28(2):258–267, 1958.

[169] S. M. Allen and J. W. Cahn. A microscopic theory for antiphase boundary motion and its application to antiphase domain coarsening. *Acta Metallurgica*, 27(6):1085–1095, 1979.

[170] B. Nestler, H. Garcke, and B. Stinner. Multicomponent alloy solidification: phase-field modeling and simulations. *Physical Review E*, 71(4):041609, 2005.

[171] Parallel algorithm for crystal evolution in 3-d. `https://www.hs-karlsruhe.de/idm/pace3d-software/`, 2015. Accessed: 2020-02-14.

[172] J. Hötzer, A. Reiter, H. Hierl, P. Steinmetz, M. Selzer, and B. Nestler. The parallel multi-physics phase-field framework Pace3d. *Journal of Computational Science*, 26:1–12, 2018.

[173] R. Rannacher. Methods for numerical flow simulation. In *Hemodynamical Flows. Modeling, Analysis and Simulation. Oberwolfach Seminars*, volume 37, pages 275–332. Birkhäuser Verlag, Basel, 2008.

[174] F. H. Harlow and J. E. Welch. Numerical calculation of time-dependent viscous incompressible flow of fluid with free surface. *The Physics of Fluids*, 8(12):2182–2189, 1965.

[175] N. Moelans. A quantitative and thermodynamically consistent phase-field interpolation function for multi-phase systems. *Acta Materialia*, 59(3):1077–1086, 2011.

[176] D. Schneider, O. Tschukin, A. Choudhury, M. Selzer, T. Böhlke, and B. Nestler. Phase-field elasticity model based on mechanical jump conditions. *Computational Mechanics*, 55(5):887–901, 2015.

[177] C. Herrmann, E. Schoof, D. Schneider, F. Schwab, A. Reiter, M. Selzer, and B. Nestler. Multiphase-field model of small strain elasto-plasticity according to the mechanical jump conditions. *Computational Mechanics*, 62(6):1399–1412, 2018.

[178] H. Westphal, G. P. Eberli, L. B. Smith, G. M. Grammer, and J. Kislak. Reservoir characterization of the Mississippian Madison formation, Wind river basin, Wyoming. *AAPG Bulletin*, 88(4):405–432, 2004.

[179] Q. Dou, Y. Sun, and C. Sullivan. Rock-physics-based carbonate pore type characterization and reservoir permeability heterogeneity evaluation, Upper San Andres reservoir, Permian Basin, west Texas. *Journal of Applied Geophysics*, 74(1):8–18, 2011.

[180] R. F. Sekerka. Equilibrium and growth shapes of crystals: how do they differ and why should we care? *Crystal Research and Technology: Journal of Experimental and Industrial Crystallography*, 40(4-5):291–306, 2005.

[181] Wikipedia: Calcite. `https://en.wikipedia.org/wiki/Calcite`. Accessed: 2019-11-22.

[182] Minerals.net: Calcite. `https://www.minerals.net/mineral/calcite.aspx`. Accessed: 2019-11-22.

[183] B. Nestler, F. Wendler, M. Selzer, B. Stinner, and H. Garcke. Phase-field model for multiphase systems with preserved volume fractions. *Physical Review E*, 78(1):011604, 2008.

[184] A. Vondrous, M. Reichardt, and B. Nestler. Growth rate distributions for regular two-dimensional grains with Read–Shockley grain boundary energy. *Modelling and Simulation in Materials Science and Engineering*, 22(2):025014, 2014.

[185] The quartz page. `http://www.quartzpage.de/gro_text.html`. Accessed: 2019-12-13.

[186] N. Prajapati, M. Selzer, and B. Nestler. Computational modeling of calcite cementation in saline limestone aquifers: a phase-field study. *Geothermal Energy*, 5(1):15, 2017.

[187] E. Ukar, S. E. Laubach, and R. Marrett. Quartz c-axis orientation patterns in fracture cement as a measure of fracture opening rate and a validation tool for fracture pattern models. *Geosphere*, 12(2):400–438, 2016.

[188] M. Plapp. Phase-field models. In *Multiphase Microfluidics: The Diffuse Interface Model*, pages 129–175. Springer, Vienna, 2012.

[189] C. J. Schenk. Porosity and textural characteristics of eolian stratification. *AAPG Bulletin*, 65(5):986–986, 1981.

[190] M. C. Demirel, A. Kuprat, D. George, and A. Rollett. Bridging simulations and experiments in microstructure evolution. *Physical Review Letters*, 90(1):016106, 2003.

[191] A. Netto. Pore-size distribution in sandstones. *AAPG Bulletin*, 77(6):1101–1104, 1993.

[192] H. Füchtbauer. Sandsteine. In *Sedimente und Sedimentgesteine, Sediment Petrologie (edited by Füchtbauer, H.)*, pages 94–187. Schweizerbart, Stuttgart, 4^{th} edition, 1988.

[193] A. Timur. An investigation of permeability, porosity, & residual water saturation relationships for sandstone reservoirs. *The Log Analyst*, 9(4):3–5, 1968.

[194] P. D. Trask. Origin and environment of source sediments. *Tulsa Geological Society Digest*, 2:24–30, 1933.

[195] S. G. Fryberger and C. J. Schenk. Pin stripe lamination: a distinctive feature of modern and ancient eolian sediments. *Sedimentary Geology*, 55(1-2):1–15, 1988.

[196] R. L. Folk. *Petrology of sedimentary rocks*. Hemphill publishing company, Austin, Texas, 1980.

[197] N. Arndt. Geothermal gradient. *Encyclopedia of astrobiology. Springer, Berlin, Heidelberg*, 2011.

[198] A. T. Bourgoyne Jr, K. K. Millheim, M. E. Chenevert, and F. S. Young Jr. *Applied drilling engineering*, volume 2. Society of Petroleum Engineers Textbook Series, Richardson, Texas, 1991.

[199] G. A. Parks. Surface and interfacial free energies of quartz. *Journal of Geophysical Research: Solid Earth*, 89(B6):3997–4008, 1984.

[200] M. B. Holness. Temperature and pressure dependence of quartz-aqueous fluid dihedral angles: the control of adsorbed H_2O on the permeability of quartzites. *Earth and Planetary Science Letters*, 117(3-4):363–377, 1993.

[201] J. D. Rimstidt and H. Barnes. The kinetics of silica-water reactions. *Geochimica et Cosmochimica Acta*, 44(11):1683–1699, 1980.

[202] P. Turner, S. Burley, D. Rey, and J. Prosser. Burial history of the Penrith sandstone (Lower Permian) deduced from the combined study of fluid inclusion and palaeomagnetic data. *Geological Society, London, Special Publications*, 98(1):43–78, 1995.

[203] Blender–a 3d modelling and rendering package. `http://www.blender.org`. Accessed: 2020-3-25.

[204] O. Walderhaug, A. Eliassen, and N. E. Aase. Prediction of permeability in quartz-rich sandstones: examples from the Norwegian continental shelf and the Fontainebleau sandstone. *Journal of Sedimentary Research*, 82(12):899–912, 2012.

[205] H. Blatt, R. Tracy, and B. Owens. *Petrology: igneous, sedimentary, and metamorphic*. W.H. Freeman, New York, 3^{rd} edition, 2006.

[206] P. Heyliger, H. Ledbetter, and S. Kim. Elastic constants of natural quartz. *The Journal of the Acoustical Society of America*, 114(2):644–650, 2003.

[207] E. Calderon, M. Gauthier, F. Decremps, G. Hamel, G. Syfosse, and A. Polian. Complete determination of the elastic moduli of α-quartz under hydrostatic pressure up to 1 GPa: an ultrasonic study. *Journal of Physics: Condensed Matter*, 19(43):436228, 2007.

[208] T. Kling, J.-O. Schwarz, F. Wendler, F. Enzmann, and P. Blum. Fracture flow due to hydrothermally induced quartz growth. *Advances in Water Resources*, 107:93–107, 2017.

[209] B. Busch. *Impact of grain coats on quartz overgrowth and Reservoir properties*. KIT Scientific Publishing, Karlsruhe, 2017.

[210] C. Miehe, N. Apel, and M. Lambrecht. Anisotropic additive plasticity in the logarithmic strain space: modular kinematic formulation and implementation based on incremental minimization principles for standard materials. *Computer methods in Applied Mechanics and Engineering*, 191(47-48):5383–5425, 2002.

[211] T. Gerasimov and L. De Lorenzis. A line search assisted monolithic approach for phase-field computing of brittle fracture. *Computer Methods in Applied Mechanics and Engineering*, 312:276–303, 2016.